High-p_T jets in $\bar{p}p$ collisions at $\sqrt{s}=630$ and 1800 GeV

B. Abbott,[56] A. Abdesselam,[11] M. Abolins,[49] V. Abramov,[24] B. S. Acharya,[16] D. L. Adams,[58] M. Adams,[36] G. A. Alves,[2] N. Amos,[48] E. W. Anderson,[41] R. Astur,[53] M. M. Baarmand,[53] V. V. Babintsev,[24] L. Babukhadia,[53] T. C. Bacon,[26] A. Baden,[45] B. Baldin,[35] P. W. Balm,[19] S. Banerjee,[16] E. Barberis,[28] P. Baringer,[42] J. F. Bartlett,[35] U. Bassler,[12] D. Bauer,[26] A. Bean,[42] M. Begel,[52] A. Belyaev,[23] S. B. Beri,[14] G. Bernardi,[12] I. Bertram,[25] A. Besson,[9] R. Beuselinck,[26] V. A. Bezzubov,[24] P. C. Bhat,[35] V. Bhatnagar,[11] M. Bhattacharjee,[53] G. Blazey,[37] S. Blessing,[33] A. Boehnlein,[35] N. I. Bojko,[24] F. Borcherding,[35] A. Brandt,[58] R. Breedon,[29] G. Briskin,[57] R. Brock,[49] G. Brooijmans,[35] A. Bross,[35] D. Buchholz,[38] M. Buehler,[36] V. Buescher,[52] V. S. Burtovoi,[24] J. M. Butler,[46] F. Canelli,[52] W. Carvalho,[3] D. Casey,[49] Z. Casilum,[53] H. Castilla-Valdez,[18] D. Chakraborty,[53] K. M. Chan,[52] S. V. Chekulaev,[24] D. K. Cho,[52] S. Choi,[32] S. Chopra,[54] J. H. Christenson,[35] M. Chung,[36] D. Claes,[50] A. R. Clark,[28] J. Cochran,[32] L. Coney,[40] B. Connolly,[33] W. E. Cooper,[35] D. Coppage,[42] M. A. C. Cummings,[37] D. Cutts,[57] G. A. Davis,[52] K. Davis,[27] K. De,[58] K. Del Signore,[48] M. Demarteau,[35] R. Demina,[43] P. Demine,[9] D. Denisov,[35] S. P. Denisov,[24] S. Desai,[53] H. T. Diehl,[35] M. Diesburg,[35] G. Di Loreto,[49] S. Doulas,[47] P. Draper,[58] Y. Ducros,[13] L. V. Dudko,[23] S. Duensing,[20] L. Duflot,[11] S. R. Dugad,[16] A. Dyshkant,[24] D. Edmunds,[49] J. Ellison,[32] V. D. Elvira,[35] R. Engelmann,[53] S. Eno,[45] G. Eppley,[60] P. Ermolov,[23] O. V. Eroshin,[24] J. Estrada,[52] H. Evans,[51] V. N. Evdokimov,[24] T. Fahland,[31] M. K. Fatyga,[52] S. Feher,[35] D. Fein,[27] T. Ferbel,[52] H. E. Fisk,[35] Y. Fisyak,[54] E. Flattum,[35] F. Fleuret,[28] M. Fortner,[37] K. C. Frame,[49] S. Fuess,[35] E. Gallas,[35] A. N. Galyaev,[24] M. Gao,[51] V. Gavrilov,[22] T. L. Geld,[49] R. J. Genik II,[25] K. Genser,[35] C. E. Gerber,[36] Y. Gershtein,[57] R. Gilmartin,[33] G. Ginther,[52] B. Gómez,[5] G. Gómez,[45] P. I. Goncharov,[24] J. L. González Solís,[18] H. Gordon,[54] L. T. Goss,[59] K. Gounder,[32] A. Goussiou,[53] N. Graf,[54] G. Graham,[45] P. D. Grannis,[53] J. A. Green,[41] H. Greenlee,[35] S. Grinstein,[1] L. Groer,[51] S. Grünendahl,[35] A. Gupta,[16] S. N. Gurzhiev,[24] G. Gutierrez,[35] P. Gutierrez,[56] N. J. Hadley,[45] H. Haggerty,[35] S. Hagopian,[33] V. Hagopian,[33] K. S. Hahn,[52] R. E. Hall,[30] P. Hanlet,[47] S. Hansen,[35] J. M. Hauptman,[41] C. Hays,[51] C. Hebert,[42] D. Hedin,[37] A. P. Heinson,[32] U. Heintz,[46] T. Heuring,[33] R. Hirosky,[61] J. D. Hobbs,[53] B. Hoeneisen,[8] J. S. Hoftun,[57] S. Hou,[48] Y. Huang,[48] R. Illingworth,[26] A. S. Ito,[35] M. Jaffré,[11] S. A. Jerger,[49] R. Jesik,[39] K. Johns,[27] M. Johnson,[35] A. Jonckheere,[35] M. Jones,[34] H. Jöstlein,[35] A. Juste,[35] S. Kahn,[54] E. Kajfasz,[10] D. Karmanov,[23] D. Karmgard,[40] R. Kehoe,[40] S. K. Kim,[17] B. Klima,[35] C. Klopfenstein,[29] B. Knuteson,[28] W. Ko,[29] J. M. Kohli,[14] A. V. Kostritskiy,[24] J. Kotcher,[54] A. V. Kotwal,[51] A. V. Kozelov,[24] E. A. Kozlovsky,[24] J. Krane,[41] M. R. Krishnaswamy,[16] S. Krzywdzinski,[35] M. Kubantsev,[43] S. Kuleshov,[22] Y. Kulik,[53] S. Kunori,[45] V. E. Kuznetsov,[32] G. Landsberg,[57] A. Leflat,[23] C. Leggett,[28] F. Lehner,[35] J. Li,[58] Q. Z. Li,[35] J. G. R. Lima,[3] D. Lincoln,[35] S. L. Linn,[33] J. Linnemann,[49] R. Lipton,[35] A. Lucotte,[9] L. Lueking,[35] C. Lundstedt,[50] C. Luo,[39] A. K. A. Maciel,[37] R. J. Madaras,[28] V. Manankov,[23] H. S. Mao,[4] T. Marshall,[39] M. I. Martin,[35] R. D. Martin,[36] K. M. Mauritz,[41] B. May,[38] A. A. Mayorov,[39] R. McCarthy,[53] J. McDonald,[33] T. McMahon,[55] H. L. Melanson,[35] X. C. Meng,[4] M. Merkin,[23] K. W. Merritt,[35] C. Miao,[57] H. Miettinen,[60] D. Mihalcea,[56] C. S. Mishra,[35] N. Mokhov,[35] N. K. Mondal,[16] H. E. Montgomery,[35] R. W. Moore,[49] M. Mostafa,[1] H. da Motta,[2] E. Nagy,[10] F. Nang,[27] M. Narain,[46] V. S. Narasimham,[16] H. A. Neal,[48] J. P. Negret,[5] S. Negroni,[10] D. Norman,[59] T. Nunnemann,[35] L. Oesch,[48] V. Oguri,[3] B. Olivier,[12] N. Oshima,[35] P. Padley,[60] L. J. Pan,[38] K. Papageorgiou,[26] A. Para,[35] N. Parashar,[47] R. Partridge,[57] N. Parua,[53] M. Paterno,[52] A. Patwa,[53] B. Pawlik,[21] J. Perkins,[58] M. Peters,[34] O. Peters,[19] P. Pétroff,[11] R. Piegaia,[1] H. Piekarz,[33] B. G. Pope,[49] E. Popkov,[46] H. B. Prosper,[33] S. Protopopescu,[54] J. Qian,[48] P. Z. Quintas,[35] R. Raja,[35] S. Rajagopalan,[54] E. Ramberg,[35] P. A. Rapidis,[35] N. W. Reay,[43] S. Reucroft,[47] J. Rha,[32] M. Ridel,[11] M. Rijssenbeek,[53] T. Rockwell,[49] M. Roco,[35] P. Rubinov,[35] R. Ruchti,[40] J. Rutherfoord,[27] A. Santoro,[2] L. Sawyer,[44] R. D. Schamberger,[53] H. Schellman,[38] A. Schwartzman,[1] N. Sen,[60] E. Shabalina,[23] R. K. Shivpuri,[15] D. Shpakov,[47] M. Shupe,[27] R. A. Sidwell,[43] V. Simak,[7] H. Singh,[32] J. B. Singh,[14] V. Sirotenko,[35] P. Slattery,[52] E. Smith,[56] R. P. Smith,[35] R. Snihur,[38] G. R. Snow,[50] J. Snow,[55] S. Snyder,[54] J. Solomon,[36] V. Sorín,[1] M. Sosebee,[58] N. Sotnikova,[23] K. Soustruznik,[6] M. Souza,[2] N. R. Stanton,[43] G. Steinbrück,[51] R. W. Stephens,[58] F. Stichelbaut,[54] D. Stoker,[31] V. Stolin,[22] D. A. Stoyanova,[24] M. Strauss,[56] M. Strovink,[28] L. Stutte,[35] A. Sznajder,[3] W. Taylor,[53] S. Tentindo-Repond,[33] J. Thompson,[45] D. Toback,[45] S. M. Tripathi,[29] T. G. Trippe,[28] A. S. Turcot,[54] P. M. Tuts,[51] P. van Gemmeren,[35] V. Vaniev,[24] R. Van Kooten,[39] N. Varelas,[36] A. A. Volkov,[24] A. P. Vorobiev,[24] H. D. Wahl,[33] H. Wang,[38] Z.-M. Wang,[53] J. Warchol,[40] G. Watts,[62] M. Wayne,[40] H. Weerts,[49] A. White,[58] J. T. White,[59] D. Whiteson,[28] J. A. Wightman,[41] D. A. Wijngaarden,[20] S. Willis,[37] S. J. Wimpenny,[32] J. V. D. Wirjawan,[59] J. Womersley,[35] D. R. Wood,[47] R. Yamada,[35] P. Yamin,[54] T. Yasuda,[35] K. Yip,[54] S. Youssef,[33] J. Yu,[35] Z. Yu,[38] M. Zanabria,[5] H. Zheng,[40] Z. Zhou,[41] M. Zielinski,[52] D. Zieminska,[39] A. Zieminski,[39] V. Zutshi,[52] E. G. Zverev,[23] and A. Zylberstejn[13]

(DØ Collaboration)

[1]*Universidad de Buenos Aires, Buenos Aires, Argentina*
[2]*LAFEX, Centro Brasileiro de Pesquisas Físicas, Rio de Janeiro, Brazil*
[3]*Universidade do Estado do Rio de Janeiro, Rio de Janeiro, Brazil*
[4]*Institute of High Energy Physics, Beijing, People's Republic of China*
[5]*Universidad de los Andes, Bogotá, Colombia*
[6]*Charles University, Prague, Czech Republic*

 ©2001 The American Physical Society

[7]*Institute of Physics, Academy of Sciences, Prague, Czech Republic*
[8]*Universidad San Francisco de Quito, Quito, Ecuador*
[9]*Institut des Sciences Nucléaires, IN2P3-CNRS, Universite de Grenoble 1, Grenoble, France*
[10]*CPPM, IN2P3-CNRS, Université de la Méditerranée, Marseille, France*
[11]*Laboratoire de l'Accélérateur Linéaire, IN2P3-CNRS, Orsay, France*
[12]*LPNHE, Universités Paris VI and VII, IN2P3-CNRS, Paris, France*
[13]*DAPNIA/Service de Physique des Particules, CEA, Saclay, France*
[14]*Panjab University, Chandigarh, India*
[15]*Delhi University, Delhi, India*
[16]*Tata Institute of Fundamental Research, Mumbai, India*
[17]*Seoul National University, Seoul, Korea*
[18]*CINVESTAV, Mexico City, Mexico*
[19]*FOM-Institute NIKHEF and University of Amsterdam/NIKHEF, Amsterdam, The Netherlands*
[20]*University of Nijmegen/NIKHEF, Nijmegen, The Netherlands*
[21]*Institute of Nuclear Physics, Kraków, Poland*
[22]*Institute for Theoretical and Experimental Physics, Moscow, Russia*
[23]*Moscow State University, Moscow, Russia*
[24]*Institute for High Energy Physics, Protvino, Russia*
[25]*Lancaster University, Lancaster, United Kingdom*
[26]*Imperial College, London, United Kingdom*
[27]*University of Arizona, Tucson, Arizona 85721*
[28]*Lawrence Berkeley National Laboratory and University of California, Berkeley, California 94720*
[29]*University of California, Davis, California 95616*
[30]*California State University, Fresno, California 93740*
[31]*University of California, Irvine, California 92697*
[32]*University of California, Riverside, California 92521*
[33]*Florida State University, Tallahassee, Florida 32306*
[34]*University of Hawaii, Honolulu, Hawaii 96822*
[35]*Fermi National Accelerator Laboratory, Batavia, Illinois 60510*
[36]*University of Illinois at Chicago, Chicago, Illinois 60607*
[37]*Northern Illinois University, DeKalb, Illinois 60115*
[38]*Northwestern University, Evanston, Illinois 60208*
[39]*Indiana University, Bloomington, Indiana 47405*
[40]*University of Notre Dame, Notre Dame, Indiana 46556*
[41]*Iowa State University, Ames, Iowa 50011*
[42]*University of Kansas, Lawrence, Kansas 66045*
[43]*Kansas State University, Manhattan, Kansas 66506*
[44]*Louisiana Tech University, Ruston, Louisiana 71272*
[45]*University of Maryland, College Park, Maryland 20742*
[46]*Boston University, Boston, Massachusetts 02215*
[47]*Northeastern University, Boston, Massachusetts 02115*
[48]*University of Michigan, Ann Arbor, Michigan 48109*
[49]*Michigan State University, East Lansing, Michigan 48824*
[50]*University of Nebraska, Lincoln, Nebraska 68588*
[51]*Columbia University, New York, New York 10027*
[52]*University of Rochester, Rochester, New York 14627*
[53]*State University of New York, Stony Brook, New York 11794*
[54]*Brookhaven National Laboratory, Upton, New York 11973*
[55]*Langston University, Langston, Oklahoma 73050*
[56]*University of Oklahoma, Norman, Oklahoma 73019*
[57]*Brown University, Providence, Rhode Island 02912*
[58]*University of Texas, Arlington, Texas 76019*
[59]*Texas A&M University, College Station, Texas 77843*
[60]*Rice University, Houston, Texas 77005*
[61]*University of Virginia, Charlottesville, Virginia 22901*
[62]*University of Washington, Seattle, Washington 98195*
(Received 4 January 2001; published 11 July 2001)

Results are presented from analyses of jet data produced in $p\overline{p}$ collisions at $\sqrt{s}=630$ and 1800 GeV collected with the DØ detector during the 1994–1995 Fermilab Tevatron Collider run. We discuss the details of detector calibration, and jet selection criteria in measurements of various jet production cross sections at $\sqrt{s}=630$ and 1800 GeV. The inclusive jet cross sections, the dijet mass spectrum, the dijet angular distributions, and the ratio of inclusive jet cross sections at $\sqrt{s}=630$ and 1800 GeV are compared to next-to-leading-order QCD predictions. The order α_s^3 calculations are in good agreement with the data. We also use the data at $\sqrt{s}=1800$ GeV to rule out models of quark compositeness with a contact interaction scale less than 2.2 TeV at the 95% confidence level.

DOI: 10.1103/PhysRevD.64.032003 PACS number(s): 12.38.Qk, 12.60.Rc

I. INTRODUCTION

The quark model which suggested that hadrons are composite particles was first proposed in the early 1960s [1] and was confirmed as the quark-parton model in a series of experiments at the Stanford Linear Accelerator Center in the late 1960s and early 1970s [2]. The model developed during the 1970s into the theory of strong interactions, quantum chromodynamics (QCD) [3], which describes the interactions of quarks and gluons (called partons). Together with the theory of electroweak interactions, QCD forms the foundation of the standard model of particle physics (SM), which, thus far, describes accurately the interactions of all known elementary particles.

Perturbative QCD (PQCD) [3] predicts the production cross sections at large transverse momentum (p_T) for parton-parton scattering in proton-antiproton ($p\overline{p}$) collisions [4–8]. The outgoing partons from the parton-parton scattering hadronize to form jets of particles. High-p_T jets were observed clearly during experimentation at the CERN Intersecting Storage Rings (ISR) [9] and the CERN $p\overline{p}$ collider [10]. Significant deviations from predictions of PQCD can only be observed if the uncertainties in both experimental measurements and theoretical predictions are small. Calculations of high-p_T jet production involve the folding of parton scattering cross sections with experimentally determined parton distribution functions (PDFs). These predictions have recently improved with next-to-leading-order (NLO) QCD calculations [11–13] and improved PDFs [14,15]. These $\mathcal{O}(\alpha_S{}^3)$ predictions reduce theoretical uncertainties to $\sim$30% [16] (where α_S is the strong coupling parameter).

In this paper we describe the production of hadronic jets as observed with the DØ detector at the Fermilab Tevatron $p\overline{p}$ collider at center-of-mass (c.m.) energies of 630 and 1800 GeV. High p_T jet production at $\sqrt{s}=1800$ GeV probes the structure of the proton where the interacting partons carry a fraction of the proton momentum, $0.1\lesssim x\lesssim 0.66$, for momentum transfers (Q) of $2.5\times 10^3\lesssim Q^2\lesssim 2.3\times 10^5$ GeV^2, where $Q^2=E_T^2$ and is equivalent to a distance scale of 10^{-4} fm (see Fig. 1). Measurements of the inclusive jet cross section, the dijet angular distribution, and the dijet mass spectrum, can be used to test the predictions of PQCD. Additionally, new phenomena such as quark compositeness [17] would reveal themselves as an excess of jet production at large transverse energy ($E_{\rm T}$) and dijet mass (M) relative to the predictions of QCD.

Previous measurements by the Collider Detector at Fermilab (CDF) Collaboration of the inclusive jet cross section [6,7] and the inclusive dijet mass spectrum [18] have reported an excess of jet production relative to a specific QCD prediction. More recent analysis of the dijet angular distribution by the CDF Collaboration [19] has excluded models of quark compositeness in which the contact interaction scale is less than 1.6 TeV at the 95% confidence level.

This paper presents a detailed description of five measurements previously published by the DØ Collaboration: the inclusive jet cross sections at $\sqrt{s}=1800$ GeV [8,20] and 630 GeV [21,22], the ratio of inclusive jet cross sections at $\sqrt{s}=630$ and 1800 GeV [21,22], the dijet angular distribution [23,24], and the dijet mass spectrum [25] at $\sqrt{s}=1800$ GeV. In addition to the analyses presented in this paper, DØ has recently measured the inclusive jet cross section as a function of $E_{\rm T}$ and pseudorapidity, $|\eta|$, at $\sqrt{s}=1800$ GeV [26] where $\eta\equiv-\ln[\tan(\theta/2)]$ and θ is the polar angle.

For jet measurements, the most critical component of the DØ detector is the calorimeter [28]. A thorough understanding of the jet energy scale, jet resolutions, and knowledge of biases caused by jet triggering and reconstruction are necessary. After detector calibration, small experimental uncertainties can be achieved and precise statements can be made about the validity of QCD predictions. These results can then be used as the basis for searches for physics beyond the standard model.

In this paper we discuss the theoretical predictions for the inclusive jet cross section, the inclusive dijet mass cross section, and the dijet angular distribution. We describe the various measurements undertaken to understand and calibrate the DØ detector for jet measurements. Finally, four different physics measurements performed at DØ are presented: the inclusive jet cross section, the ratio of inclusive jet cross sections, the dijet angular distribution, and the dijet mass spectrum. The measurements presented here constitute a stringent test of QCD, with a total uncertainty substantially reduced relative to previous measurements. Further, the results represent improved limits on the existence of phenomena not predicted by the standard model.

II. CALORIMETER

The DØ detector is described in detail elsewhere [28,29]. The DØ uranium-liquid argon sampling calorimeters are uniform in structure and provide coverage for a pseudorapidity range $|\eta|<4.5$. They are nearly compensating with an e/π

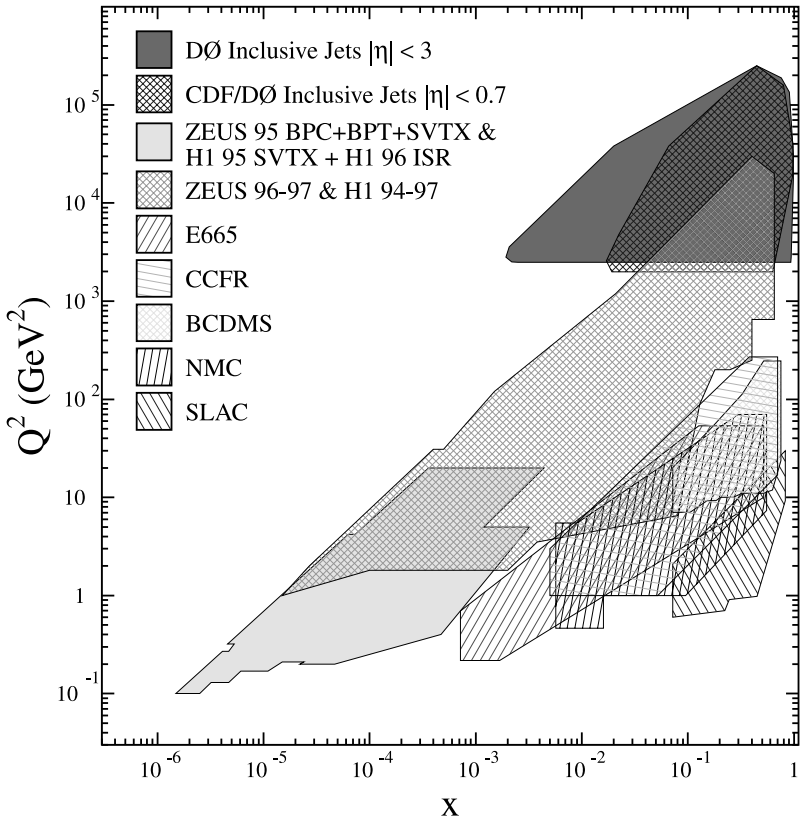

FIG. 1. The x and Q^2 range of the data set analyzed by the DØ experiment at $\sqrt{s}=1.8$ TeV (DØ [8] and CDF [7] inclusive jets with $|\eta|<0.7$) compared with the data used to produce PDFs [27]. Also shown is the extended x and Q^2 reach of the DØ measurement of the inclusive jet cross section with $|\eta|<3$ as presented in Ref. [26].

ratio of less than 1.05 above 30 GeV. The central and end calorimeters are approximately 7 and 9 interaction lengths deep respectively, ensuring containment of most particles except high-p_T muons and neutrinos. The calorimeters are segmented into cells of size $\Delta\eta\times\Delta\phi=0.1\times0.1$, where ϕ is the azimuthal angle. These characteristics along with excellent energy resolution for electrons ($\sim15\%/\sqrt{E[\mathrm{GeV}]}$) and pions ($\sim50\%/\sqrt{E[\mathrm{GeV}]}$) make the DØ calorimeters especially well suited for jet measurements.

The calorimeter is divided into three sections (see Fig. 2): a central calorimeter (CC) covering low values of pseudorapidity, two end calorimeters (EC) covering forward and backward pseudorapidities, and the Intercryostat Detector (ICD) covering the gaps between the CC and EC ($0.8\leqslant|\eta|\leqslant1.6$). The CC and EC calorimeters each consist of an inner electromagnetic (EM) section, a fine hadronic (FH) section, and a coarse hadronic (CH) section. Each EM section is 21 radiation lengths deep and is divided into four longitudinal samples. The hadronic sections are divided into four (CC) and five (EC) layers. The ICD consists of scintillator tiles inserted in the space between the CC and EC cryostats. The Tevatron accelerator's Main Ring, which is used for preaccelerating protons, passes through the CH calorimeters.

III. JET DEFINITIONS

A jet is a collection of collimated particles produced by the hadronization of a high-E_{T} quark or gluon. In the measurements presented in this paper, we measure the energy and direction of the jets produced in $p\bar{p}$ interactions and compare the measurements to various theoretical predictions.

In addition to the jets produced by the high-p_T parton-parton scattering, there are many particles produced by the hadronization of the partons in the proton and antiproton that were not involved in the hard scattering process. Because of this there is no unequivocal method for experimentally selecting the particles that belong to a jet produced in high-p_T scattering. It is preferable to use a standard definition of a jet to facilitate comparisons of measurements from different experiments, and with theoretical predictions. In 1990 the so-called Snowmass Jet Algorithm [30] was adopted as a standard definition.

A jet algorithm can be run on several different input variables: calorimeter cells, and particles or partons produced by a Monte Carlo simulation. To differentiate the results of the same algorithm being run on these different input we describe the resulting jets as follows: A jet (or calorimeter jet) is the result of the jet algorithm being run on calorimeter cells; a particle jet is created from particles produced by a Monte Carlo simulation after the hadronization step; finally, a parton jet is formed from partons before hadronization takes place.

A. The Snowmass accord

The Snowmass Jet Algorithm defines a jet as a collection of partons, particles, or calorimeter cells contained within a cone of opening angle $\mathcal{R}$. All objects in an event have a distance from the jet center, $\mathcal{R}_i\equiv\sqrt{(\eta_i-\eta_{\mathrm{jet}})^2+(\phi_i-\phi_{\mathrm{jet}})^2}$, where η_{jet} and ϕ_{jet} define the direction of the jet and (η_i, ϕ_i), are the coordinates of the parton, particle, or center of

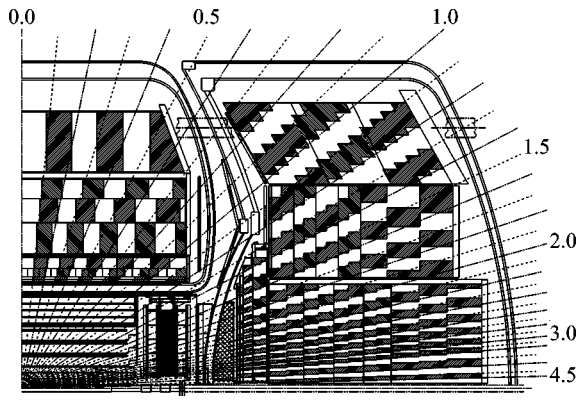

FIG. 2. A schematic view of one quarter of the DØ calorimeters. The shading pattern indicates the distinct readout cells. The rays indicate the pseudorapidity intervals defined from the center of the detector.

the calorimeter cell. If $\mathcal{R}_i \leqslant \mathcal{R}$ then the object is part of the jet. The Snowmass suggested value of $\mathcal{R}=0.7$ was used in these measurements. The E_{T} of the jet is given by

$$E_{\mathrm{T}} \equiv \sum_{i \in \mathcal{R}_i \leqslant \mathcal{R}} E_T^i, \tag{3.1}$$

where i is an index for the ith parton or cell. The direction of the jet is then given by

$$\eta_{\mathrm{jet}} = \frac{1}{E_{\mathrm{T}}} \sum_{i \in \mathcal{R}_i \leqslant \mathcal{R}} E_T^i \eta^i, \tag{3.2}$$

$$\phi_{\mathrm{jet}} = \frac{1}{E_{\mathrm{T}}} \sum_{i \in \mathcal{R}_i \leqslant \mathcal{R}} E_T^i \phi^i.$$

The Snowmass algorithm gives a procedure for finding the jets:

Determine a list of jet "seeds," each with a location η_{jet}, ϕ_{jet}.

Form a jet cone with direction η_{jet}, ϕ_{jet}.

Recalculate the E_{T} and direction of the jet.

Repeat steps 2 and 3 until the jet direction is stable.

The definition of the jet seed is not given by the algorithm. At the parton level these seeds could be the partons, points lying between pairs of partons, or even a set of points randomly located in η-ϕ space. Experimentally, the seed could be defined as any cell above a given E_{T} threshold, all cells in the calorimeter, or clusters of calorimeter cells. It is up to each experimentalist or theorist to define a seed.

B. The DØ experiment's jet algorithm

At the calorimeter level in the DØ experiment, jets are defined in two sequential procedures. In the first, or clustering, procedure all the energy depositions that belong to a jet are accumulated, and in the second the η, ϕ, and E_{T} of the jet are defined. The clustering consists of the following steps:

(1) Calorimeter towers (a set of four calorimeter cells of size $\Delta\eta \times \Delta\phi = 0.2 \times 0.2$) with $E_{\mathrm{T}} > 1$ GeV are ordered in E_{T}. Starting with the highest-E_{T} tower, preclusters are formed from contiguous towers around these seed towers.

(2) The jet direction ($\eta_{\mathrm{jet}}, \phi_{\mathrm{jet}}$) is calculated using Eq. (3.2) from the energy deposit pattern in a fixed cone of size $\mathcal{R}$ around the precluster center.

(3) The energy deposited in a cone of size $\mathcal{R}$ around the jet axis is summed and the jet direction ($\eta_{\mathrm{jet}}, \phi_{\mathrm{jet}}$) is recalculated using the Snowmass algorithm [Eq. (3.2)].

(4) Step (3) is iterated until the jet direction is stable. This is typically achieved in two or three iterations.

(5) Only jets with $E_{\mathrm{T}} > 8$ GeV are retained.

(6) Jets are merged or split according to the following criteria: two jets are merged into one jet if more than 50% of the E_{T} of the jet with the smaller E_{T} is contained in the overlap region. If less than 50% of the E_{T} is contained in the overlap region, the jets are split into two distinct jets and the energy of each calorimeter cell in the overlap region is assigned to the nearest jet. The jet directions are recalculated using an alternative definition as given in Eq. (3.3).

The DØ jet algorithm and the Snowmass algorithm calculate the final direction of the jet differently. In the DØ jet algorithm the final η and ϕ of the jet are defined as

$$\theta_{\mathrm{jet}} = \tan^{-1}\left[\frac{\sqrt{\left(\sum_i E_x^i\right)^2 + \left(\sum_i E_y^i\right)^2}}{\sum_i E_z^i}\right]$$

$$\phi_{\mathrm{jet}} = \tan^{-1}\left(\frac{\sum_i E_y^i}{\sum_i E_x^i}\right) \tag{3.3}$$

$$\eta_{\mathrm{jet}} = -\ln[\tan(\theta_{\mathrm{jet}}/2)]$$

where i corresponds to all towers whose centers are within the jet radius $\mathcal{R}$, $E_x^i = E_i \sin\theta_i \cos\phi_i$, $E_y^i = E_i \sin\theta_i \sin\phi_i$, and $E_z^i = E_i \cos\theta_i$.

Applying the 8 GeV E_{T} threshold to jets before merging and splitting has two important consequences. The first is that two jets of $E_{\mathrm{T}} < 8$ GeV cannot be merged into a single jet to create a jet with $E_{\mathrm{T}} > 8$ GeV. The second is that jets may have $E_{\mathrm{T}} < 8$ GeV if they were involved in splitting.

C. Corrected jets

In this paper a "true" or corrected jet is the jet that would be found by the DØ jet algorithm if it was applied to the particles produced by the high-p_T parton-parton scattering before they hit the calorimeter. The jet does not include the particles produced by hadronization of the partons not involved in the hard scattering (the underlying event). The differences between jets observed in the calorimeter and the "true" jets are determined using Monte Carlo (MC) simulations of $p\bar{p}$ interactions. The direction and E_{T} of the "true"

jets are calculated using the Snowmass definition [see Eqs. (3.1) and (3.2)] and are denoted by $E_T^{\rm ptcl}$, $\eta^{\rm ptcl}$, and $\phi^{\rm ptcl}$ (where ptcl denotes particle).

D. Differences between the DØ and Snowmass algorithms in data

Because the DØ and Snowmass algorithms calculate the location, and hence angle, of the jet differently, a study to measure the differences was performed. The same data events were reconstructed using the two different algorithms and the differences in location were compared. There were no differences in the $E_{\rm T}$ or ϕ of the jets. However, there were small differences in the jet $|\eta|$, which increase as a function of the $|\eta|$ of the jets and decrease as the transverse energy of the jets increases. Figure 3 shows the average difference between the $|\eta|$ of jets with $E_{\rm T}>40$ GeV reconstructed using the two different algorithms. As can be seen, the difference is small, even at a large $|\eta|$.

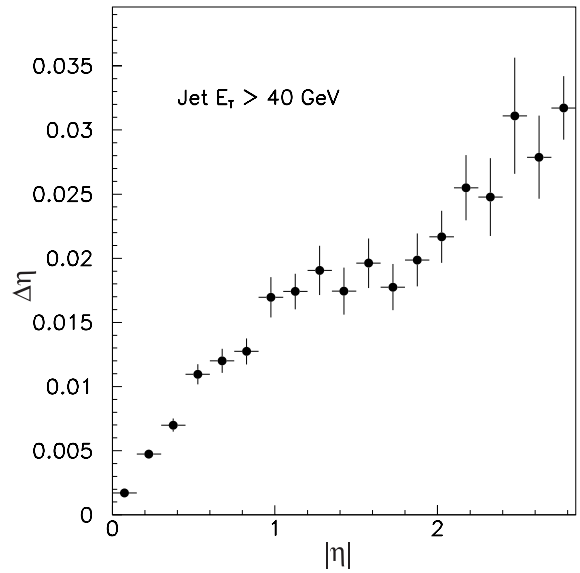

FIG. 3. The average difference between the $|\eta|$ of jets reconstructed using the DØ algorithm and the Snowmass algorithm for DØ data.

E. Jet algorithms at NLO

In PQCD calculations of parton-parton scattering at leading order [LO, $\mathcal{O}(\alpha_S^2)$] there can only be two partons in the final state. These partons are well separated and always form two jets when the Snowmass algorithm is applied. At next-to-leading order [NLO, $\mathcal{O}(\alpha_S^3)$], three partons can be produced in the final state. The Snowmass algorithm at the NLO parton level is illustrated in Fig. 4(a). For any two partons in the final state, the seeds direction is given by applying Eq. (3.2) to the two partons. If the partons lie within a distance $\mathcal{R}$ from the seed's direction the two partons are combined to form a jet.

In the Snowmass algorithm the partons contributing to a single jet can have a maximum separation of $2\mathcal{R}$. Consider a two parton final state with the partons separated by $2\mathcal{R}$. The experimentally observed energy pattern will be determined by the parton showering, hadronization, and calorimeter response. Application of the DØ jet algorithm to the calorimeter energy deposition that results from the hadronization of the two partons will produce one or two jets depending on the splitting and merging criteria. The Snowmass algorithm is only capable of finding one jet, and hence cannot match the experimental measurement.

This example illustrates the different treatment of jets at the parton and calorimeter level. To accommodate the differences between the jet definitions at the parton and calorimeter levels, an additional, purely phenomenological parameter has been suggested in Ref. [31]. The variable is called $\mathcal{R}_{\rm sep}$ and is the maximum allowed distance ($\Delta\mathcal{R}$) between two partons in a parton jet, divided by the cone size used: $\mathcal{R}_{\rm sep}=\Delta\mathcal{R}/\mathcal{R}$. This algorithm is illustrated in Fig. 4(b) and is referred to as the modified Snowmass algorithm.

The value of $\mathcal{R}_{\rm sep}$ depends on details of the jet algorithm used in each experiment. At the parton level $\mathcal{R}_{\rm sep}$ is the distance between two partons when the clustering algorithm switches from a one-jet to a two-jet final state, even though both partons are contained within the jet defining cone. The value of $\mathcal{R}_{\rm sep}$ depends on the experimental splitting or merging scheme. After several studies an $\mathcal{R}_{\rm sep}$ value of 1.3 was found to best simulate the DØ merging and splitting criteria [32].

F. Jet reconstruction efficiency

The jet algorithm does not reconstruct all jets with the same efficiency. Primarily this is due to calorimeter energy clusters not containing a seed tower of $E_{\rm T}$ greater than 1 GeV. Since the jet algorithm explicitly depends on the $E_{\rm T}$ of a seed tower used to begin searching for a jet, the seed tower distributions are studied to determine if jets are likely to have seed towers below threshold. Figure 5 shows the seed-tower-$E_{\rm T}$ distribution of jets for an $E_{\rm T}$ range of 18 to 20 GeV (other $E_{\rm T}$ ranges have similar distributions). The distribution is fitted with

$$A\exp\left[\frac{-0.5(-W+e^W)}{\sqrt{2}\lambda}\right] \tag{3.4}$$

where $W=(E_{\rm T}-\chi)/\lambda$, and A, χ, and λ are free parameters in the fit. Assuming that the seed towers are smoothly distributed in $E_{\rm T}$, the fraction of jets not containing a seed tower exceeding 1 GeV is determined from the fit and used to calculate the jet reconstruction efficiency. Figure 6 shows the reconstruction efficiency for jets as a function of jet $E_{\rm T}$. For jets with an $E_{\rm T}$ of 20 GeV and $\mathcal{R}=0.7$, the reconstruction efficiency is 99%.

G. Biases in the jet algorithm

The η dependence of the calorimeter energy response together with algorithm related effects may result in a difference (bias) between the η position of the jet at particle level and the jet reconstructed in the calorimeter. The η of the jet, assuming perfect position resolution, is

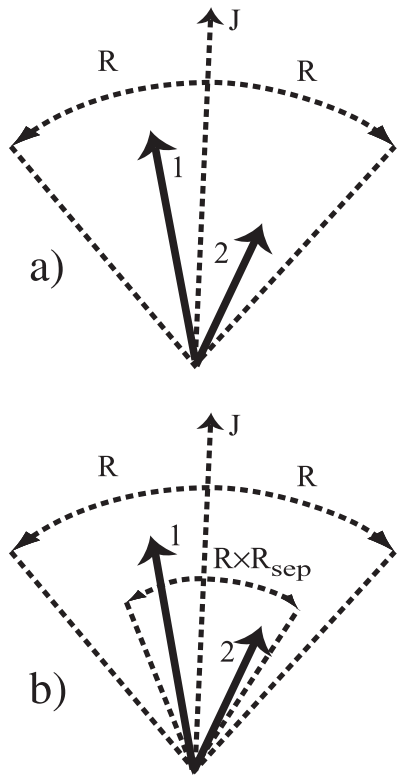

FIG. 4. Illustration and description of the jet definitions at NLO parton level as used by the DØ experiment. (a) The jet definition in NLO according to Snowmass. Parton -1- and -2- are combined into jet -J-, if the parton distance to the jet axis is less than R. The jet axis is defined by partons 1 and 2, according to the Snowmass definition. (b) The jet definition in NLO according to the modified Snowmass with $\mathcal{R}_{\rm sep}$. Use the standard Snowmass clustering, but in addition require the distance between the two partons to be less than $\mathcal{R}\times\mathcal{R}_{\rm sep}$.

$$\eta^{\rm ptcl}=\eta+\rho(E,\eta) \tag{3.5}$$

where $\rho(E,\eta)$ is the possible bias. To measure the bias, the HERWIG [33] Monte Carlo event generator and the DØ detector simulation, DØGEANT [34], are used. Jets are reconstructed at both the particle and calorimeter level. Statistically, $\langle\rho(E,\eta)\rangle$ can be obtained as $\langle\eta^{\rm ptcl}-\eta\rangle$ where a matching criterion is used to associate the particle jet to the reconstructed calorimeter jet. Figure 7 shows the η bias for all jet energies as a function of η. The bias in η is less than 0.02 for all η. The magnitude of the bias is greatest when part of the jet falls into the intercryostat region ($0.8<\eta<1.6$), which is the least instrumented region of the calorimeter.

A similar study was performed to measure a possible bias in ϕ (azimuth). Since the calorimeter has a symmetric tower structure in ϕ, no bias is expected. The bias in ϕ (azimuth) was measured to be small — much less than 0.01 radians. Any bias introduced by this effect will be small for most physics analyses since the $\Delta\mathcal{R}$ between jets is typically used rather than the absolute ϕ or η position. The analyses presented in this publication are not corrected for these effects.

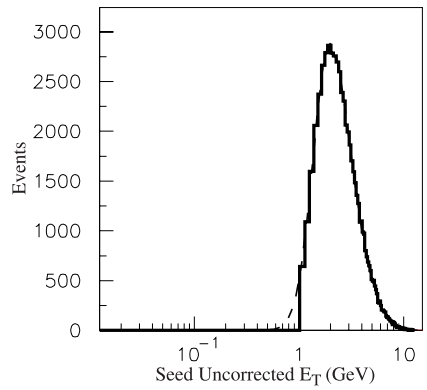

FIG. 5. Seed tower distributions for $\mathcal{R}=0.7$ cone jets with an $E_{\rm T}$ range of 18–20 GeV. The data is represented by the solid histogram and the fit is given by the dashed curve.

IV. THEORETICAL PREDICTIONS

A. NLO QCD predictions

Within the framework of PQCD, high $E_{\rm T}$ jet production can be described as an elastic collision between a single parton from the proton and a single parton from the antiproton [3]. After the collision, the outgoing partons form localized streams of particles called "jets." Predictions for the inclusive jet cross section, the dijet angular distribution, and the dijet mass spectrum are in general given by [3]

$$\sigma=\sum_{ij}\int dx_1\,dx_2\,f_i(x_1,\mu_F^2)f_j(x_2,\mu_F^2)\times\hat{\sigma}\left[x_1P_1,x_2P_2,\alpha_S(\mu_R^2),\frac{Q^2}{\mu_F^2},\frac{Q^2}{\mu_R^2}\right] \tag{4.1}$$

where $f_{i(j)}(x_{1(2)},\mu_F^2)$ represent the PDFs of the proton (antiproton) defined at factorization scale μ_F, $\hat{\sigma}$ is the parton

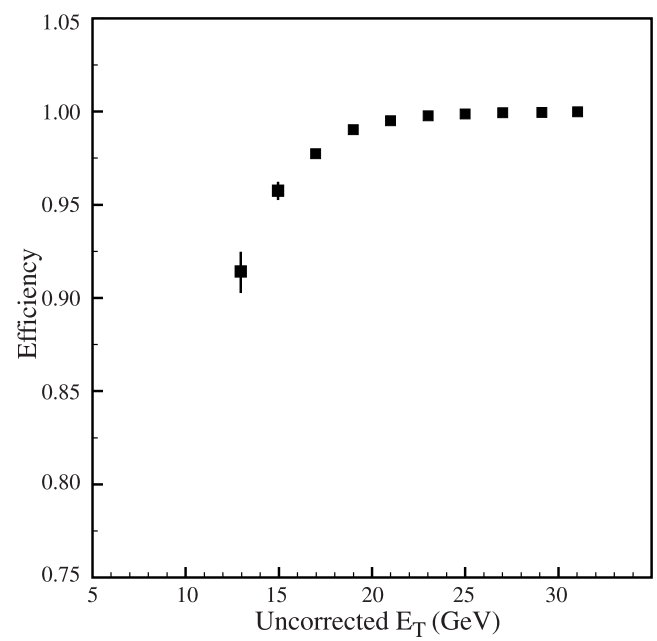

FIG. 6. Reconstruction efficiency as a function of jet $E_{\rm T}$.

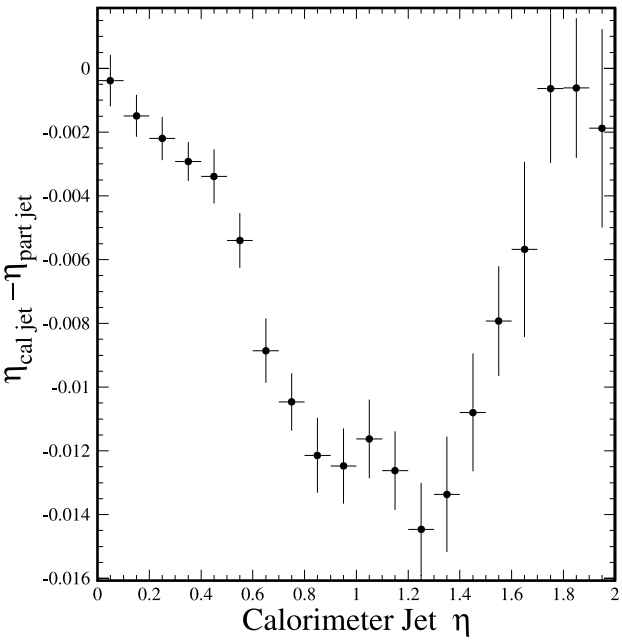

FIG. 7. HERWIG Monte Carlo simulation of the η bias for all jet energies as a function of the reconstructed jet η.

scattering cross section, $P_{1(2)}$ is the momentum of the proton (antiproton), $x_{1(2)}$ is the fraction of the proton (antiproton) momentum carried by the scattered parton, Q is the hard scale that characterizes the parton scattering (which could be the E_{T} of a jet, the dijet mass of the event, etc.), and μ_R is the renormalization scale.

The parton scattering cross sections have been calculated to next-to-leading order [NLO, $\mathcal{O}(\alpha_S^3)$]. The perturbation series requires renormalization to remove ultraviolet divergences. This introduces a second scale to the problem, μ_R. In addition, an arbitrary factorization scale, μ_F, is introduced to remove the infrared divergences. Qualitatively, it represents the scale that separates the short- and long-range processes. A parton emitted with transverse momentum relative to the proton less than the scale μ_F will be included in the PDF, while a parton emitted at large transverse momentum will be included in $\hat{\sigma}$. The scales μ_R and μ_F should be chosen to be of the same order as the hard scale, Q, of the interaction. The larger the number of terms included in the perturbative expansion, the smaller the dependence on the values of μ_R and μ_F. If all orders of the expansion could be included, the calculation should have no dependence on the choice of scales. In this article the renormalization scale is written as the product of a constant, D, and the hard scale of the interaction, $\mu = DQ$. Typically, the renormalization and factorization scales are set to the same value, $\mu = \mu_R = \mu_F$.

Several PQCD NLO calculations have been performed [11–13]. In this paper we use the event generator JETRAD [13] and a version of the analytic calculation EKS [12] that integrates the cross section over bins. Both programs require the selection of a renormalization and factorization scale, a set of parton distribution functions, and a jet clustering algorithm. Two partons are combined if they are contained within a cone of opening angle $\mathcal{R} = \sqrt{\Delta\eta^2 + \Delta\phi^2} = 0.7$, and are also within $\mathcal{R}_{\mathrm{sep}} = 1.3$ (see Sec. III). The authors of JETRAD have provided several choices for the renormalization scale. We have chosen a scale proportional to the E_{T} of the leading jet: $\mu = DE_T^{\max}$, where D is constant in the range $0.25 \leqslant D \leqslant 2.00$. An alternative scheme sets the scale to be proportional to the center-of-mass energy of the two outgoing partons: $\mu = C\sqrt{\hat{s}} = C\sqrt{x_1 x_2 s}$ where C is constant in the range $0.25 \leqslant C \leqslant 1.00$, $x_1 = \Sigma E_{\mathrm{Ti}} e^{\eta_i}/\sqrt{s}$, $x_2 = \Sigma E_{\mathrm{Ti}} e^{-\eta_i}/\sqrt{s}$, and $i = 1, \ldots, n$ where n is the number of jets in the event. The authors of EKS prefer a different definition of the renormalization scale: the E_{T} of each jet in the event, $\mu = DE_T^{\mathrm{jet}}$ (a version of EKS that uses the renormalization scale $\mu = DE_T^{\max}$ is also available).

Several choices of PDF are considered. The CTEQ3M [35] and Martin-Roberts-Stirling set A′ [MRS(A′)] [36] PDFs are fits to collider and fixed target data sets published before 1994. CTEQ4M [14] updates these fits using data published before 1996, and CTEQ4A repeats the fits with values of $\alpha_S(M_Z)$ fixed in the range 0.110 to 0.122 [CTEQ4M corresponds to an $\alpha_S(M_Z)$ of 0.116]. CTEQ4HJ [14] adjusts the gluon distributions to fit a CDF inclusive jet cross section measurement [7] by increasing the effective weighting of the CDF data. Martin, Roberts, Stirling, and Thorne (MRST) [15] incorporate all data published before 1998. In addition to the standard MRST PDF, two alternative PDFs are provided that vary the gluon distributions within the range allowed by experimental observations. The resulting distributions are called MRST($g\uparrow$) and MRST($g\downarrow$).

Since the publication of the MRST and CTEQ4 PDFs, problems were found in the implementations of the QCD evolution of the parton distributions in Q^2 [37]. This was caused by approximations to NLO QCD to reduce the time required for computation. The removal of these approximations could lead to changes of approximately 5% in the theoretical predictions presented in this paper. Currently, PDFs calculated without the approximations are not available for use with JETRAD and EKS.

1. Inclusive jet cross section

The inclusive jet cross section may be expressed in several ways. Theoretical calculations are normally expressed in terms of the invariant cross section

$$E\frac{d^3\sigma}{dp^3}. \tag{4.2}$$

In the DØ experiment the measured variables are the transverse energy (E_{T}) and pseudorapidity (η). In terms of these variables, the cross section is expressed as

$$\frac{d^2\sigma}{dE_{\mathrm{T}}\,d\eta}, \tag{4.3}$$

where the two are related by

$$E\frac{d^3\sigma}{dp^3} \equiv \frac{d^3\sigma}{d^2p_T\,dy} \rightarrow \frac{1}{2\pi E_T}\frac{d^2\sigma}{dE_{\mathrm{T}}\,d\eta}, \tag{4.4}$$

where y is the rapidity of the jet. The final expression follows if the jets are assumed to be massless. For most measurements, the cross section is averaged over some range of pseudorapidity: in this paper $|\eta|<0.5$ and $0.1<|\eta|<0.7$.

The inclusive jet cross section measures the probability of observing a hadronic jet with a given $E_{\rm T}$ and η in a $p\overline{p}$ collision. The term "inclusive" indicates that the presence or absence of additional objects in an event does not affect the selection of the data sample. An event which contains three jets that pass the selection criteria, for instance, will be entered into the cross section three times. The inclusive measurement is sometimes denoted $\sigma(p\overline{p}\rightarrow \text{jet}+X)$.

Theoretical predictions for the inclusive jet cross section are generated using the JETRAD and EKS programs. Our reference prediction is the JETRAD calculation with $\mu=0.5E_T^{\max}$, $\mathcal{R}_{\rm sep}=1.3$, and the CTEQ3M PDF. The predictions are smoothed by fitting to the function

$$AE_T^{-\alpha}\left(1-\frac{2E_{\rm T}}{\sqrt{s}}\right)^{\beta}\mathcal{P}_6(E_{\rm T}), \tag{4.5}$$

where $\mathcal{P}_6(E_{\rm T})$ is a sixth order polynomial. The resulting uncertainty due to smoothing is less than 2% for a given $E_{\rm T}$. The uncertainty in the calculations resulting from the choices of different renormalization scales and PDFs is approximately 30% and varies as a function of $E_{\rm T}$ [16]. Figure 8 shows the variations in the predictions for the inclusive jet cross section at $\sqrt{s}=1800$ GeV for JETRAD. The uncertainties in the inclusive jet cross section at $\sqrt{s}=630$ GeV are of a similar size.

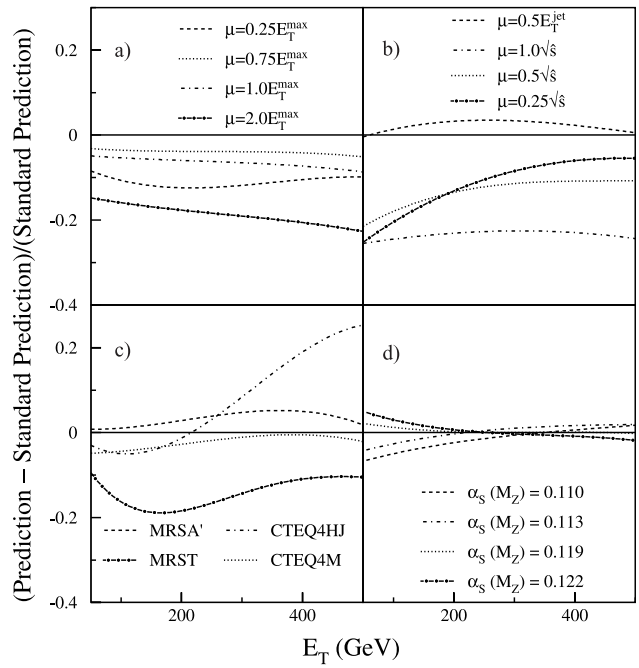

FIG. 8. The difference between alternative predictions and the reference prediction ($\mu=0.5E_T^{\max}$, CTEQ3M) for the inclusive jet cross section for $|\eta^{\rm jet}|<0.5$ at $\sqrt{s}=1.8$ TeV. Shown are the alternative predictions for the choices (a) $\mu=(0.25,\ 0.75,\ 1.0,\ 2.0)E_T^{\max}$, (b) $\mu=(0.25,\ 0.5,\ 1.0)\sqrt{\hat{s}}$ and $0.5E_T^{\rm jet}$, (c) CTEQ4M, CTEQ4HJ, MRS(A′), and MRST, and (d) for $\alpha_S=0.110-0.122$ using the CTEQ4A PDFs compared with the calculation using CTEQ4M, for which $\alpha_S=0.116$.

2. Ratio of inclusive jet cross sections at $\sqrt{s}=$ 1800 and 630 GeV

While it is possible to compare the inclusive jet cross sections as a function of $E_{\rm T}$ for both center-of-mass energies, the data will differ greatly in both magnitude and $E_{\rm T}$ range [see Fig. 9(a)]. If we express the cross section as a dimensionless quantity

$$E_T^4 E\frac{d^3\sigma}{dp^3}\equiv\frac{E_T^3}{2\pi}\frac{d^2\sigma}{dE_{\rm T}\,d\eta}, \tag{4.6}$$

and calculate it as a function of $x_T\equiv 2E_{\rm T}/\sqrt{s}$, the "scaling" hypothesis, which is motivated by the quark-parton model, predicts that it will be independent of the center-of-mass energy. However, QCD leads to scaling violation through the running of α_S and the evolution of the PDFs.

By taking the ratio of the cross sections at $\sqrt{s}=1800$ and 630 GeV, many of the theoretical and experimental uncertainties are reduced. Variations in the prediction resulting from the choice of renormalization scale, factorization scale, and PDF are approximately 10% and vary as a function of x_T. This is a significant reduction in the theoretical uncertainty compared to the uncertainties in the inclusive jet cross sections. The theoretical predictions for the ratio of the inclusive jet cross sections are calculated using the JETRAD and EKS programs. Figure 10 shows the variations in the ratio between inclusive jet cross sections at $\sqrt{s}=630$ and 1800 GeV for JETRAD.

3. Dijet angular distributions

At leading order two jets are produced. The invariant mass of the jets is given by

$$M^2\equiv\hat{s}=4p_T^2\cosh^2(\Delta y/2) \tag{4.7}$$

where $\hat{s}=x_1x_2s$, is the c.m. energy squared of the interacting partons, and Δy is the separation in rapidity of the two jets. If we assume that the jets are massless we can write the dijet invariant mass as

$$M^2=2E_T^{\rm jet1}E_T^{\rm jet2}[\cosh(\Delta\eta)-\cos(\Delta\phi)], \tag{4.8}$$

where ϕ is the azimuthal angle with respect to the beam. Since the dijet mass represents the center-of-mass energy of the parton-parton interaction, it directly probes the parton scattering cross section. The presence of higher-order processes can result in the production of additional jets. In this case the mass is calculated using the two highest-$E_{\rm T}$ jets in the event.

If only two partons are produced in a parton-parton interaction, and we neglect the intrinsic transverse momentum of the scattering partons, the two jets will be back-to-back in

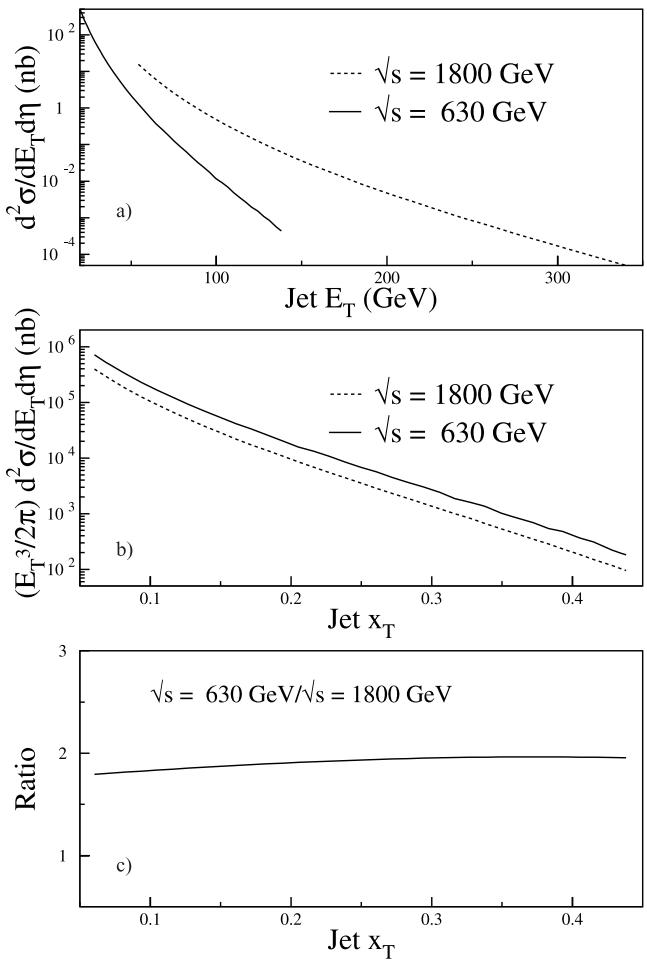

FIG. 9. The expected NLO inclusive jet cross sections at $\sqrt{s}=1800$ (dashed line) and at 630 GeV (solid line) are displayed in panel (a). Without scaling violations, the scaled dimensionless cross sections given in (b) would be independent of center-of-mass energies. This is clearly not the case, as can be seen in panel (c), which shows the ratio of the NLO dimensionless inclusive jet cross sections at $\sqrt{s}=630$ and 1800 GeV for $|\eta^{\rm jet}|<0.5$.

azimuth and balance in transverse momentum. The resulting two-jet inclusive cross section at LO can be written as a function of the p_T and rapidity (y_3, y_4) of the jets [3]

$$\frac{d^3\sigma}{dy_3\,dy_4\,dp_T^2}. \tag{4.9}$$

This can be rewritten in terms of the dijet invariant mass and the center of mass scattering angle, $\theta^\star$, using the transformation [3]

$$dp_T^2\,dy_3\,dy_4 \equiv 4dx_1\,dx_2\,d\cos\theta^\star \tag{4.10}$$

resulting in

$$\frac{d^2\sigma}{dM\,d\cos\theta^\star}=\sum_{ij}\int_0^1 dx_1\,dx_2\,\delta(x_1x_2s-M^2)\frac{d\hat{\sigma}_{ij}}{d\cos\theta^\star}. \tag{4.11}$$

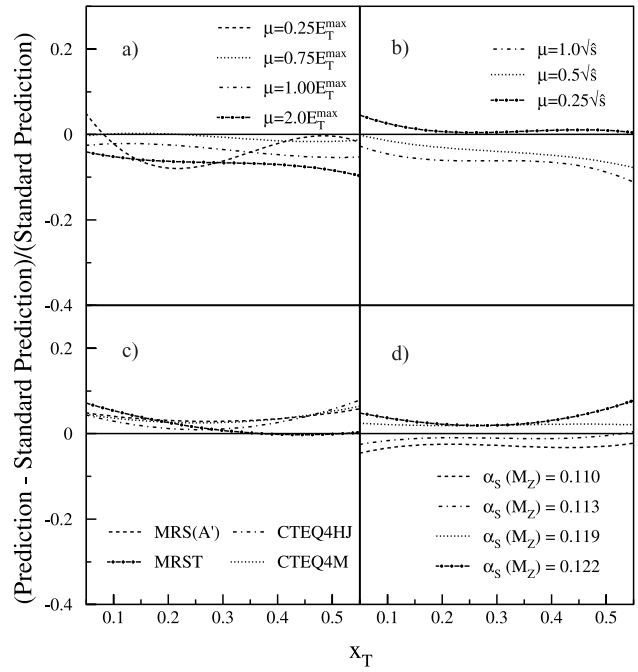

FIG. 10. The difference between alternative predictions and the reference prediction ($\mu=0.5E_T^{\rm max}$, CTEQ3M) of the ratio of inclusive jet cross sections at $\sqrt{s}=630$ and 1800 GeV for $|\eta^{\rm jet}|<0.5$. Shown are the alternative predictions for the choices (a) $\mu=(0.25, 0.75, 1.0, 2.0)E_T^{\rm max}$, (b) $\mu=(0.25, 0.5, 1.0)\sqrt{\hat{s}}$ and $0.5E_T^{\rm jet}$, (c) CTEQ4M, CTEQ4HJ, MRS(A′), and MRST, and (d) for $\alpha_S=0.110-0.122$ using the CTEQ4A PDFs compared with the calculation using CTEQ4M, for which $\alpha_S=0.116$.

The dijet angular distribution as measured in the dijet center-of-mass frame is sensitive to the QCD matrix elements. Angular distributions for the $qg\to qg$, $q\bar{q}\to q\bar{q}$, and $gg\to gg$ processes are similar. The properties of parton-parton scattering are almost independent of the partons involved (see Fig. 11). The dominant process in QCD parton-parton scattering is t-channel exchange, which results in angular distributions peaked at small center-of-mass scattering angles. Many theoretical predictions for phenomenology beyond the SM have an isotropic angular distribution and could be detected using the measurement of the dijet angular distribution.

At small center-of mass-scattering angles, $\theta^\star$, the dijet angular distribution predicted by leading order QCD is proportional to the Rutherford cross section:

$$\frac{d\hat{\sigma}}{d\cos\theta^\star}\sim\frac{1}{\sin^4(\theta^\star/2)}. \tag{4.12}$$

It is conventional to measure the angular distribution in the variable χ, rather than $\cos\theta^\star$, where

$$\chi=\frac{1+|\cos\theta^\star|}{1-|\cos\theta^\star|}=\exp(|\Delta\eta|). \tag{4.13}$$

Plotting the dijet angular distribution in the variable χ flattens out the distribution and facilitates comparison to theory

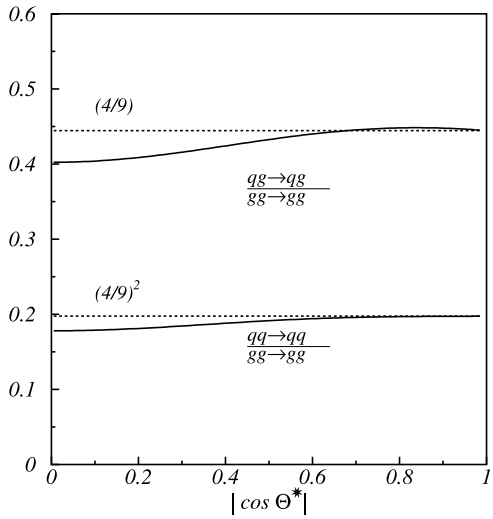

FIG. 11. Quark-antiquark and quark-gluon angular distributions, normalized to the angular distribution for gluon-gluon scattering. The horizontal lines at 4/9 and $(4/9)^2$ represent the color factors.

[3] ($d\sigma/d\chi$ is uniform for Rutherford scattering). The differential angular cross section measured in this analysis is

$$\frac{d^3\sigma}{dM\,d\chi\,d\eta_{\rm boost}}, \tag{4.14}$$

where $\eta_{\rm boost}=0.5(\eta_1+\eta_2)$. The predictions are calculated using JETRAD.

4. Inclusive differential dijet mass cross section

The inclusive triple differential dijet mass cross section is obtained by integrating over $\cos\theta^\star$ and is given by

$$\frac{d^3\sigma}{dM\,d\eta^{\rm jet1}\,d\eta^{\rm jet2}} \tag{4.15}$$

where $\eta^{\rm jet1,2}$ are the pseudorapidities of the jets. We integrate the cross section over a range of pseudorapidity such that both jets satisfy $|\eta^{\rm jet}|<1.0$. The NLO predictions for this cross section are calculated using JETRAD. The JETRAD predictions were smoothed by fitting them to an ansatz function of the form

$$AM^{-\alpha}\exp[-\beta M-\gamma M^2-\delta M^3]\mathcal{P}_n(M) \tag{4.16}$$

where $\mathcal{P}_n(M)$ is a polynomial of degree $n\leqslant 6$ and α, β, γ, and δ are fit parameters. The uncertainty due to the form of the ansatz function not being quite right is estimated to be $<2\%$. The uncertainties in the theoretical predictions are due to the choice of μ and PDF, and are approximately 40–50 % with some dependence on M (see Fig. 12).

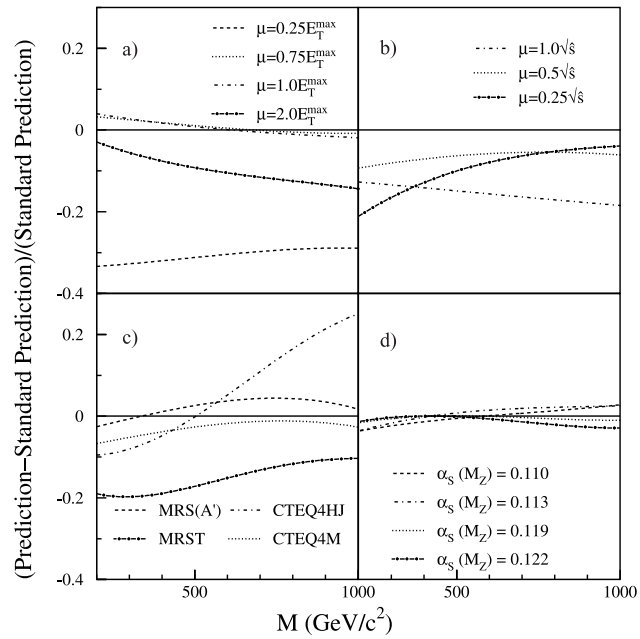

FIG. 12. The differences between the alternative predictions and the reference prediction ($\mu=0.5E_T^{\rm max}$, CTEQ3M) of the inclusive dijet mass cross section [Eq. (4.15)] at $\sqrt{s}=1800$ GeV for $|\eta^{\rm jet}|<1.0$. Shown are the alternative predictions for the choices (a) $\mu=(0.25, 0.75, 1.0, 2.0)E_T^{\rm max}$, (b) $\mu=(0.25, 0.5, 1.0)\sqrt{\hat{s}}$ and $0.5E_T^{\rm jet}$, (c) CTEQ4M, CTEQ4HJ, MRS(A′), and MRST, and (d) for $\alpha_S=0.110-0.122$ using the CTEQ4A PDFs compared with the calculation using CTEQ4M, for which $\alpha_S=0.116$.

B. Quark compositeness

The existence of three generations of quarks and leptons suggests that they may not be fundamental particles. For example, it has been proposed [17] that they could be composed of "preons" which interact via a new strong interaction called metacolor. Below a characteristic energy scale Λ, the preons form metacolor singlets that are the quarks. The scale Λ characterizes both the strength of the preon coupling and the physical size of the composite state (Λ is defined so that $g^2/4\pi=1$). Limits are set assuming that all quarks are composite and $\Lambda\gg\sqrt{\hat{s}}$ (where $\sqrt{\hat{s}}$ is the center of mass energy of the colliding partons), so that quarks appear to be point-like. Hence, the substructure coupling can be approximated by a four-fermion contact interaction described by an effective Lagrangian [17]:

$$\begin{aligned}\mathcal{L}=\frac{g}{2\Lambda^2}\Big\{&\eta^0_{LL}(\overline{q}_L\gamma^\mu q_L)(\overline{q}_L\gamma_\mu q_L)+\eta^0_{LR}(\overline{q}_L\gamma^\mu q_L)(\overline{q}_R\gamma_\mu q_R)\\&+\eta^0_{RL}(\overline{q}_R\gamma^\mu q_R)(\overline{q}_L\gamma_\mu q_L)+\eta^0_{RR}(\overline{q}_R\gamma^\mu q_R)(\overline{q}_R\gamma_\mu q_R)\\&+\eta^1_{LL}\left(\overline{q}_L\gamma^\mu\frac{\lambda_a}{2}q_L\right)\left(\overline{q}_L\gamma_\mu\frac{\lambda_a}{2}q_L\right)+\eta^1_{LR}\left(\overline{q}_L\gamma^\mu\frac{\lambda_a}{2}q_L\right)\\&\times\left(\overline{q}_R\gamma_\mu\frac{\lambda_a}{2}q_R\right)+\eta^1_{RL}\left(\overline{q}_R\gamma^\mu\frac{\lambda_a}{2}q_R\right)\left(\overline{q}_L\gamma_\mu\frac{\lambda_a}{2}q_L\right)\\&+\eta^1_{RR}\left(\overline{q}_R\gamma^\mu\frac{\lambda_a}{2}q_R\right)\left(\overline{q}_R\gamma_\mu\frac{\lambda_a}{2}q_R\right)\Big\},\end{aligned} \tag{4.17}$$

where $\eta^{0,1}_{HH}=0,\pm1$, and $H=L,R$ for left- or right-handed quarks. $\eta^{0(1)}_{HH}$ terms correspond to color-singlet (octet) contact interactions. These contact interactions modify the cross

sections for quark-quark scattering. Limits are presented in Secs. XIII and XIV for the cases [17,38]:

$\Lambda^{\pm}_{LL}$, where $\eta^0_{LL}=\pm 1$.
$\Lambda^{\pm}_{V}$, where $\eta^0_{LL}=\eta^0_{RR}=\eta^0_{RL}=\eta^0_{LR}=\pm 1$.
$\Lambda^{\pm}_{A}$, where $\eta^0_{LL}=\eta^0_{RR}=-\eta^0_{RL}=-\eta^0_{LR}=\pm 1$.
$\Lambda^{\pm}_{(V-A)}$, where $\eta^0_{LL}=\eta^0_{RR}=0;\eta^0_{RL}=\eta^0_{LR}=\pm 1$.
$\Lambda^{\pm}_{V_8}$, where $\eta^1_{LL}=\eta^1_{RR}=\eta^1_{RL}=\eta^1_{LR}=\pm 1$.
$\Lambda^{\pm}_{A_8}$, where $\eta^1_{LL}=\eta^1_{RR}=-\eta^1_{RL}=-\eta^1_{LR}=\pm 1$.
$\Lambda^{\pm}_{(V-A)_8}$, where $\eta^1_{LL}=\eta^1_{RR}=0;\eta^1_{RL}=\eta^1_{LR}=\pm 1$.

Currently, there are no NLO compositeness calculations available; therefore LO calculations are used. The ratio of each LO prediction including compositeness to the LO prediction with no compositeness ($\Lambda=\infty$) is used to scale the JETRAD NLO prediction:

$$\sigma(\text{composite})=\frac{\sigma(\Lambda=X)_{\text{LO}}}{\sigma(\Lambda=\infty)_{\text{LO}}}\sigma(\Lambda=\infty)_{\text{NLO}}. \quad (4.18)$$

C. Coloron limits

A flavor-universal coloron model [38] inspired by technicolor has been proposed to explain the nominal excess in the inclusive jet cross section as measured by CDF [7]. The model is minimal in its structure in that it involves the addition of one new interaction, one new scalar multiplet, and no new fermions. The QCD gauge group is extended to $SU(3)_1\times SU(3)_2$. At low energies, due to symmetry breaking, this results in the existence of ordinary massless gluons and an octet of heavy coloron bosons. Below the mass of the colorons (M_c), coloron-exchange can be approximated by the effective four-fermion interaction:

$$\mathcal{L}_{\text{eff}}=-\frac{g_3^2\cot^2\theta}{2!M_c^2}\left(\bar{q}\gamma^{\mu}\frac{\lambda_a}{2}q\right)\left(\bar{q}\gamma_{\mu}\frac{\lambda_a}{2}q\right) \quad (4.19)$$

where $\cot\theta$ represents the mixing between colorons and gluons, and $g_3^2\equiv 4\pi\alpha_S$. If $\Lambda^{-}_{V_8}\sqrt{\alpha_s}=M_c/\cot\theta$, this corresponds to Eq. (4.17) with $\eta^1_{LL}=\eta^1_{LR}=\eta^1_{RL}=\eta^1_{RR}=-1$ and would represent new color-octet vector current-current interactions. Such interactions could arise from quark compositeness or from non-standard gluon interactions (e.g. gluon compositeness) [39].

The phenomenology of the coloron has been studied [40] and limits have been placed on M_c and $\cot\theta$. Constraints on the size of the radiative corrections of the weak-interaction ρ parameter require $M_c/\cot\theta>450$ GeV [38], and a direct search for colorons in the dijet mass spectrum by the CDF Collaboration excludes colorons with mass below 1 TeV for $\cot\theta\lesssim 1.5$ [41].

V. TRIGGERING

The DØ trigger was based on a multi-level system. The level 0 (LØ) and level 1 (L1) triggers were hardware triggers. The LØ trigger consisted of two scintillating hodoscopes, one on each side of the interaction region. Coincident signals in the two hodoscopes indicate an inelastic collision and provide timing information for calculation of the position of the z-vertex of the interaction. The L1 trigger required a specified number of calorimeter trigger tiles ($\Delta\eta\times\Delta\phi=0.8\times 1.6$) or towers ($\Delta\eta\times\Delta\phi=0.2\times 0.2$) above certain E_{T} thresholds. Different trigger versions with slightly different L1 requirements were instrumented during the run. If a L1 rate was too large, a prescale was used to reduce the rate to an acceptable level. These prescale values were adjusted during the course of a beam store. A prescale of P allows only 1 out of every P events to be sent to the next level. Finally, level 2 (L2) was a software trigger which selected the data to be written to tape. A fast jet algorithm used at L2 defines jet E_{T} as the sum of the transverse energy within a cone of opening angle $\mathcal{R}=0.7$ centered on the E_{T}-weighted center of a L1 trigger tile or tower.

The L2 triggers used in the QCD analyses at $\sqrt{s}=1800$ GeV are called JET_30, JET_50, JET_85, and JET_115. The names follow the nomenclature that a JET_X trigger at L2 requires at least one jet with E_T greater than X GeV. During the running at $\sqrt{s}=630$ GeV the L2 triggers were JET_12, JET_2_12, and JET_30. A complete description of the L1 and L2 trigger requirements is given in Table I.

A study was performed to determine the trigger efficiency as a function of jet E_{T} for all triggers used in DØ QCD analyses. There is an efficiency for an event to pass the L1 trigger, and an efficiency for an event to pass the L2 trigger given that it passed L1. The combined efficiency to pass both L1 and L2 is

$$\epsilon^{\text{total}}_{\text{event}}=\epsilon^{\text{L1}}_{\text{event}}\times\epsilon^{\text{L2}|\text{L1}}_{\text{event}} \quad (5.1)$$

where $\epsilon^{\text{L2}|\text{L1}}_{\text{event}}$ is the efficiency for an event to pass L2 when it has passed L1. The L1 and L2 event efficiencies ($\epsilon^{\text{L1}}_{\text{event}}$ and $\epsilon^{\text{L2}|\text{L1}}_{\text{event}}$) depend on the event topology (E_{T} and η of the jets in the event). The event trigger efficiency as a function of single jet efficiencies for an event with N_{jets} is given by

$$\epsilon_{\text{event}}=1-\prod_{i=1}^{N_{\text{jets}}}[1-\epsilon_i(E_{Ti},\eta_i)], \quad (5.2)$$

where ϵ_i is the single jet efficiency for the ith jet. The product represents the probability that none of the jets in the event pass the trigger requirements.

The efficiency of the L1 trigger with the least restrictive requirements was measured using a data set that was required to pass only the LØ trigger. The single jet efficiency is given by the fraction of jets that satisfy the L1 requirements at a given E_{T}. The L1 efficiencies for more restrictive L1 triggers (MRT) were calculated using data samples that were required to pass a less restrictive L1 trigger (LRT). This allows the L1 efficiency of the more restrictive trigger to be calculated relative to the less restrictive trigger (given by $\epsilon_{\text{MRT,LRT}}$). Hence the efficiency for a given L1 trigger is given by the product of the efficiencies of all less restrictive triggers at a given E_{T}. For example, the L1 efficiency for the Jet_85 trigger is given by

$$\epsilon^{\text{L1}}_{\text{Jet_85}}=\epsilon^{\text{L1}}_{\text{Jet_85,Jet_50}}\times\epsilon^{\text{L1}}_{\text{Jet_50,Jet_30}}\times\epsilon^{\text{L1}}_{\text{Jet_30,LØ}}. \quad (5.3)$$

TABLE I. Typical trigger configurations used in inclusive analyses. The L1 and L2 requirements are shown for each trigger. Also shown are the leading uncorrected jet E_T at which the average event trigger efficiency exceeds 98%. Redundant lower-E_T thresholds at L1 were used to provide extended lists of seeds for jet clustering at L2.

Trigger	Level 1 (GeV)	Level 2 (GeV)	98% efficient
	$\sqrt{s}=1800$ GeV		
JET_30	1 tile >15 & 1 tile >6	1 jet with $E_T>30$	45 GeV
JET_50	1 tile >15 & 1 tile >6	1 jet with $E_T>50$	75 GeV
JET_85	1 tile >35 & 2 tiles >6	1 jet with $E_T>85$	105 GeV
JET_115	1 tile >45 & 1 tile >6	1 jet with $E_T>115$	170 GeV
	$\sqrt{s}=630$ GeV		
JET_12	1 tower >2	1 jet with $E_T>12$	20 GeV
JET_2_12	2 towers >2	1 jet with $E_T>12$	30 GeV
JET_30	1 tile >15	1 jet with $E_T>30$	45 GeV

The L2 trigger efficiencies for single jets are measured with respect to the L1 trigger. The fraction of these events which have a L2 jet above threshold determines the L2 single jet efficiency. Figure 13 shows the event efficiency for Jet_85 as a function of E_T.

Table I shows the typical trigger requirements and the E_T value for the leading E_T jet at which each trigger averages an efficiency exceeding 98%. The leading jet's E_T must be significantly higher than the L2 threshold in order for the trigger to be efficient.

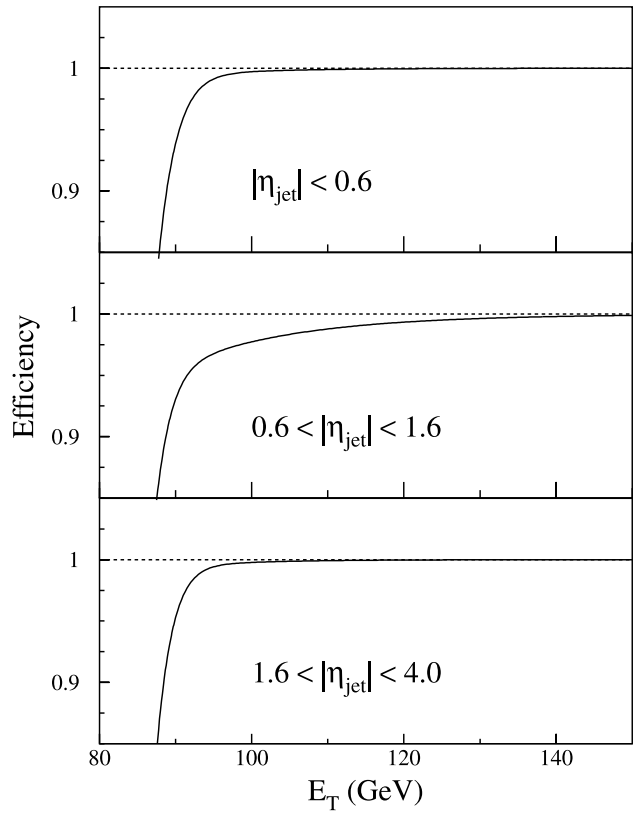

FIG. 13. Average event efficiency for JET_85 as a function of leading jet E_T and for three different pseudorapidity regions.

VI. LUMINOSITY

The beam luminosity was calculated from the counting rate of the LØ counters and the cross section subtended by these counters. The cross section was determined using the geometric acceptance of the LØ hodoscopes, the LØ hardware efficiency, and the world average (WA) of the $\overline{p}p$ inelastic cross section measurements. The cross section of observed events in the LØ was found to be $\sigma_{L\text{Ø}}=43.1\pm1.9$ mb at $\sqrt{s}=1800$ GeV [42] and $\sigma_{L\text{Ø}}=32.9\pm1.1$ mb at $\sqrt{s}=630$ GeV (see [43] for a description of the method used). The effective luminosity was determined independently for each trigger on a run-by-run basis taking into account each trigger's prescale, the LØ inefficiency, and the detector deadtime. The WA $\overline{p}p$ cross section at $\sqrt{s}=1800$ GeV used in this paper is based on measurements by the E710 Collaboration [44], the CDF Collaboration [45], and the E811 Collaboration [46]. At $\sqrt{s}=630$ GeV there is no complete measurement of the $\overline{p}p$ cross section. Hence, the $\overline{p}p$ cross section was obtained by interpolating between the WA $\overline{p}p$ cross sections measured at $\sqrt{s}=546$ and 1800 GeV [43]. The WA $\overline{p}p$ cross section at $\sqrt{s}=546$ GeV is based on measurements by the UA4 [47] and CDF [45] Collaborations. The CDF Collaboration only uses its measurement of the $\overline{p}p$ cross section to determine its luminosity. Due to the different methods used to measure the luminosity, there is a systematic shift between CDF and DØ measured cross sections, such that given identical data sets any CDF cross section measurement would be 6.1% higher than the corresponding DØ cross section [42].

The integrated luminosities at $\sqrt{s}=1800$ GeV as measured using LØ for the Jet_30, Jet_50, Jet_85, and Jet_115 triggers are 0.368, 4.89, 56.7, and 95.7 pb^{-1} respectively, with an uncertainty of 5.1%. The luminosities at $\sqrt{s}=630$ GeV for the JET_12, JET_2_12, and, JET_30 were 5.12, 31.9 and 538 nb^{-1} respectively with an uncertainty of 4.4%.

The luminosity required corrections due to small discrepancies in the luminosity calculation during different running periods at $\sqrt{s}=1800$ GeV. The initial luminosities for triggers Jet_85 and Jet_115 were taken from the luminosity calculation exclusively determined with the LØ counters. The inclusive jet cross sections calculated with the first 7.3 pb^{-1} of the data sample showed a 10% difference for Jet_115. The luminosity has been adjusted so that the dijet mass spectrum for the first 7.3 pb^{-1} matches that of the remaining data. This adjustment was also applied to Jet_85. Thus the luminosities

for Jet_85 and Jet_115 are 56.5 and 94.9 pb^{-1} respectively, a change of 0.7% from the value obtained using the LØ counters. This difference was added linearly to the 5.1% error on the initial luminosity value for a total error of 5.8%.

In addition, for a part of the run the Jet_30 and Jet_50 triggers each required a single interaction at LØ. The luminosities of Jet_30 and Jet_50 from the LØ calculation are estimated to be accurate only to 10% due to uncertainties in the efficiency of the single interaction requirement. The luminosity for the Jet_50 trigger was determined by matching the Jet_50 cross section to the Jet_85 cross section, and the Jet_30 cross section was matched to the Jet_50 cross section in regions of overlap. The trigger matching is analysis dependent; each analysis presented in this paper used the cross section of interest to match the triggers. The results obtained for the different measurements are consistent. The trigger matching errors are added in quadrature to the 5.8% error on Jet_85. The final luminosity and error for each trigger is shown in Table II.

Since the analyses [8,25] were first presented, the E811 Collaboration measurement of the total inelastic cross section was published [46]. Including this measurement in the WA changed the observed LØ cross section from $\sigma_{\text{LØ}} = 44.5 \pm 2.4$ mb to $\sigma_{\text{LØ}} = 43.1 \pm 1.9$ mb at $\sqrt{s} = 1800$ GeV. This changed the integrated luminosity of Jet_115 from 91.9 ± 5.6 pb^{-1} to 94.9 ± 4.7 pb^{-1}, an increase of 3.2%. Hence all cross sections at $\sqrt{s} = 1800$ GeV reported in this paper are reduced by 3.1% from the previously published results. It is worth noting that the inclusion of the E811 result had no perceptible impact on the cross section interpolation to 630 GeV.

The luminosity calculation consists of three distinct ingredients: the geometric acceptance of the LØ hodoscopes, the LØ hardware efficiency, and the $p\bar{p}$ inelastic cross section. The luminosity uncertainties are listed in Table III. The largest contribution to the luminosity uncertainty at $\sqrt{s} = 1800$ GeV derives from the world average (WA) $p\bar{p}$ total cross section. The $p\bar{p}$ cross section at $\sqrt{s} = 630$ GeV was determined from a fit to the values at $\sqrt{s} = 546$ and 1800 GeV [43] (see Fig. 14).

Two Monte Carlo minimum-bias event generators (MBR [48] and DTUJET [49]) were used to determine the geometric acceptance of the LØ hodoscopes. The difference in acceptance between the two MC results was taken as a source of systematic uncertainty for each $\sqrt{s}$. The consistent behavior of each generator relative to the other between center-of-mass energies indicates that the systematic uncertainty may be considered completely correlated. Although the geometric acceptance of the LØ hodoscopes for diffractive processes must be considered in luminosity calculations, the uncertainty in the non-diffractive acceptance dominates.

A study of zero-bias events (a random sampling of the detector during a beam-beam crossing) determined the hardware efficiency of LØ. Because the same estimation of the uncertainty appears in the calculation of the luminosities at both $\sqrt{s}$ values, the uncertainties are completely correlated. Table III lists the systematic uncertainty in the hardware efficiency for both center-of-mass energies.

TABLE II. Corrected luminosity and errors for the inclusive jet triggers. The trigger matching for Jet_30 and Jet_50 at $\sqrt{s} = 1800$ GeV was carried out using the dijet mass cross section.

Trigger	Luminosity	Error
	$\sqrt{s} = 1800$ GeV	
JET_30	0.364 pb^{-1}	7.8%
JET_50	4.84 pb^{-1}	7.8%
JET_85	56.5 pb^{-1}	5.8%
JET_115	94.9 pb^{-1}	5.8%
	$\sqrt{s} = 630$ GeV	
JET_12	5.12 nb^{-1}	4.4%
JET_2_12	31.9 nb^{-1}	4.4%
JET_30	538. nb^{-1}	4.4%

VII. THE EVENT VERTEX

The location of the event vertex was determined using the central tracking system [28], which provides charged particle tracking over the region $|\eta| < 3.2$. It measures the trajectory of charged particles with a resolution of 2.5 mrad in ϕ and 28 mrad in θ. From these measurements the position of the interaction vertex along the beam direction (z) can be determined with a resolution of 8 mm.

As the instantaneous luminosity increases, the average number of $p\bar{p}$ inelastic collisions per beam crossing increases. Hence there is the possibility of selecting the incorrect interaction vertex. If the incorrect vertex is chosen as the primary vertex, jet E_{T} and event missing transverse energy ($\not{E}_T$) will be miscalculated. This may result in a significant contribution to the jet spectra at very high-E_{T} since the high rate of jet production at lower E_{T} can cause contamination in the lower rate regions. Visual scanning of the high-E_{T} jets shows that approximately 10% have misidentified interaction vertices.

In order to study the effects of multiple interactions, a software tool called MITOOL [50] was developed to provide information about the number of interactions. This tool uses the LØ hodoscopes, the calorimeter, and the central tracker in order to evaluate the number of interactions. A sum-of-times inconsistent with a single interaction from the LØ hodoscopes indicates the possibility of the presence of more than one interaction. The total energy in the calorimeter pro-

TABLE III. Uncertainties in the luminosity calculation excluding trigger matching.

Source of uncertainty	Uncertainty (%)	
	1800 GeV	630 GeV
World average $p\bar{p}$ cross sections	3.70	2.75
Hardware efficiency	2.32	3.12
Geometric acceptance	2.73	1.51
Time dependencies	0.70	0.00
All sources	5.81	4.43

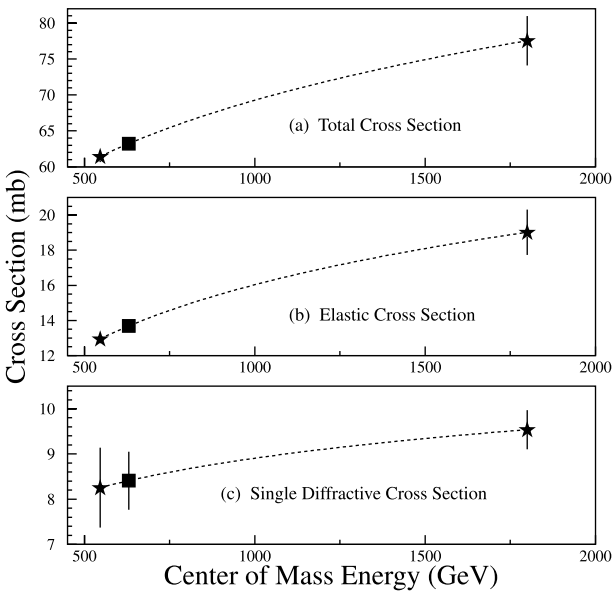

FIG. 14. The three fits to the world average $p\bar{p}$ cross sections. The stars depict the WA cross sections at $\sqrt{s}=546$ and 1800 GeV, and the closed square shows the interpolation to $\sqrt{s}=630$ GeV. A fluctuation of the 1800 GeV point directly influences the interpolated value at 630 GeV, particularly in the case of the total cross section (a).

vides evidence of multiple interactions. If the total measured energy of an event is greater than 1.8 TeV, a multiple interaction is likely. Additional information from the number of vertices found with the central tracker is also used. Using this information the most probable number of $p\bar{p}$ interactions in the event is calculated.

To a good approximation, the jet E_{T} and η can be calculated for the second $p\bar{p}$ vertex using the measured vertex z-position and a simple geometric conversion. Thus for all the jets in an event, the absolute magnitude of the vector sum of the jet E_{T}, denoted $S_T=|\Sigma\vec{E}_T^{\mathrm{jet}}|$, can be calculated for each vertex. Except for soft radiation falling below the jet reconstruction threshold, S_T will be equal in magnitude to the $\not{E}_T$. Since QCD events should contain little $\not{E}_T$, the correct vertex was selected by choosing the vertex with the minimum S_T.

VIII. JET AND EVENT SELECTION

The existence of random spurious energy deposits in the calorimeter may either fake or modify a real jet. Some sources of noise are electronic failures, cosmic ray showers, or accelerator losses due to Main Ring activity. A series of quality cuts was developed to remove this contamination.

A. Removal of "hot" cells

Before jet reconstruction, a cell suppression algorithm was implemented to suppress any cell with an unusually high deposition of energy relative to its longitudinal neighbors (a "hot" cell). Specifically, if a cell had more than 10 GeV of energy and more than 20 times the average energy of its immediate longitudinal neighbors, the cell energy was set to zero. This algorithm is successful in removing isolated high energy cells due to noise; however, the algorithm can also degrade the response to jets.

Approximately 10% of the events have one or more suppressed cells. The rapidity distribution of the suppressed cells is very "jet-like" with a central plateau. A cell was restored to a jet if it was within $\Delta\mathcal{R}=0.7$ of the original jet direction and if the cumulative total of hot cell E_{T} was no more that 50% of the original jet E_{T}. The jet rapidity and azimuth were then recalculated using the Snowmass definitions [Eq. (3.2)]. The event $\not{E}_T$ was also adjusted if a cell was restored to a jet.

The restoration algorithm has been shown to be 99% efficient by fitting the $\Delta\mathcal{R}$ and restored cell fraction (the hot cell E_{T} divided by the jet's original E_{T}) distributions and estimating the inefficiency in the cut regions. An event scan with restored jets (using relaxed restoration criteria) above 260 GeV showed no inefficiency. Less than 5% of these new jets are contaminated. For those events with a single suppressed cell, the $\not{E}_T$ is significantly reduced by the cell restoration. The kinematic variables (E_{T}, η, and ϕ) of the high-E_{T} jets which included a restored cell were compared to the kinematic variables calculated with a full reconstruction in which the suppression algorithm was disabled. The differences were small and well within the characteristic resolutions of the variables.

B. Quality cuts

Even after the removal of isolated anomalously large cell energies, there still remain spurious jets. Quality cuts were developed to remove these fake jets. The quality cuts were applied on either the jet or to the event.

The jet quality cuts are based on the distribution of energy within the jet. Three standard variables are used:

(1) Electromagnetic fraction (EMF) — the fraction of the jet energy contained in the electromagnetic section of the calorimeter. Jets are retained if

$$\mathrm{EMF}\leqslant 0.95 \quad (1.2<|\eta_{\mathrm{det}}|<1.6),$$

$$0.05\leqslant \mathrm{EMF}\leqslant 0.95 \quad (\text{otherwise}), \tag{8.1}$$

where η_{det} is the pseudorapidity of the jet calculated using a vertex position of $z=0$. The cut EMF>0.05 is not applied for $1.2<|\eta_{\mathrm{det}}|<1.6$ because of the gap between the CC and EC calorimeters (Sec. II).

(2) Coarse hadronic fraction (CHF) — the fraction of the jet energy contained in the coarse hadronic section of the calorimeter. This cut is designed to remove fake jets introduced by main ring particles depositing energy in the calorimeter. Jets are retained if

$$\mathrm{CHF}<0.4. \tag{8.2}$$

(3) Hot cell fraction (HCF) — the ratio of the most energetic cell of a jet to the second most energetic cell. Jets are retained if

$$\mathrm{HCF} < 10.0. \tag{8.3}$$

A cut on $\not{E}_T$ is also used to remove bad events. Since QCD events are expected to have no intrinsic $\not{E}_T$, a cut on events with large $\not{E}_T$ typically used

$$\frac{\not{E}_T}{E_T^{\mathrm{jet1}}} < 0.7, \tag{8.4}$$

where E_T^{jet1} is the transverse energy of the highest E_{T} jet in the event. In the case of the inclusive jet analysis, the measurement is more susceptible to contamination from events in which the primary vertex is located outside of the tracking detector and a vertex due to an additional minimum bias event is identified as the primary vertex, leading to an overestimate of the jet E_{T}. In this case it is found that a $\not{E}_T$ cut of

$$\frac{\not{E}_T}{E_T^{\mathrm{jet1}}} < 0.3 \quad \text{if } E_T^{\mathrm{jet1}} > 100 \text{ GeV},$$

$$\not{E}_T < 30 \text{ GeV} \quad \text{if } E_T^{\mathrm{jet1}} \leqslant 100 \text{ GeV} \tag{8.5}$$

removes the contamination.

Since the data collected at $\sqrt{s} = 630$ GeV were taken at low instantaneous luminosity, there were fewer events with multiple interactions and incorrectly identified vertices. As a result, the quality cuts on the data were adjusted to maximize efficiency without increasing contamination. The resulting cuts are

$$\mathrm{EMF} < 0.90, \tag{8.6}$$

$$\mathrm{CHF} < 0.4, \tag{8.7}$$

$$\mathrm{HCF} < 20.0, \tag{8.8}$$

$$\frac{\not{E}_T}{E_T^{\mathrm{jet1}}} < 0.7. \tag{8.9}$$

C. Efficiency

The efficiencies of the quality cuts were measured. The data sample used to calculate the efficiencies was selected by making cuts in η and ϕ. We verified that the changes in shape of the EMF, HCF, and CHF distributions due to the $\not{E}_T$ were negligible.

To calculate the total efficiency, each individual efficiency is measured. First the $\not{E}_T$ cut is applied to the data and the efficiency of the EMF cut is calculated. Figure 15 illustrates the EMF distribution after the $\not{E}_T$ cut is applied. Contamination is visible as small peaks near EMF≈ 0 or 1. A Gaussian-like curve is projected under the noise signal and used to estimate the data signal lost due to the cut. After the $\not{E}_T$ and EMF cuts are applied, the HCF efficiency is measured [Fig. 16(a) shows the HCF distribution]. Then after both the EMF and HCF cuts were made, the efficiency of the CHF cut is measured. The total jet efficiency is calculated by multiplying the individual cut efficiencies together.

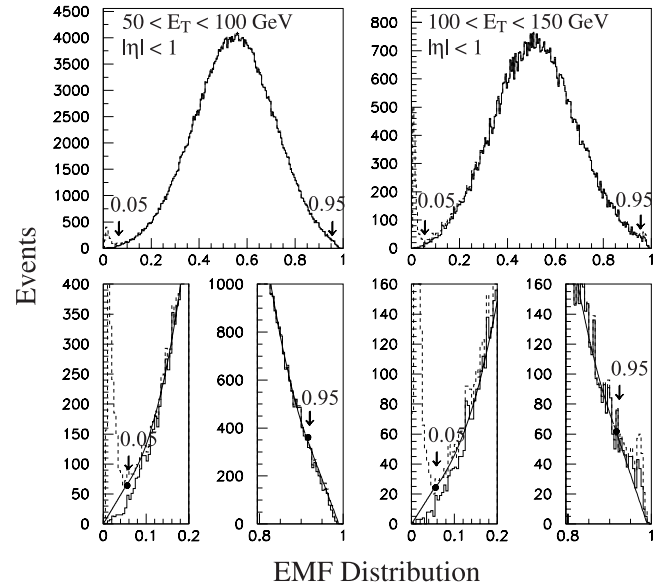

FIG. 15. The measured EMF distributions for different E_{T} ranges. The lower plots show the cut values and the fit used to calculate the efficiency of the cut. The dashed histogram shows the full data sample and the solid histogram shows a data sample with minimal noise contamination. The arrows indicate the cut values. The peaks at EMF ≈ 0 or 1 are due to contamination.

The standard jet cuts remove most of the noise from the sample; however, there is still some contamination at high E_{T} due to cosmic rays and "Main Ring Events." The $\not{E}_T$ cut removes this remaining noise. By fitting this distribution in regions of the calorimeter where the noise effects are negligible, an extrapolation can be used to determine the efficiency. Figure 16(b) shows the $\not{E}_T$ distribution used to calculate the efficiency. The inclusive jet efficiencies as a function of jet E_{T} in the central region at $\sqrt{s} = 1800$ GeV are shown in Fig. 17. Figure 18 shows the efficiency of the $\not{E}_T$ cut for dijet events. The efficiencies of the quality cuts used at $\sqrt{s} = 630$ GeV are given in Fig. 19. The efficiency of the $\not{E}_T$ cut at $\sqrt{s} = 630$ GeV is $>99\%$.

D. Contamination

In order to measure the remaining contamination after all quality cuts have been implemented, two separate studies were performed. Residual contamination was estimated by overlapping the observed hot cell distribution on a simulated inclusive jet sample. The simulated cross section changed by less that 1% after imposition of the jet quality cuts. The simulation also indicated that the jet quality cuts reject $>99\%$ of the "fake" jets with $E_{\mathrm{T}} = 500$ GeV.

To measure the contamination due to misvertexing, events at high-E_{T} were visually inspected. Misvertexing tends to cause lower E_{T} jets to migrate to higher E_{T}. Since the cross section is steeply falling, this can corrupt the high-E_{T} cross section. This study shows that after the vertex selection procedure has been applied, less than 1% of the events are contaminated at high E_{T}.

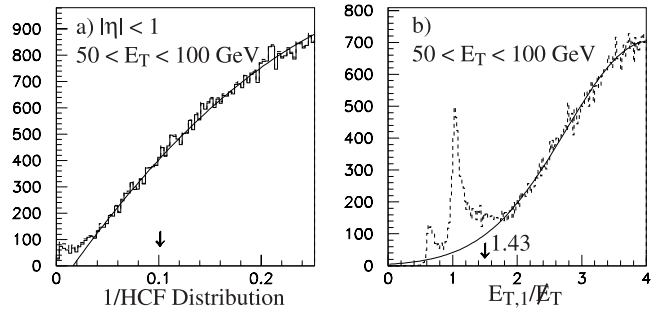

FIG. 16. (a) The 1/HCF distribution. The arrow shows the location of the cut for $\sqrt{s}=1800$ GeV. (b) The distribution of $E_T^{\rm jet1}/\not{E}_T$. The arrow at $E_T^{\rm jet1}/\not{E}_T=1.43$ corresponds to the $\not{E}_T/E_T^{\rm jet1}$ cut of 0.7. The peak at 1.0 is due to contamination from cosmic rays and the main ring. The dashed histograms show the distributions for the full data samples.

IX. JET ENERGY SCALE

The *in situ* jet energy calibration uses reconstructed collider data, and is described in more detail in [51]. The measured energy of a jet $E_{\rm jet}^{\rm meas}$ depends strongly on the jet definition. The particle-level (true) jet energy $E_{\rm jet}^{\rm ptcl}$ is defined as the energy of a jet consisting of final-state particles produced by the high-p_T parton-parton scattering, and found using the Snowmass algorithm. The jet should not include the particles produced by the underlying event (Sec. III C). The jet energy scale corrects the measured jet energy, on average, back to the energy of the final-state particle-level jet. $E_{\rm jet}^{\rm ptcl}$ is determined as

$$E_{\rm jet}^{\rm ptcl}=\frac{E_{\rm jet}^{\rm meas}-E_{\rm O}}{R_{\rm jet}S_h} \tag{9.1}$$

where:

$E_{\rm O}$ is an offset, which includes the underlying event, noise from radioactive decays in the uranium absorber, the effects of previous interactions (pile-up), and the contribution from additional $\bar{p}p$ interactions in the event;

$R_{\rm jet}$ is the calorimeter energy response to jets. $R_{\rm jet}$ is typically less than unity due to energy deposited in uninstrumented regions of the detector, and differences in the response to electromagnetic and hadronic particles ($e/h>1$);

S_h is the fraction of the jet energy that showered inside the algorithm cone at the calorimeter level;

The calibration is performed using data taken in $\bar{p}p$ collisions at $\sqrt{s}=1800$ GeV and 630 GeV.

A. Offset correction, $E_{\rm O}$

The total offset correction is measured as a transverse energy density in η-ϕ space and subdivided as $D_O=D_{ue}+D_\Theta$. D_{ue} represents the contribution due to the underlying event, i.e. energy associated with the spectator partons in a $\bar{p}p$ event. D_Θ accounts for uranium noise, pile-up, and energy from additional $\bar{p}p$ interactions. The offset correction E_O is given by D_O multiplied by the η-ϕ area of the jet.

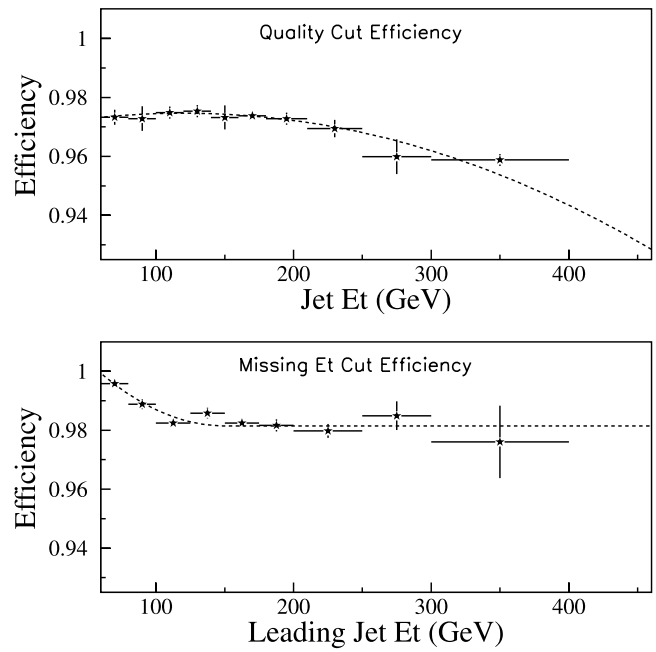

FIG. 17. Top: The efficiency of the standard jet quality cuts for $|\eta|<0.5$ [Eqs. (8.1), (8.2), and (8.3)] at $\sqrt{s}=1800$ GeV. Bottom: The efficiency of the $\not{E}_T$ cut used in the inclusive jet analysis [Eq. (8.5)] at $\sqrt{s}=1800$ GeV. The dotted curves show fits to the measured efficiencies.

D_Θ is determined from a zero-bias sample (a random sampling of the detector during a beam-beam crossing). D_{ue} is measured using the difference in average transverse energy density between minimum-bias events (where a $\bar{p}p$ interaction has occurred, usually inelastic scattering) and zero-bias events. The η dependencies of both quantities and the luminosity dependence of D_Θ are shown in Figs. 20 and 21. The statistical and systematic errors of the offset correction are 8% and 0.25 GeV respectively.

B. Response correction, $R_{\rm jet}$

DØ makes a direct measurement of the jet energy response using conservation of p_T in photon-jet (γ-jet) events

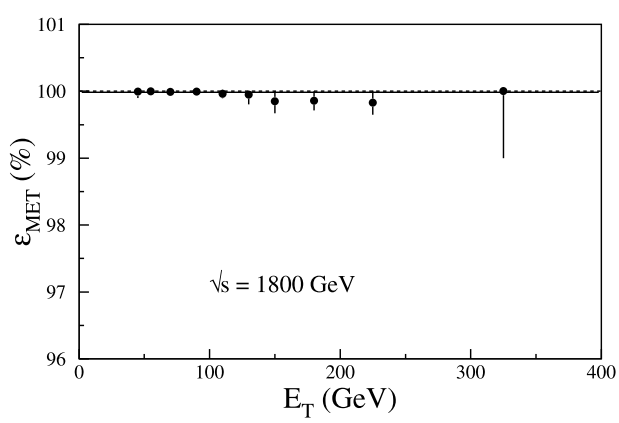

FIG. 18. The efficiency of the $\not{E}_T$ cut used in the dijet analyses at $\sqrt{s}=1800$ GeV [Eq. (8.4)].

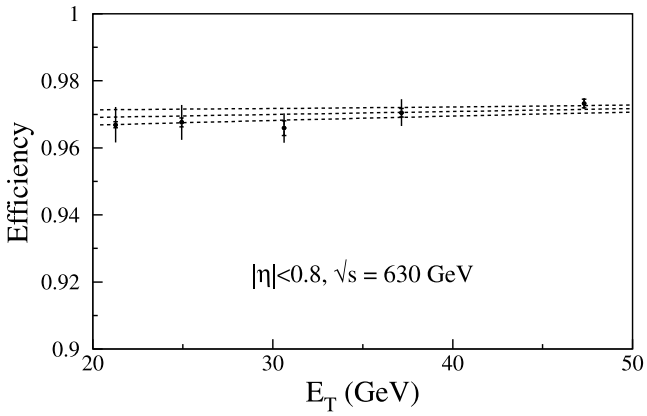

FIG. 19. The efficiency of the standard jet quality cuts for $|\eta|<0.8$ at $\sqrt{s}=630$ GeV [Eqs. (8.6), (8.7), and (8.8)]. The three curves show the fit to the efficiencies and the uncertainty in the fit.

[51]. The electromagnetic energy scale is determined from the DØ $Z(\rightarrow e^+e^-)$, J/ψ, and π^0 data samples, using the masses of these known resonances. In the case of a γ-jet two body process, the jet response can be measured through

$$R_{\rm jet}=1+\frac{\vec{\not{E}}_T\hat{n}_{T\gamma}}{E_{T\gamma}}, \tag{9.2}$$

where $E_{T\gamma}$ and $\hat{n}_{T\gamma}$ are the transverse energy and direction of the photon. To avoid response and trigger biases, $R_{\rm jet}$ is binned in terms of $E'=E_{T\gamma}\times\cosh(\eta_{\rm jet})$ and then mapped onto $E_{\rm jet}^{\rm meas}$. E' depends only on photon variables and jet pseudorapidity, which are both measured with very good resolution.

1. η-dependent corrections

Most measurements need a high degree of accuracy in the jet energy scale at all rapidities. An η-dependent correction becomes necessary. The cryostat factor $F_{\rm cry}$ is defined as the ratio $R_{\rm jet}^{\rm EC}/R_{\rm jet}^{\rm CC}$. The measured factor 0.977 ± 0.005 is constant as a function of E'. This was expected because the CC and the EC calorimeters use the same technology.

The intercryostat region (IC), which covers the pseudorapidity range $0.8<|\eta|<1.6$, is the least well-instrumented region of the calorimeter system. A substantial amount of energy is lost in the cryostat walls, module end plates, and support structures. An IC correction is performed after the $F_{\rm cry}$ correction and before the energy-dependent response correction. Because the energy dependence of $R_{\rm jet}$ is included in $R_{\rm jet}$ as a function of η, this function is not a constant, but should be smooth. The IC correction is set so that the response as a function of η agrees with the fit to the functional form, $R_{\rm jet}=a+b\cdot\ln[\cosh(\eta)]$, of the CC and EC response, as shown in Fig. 22.

2. Energy-dependent correction

Following the above procedure, the energy dependence of $R_{\rm jet}$ is then determined as a function of E' as illustrated in Fig. 23. Uniformity of the calorimeters allows the use of data

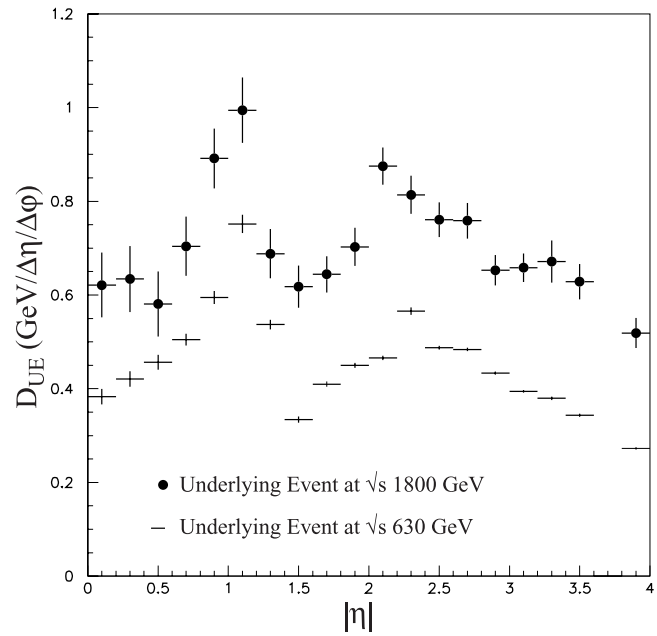

FIG. 20. Physics underlying event $E_{\rm T}$ density D_{ue} versus η for events with $\sqrt{s}=1.8$ TeV and $\sqrt{s}=630$ GeV.

from both the CC and the EC to measure $R_{\rm jet}$. The rapidly falling photon cross sections limit the use of CC data to energies $\lesssim 120$ GeV. EC data are used to extend the energy reach to ~ 300 GeV. We exploit the fact that jet energy in the EC is larger than in the CC for the same E_T. Monte Carlo data are also included at the highest energy to constrain the extrapolation. A set of γ-jet events is generated using HERWIG [33], processed through the DØ GEANT [34] detector simulation, and reconstructed with the standard photon and

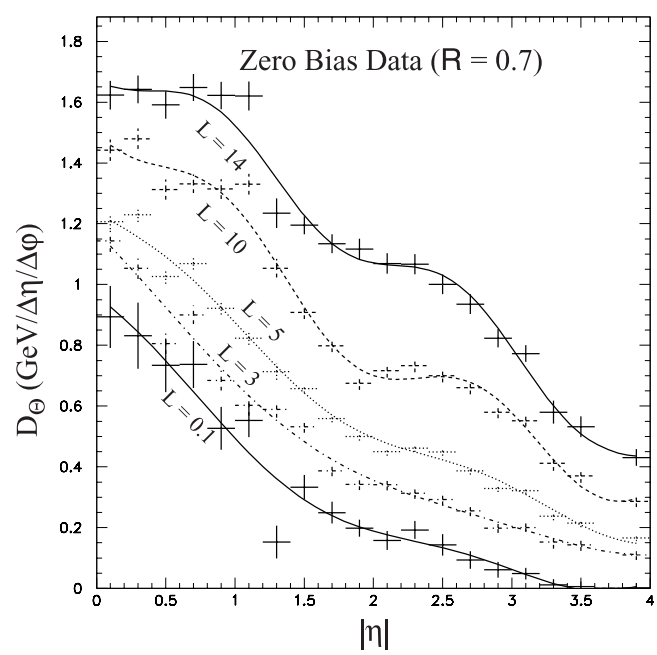

FIG. 21. D_Θ versus η for different luminosities in units of 10^{30} cm^{-2} sec^{-1} at $\sqrt{s}=1.8$ TeV.

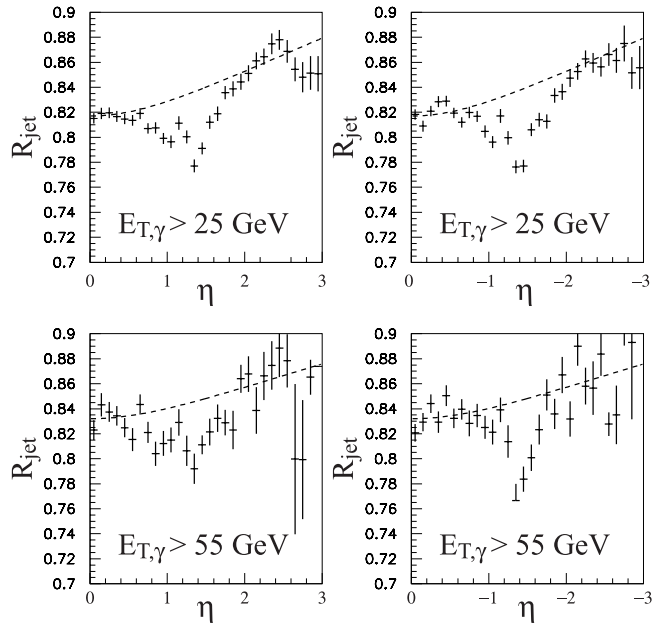

FIG. 22. Response versus η for γ-jet data before the η-dependent correction. The dashed line is the fit to the expected IC response.

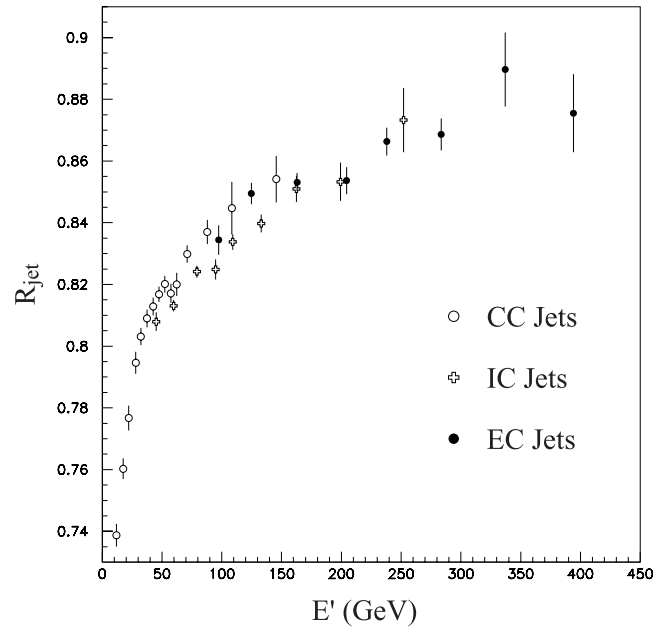

FIG. 23. R_{jet} versus E' measured in the CC, IC and EC calorimeter regions after η dependent corrections.

jet algorithms. The Monte Carlo simulation is improved by incorporating the single particle response of the calorimeter as measured in test beam.

The response versus energy for the $\mathcal{R}=0.7$ cone algorithm is shown in Fig. 23. The CC and EC data, and the expected response from MC at $E_T=500$ GeV are fit with the functional form $R_{jet}(E)=a+b\cdot\ln(E)+c\cdot\ln(E)^2$ (see Fig. 24). This function is motivated by the hadronic shower becoming gradually more "electromagnetic" (EM) with increasing energy [52]. If e and h are the responses of the calorimeter to the EM and non-EM components of a hadronic shower, and π is the response to charged pions, then $e/\pi=1/[h/e-\langle f_{EM}\rangle(h/e-1)]$. The functional form for the mean electromagnetic fraction of the jet $\langle f_{EM}\rangle$ is $\sim\alpha\cdot\ln(E)$, giving the expected logarithmic dependence for energy carried by the charged pions and, therefore, jets.

In addition to the uncertainty from the fit (1.5%, 0.5%, 1.6% for 20, 100, 450 GeV jets respectively), there is also a $\sim$0.5% uncertainty from the W boson background in the photon sample. Some of the events in the γ-jet sample are not two-body processes. In the IC region, the η-dependent corrections contribute an additional $\sim$1% uncertainty.

C. Showering correction, S_h

As a jet of particles strikes the detector, it interacts with the calorimeter material producing a wide shower of particles. Some particles directed inside the cone deposit a fraction of their energy outside the cone (and vice versa) as the shower develops inside the calorimeter. We do not correct for any QCD radiation or particles that are radiated from the cone; we only correct for the effects of the detector.

The correction for this showering is determined using jet energy density profiles from data and particle-level HERWIG [33] Monte Carlo program. The data contains the contributions of both gluon radiation and showering effects outside the cone. The former contribution is subtracted using the particle-level Monte Carlo profiles. S_h is defined as the inverse of the measured correction factor; that means S_h is the fraction of the jet energy showered inside the algorithm cone in the calorimeter [Eq. (9.1)]. The showering correction is negligible for $\mathcal{R}=0.7$ cone jets above $\sim$100 GeV in the central region ($|\eta|<1.0$) with an uncertainty of $\sim$1%. Both the correction and uncertainty are larger for lower energies, higher η, and smaller cone sizes.

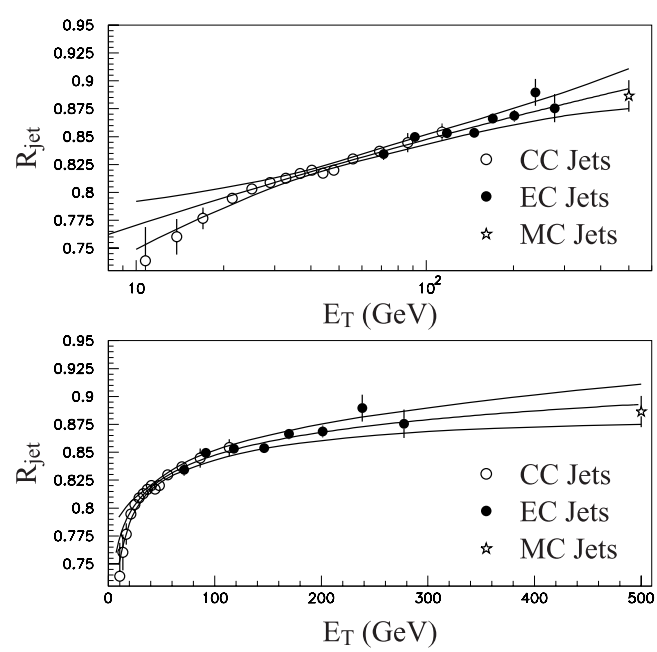

FIG. 24. R_{jet} versus energy for the $\mathcal{R}=0.7$ cone jet algorithm. The solid lines are the fit and the associated uncertainty band.

D. Correlations of the uncertainties

The uncertainties in the jet energy scale can be separated into five sources: offset, η-dependent corrections, response corrections, method, and showering corrections. The correlations of these uncertainties as a function of E_{T} and η have been studied:

(1) *Offset.* This is the dominant uncertainty at low E_{T} but is unimportant at high E_{T}. The uncertainty due to the offset correction is divided into two parts: a systematic error related to uncertainties in the method which is correlated as a function of E_{T}, and a statistical error that is uncorrelated as a function of pseudorapidity due to the finite size of the data sample used to determine the offset.

(2) *η-dependent correction.* The uncertainty due to this correction was separated into two parts. The first is due to the cryostat factor and is correlated as a function of E_{T} and η. The second is the IC correction, which is uncorrelated as a function of E_{T} and η.

(3) *Response correction.* The uncertainty associated with the hadronic response is unimportant at low E_{T} but dominant at high E_{T}. As a result of using a fit, the uncertainty is partially correlated as a function of E_{T}. The correlation matrices for various jet cone sizes can be found in Ref. [51].

(4) *Method.* The uncertainty in the method used to determine the energy scale correction arises from the data selection requirements, and punch-through at very high energies. The method uncertainty is correlated as a function of E_{T}.

(5) *Showering correction.* The uncertainty due to this correction is small except at very low E_{T} and is considered to be fully correlated as a function of E_{T}.

E. Summary and verification studies

Figure 25 shows the magnitude of the correction and uncertainty for $\mathcal{R}=0.7$ cone jets with $\eta=0$. The overall correction factor to jet energy in the central calorimeter is 1.160 ± 0.018 and 1.120 ± 0.025 at 70 GeV and 400 GeV, respectively. Point-to-point correlations in the energy uncertainty are very high for jets with $200<E_{\mathrm{T}}<450$ GeV.

The accuracy of the jet energy scale correction is verified using a HERWIG γ-jet sample and the DØGEANT detector simulation. A Monte Carlo jet energy scale is derived and the corrected jet energy is compared directly to the energy of the associated particle jet. Figure 26 shows the ratio of calorimeter to particle jet energy before (open circles) and after (full circles) the jet scale correction in the CC. The ratio is consistent with unity to within $\sim0.5\%$.

X. JET RESOLUTIONS

The observed energy distributions are smeared due to resolution effects. The fractional energy resolution σ_E/E may be parametrized as

$$\frac{\sigma_E}{E}=\sqrt{\frac{N^2}{E^2}+\frac{S^2}{E}+C^2}. \tag{10.1}$$

The nature of the incident particles, sampling fluctuations, and showering fluctuations, contribute mostly to the sampling term, S. Detector imperfections and deviations from an electron-hadron single particle response of unity, limit the resolution at high energies and are described by the constant term, C. Noise fluctuations (including the effects of multiple interactions) affect the low energy range and are given by the noise term, N.

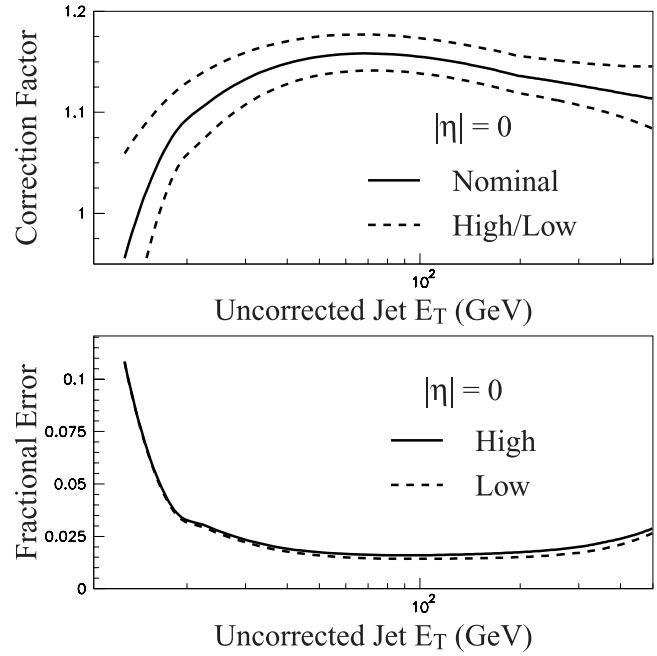

FIG. 25. Corrections and errors for $\eta_{\mathrm{jet}}=0.0$, $\mathcal{R}=0.7$. The high (low) curve depicts the $+(-)1\sigma$ uncertainties.

In the analyses reported here, we measure the E_{T} of the jets; hence we need to measure the resolution of E_{T}, which will have the same form:

$$\frac{\sigma_{E_T}}{E_{\mathrm{T}}}=\sqrt{\frac{N^2}{E_{\mathrm{T}}^2}+\frac{S^2}{E_{\mathrm{T}}}+C^2}. \tag{10.2}$$

The relationship between σ_E/E and $\sigma_{E_T}/E_{\mathrm{T}}$ depends on the η resolution, σ_η. Using $E_{\mathrm{T}}=E/\cosh\eta$ and assuming that σ_{E_T} and σ_η are uncorrelated then

$$\left(\frac{\sigma_{E_T}}{E_{\mathrm{T}}}\right)^2\approx\left(\frac{\sigma_E}{E}\right)^2+|\tanh\eta|^2\sigma_\eta^2. \tag{10.3}$$

In addition to the detector resolution, other contributions must be folded into the resolutions used for physics analyses. These are, for example, fluctuations of the out-of-cone losses, and the fluctuations of the vertex z-position about its measured value.

Using DØ dijet data we derive the energy resolutions using energy conservation in the transverse plane. The following criteria are applied to dijet events in order to eliminate sources of contamination due to additional low-E_{T} jets:

The z-coordinate of the interaction vertex must be within 50 cm of the center of the detector.

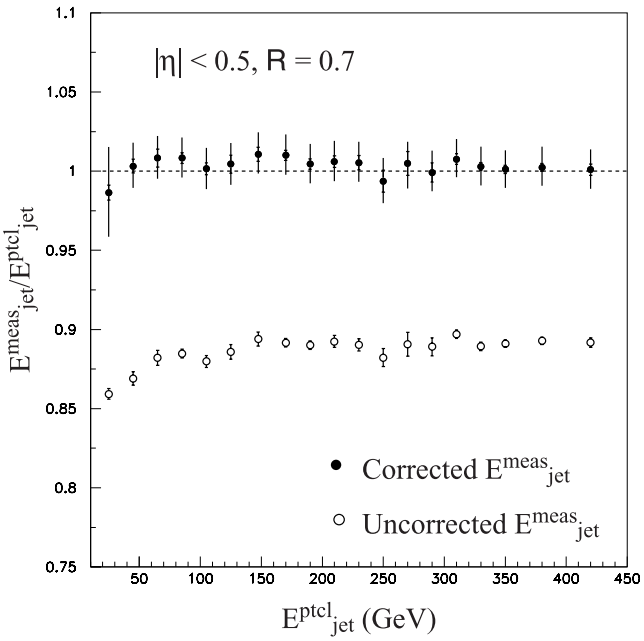

FIG. 26. Monte Carlo verification test. Corrected $E_{\rm jet}^{\rm meas}/E_{\rm jet}^{\rm ptcl}$ ratio is consistent with 1.0 within errors. The inner error bars depict the statistical error due to the size of the Monte Carlo sample, and the outer error bars represent the systematic uncertainty on the energy scale.

The two leading-$E_{\rm T}$ jets must be back-to-back ($\Delta\phi > 175°$).

If there is a third jet in the event, it must have $E_T^{\rm jet3}$ less than a specified value.

All jets in the event must satisfy the jet quality cuts.

Both leading jets are required to be in the same η region so that their resolutions are similar, i.e. $|\eta^{\rm jet1}| \approx |\eta^{\rm jet2}|$.

The dijet balance method is based on the asymmetry variable A, which is defined as

$$A = \frac{E_T^{\rm jet1} - E_T^{\rm jet2}}{E_T^{\rm jet1} + E_T^{\rm jet2}}, \tag{10.4}$$

where $E_T^{\rm jet1}$ and $E_T^{\rm jet2}$ are the randomly ordered transverse energies of the two leading-$E_{\rm T}$ jets in an event. The variance of the asymmetry distribution can be written as

$$\sigma_A^2 = \left|\frac{\partial A}{\partial E_T^{\rm jet1}}\right|^2 \sigma_{E_T^{\rm jet1}}^2 + \left|\frac{\partial A}{\partial E_T^{\rm jet2}}\right|^2 \sigma_{E_T^{\rm jet2}}^2 . \tag{10.5}$$

Assuming $E_{\rm T} \equiv E_T^{\rm jet1} = E_T^{\rm jet2}$ and $\sigma_{E_T} \equiv \sigma_{E_T^{\rm jet1}} = \sigma_{E_T^{\rm jet2}}$, the fractional transverse energy can be expressed as a function of σ_A in the following way:

$$\left(\frac{\sigma_{E_T}}{E_{\rm T}}\right) = \sqrt{2}\sigma_A . \tag{10.6}$$

Figure 27 shows the asymmetry distributions A for different $E_{\rm T}$ bins. The asymmetry distributions show minimal tails ($\ll 1\%$) and are well-described by a Gaussian distribution.

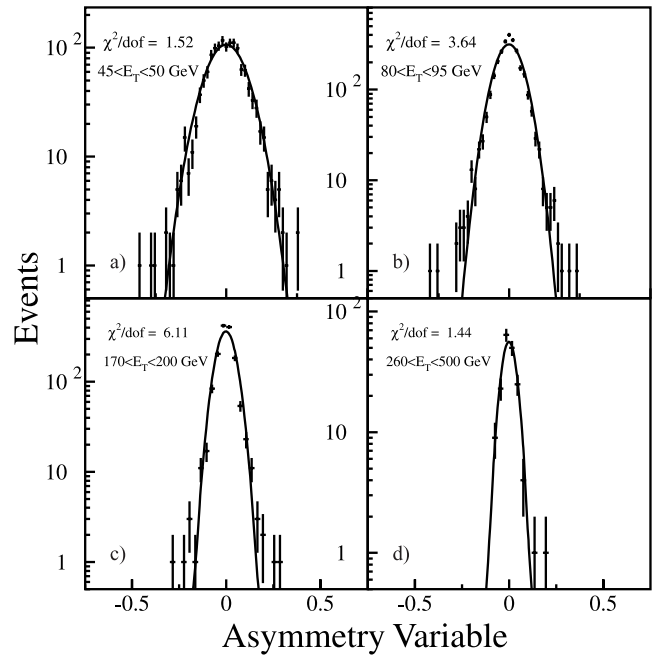

FIG. 27. Asymmetry distribution in several E_T bins for jets with $|\eta| < 0.5$ and $E_T^{\rm jet3} < 8$ GeV.

A. Soft radiation correction

Although the $\Delta\phi$ and third-jet $E_{\rm T}$ cuts ($\Delta\phi > 175°$ and $E_T^{\rm jet3} < 8$ GeV) are designed to remove events with more than two reconstructed jets, events may still contain soft radiation that prevents the two leading-$E_{\rm T}$ jets from balancing in the transverse plane; therefore the measured resolutions are overestimates of the hypothetical ''true resolutions.'' To evaluate this bias, the resolutions were determined from samples with different $E_T^{\rm jet3}$ cuts: 8, 10, 12, 15, and 20 GeV. The resolutions are then extrapolated to a ''true'' dijet system with $E_T^{\rm jet3} = 0$. Figure 28 shows the fractional jet resolutions as a function of $E_T^{\rm jet3}$ cut for several $E_{\rm T}$ bins.

This procedure is repeated for every $E_{\rm T}$ bin. We expect the correction for additional radiation in the event to be continuous as a function of jet $E_{\rm T}$ and to be given by a function $K(E_{\rm T})$. Because the soft radiation bias should primarily affect small values of $E_{\rm T}$ but be negligible at high $E_{\rm T}$, we parametrize the soft radiation correction $K(E_{\rm T})$ with the function:

$$K(E_{\rm T}) = 1 - \exp(-a_0 - a_1 E_{\rm T}). \tag{10.7}$$

For the pseudorapidity bin $|\eta| < 0.5$, $a_0 = 2.20$ and $a_1 = 0.0055$ (Fig. 29). This parametrization corrects the resolutions of each $E_{\rm T}$ bin for the effects of soft radiation.

Note that the point-to-point correlations in Fig. 29 are very large because each data point represents a subsample of the data point to its immediate right. In addition, it is not clear that the linear trend continues down to $E_T^{\rm jet3} = 0$; hence we do not use the errors obtained from the fits to calculate the error on the corrected resolutions. The uncertainty in the extrapolation is the sum in quadrature of the following: the uncertainty in the resolution at $E_T^{\rm jet3} > 8$ GeV, the difference

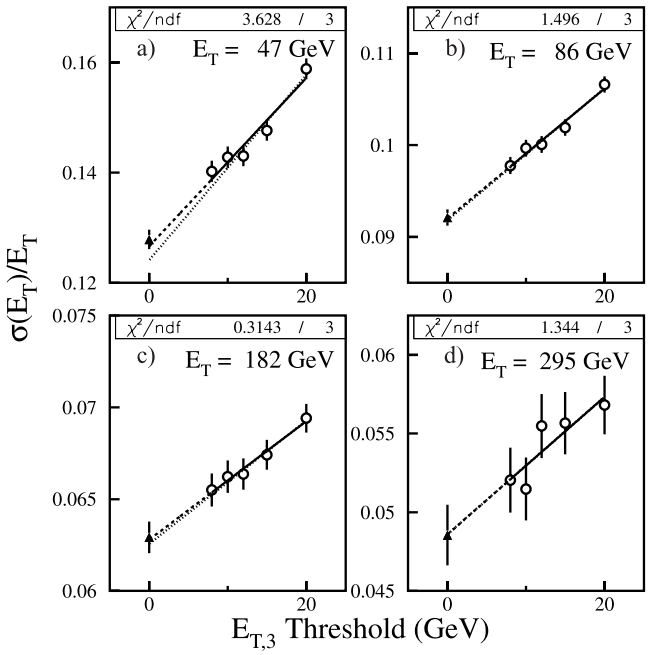

FIG. 28. Resolutions as a function of the cut on $E_T^{\rm jet3}$ for different $E_{\rm T}$ bins ($|\eta|<0.5$). The solid line shows the fit to the data points, the dashed line shows the extrapolation to $E_T^{\rm jet3}=0$, and the dotted line shows the fit excluding the $E_T^{\rm jet3}<8$ GeV point.

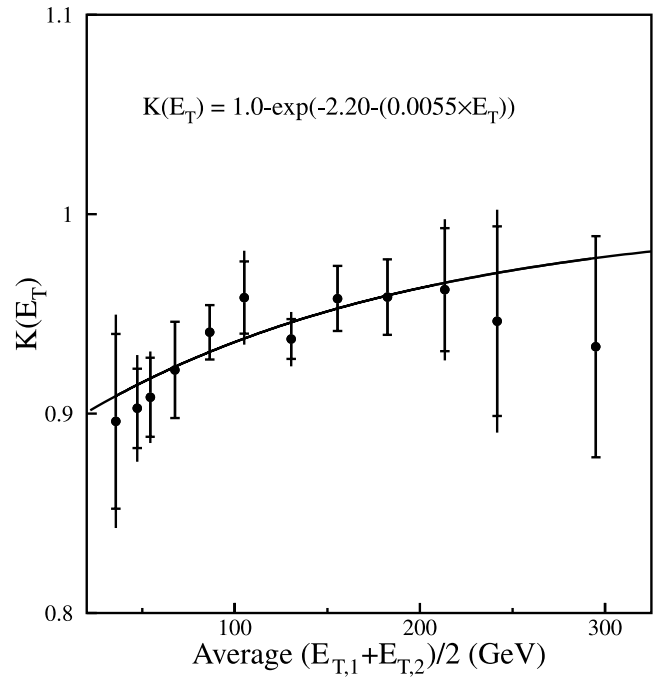

FIG. 29. The soft radiation correction, $K(E_{\rm T})$, as a function of $E_{\rm T}$ ($|\eta|<0.5$). The error bars show the total uncertainty in the point-to-point correlations. The inner error bars show the uncertainty in the resolutions measured with $E_T^{\rm jet3}>8$ GeV.

in the extrapolation to $E_T^{\rm jet3}=0$ including and excluding the sample with the $E_T^{\rm jet3}$ cut of 8 GeV, and the uncertainty in the fit to the point-to-point correlations.

B. Particle jet imbalance

Since we are correcting our measurements to the particle level, we must not include the effects of hadronization of the quarks and gluons in the resolutions. The energy carried by particles emitted outside the particle-level cone does not belong to the particle jet. In other words, at LO the total $\vec{p}_{\rm T}$ of a dijet event at the particle level is zero, but the two reconstructed particle jets do not necessarily balance, since there could be particles emitted outside the cones. The asymmetry distribution measures the detector resolution convoluted with the contribution of the dijet imbalance at the particle level. The latter must be removed.

The particle-level resolution is obtained by applying the same techniques as used on the data to a HERWIG [33] Monte Carlo sample, e.g. no energy fluctuations. The calorimeter resolution is obtained by removing the particle-level resolution using

$$\left(\frac{\sigma_{E_{\rm T}}}{E_{\rm T}}\right)^2=\left(\frac{\sigma_{E_{\rm T}}}{E_{\rm T}}\right)^2_{\rm data}-\left(\frac{\sigma_{E_{\rm T}}}{E_{\rm T}}\right)^2_{\rm MC}. \tag{10.8}$$

The fractional $E_{\rm T}$ resolutions before the particle jet imbalance correction are shown in Fig. 30 along with the MC data used to calculate the particle jet imbalance correction. The fully-corrected resolutions are given in Table IV.

C. Studies of systematic uncertainties

In principle, the soft radiation correction should remove the effects of additional gluon radiation in the data sample; however, this may not be the case because not all the particles present in the detector appear in reconstructed jets. It is also possible that the requirement that jets be back-to-back ($\Delta\phi>175°$) preferentially selects events with better-than-average resolution. The possible size of these effects is studied by changing the back-to-back requirement to $\Delta\phi>165°$ and repeating the determination of the resolutions. The result of this study is shown in Fig. 31. The resulting resolutions are slightly higher than the resolutions calculated with a cut of $\Delta\phi>175°$ and this difference is included in the overall systematic error.

Some analyses require a tighter cut on the $\not{E}_T$ than the standard cut. In particular, the measurement of the inclusive jet cross section requires a $\not{E}_T$ cut of $\not{E}_T/E_T^{\rm jet1}<0.3$ when $E_T^{\rm jet1}>100$ GeV, or $\not{E}_T<30$ GeV when $E_T^{\rm jet1}<100$ GeV. Any strengthening of the $\not{E}_T$ requirement will implicitly reduce the difference between the $E_{\rm T}$'s of the two jets selected and also reduce the amount of soft gluon radiation; hence the resolutions should improve. The resolution parametrization using this $\not{E}_T$ cut is depicted in Fig. 31.

The fractional $E_{\rm T}$ resolutions are parametrized using Eq. (10.2) for all rapidities ($|\eta|<1$) and are given in Table V and are plotted in Figs. 31 and 32.

D. Jet resolutions at $\sqrt{s}=630$ GeV

The jet resolutions at $\sqrt{s}=630$ GeV are measured using the same techniques as the resolutions at $\sqrt{s}=1800$ GeV.

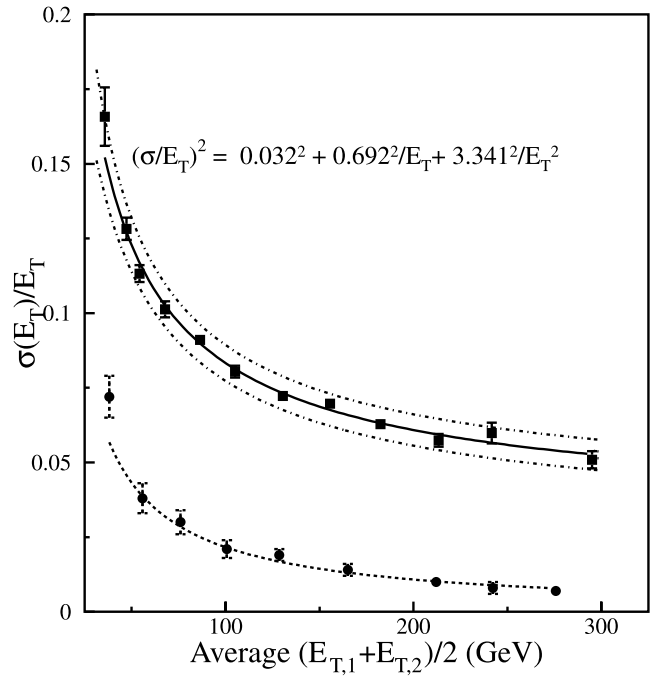

FIG. 30. σ_{E_T/E_T} as a function of average E_T for $|\eta|<0.5$. The data points (squares) indicate the resolutions after the soft radiation correction and the solid curve shows the fit to the resolutions. The dash-dot lines show the systematic uncertainty due to the method. The dashed line is a fit to the particle-level resolutions obtained from MC points (circles).

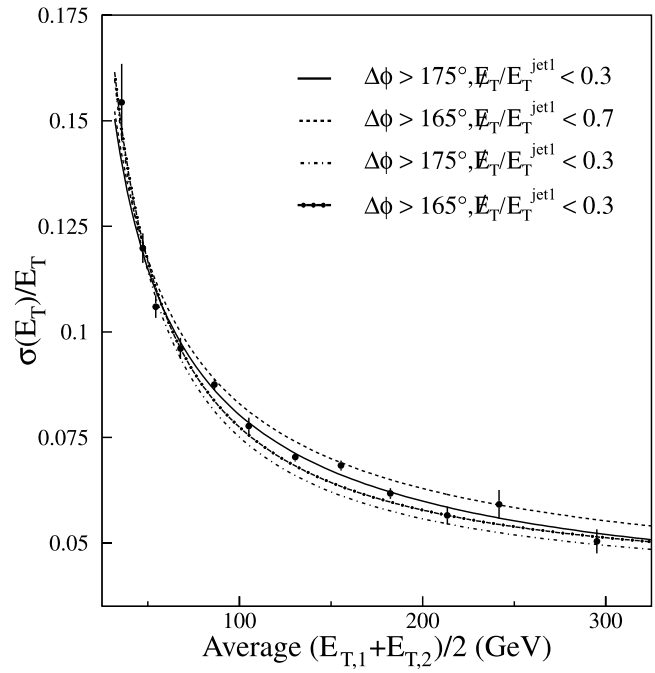

FIG. 31. Fully corrected σ_{E_T}/E_T as a function of average E_T for $|\eta|<0.5$ (i.e. the soft radiation correction and the particle-level dijet imbalance corrections have been applied). The data points (solid curve) show the resolution as calculated with cuts $\not{E}_T/E_T^{jet1}<0.7$ and $\Delta\phi>175°$. The dashed line shows the effect of using a cut of $\Delta\phi>165°$. In addition, the effects of using a $\not{E}_T$ cut of $\not{E}_T/E_T^{jet1}<0.3$ when $E_T^{jet1}>100$ GeV, or $\not{E}_T<30$ GeV when $E_T^{jet1}<100$ GeV are shown (dash-dot and solid-dots lines).

These resolutions are supplemented at low values of jet E_T by resolutions measured using photon-jet events.

The energy resolution for photons is approximately 10 times better than that for a jet, allowing a convenient redefinition of Eq. (10.4). The photon-jet asymmetry is defined as

$$A_{\gamma,\mathrm{jet}}=\frac{E_T^{\gamma}-E_T^{\mathrm{jet}}}{E_T^{\gamma}}, \tag{10.9}$$

where E_T^{γ} and E_T^{jet} are the fully corrected photon and jet transverse energies, respectively. If one approximates $E_T^{\gamma}\approx E_T^{\mathrm{jet}}\equiv E_T$ as before, and takes $\delta E_T^{\gamma}\approx 0$, the standard deviation of the photon-jet asymmetry identically becomes the fractional jet resolution:

$$\left(\frac{\sigma_{E_T}}{E_T}\right)=\sigma_{A_{\gamma,\mathrm{jet}}}. \tag{10.10}$$

Figure 33 displays a typical distribution of photon-jet asymmetry.

As described in previous sections, the measured resolution is adjusted to reflect third-jet biases and the particle-jet asymmetry. The results bolster the low-statistics dijet results at $\sqrt{s}=630$ GeV. The resulting resolutions are given in Table VI and are compared with the resolutions at $\sqrt{s}=1800$ GeV in Fig. 34. It is clear that the resolutions at the different center-of-mass energies are significantly different (a probability of agreement of 0.0007).

TABLE IV. The measured jet resolutions at $\sqrt{s}=1800$ GeV and their uncertainties.

$\langle E_T\rangle$ (GeV)	$\sigma(E_T)/E_T$	$\Delta[\sigma(E_T)/E_T]$
35.75	0.154	0.009
47.32	0.120	0.004
54.25	0.106	0.003
67.70	0.096	0.003
86.43	0.088	0.001
105.08	0.078	0.002
130.42	0.070	0.001
155.54	0.068	0.001
182.40	0.062	0.001
213.44	0.056	0.002
241.69	0.059	0.003
295.10	0.050	0.003

Parametrization of the jet resolutions

There are several parametrization choices that can be used to fit the data at both center-of-mass energies. We considered five alternative parametrizations of the resolutions:

(1) Fit the data simultaneously with Eq. (10.2): the CSN model.

(2) Fit the data with common C and S terms and different noise terms (N_{1800}, N_{630}) at the two c.m. energies: the CSNN model.

TABLE V. The resolution fit parameters at $\sqrt{s}=1800$ GeV.

	Fit variables for a $\not{E}_T$ cut of $\not{E}_T/E_T^{\rm jet1}<0.7$		
η	C	S	N
$\lvert\eta\rvert<0.5$	0.033 ± 0.006	0.686 ± 0.065	2.621 ± 0.810
$0.5<\lvert\eta\rvert<1.0$	0.047 ± 0.008	0.783 ± 0.137	0.590 ± 9.334
$0.1<\lvert\eta\rvert<0.7$	0.040 ± 0.013	0.641 ± 0.160	2.891 ± 1.413
	Fit variables for a $\not{E}_T$ cut of $\not{E}_T/E_T^{\rm jet1}<0.3$		
η	C	S	N
$\lvert\eta\rvert<0.5$	0.037 ± 0.002	0.514 ± 0.027	4.009 ± 0.202
$0.5<\lvert\eta\rvert<1.0$	0.036 ± 0.006	0.736 ± 0.059	1.972 ± 0.904
$0.1<\lvert\eta\rvert<0.7$	0.038 ± 0.005	0.550 ± 0.074	3.654 ± 0.487

(3) Fit the data with common C and N terms and different sampling terms (S_{1800}, S_{630}) at the two c.m. energies: the CSSN model (Fig. 35).

(4) Fit the data with a common C term and different sampling and noise terms at the two c.m. energies: the CSSNN model.

(5) Fit the data with no common terms: the CCSSNN model.

A model where only the C term was allowed to vary between the two c.m. energies was not considered because C depends on the physical structure of the calorimeter, and hence should not change. The χ^2 and numbers of degrees of freedom for these five models are calculated and compared in Table VII. The fit parameters are given in Table VIII.

It is clear from the χ^2 of the parametrizations that the data cannot be represented by a single fit with common C, S, and N (CSN model). Of the other models, the CSSN model gives the best fit to the data. If we allow additional parameters to be included in the fit, the χ^2 does not improve significantly. The CSNN model does not fit the data as well. The noise distribution in the calorimeter is similar at the two different c.m. energies (Fig. 36); hence the CSSN parametrization model was chosen to fit the resolutions. The cause of the change in sampling term as a function of c.m. energy is not known. We have some evidence that the cause of the change in the sampling term as a function of c.m. energy may be attributable to the change in the mix of quarks and gluons at fixed E_T [53], but this has not been proven for lack of sufficient computing resources, and the ultimate reason for this effect is therefore not yet fully understood.

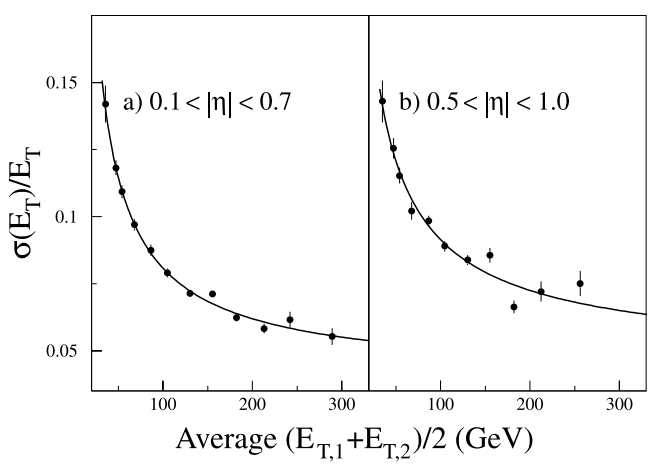

FIG. 32. Fully corrected σ_{E_T} as a function of $E_{\rm T}$ for different rapidity regions.

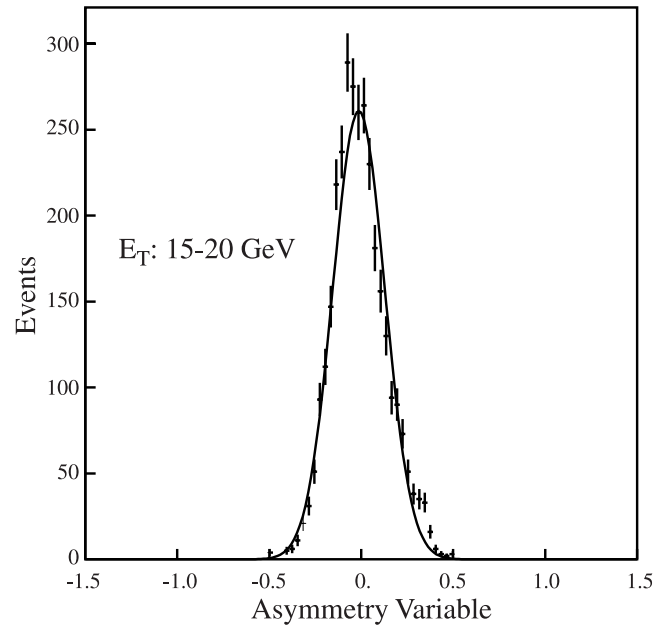

FIG. 33. Distribution of photon-jet asymmetry for jet $E_{\rm T}$ between 15 and 20 GeV in the central region.

E. Monte Carlo consistency tests

To verify the resolution extraction methods, a Monte Carlo study compared events with and without the detector simulation. The jet resolutions of the MC sample are measured in two ways; the first is the asymmetry method, and the second is a direct measurement of the resolutions. If the $E_{\rm T}$ of a jet as measured by the calorimeter is simply denoted by E_T, and the $E_{\rm T}$ as measured at the particle-level is denoted by $E_T^{\rm ptcl}$, then the jet resolution can be derived from the ratio

TABLE VI. The measured jet resolutions (and uncertainties) at $\sqrt{s}=630$ GeV.

Data set	$\langle E_{\rm T}\rangle$ (GeV)	$\sigma(E_{\rm T})/E_{\rm T}$	$\Delta[\sigma(E_{\rm T})/E_{\rm T}]$
γ-jet	13.51	0.205	0.023
γ-jet	17.81	0.217	0.048
γ-jet	21.52	0.175	0.016
γ-jet	24.27	0.169	0.019
jet-jet	26.28	0.148	0.012
jet-jet	34.35	0.117	0.015
jet-jet	40.87	0.114	0.010
jet-jet	52.27	0.097	0.009
jet-jet	59.12	0.079	0.007
jet-jet	70.53	0.075	0.006

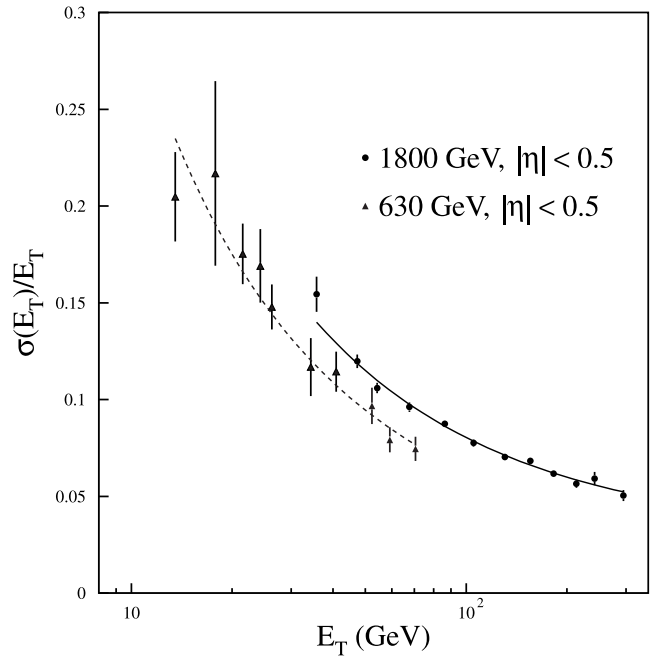

FIG. 34. The single jet resolutions at $\sqrt{s}=630$ GeV (triangles) and 1800 GeV (circles). The resolutions at the two center-of-mass energies have been fitted separately to Eq. (10.2). The fit to the $\sqrt{s}=1800$ GeV data is the solid line, and the fit to the $\sqrt{s}=630$ GeV data is the dashed line.

$$\frac{E_T^{\rm ptcl}-E_{\rm T}}{E_T^{\rm ptcl}}. \tag{10.11}$$

Figure 37 shows the differences in the resolutions as measured by the two methods. The differences between the two

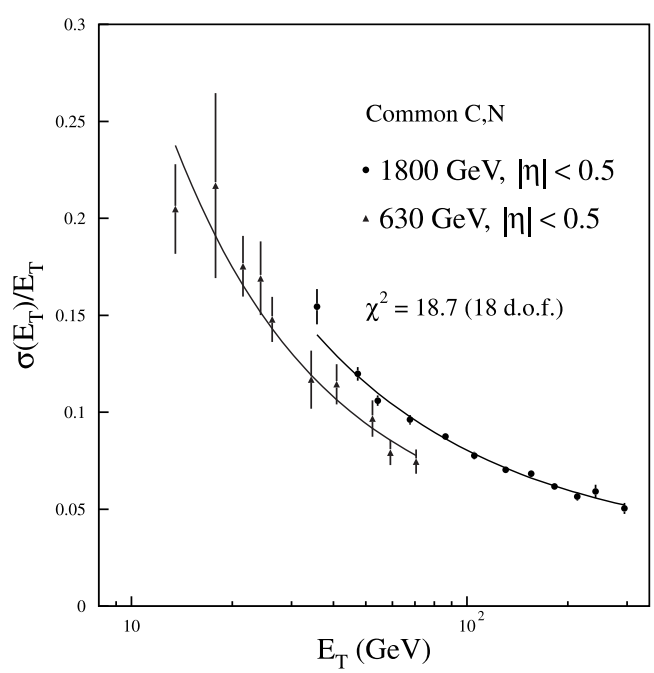

FIG. 35. The single jet resolutions at $\sqrt{s}=630$ GeV (triangles) and 1800 GeV (circles). The resolutions at the two center of mass energies have been fitted using the CSSN model (solid lines).

TABLE VII. χ^2 for the different models that can be used to parametrize the single jet resolutions.

Model	χ^2	Degrees of freedom	Probability
CSN	44.9	19	0.0007
CSNN	25.5	18	0.11
CSSN	18.7	18	0.41
CSSNN	17.9	17	0.35
CCSSNN	17.9	16	0.33

are scattered about zero, indicating lack of bias in the method. The differences between the two methods, less than 1%, indicates the magnitude of the systematic uncertainty, which can be parametrized as

$$\Delta\left(\frac{\sigma_{E_T}}{E_T}\right)=\frac{2.0}{E_{\rm T}^2}+0.01. \tag{10.12}$$

Subsequent to the publication by DØ of the inclusive jet cross section [8] (Sec. XI) and the dijet mass spectrum [25] (Sec. XIV) at $\sqrt{s}=1800$ GeV the MC closure data for the resolutions were reexamined (see Fig. 38). As a result of this, the MC closure error at $\sqrt{s}=1800$ GeV was reduced for $E_{\rm T}>40$ GeV:

TABLE VIII. The fit parameters for all models used to fit the resolution data. The correlation matrix for the CSSN model is also given.

Model	Parameter	Value	Statistical error
CSN	N	1.098	1.128
	S	0.745	0.038
	C	0.028	0.004
CSSN	N	2.571	0.309
	S_{1800}	0.691	0.027
	S_{630}	0.510	0.057
	C	0.032	0.003
	Correlation matrix		
1.000	−0.812	−0.838	0.575
−0.812	1.000	0.751	−0.902
−0.838	0.751	1.000	−0.589
0.575	−0.902	−0.589	1.000
CSNN	N_{1800}	3.543	0.399
	N_{630}	1.907	0.437
	S	0.590	0.049
	C	0.040	0.003
CSSNN	N_{1800}	2.510	0.893
	N_{630}	2.587	0.374
	S_{1800}	0.696	0.068
	S_{630}	0.509	0.063
	C	0.031	0.007

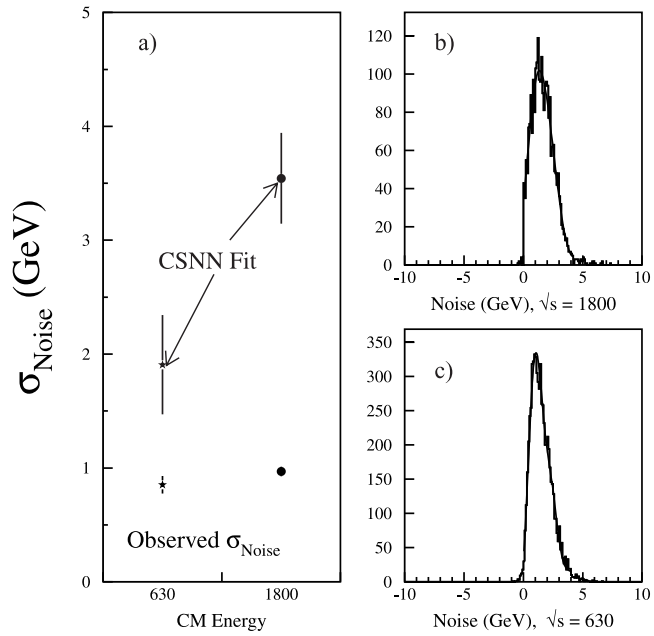

FIG. 36. (a) The average value and rms width of the calorimeter noise distributions is given by the two lower points. The two upper points are the values of the N parameter obtained in the fit to the resolution data using the CSNN model. (b) and (c): The noise distribution found within a standard jet cone at each center-of-mass energy (the cone used to measure the noise is required to be at least 90° in ϕ from any other jet in the event).

$$\Delta\left(\frac{\sigma_{E_T}}{E_{\rm T}}\right)_{\sqrt{s}=630\ \rm GeV}=\frac{2.23}{E_{\rm T}^2}+0.0021,$$

$$\Delta\left(\frac{\sigma_{E_T}}{E_{\rm T}}\right)_{\sqrt{s}=1800\ \rm GeV}=\frac{14.1}{E_{\rm T}^2}+0.0024. \tag{10.13}$$

The effect of reducing the error on the inclusive jet cross section and dijet mass spectrum was negligible, and hence the results were not updated. The reduced errors are important for the analysis of the ratio of inclusive jet cross sections at $\sqrt{s}=630$ and 1800 GeV [21] (Sec. XII).

In Fig. 39 the measured resolutions are compared with the CSSN fit. The shaded region shows the size of the fit uncertainty, and the hatched region shows the size of the fit and MC closure uncertainties added in quadrature. Also shown are the other models. It is clear that the combined fit and MC closure uncertainties are of reasonable size and that the total uncertainties are not underestimated.

F. η and ϕ resolutions

After the η-bias correction is applied, the average η of the reconstructed jet is equal to the η of a particle-level jet, but due to calorimeter showering effects, both η and ϕ resolutions remain non-zero. The η resolution is obtained by using HERWIG Monte Carlo and studying $\eta_{\rm ptcl}-\eta$ as a function of jet energy and η. Figure 40 shows the η-resolution as a function of jet energy for different energy regions. The distributions show no tails and are well-described by a Gaussians. The ϕ resolution is determined by measuring $\phi_{\rm ptcl}-\phi$ as a function of jet energy and η. Figure 41 shows the ϕ resolutions which are similar in magnitude to the η resolutions.

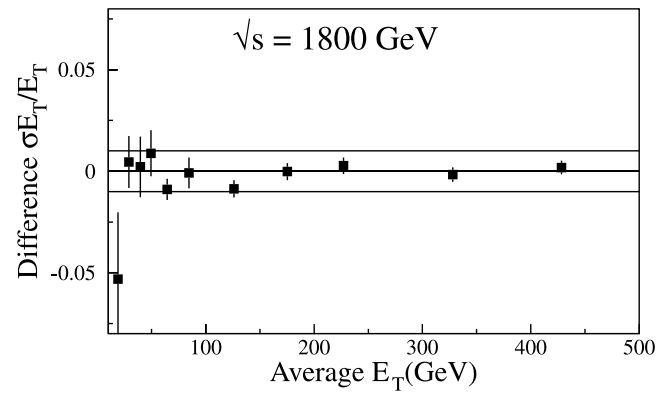

FIG. 37. Resolution closure from HERWIG Monte Carlo simulation; the difference in resolution obtained using the two techniques. The degree of closure is within 1% for all data points above 25 GeV.

XI. INCLUSIVE JET CROSS SECTION AT $\sqrt{s}=1800$ GeV

In this section we describe the measurement of the inclusive jet cross section in the pseudorapidity ranges $|\eta|<0.5$ and $0.1<|\eta|<0.7$. The inclusive jet cross section is given by

$$\frac{d^2\sigma}{dE_{\rm T}d\eta}=\frac{N_iC_i}{\mathcal{L}_i\epsilon_i\Delta E_{\rm T}\Delta\eta} \tag{11.1}$$

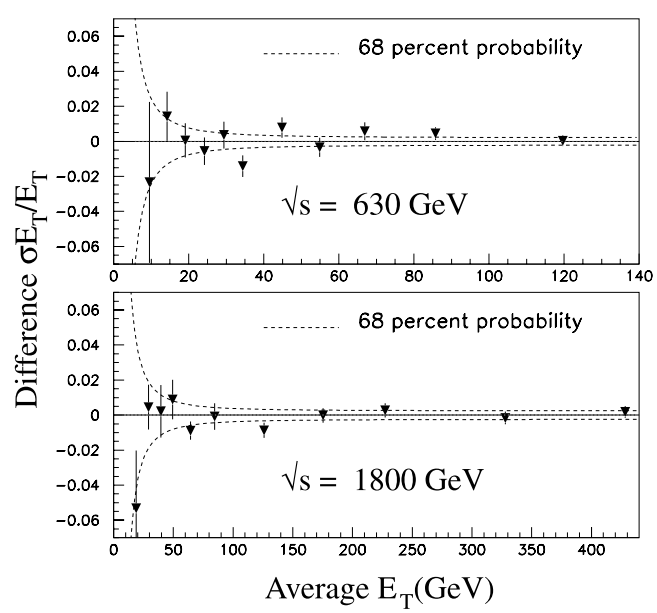

FIG. 38. The improved resolution closure obtained using the HERWIG Monte Carlo simulation, for both center-of-mass energies. For most of the kinematic range, the degree of closure lies within a fraction of a percent.

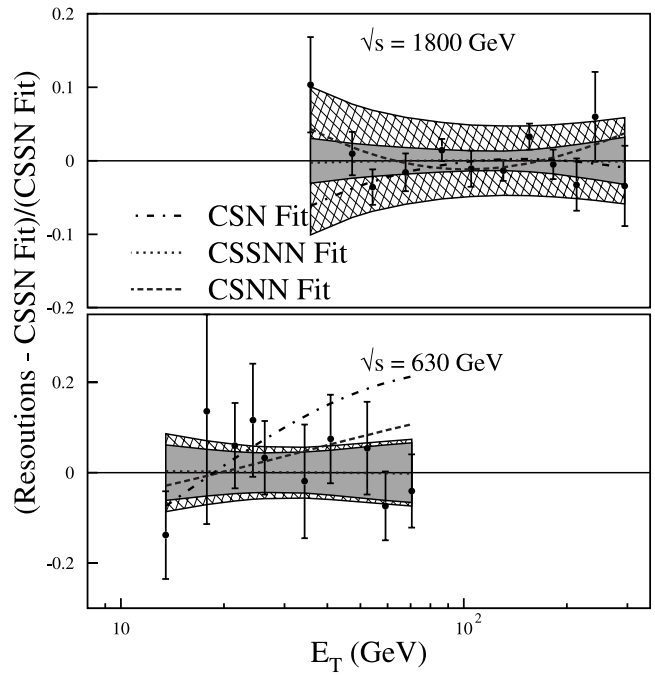

FIG. 39. A comparison of the measured jet resolutions and the fit using the CSSN model. Also shown are curves representing comparisons between the different models and CSSN. The shaded regions show the uncertainty in the fit. The hatched region shows the magnitude of the fit and MC closure uncertainties added in quadrature.

where N_i is the number of accepted jets in E_{T} bin i of width ΔE_{T}, C_i is the resolution unsmearing correction, $\mathcal{L}_i$ is the integrated luminosity, ϵ_i is the efficiency of the trigger, vertex selection, and the jet quality cuts, and $\Delta\eta$ is the width of the pseudorapidity bin.

A. Data selection

The selected data are events with one or more jets which satisfy the requirements of the inclusive jet triggers. Jets are required to pass the standard jet quality criteria to be included in the cross section sample (Sec. VIII). The $\not{E}_T$ of the event is required to satisfy Eq. (8.5). The vertex of the event must be within 50 cm of $z=0$. The efficiency for each jet is then given by the product of the efficiencies of the jet quality cuts (ϵ_{jet}), the efficiency of the cut on $\not{E}_T$ (ϵ_{met}), the efficiency for an event to pass the trigger ($\epsilon_{\mathrm{trigger}}$), and the efficiency for passing the vertex cut ($\epsilon_{\mathrm{vertex}}$):

$$\epsilon_i=\epsilon_{\mathrm{jet}}\epsilon_{\mathrm{met}}\epsilon_{\mathrm{trigger}}\epsilon_{\mathrm{vertex}}. \tag{11.2}$$

The values of ϵ_{jet} and ϵ_{met} are plotted in Fig. 17. The efficiency of the vertex requirement is $90\pm1\%$.

B. Filter efficiency and luminosity matching

Figure 42 shows the cross section ratios for Jet_50/Jet_30, Jet_85/Jet_50 and Jet_115/Jet_85. Since the denominator in each ratio represents a less restrictive trigger than the numerator, the numerator trigger is efficient where the ratio stabilizes at a constant value. Thus Jet_50, Jet_85, and Jet_115 are efficient above 90, 130, and 170 GeV, respectively. The efficiency for Jet_30 was determined to be 100% at 50 GeV (Sec. V).

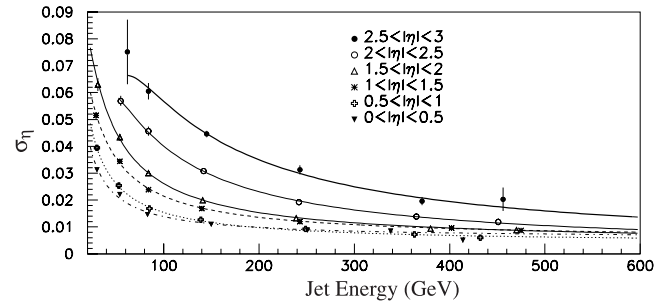

FIG. 40. η resolution as a function of the particle-level jet energy using a HERWIG simulation.

The determination of the integrated luminosity for each of the jet triggers is described in detail in Sec. VI. The luminosity used for Jet_50 is determined by matching the Jet_50 inclusive jet cross section to the Jet_85 cross section above 130 GeV, introducing a 1.1% statistical error. The Jet_30 luminosity is determined by matching to the Jet_50 cross section above 90 GeV, which results in a 1.4% statistical error. Hence the matching error for Jet_30 is given by 1.1% and 1.4% added in quadrature, or 1.7%. These errors are added to the 5.8% error on Jet_85. The final Jet_30 and Jet_50 luminosities are then 0.350 pb^{-1} and 4.76 pb^{-1} with errors of 6.1% and 5.9%, respectively.

Figure 43 shows E_{T} spectra for the four jet triggers, without luminosity normalization, in the central rapidity region ($|\eta|<0.5$) after efficiency and energy corrections.

C. Observed cross section

Figure 44 shows the central cross section compiled from the four triggers. As suggested by the cross section ratios, and in order to maximize statistics, the spectrum from $60\leqslant E_{\mathrm{T}}\leqslant 90$ GeV is taken from the Jet_30 data, 90−130 GeV from Jet_50, 130−170 GeV from Jet_85, and above 170 GeV from Jet_115. The three data sets in Fig. 44 correspond to the low, nominal, and high energy scale corrections. The differences can be considered to be an error estimate on the cross section which dominates all other sources of error (luminosity, jet, missing E_{T}, and vertex cuts).

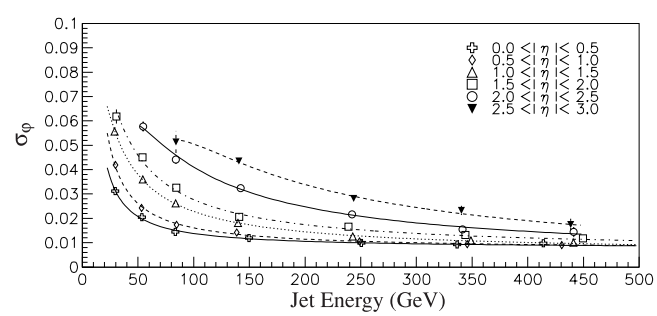

FIG. 41. ϕ resolution as a function of the particle-level jet energy using a HERWIG simulation.

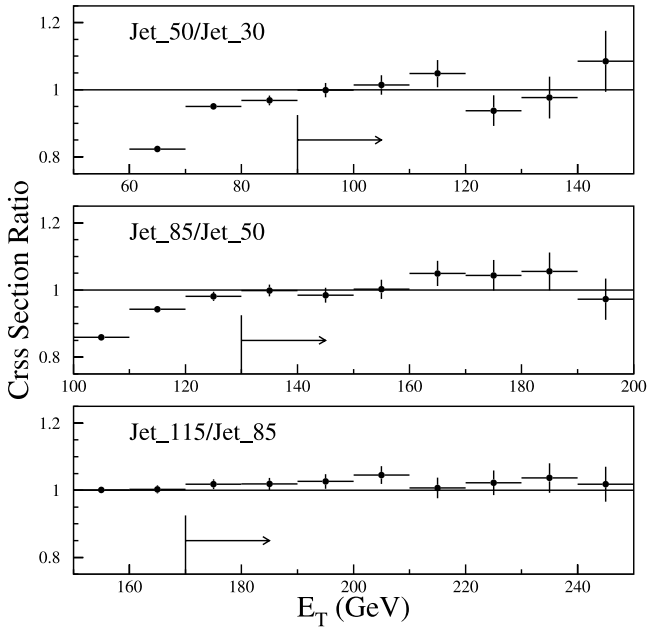

FIG. 42. Inclusive cross section ratios. The arrows signify the E_T above which the higher threshold trigger is used.

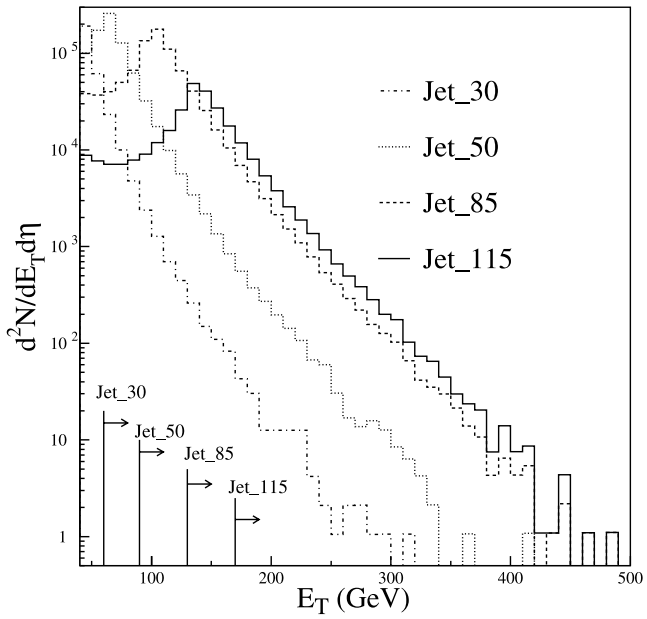

FIG. 43. Energy-corrected E_T spectra for Jet_115 (solid line), Jet_85 (dashed), Jet_50 (dotted), and Jet_30 (dot-dashed). The arrows signify the E_T range in which each trigger's spectrum is used.

D. Highest E_T event scanning

Since the cross section decreases rapidly as the E_T increases, a small amount of contamination can have a significant effect on the measured cross sections at large E_T. The data set included 46 events that passed selection cuts and contained a central jet ($|\eta| \leqslant 0.7$) with transverse energy greater than 375 GeV. These events were visually scanned for contamination. We defined an event to be "good" if it had at least two jets with well-contained energy, if there were no isolated cells forming jets, and if there was no activity in the muon chambers consistent with cosmic ray interactions associated with the event. These conditions were intended to reject high-E_T jets arising from noisy calorimeter cells, cosmic rays, or beam halo from the main ring, which passes through the DØ detector [28]. The 46 events contained 62 jets with E_T greater than 375 GeV. Seven of these jets included restored cells and seven of the events preferred the second vertex. All of the events passed visual inspection.

E. Resolution unfolding

The steep E_T spectrum is distorted by jet energy resolution. The distortion was corrected by using an ansatz function for the cross section,

$$\exp(A)E_T^{\alpha}\left(1-\frac{2E_T}{\sqrt{s}}\right)^{\beta}, \tag{11.3}$$

smearing it with the measured resolution (Table V), and comparing the smeared result with the measured cross section. The parameters A, α, and β were varied until the best fit was found between the observed cross section and the smeared trial spectrum. The χ^2 for the fit is 21.2 for 24 bins and three parameters, corresponding to 21 degrees of freedom (Table IX). Figure 45 shows an example of the energy scale corrected data with the best-fit smeared and unsmeared ansatz functions. Simulations have shown that η-smearing causes negligible changes in the inclusive cross sections [20].

Figure 46 shows the unsmearing correction as a function of transverse energy. The observed cross section is multiplied

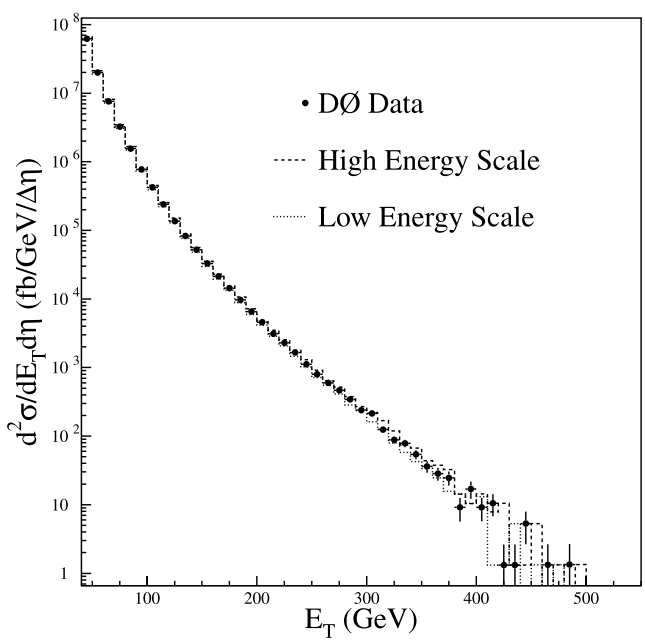

FIG. 44. Energy-corrected and luminosity-normalized E_T spectra. The points with error bars correspond to the nominal energy scale correction. The dashed (dotted) histogram corresponds to the high (low) energy scales corrections.

TABLE IX. Unsmearing ansatz function parameters for the inclusive jet cross section (in fb) at $\sqrt{s}=1800$ GeV.

Rapidity range	Parameter	Value
$\lvert\eta\rvert<0.5$	A	37.28
	α	-5.04
	β	8.23
$0.1<\lvert\eta\rvert<0.7$	A	37.30
	α	-5.05
	β	8.37

by this correction. The central curve shows the nominal correction. The change in cross section is greatest at low E_{T} due to the steepness of the inclusive spectra and the relatively poor, rapidly changing jet resolution. The magnitude of the correction is -13% at 64.6 GeV, drops to $\approx -6\%$ at 205 GeV, and then rises to -12% at 461 GeV.

The two outer curves of Fig. 46 show the extent of the uncertainties in the nominal correction due to the resolution uncertainties. This error was estimated directly with the data by unfolding with the upper and lower estimates of the resolution curves. For $\lvert\eta\rvert<0.5$ the maximum error is 3%. Varying the fit parameters by up to 3 standard deviations results in negligible changes in the resolution correction.

The resolution correction errors due to the fit procedure and statistical fluctuations of the data were estimated by performing the unfolding procedure on distributions simulated with JETRAD. A generated theoretical distribution was smeared with a resolution function. The ratio of the generated theoretical distribution to the smeared theoretical distribution was taken as the "true" unsmearing correction. Next, the previously described unfolding procedure was applied to the "smeared theory" and the resulting unsmearing correction was compared with the "true" unsmearing correction. The difference between the two corrections provided a measurement of the unfolding error. Above $E_{\mathrm{T}}=50$ GeV, the differences were less than 1%. The error due to statistical fluctuation was estimated by simulating many jet samples containing the same total number of jets as the data sample. The statistical fluctuations between the different simulated samples lead to an error below 0.25% in any E_{T} bin. A detailed description of this unfolding, and the unfolding error estimation procedures can be found in Ref. [20].

F. Unfolded cross section

The central inclusive jet cross section is shown in Fig. 47. The cross section values are plotted in each bin at the E_{T} value for which the average integrated cross section is equal to the value of the analytical function [Eq. (11.3)] fitted to the cross-section [54]. The error bars are purely statistical and are visible only for the highest E_{T} value. The error band indicates a one standard deviation variation of all systematic uncertainties, except the 5.8% uncertainty on the absolute normalization. The measured cross section is compared to the inclusive cross section for the same E_{T} values calculated with the JETRAD program using the CTEQ3M PDF and the scale $\mu=0.5E_T^{\max}$. This prediction lies within the error band for all E_{T} bins. Table X lists the cross sections for $\lvert\eta\rvert<0.5$ and $0.1<\lvert\eta\rvert<0.7$.

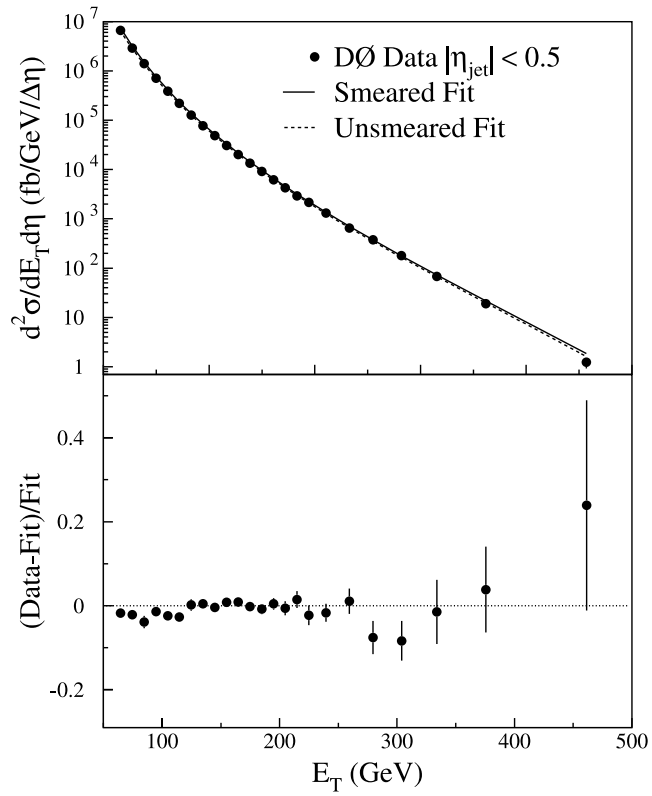

FIG. 45. Data with smeared and unsmeared fit hypotheses [Eq. (11.3)]. The lower pane shows the smeared fit residuals, (data-smeared fit)/smeared fit.

G. Cross section uncertainties

The cross section uncertainties are dominated by the uncertainties in the energy scale correction. Table XI summa-

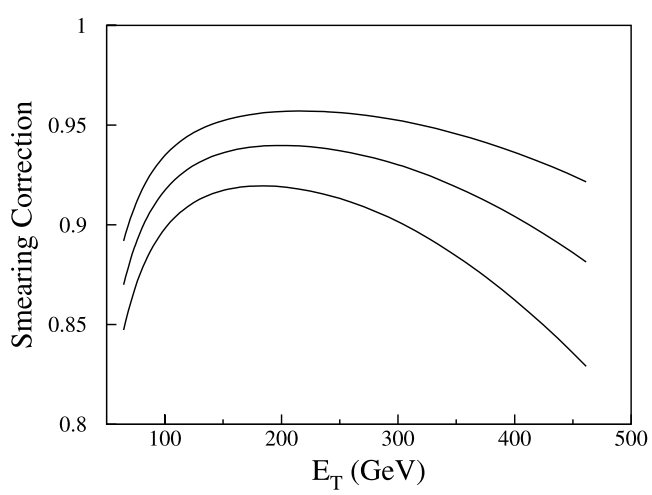

FIG. 46. The nominal unsmearing correction is given by the central line. See the text for an explanation of the other curves.

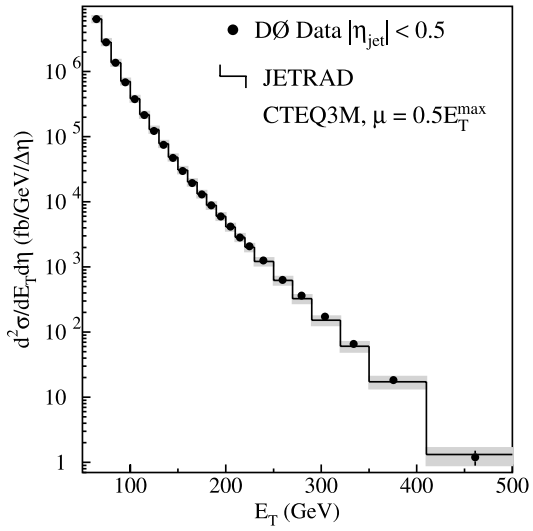

FIG. 47. The $|\eta|<0.5$ inclusive jet cross section. Statistical uncertainties are invisible on this scale except for the highest E_T bin. The histogram represents the JETRAD prediction and the shaded band represents the $\pm 1\sigma$ systematic uncertainty band about the prediction excluding the 5.8% luminosity uncertainty.

rizes the uncertainties in the unfolded cross section. A detailed list of the uncertainties and their magnitudes is given in Tables XII and XIII. Figure 48 shows the various uncertainties for the $|\eta|<0.5$ cross section. The second uppermost curve shows the uncertainty in the energy scale, which varies from 8% at low E_T to 30% at 450 GeV. Clearly, this contribution dominates all other sources of error except at low E_T where the 5.8% luminosity error is of comparable magnitude. The other sources of error (jet and event selection, trigger matching, and jet resolution) are relatively small.

Most of the systematic uncertainties in the inclusive jet cross section are highly correlated as a function of E_T. The uncertainties are separated into three ''types,'' depending on the correlation (ρ) between two bins:

$\rho=1$: ''Completely correlated,'' indicating that a 1σ fluctuation in an error at a particular E_T bin is accompanied by a 1σ fluctuation at all other E_T bins (Fig. 49).

$\rho=\rho(E_{T1},E_{T2})\in[-1,1]$: ''Partially correlated,'' possessing a varying degree of correlation in E_T. A 1σ fluctuation thus implies a less than 1σ fluctuation elsewhere (Fig. 50); negative ρ indicates the shifts will have opposite directions at the two points. This type of error is the most complicated to calculate and propagate.

$\rho=0$: ''Uncorrelated,'' statistical in nature or otherwise independent of one another. Some small errors with unknown (but probably positive) E_T correlation are treated as uncorrelated for simplicity. Such treatment is conservative.

The uncertainties due to jet selection are correlated as a function of E_T. The uncertainties due to unsmearing are also correlated. The luminosity uncertainty is correlated as a function of E_T. The trigger matching uncertainties are correlated as a function of E_T for bins that are derived from the same trigger sample and uncorrelated for all other bins. The energy scale errors are partially correlated as a function of E_T and are discussed below.

The energy scale calibration is implemented as a series of corrections, each with its own uncertainty (Sec. IX). The uncertainty due to the energy scale is separated into several components so that the correlations as a function of E_T can be studied (Fig. 51). The energy scale uncertainties were calculated with a Monte Carlo simulation of the inclusive jet cross section. At each uncorrected E_T the simulation generated an ensemble of jets with rapidity, vertex position, luminosity, and variable correlations derived from the data. Figure 51 shows the components of energy scale uncertainty as a function of E_T. The E_T of each of the simulated jets was then corrected and the resulting uncertainty in the jet cross section calculated. These uncertainties are in good agreement with the uncertainties derived from the data.

The uncertainties due to the offset correction, the η-dependent correction, the showering correction, and the method are all correlated as a function of E_T. The hadronic response uncertainty is partially correlated as a function of E_T (Sec. IX). The hadronic response correlations are illustrated in Fig. 52 and are given in Table XIV. In addition, the response uncertainties are only approximated by a Gaussian uncertainty distribution. Tables XV and XVI give the actual uncertainties for a given percentage confidence level (C.L.), i.e. if one has a $+20\%$ error in the cross section at a given E_T corresponding to 95% C.L., then with 95% probability the response errors will cause a deviation in the cross section of $\leqslant 20\%$. The correlations for the total systematic uncertainties are given in Table XVII.

H. Comparison of the data to theory

Figures 53 and 54 show the fractional difference between the data, D, and a JETRAD theoretical prediction, T, normalized by the prediction, $[(D-T)/T]$, for $|\eta|<0.5$ and $0.1<|\eta|<0.7$ respectively. The JETRAD prediction was generated with $\mu=0.5E_T^{max}$, $\mathcal{R}_{sep}=1.3$, and several different choices of PDF. The error bars represent statistical errors only. The outer bands represent the total cross section error excluding the 5.8% luminosity uncertainty. Given the experimental and theoretical uncertainties, the predictions are in agreement with the data; in particular, the data above $E_T=350$ GeV show no indication of an excess relative to QCD.

The data and theory can be compared quantitatively with a χ^2 test incorporating the uncertainty covariance matrix (Table XVII [55]). The χ^2 is given by

$$\chi^2=\sum_{i,j}\delta_i V_{ij}^{-1}\delta_j \tag{11.4}$$

where δ_i is the difference between the data and theory for a given E_T bin, and V_{ij} is element i,j of the covariance matrix:

$$V_{ij}=\rho_{ij}\Delta\sigma_i\Delta\sigma_j, \tag{11.5}$$

where $\Delta\sigma$ is the sum of the systematic error and the statistical error added in quadrature if $i=j$ and the systematic

TABLE X. The $|\eta|<0.5$ and $0.1<|\eta|<0.7$ cross sections (Eq. 11.1). Also given is the value of the fit to the cross section using Eq. (11.3).

	$\lvert\eta\rvert<0.5$				$0.1<\lvert\eta\rvert<0.7$			
Bin Range (GeV)	Plotted E_T (GeV)	Cross Sec. $\pm$ Stat. (fb/GeV/$\Delta\eta$)	Sys. Uncer.(%)	Fitted Cross Sec. (fb/GeV/$\Delta\eta$)	Plotted E_T (GeV)	Cross Sec. $\pm$ Stat. (fb/GeV/$\Delta\eta$)	Sys. Uncer.(%)	Fitted Cross Sec. (fb/GeV/$\Delta\eta$)
60–70	64.6	$(6.39\pm0.04)\times10^6$	±10	6.27×10^6	64.6	$(6.26\pm0.04)\times10^6$	±10	6.13×10^6
70–80	74.6	$(2.80\pm0.03)\times10^6$	±10	2.74×10^6	74.6	$(2.74\pm0.03)\times10^6$	±10	2.67×10^6
80–90	84.7	$(1.36\pm0.02)\times10^6$	±10	1.31×10^6	84.7	$(1.34\pm0.02)\times10^6$	±10	1.28×10^6
90–100	94.7	$(6.84\pm0.04)\times10^5$	±10	6.74×10^5	94.7	$(6.66\pm0.04)\times10^5$	±10	6.53×10^5
100–110	104.7	$(3.76\pm0.03)\times10^5$	±10	3.67×10^5	104.7	$(3.63\pm0.03)\times10^5$	±10	3.54×10^5
110–120	114.8	$(2.14\pm0.02)\times10^5$	±10	2.08×10^5	114.8	$(2.07\pm0.02)\times10^5$	±10	2.01×10^5
120–130	124.8	$(1.23\pm0.02)\times10^5$	±10	1.23×10^5	124.8	$(1.19\pm0.01)\times10^5$	±10	1.18×10^5
130–140	134.8	$(7.46\pm0.04)\times10^4$	±10	7.49×10^4	134.8	$(7.16\pm0.03)\times10^4$	±10	7.18×10^4
140–150	144.8	$(4.71\pm0.03)\times10^4$	±10	4.69×10^4	144.8	$(4.51\pm0.03)\times10^4$	±10	4.48×10^4
150–160	154.8	$(2.97\pm0.02)\times10^4$	±10	3.00×10^4	154.8	$(2.83\pm0.02)\times10^4$	$+11,-10$	2.86×10^4
160–170	164.8	$(1.94\pm0.02)\times10^4$	$+11,-10$	1.96×10^4	164.8	$(1.83\pm0.02)\times10^4$	±11	1.86×10^4
170–180	174.8	$(1.30\pm0.01)\times10^4$	±11	1.30×10^4	174.8	$(1.23\pm0.01)\times10^4$	±11	1.23×10^4
180–190	184.8	$(8.83\pm0.10)\times10^3$	±11	8.75×10^3	184.8	$(8.38\pm0.09)\times10^3$	±11	8.28×10^3
190–200	194.8	$(5.95\pm0.08)\times10^3$	±11	5.98×10^3	194.8	$(5.64\pm0.07)\times10^3$	$+12,-11$	5.64×10^3
200–210	204.8	$(4.15\pm0.07)\times10^3$	$+12,-11$	4.13×10^3	204.8	$(3.93\pm0.06)\times10^3$	$+12,-11$	3.88×10^3
210–220	214.8	$(2.84\pm0.06)\times10^3$	$+12,-11$	2.88×10^3	214.8	$(2.67\pm0.05)\times10^3$	±12	2.70×10^3
220–230	224.8	$(2.08\pm0.05)\times10^3$	±12	2.03×10^3	224.8	$(1.95\pm0.04)\times10^3$	$+13,-12$	1.90×10^3
230–250	239.4	$(1.26\pm0.03)\times10^3$	$+13,-12$	1.24×10^3	239.4	$(1.17\pm0.02)\times10^3$	$+13,-12$	1.15×10^3
250–270	259.4	$(6.34\pm0.19)\times10^2$	$+14,-13$	6.40×10^2	259.4	$(5.84\pm0.17)\times10^2$	$+14,-13$	5.94×10^2
270–290	279.5	$(3.65\pm0.15)\times10^2$	$+14,-13$	3.39×10^2	279.5	$(3.21\pm0.12)\times10^2$	$+15,-14$	3.13×10^2
290–320	303.9	$(1.73\pm0.08)\times10^2$	$+16,-14$	1.60×10^2	303.9	$(1.56\pm0.07)\times10^2$	$+16,-15$	1.47×10^2
320–350	333.9	$(6.60\pm0.50)\times10^1$	$+17,-16$	6.50×10^1	333.9	$(6.06\pm0.44)\times10^1$	$+18,-16$	5.91×10^1
350–410	375.7	$(1.83\pm0.19)\times10^1$	$+21,-18$	1.91×10^1	375.7	$(1.48\pm0.15)\times10^1$	$+22,-19$	1.72×10^1
410–560	461.1	$(1.20\pm0.30)\times10^0$	$+30,-25$	1.57×10^0	460.9	$(1.05\pm0.25)\times10^0$	$+31,-26$	1.39×10^0

error if $i\neq j$, and ρ_{ij} is the correlation between the systematic uncertainties of E_T bins as given in Table XVII. The systematic uncertainty is given by the percentage uncertainty times the theoretical prediction (see Appendix for a discussion of the χ^2). The resulting χ^2 values are given in Table XVIII for all of the theoretical choices described above. The choice of PDF and renormalization scale is varied. Each comparison has 24 degrees of freedom.

All but one of the JETRAD predictions adequately describe the $|\eta|<0.5$ and $0.1<|\eta|<0.7$ cross sections. For these, the probabilities for χ^2 to exceed the listed values are between 11% and 86%. The prediction using CTEQ4HJ and $\mu=0.5E_T^{\max}$ produces the highest probability for both measurements. The prediction with the MRST($g\downarrow$) PDF has a probability of agreement with the data of 0.3%, and thus is incompatible with our data.

TABLE XI. Unfolded cross section errors.

Source	Percentage	Comment
Jet and event selection	<2	Correlated
Luminosity	5.8	Correlated
Luminosity match		
60– 90 GeV	1.7	Statistical, Correlated
90–130 GeV	1.1	Trigger-to-trigger
Energy Scale	15–30	Mostly correlated
Unfolding		
Resolution function	1–3	Correlated
Closure	1–2	Correlated

Comparisons between the data and EKS calculations using various PDFs, $\mathcal{R}_{\rm sep}=1.3$, and with renormalization scales $\mu=(0.25, 0.50, 0.75, 1.00, 1.25, 1.50, 1.75, 2.00)E_T$ (where $E_T=E_T^{\max}$ and $E_T^{\rm jet}$) are also made (Table XIX). The EKS predictions give a reasonable description of the $|\eta|<0.5$ cross section. However, unlike the JETRAD predictions, the EKS calculation using CTEQ3M and $\mu=0.25E_T^{\max}$ has the highest probability of agreement. The EKS predictions for $0.1<|\eta|<0.7$ all give χ^2 values with probabilities $\leqslant 12\%$ for the choices examined.

I. Comparison with previously published results

The top panel in Fig. 55 shows $(D-T)/T$ for our data in the $0.1\leqslant|\eta|\leqslant0.7$ region relative to a JETRAD calculation using the CTEQ4HJ PDF, $\mu=0.5E_T^{\max}$, and $\mathcal{R}_{\rm sep}=1.3$. Also shown are the previously published CDF data from the 1992–1993 Fermilab Tevatron running period [7] relative to

TABLE XII. Percentage $|\eta|<0.5$ cross section uncertainties. The last row gives the nature of the E_T bin-to-bin correlations: 0 signifies uncorrelated uncertainties, 1 correlated, and p partially correlated.

E_T GeV	Stat Error	Jet Sel	Lumin	Lumin Match	Unsmearing		Energy Scale									
							Underlying		η		Method		Shower		Response	
					High	Low	High	Low	High	Low	High	Low	High	Low	High	Low
64.6	0.7	0.5	5.8	1.8	2.5	−2.6	5.3	−5.0	0.2	−0.2	3.4	−3.2	4.7	−4.6	1.1	−1.0
74.6	1.0	0.5	5.8	1.8	2.3	−2.4	4.7	−4.5	0.2	−0.2	3.5	−3.3	4.8	−4.7	1.2	−1.1
84.7	1.5	0.5	5.8	1.8	2.1	−2.2	4.2	−4.1	0.2	−0.2	3.5	−3.5	4.9	−4.8	1.5	−1.3
94.7	0.6	0.5	5.8	1.1	1.9	−2.1	3.8	−3.7	0.2	−0.2	3.6	−3.5	5.0	−4.9	1.9	−1.9
104.7	0.8	0.5	5.8	1.1	1.9	−2.1	3.5	−3.4	0.2	−0.2	3.6	−3.6	5.1	−5.1	2.2	−2.2
114.8	1.0	0.5	5.8	1.1	1.8	−2.0	3.2	−3.1	0.2	−0.2	3.7	−3.6	5.3	−5.1	2.6	−2.5
124.8	1.4	0.5	5.8	1.1	1.8	−2.0	3.0	−2.9	0.2	−0.2	3.9	−3.7	5.4	−5.2	2.8	−2.8
134.8	0.5	0.5	5.8	0.0	1.7	−2.0	2.9	−2.8	0.2	−0.2	4.1	−3.9	5.6	−5.4	3.1	−3.0
144.8	0.6	0.5	5.8	0.0	1.7	−2.0	2.7	−2.6	0.2	−0.2	4.1	−3.9	5.6	−5.5	3.3	−3.2
154.8	0.8	0.5	5.8	0.0	1.7	−2.0	2.5	−2.5	0.3	−0.3	4.3	−3.9	5.9	−5.6	3.7	−3.4
164.8	1.0	0.5	5.8	0.0	1.7	−2.1	2.4	−2.4	0.3	−0.3	4.5	−4.1	5.9	−5.7	3.9	−3.6
174.8	0.9	0.5	5.8	0.0	1.7	−2.1	2.3	−2.3	0.3	−0.3	4.7	−4.2	6.1	−5.9	4.1	−3.9
184.8	1.1	0.5	5.8	0.0	1.8	−2.1	2.2	−2.2	0.3	−0.3	4.9	−4.3	6.2	−6.0	4.3	−4.2
194.8	1.4	0.5	5.8	0.0	1.8	−2.2	2.1	−2.1	0.3	−0.3	5.1	−4.4	6.4	−6.2	4.5	−4.4
204.8	1.7	0.5	5.8	0.0	1.8	−2.2	2.1	−2.0	0.3	−0.3	5.3	−4.5	6.5	−6.3	4.8	−4.6
214.8	2.0	0.5	5.8	0.0	1.9	−2.3	2.0	−2.0	0.3	−0.3	5.6	−4.5	6.7	−6.4	5.2	−5.0
224.8	2.4	0.5	5.8	0.0	1.9	−2.4	2.0	−1.9	0.3	−0.3	5.8	−4.7	6.9	−6.6	5.4	−5.2
239.4	2.1	0.5	5.8	0.0	2.0	−2.5	1.9	−1.9	0.3	−0.3	6.1	−4.9	7.1	−6.8	5.8	−5.7
259.4	3.0	0.5	5.8	0.0	2.1	−2.6	1.8	−1.8	0.3	−0.3	6.6	−5.1	7.5	−7.2	6.4	−6.3
279.5	4.0	0.6	5.8	0.0	2.2	−2.8	1.8	−1.8	0.4	−0.3	7.1	−5.4	7.9	−7.5	7.1	−6.9
303.9	4.7	0.6	5.8	0.0	2.4	−3.1	1.8	−1.8	0.4	−0.4	7.9	−5.7	8.4	−7.9	8.3	−7.8
333.9	7.6	0.7	5.8	0.0	2.7	−3.5	1.8	−1.7	0.4	−0.4	9.0	−6.1	9.1	−8.6	9.8	−9.3
375.7	10.2	1.0	5.8	0.0	3.2	−4.2	1.7	−1.7	0.5	−0.5	10.8	−6.8	10.2	−9.6	12.4	−11.7
461.1	25.0	2.1	5.8	0.0	4.6	−5.9	1.7	−1.7	0.6	−0.6	15.0	−8.6	13.2	−12.0	20.3	−18.2
Correl.	0	1	1	p	1	1	1	1	1	1	1	1	1	1	p	p

the same JETRAD calculation. For this rapidity region, we have carried out a χ^2 comparison between our data and the nominal curve describing the central values of the data of Ref. [7]. Comparing our data to the nominal curve, as though it were theory, we obtain a χ^2 of 56.5 for 24 degrees of freedom (probability of 0.02%). Thus our data cannot be described with this parametrization. As illustrated in the middle panel of Fig. 55, our data and the curve differ at low and high E_T; such differences cannot be accommodated by the highly correlated uncertainties of our data. If we include the systematic uncertainties of the data of Ref. [7] in the covariance matrix, the χ^2 is reduced to 30.8 (probability of 16%), representing acceptable agreement.

J. Rapidity dependence of the inclusive jet cross section

DØ has subsequently extended the measurement of the inclusive jet cross section as a function of E_T to $|\eta|<3$ in several bins of pseudorapidity [26]. In this analysis the details of the jet energy scale corrections, single jet resolutions, and vertex selection were updated to minimize uncertainties for jets at large pseudorapidity ($|\eta|>1.5$). These cross sections are compared with JETRAD predictions generated with $\mu=0.5E_T^{\max}$, $\mathcal{R}_{\rm sep}=1.3$, and similar choices of PDF given in Table XVIII. The data and theory were also compared using the same χ^2 test as used in this paper (Sec. XI H). The data indicate an preference for the CTEQ4HJ, MRST($g\uparrow$), and CTEQ4M PDFs [26].

K. Conclusions

We have made the most precise measurement to date of the inclusive jet cross section for $E_T\geqslant 60$ GeV at $\sqrt{s}=1800$ GeV. No excess production of high-E_T jets is observed. QCD predictions are in good agreement with the observed cross section for most standard parton distribution functions and different renormalization scales ($\mu=0.25-2.00E_T$ where $E_T = E_T^{\max}$ or $E_T^{\rm jet}$).

XII. RATIO OF INCLUSIVE JET CROSS KECTIONS AT $\sqrt{s}=1800$ AND 630 GeV

A. Inclusive jet cross section at $\sqrt{s}=630$ GeV

The inclusive jet cross section for $|\eta|<0.5$ at $\sqrt{s}=630$ GeV consists of data collected with three triggers: Jet_12,

TABLE XIII. Percentage $0.1<|\eta|<0.7$ cross section uncertainties. The last row gives the nature of the E_{T} bin-to-bin correlations: 0 signifies uncorrelated uncertainties, 1 correlated, and p partially correlated.

E_{T} GeV	Stat Error	Jet Sel	Lumin	Lumin Match	Unsmearing		Energy Scale									
					High	Low	Underlying		η		Method		Shower		Response	
							High	Low	High	Low	High	Low	High	Low	High	Low
64.6	0.6	0.5	5.8	1.8	2.3	−2.6	5.3	−5.0	0.6	−0.6	3.4	−3.2	4.8	−4.8	1.1	−1.1
74.6	0.9	0.5	5.8	1.8	2.1	−2.4	4.7	−4.5	0.6	−0.6	3.5	−3.4	4.9	−4.7	1.3	−1.1
84.7	1.4	0.5	5.8	1.8	2.0	−2.3	4.2	−4.1	0.6	−0.6	3.5	−3.5	5.0	−4.9	1.6	−1.5
94.7	0.5	0.5	5.8	1.1	1.9	−2.2	3.8	−3.7	0.6	−0.6	3.6	−3.5	5.1	−5.0	2.1	−2.1
104.7	0.7	0.5	5.8	1.1	1.8	−2.2	3.5	−3.4	0.7	−0.7	3.7	−3.6	5.2	−5.2	2.3	−2.3
114.7	1.0	0.5	5.8	1.1	1.8	−2.1	3.2	−3.1	0.7	−0.7	3.8	−3.6	5.5	−5.2	2.7	−2.6
124.8	1.3	0.5	5.8	1.1	1.8	−2.1	3.0	−2.9	0.7	−0.7	3.9	−3.7	5.5	−5.4	2.9	−2.9
134.8	0.5	0.5	5.8	0.0	1.8	−2.1	2.8	−2.8	0.7	−0.7	4.1	−3.9	5.7	−5.5	3.2	−3.1
144.8	0.6	0.5	5.8	0.0	1.8	−2.2	2.7	−2.6	0.7	−0.7	4.2	−4.0	5.8	−5.6	3.6	−3.3
154.8	0.8	0.5	5.8	0.0	1.8	−2.2	2.5	−2.5	0.8	−0.8	4.4	−4.0	5.9	−5.8	3.7	−3.5
164.8	0.9	0.5	5.8	0.0	1.8	−2.2	2.4	−2.4	0.8	−0.8	4.6	−4.2	6.0	−5.9	4.0	−3.8
174.8	0.9	0.5	5.8	0.0	1.8	−2.3	2.3	−2.3	0.8	−0.8	4.8	−4.2	6.2	−6.0	4.2	−4.0
184.8	1.1	0.5	5.8	0.0	1.9	−2.4	2.2	−2.2	0.8	−0.8	5.0	−4.3	6.4	−6.2	4.4	−4.4
194.8	1.3	0.5	5.8	0.0	1.9	−2.4	2.1	−2.1	0.8	−0.8	5.2	−4.4	6.5	−6.3	4.7	−4.4
204.8	1.6	0.5	5.8	0.0	1.9	−2.5	2.1	−2.0	0.9	−0.9	5.4	−4.5	6.7	−6.5	5.0	−4.8
214.8	1.9	0.5	5.8	0.0	2.0	−2.6	2.0	−2.0	0.9	−0.9	5.7	−4.6	6.9	−6.6	5.3	−5.0
224.8	2.2	0.5	5.8	0.0	2.0	−2.7	2.0	−2.0	0.9	−0.9	6.0	−4.8	7.0	−6.7	5.6	−5.5
239.4	2.0	0.5	5.8	0.0	2.1	−2.8	1.9	−1.9	1.0	−0.9	6.2	−4.9	7.3	−6.9	6.0	−5.8
259.4	2.9	0.5	5.8	0.0	2.3	−3.0	1.9	−1.9	1.0	−1.0	6.8	−5.1	7.7	−7.2	6.7	−6.4
279.5	3.9	0.6	5.8	0.0	2.4	−3.3	1.8	−1.8	1.1	−1.0	7.4	−5.4	8.0	−7.6	7.5	−7.2
303.9	4.5	0.6	5.8	0.0	2.7	−3.6	1.8	−1.8	1.1	−1.1	8.1	−5.7	8.5	−8.0	8.7	−8.3
333.9	7.2	0.7	5.8	0.0	3.0	−4.1	1.8	−1.8	1.2	−1.2	9.3	−6.2	9.2	−8.6	10.2	−9.8
375.7	10.3	1.0	5.8	0.0	3.6	−4.9	1.8	−1.7	1.3	−1.3	11.1	−6.9	10.3	−9.7	13.5	−12.5
460.9	24.3	2.1	5.8	0.0	5.2	−7.0	1.7	−1.7	1.6	−1.6	15.1	−8.7	13.3	−12.2	21.8	−19.4
Correl.	0	1	1	p	1	1	1	1	1	1	1	1	1	1	p	p

Jet_2_12, and Jet_30. To form the inclusive jet cross section, an E_{T} region of each trigger is selected to maximize statistical power while maintaining full trigger efficiency. Any given cross section bin receives contributions from one and only one trigger. The luminosity in any given bin is the luminosity exposure for that trigger (given in Table II).

The inclusive jet cross section at $\sqrt{s}=1800$ GeV was determined prior to the 630 GeV analysis. To facilitate the ratio calculation as a function of $x_T \equiv 2E_{\mathrm{T}}/\sqrt{s}$, the bin boundaries for the 630 GeV analysis were selected such that

$$E_T^{630}=\frac{630}{1800}E_T^{1800}, \tag{12.1}$$

i.e., such that the bin edges match in x_T space. Most of the resulting bins are 3.5 GeV wide, but some bins have a width of 7.0 GeV, 10.5 GeV, or more.

Figure 56 displays the observed cross section at $\sqrt{s}=630$ GeV. The three different symbols indicate the E_{T} region for each jet trigger. Vertical lines (mostly hidden by the symbols) indicate the statistical uncertainty on each point.

The cross section is corrected for the effects of jet resolution using the same method as used for the $\sqrt{s}=1800$ GeV cross section (Sec. XI E). The single jet resolutions at $s=630$

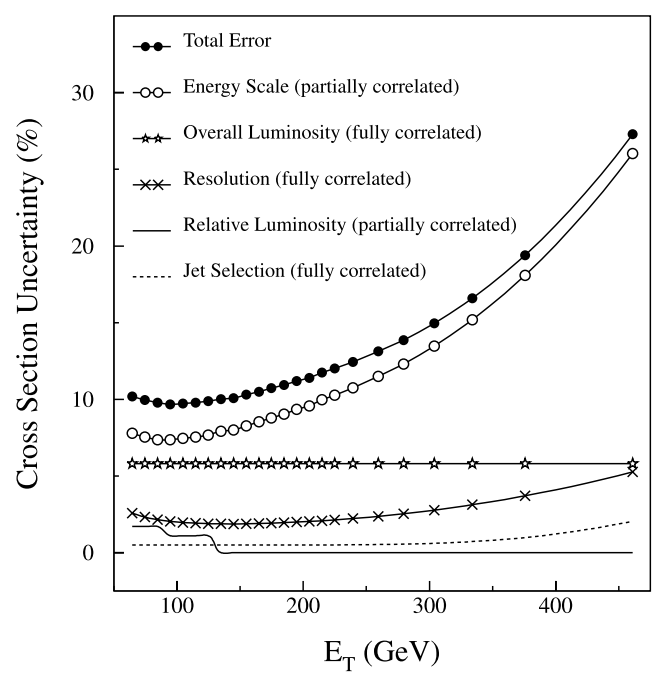

FIG. 48. Contributions to the $|\eta|<0.5$ inclusive jet cross section uncertainty plotted by component.

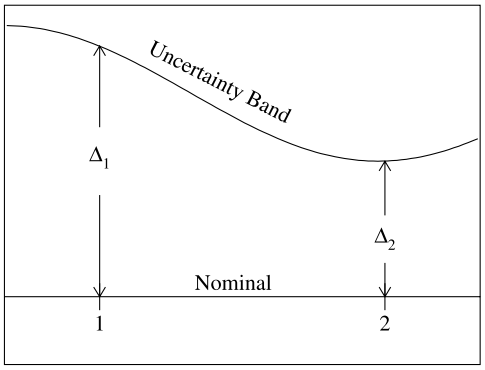

FIG. 49. Example of an error band relative to some nominal distribution (illustrated here with a flat line). If the errors at points **1** and **2** are completely correlated, then a one standard deviation (1σ) Δ_1 at the first position necessarily results in a 1σ Δ_2 at the second position.

GeV are given in Sec. X D. The resulting ansatz fit parameters are given in Table XX and the unsmearing correction is plotted in Fig. 57.

The resulting inclusive jet cross section at $\sqrt{s}=630$ GeV is given in Table XXI and is plotted in Fig. 58. The uncertainties in the cross section are given in Table XXII and are also plotted in Fig. 59. The bin-to-bin correlations of the uncertainties are shown in Fig. 60 and are given in Table XXIII.

The magnitude of the energy scale uncertainties are larger for the cross section at $\sqrt{s}=630$ GeV than at $\sqrt{s}=1800$ GeV (Table XII). This is caused by several factors. The cross section at 630 GeV begins with jet $E_{\mathrm{T}}>20$ GeV compared with 60 GeV at $\sqrt{s}=1800$ GeV. The uncertainty in the energy scale offset correction (which is additive) has a much larger effect on 20 GeV jets than on 60 GeV jets. For $E_{\mathrm{T}}>60$ GeV the cross section at $\sqrt{s}=630$ GeV is much steeper than the cross section at 1800 GeV, hence the same uncertainty in the energy scale will lead to a larger uncertainty in the cross section.

Figures 61 and 62 show the fractional differences between the data and several JETRAD predictions using different

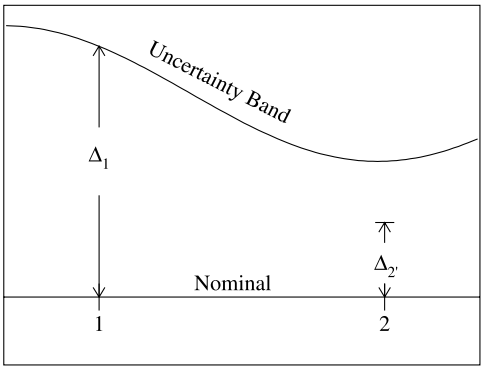

FIG. 50. If the errors at points **1** and **2** are partially correlated, then a full 1σ Δ_1 at the first position results in a smaller than 1σ $\Delta_{2'}$ at the second position. The correlation factor illustrated here is 0.55.

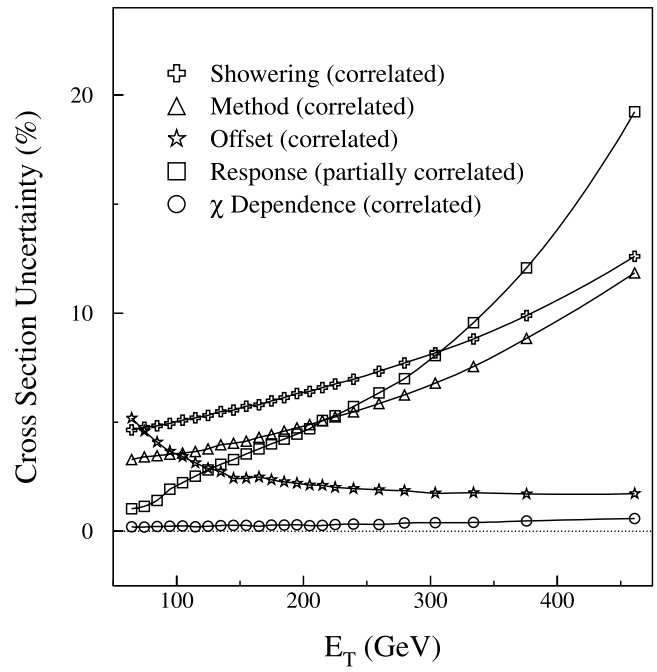

FIG. 51. Percentage cross section errors for $|\eta|<0.5$ associated with the components of energy scale correction.

choices of renormalization scale and PDF. These NLO QCD predictions are in reasonable agreement with the data. The data and predictions are compared quantitatively using a χ^2 test (Sec. XI H). The resulting χ^2 values are given in Table XXIV; each comparison has 20 degrees of freedom. All but two of the JETRAD predictions adequately describe the cross section at $\sqrt{s}=630$ GeV. For these, the probabilities for χ^2 to exceed the listed values are between 6.4% and 78%. The prediction using MRST($g\uparrow$) and $\mu=0.5E_T^{\max}$ produces the

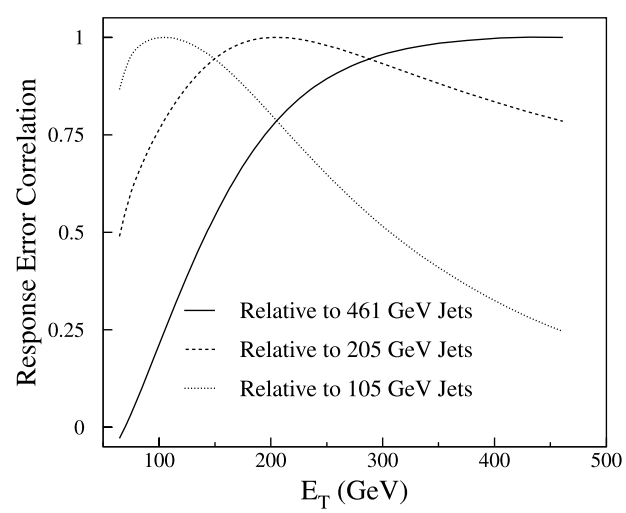

FIG. 52. The correlations of the uncertainty due to the hadronic response correction as a function of E_{T}. The solid curve shows the correlations relative to the 461 GeV bin, the dashed curve with respect to the 205 GeV bin, and the dotted curve with respect to the 105 GeV bin.

TABLE XIV. The correlations for the uncertainty due to the energy scale response for $|\eta^{\rm jet}|<0.5$, and $0.1<|\eta^{\rm jet}|<0.7$. The correlation values above the diagonal are the correlations for $|\eta^{\rm jet}|<0.5$ and the correlations below the diagonal correspond to $0.1<|\eta^{\rm jet}|<0.7$. In both cases the correlation matrices are symmetric.

	1	2	3	4	5	6	7	8	9	10	11	12	13	14	15	16	17	18	19	20	21	22	23	24	
	1.00	0.97	0.94	0.90	0.87	0.83	0.80	0.76	0.72	0.68	0.64	0.60	0.56	0.53	0.49	0.45	0.42	0.37	0.31	0.26	0.20	0.14	0.07	-0.03	1
		1.00	0.99	0.97	0.95	0.92	0.90	0.86	0.83	0.79	0.75	0.72	0.68	0.64	0.60	0.56	0.53	0.48	0.41	0.35	0.29	0.22	0.15	0.03	2
1	1.00		1.00	0.99	0.98	0.96	0.94	0.92	0.89	0.85	0.82	0.78	0.75	0.71	0.67	0.64	0.60	0.55	0.49	0.43	0.37	0.30	0.22	0.10	3
2	0.97	1.00		1.00	1.00	0.99	0.97	0.95	0.93	0.90	0.87	0.84	0.80	0.77	0.74	0.70	0.67	0.62	0.56	0.50	0.44	0.37	0.29	0.17	4
3	0.94	0.99	1.00		1.00	1.00	0.99	0.97	0.95	0.93	0.91	0.88	0.85	0.82	0.79	0.76	0.72	0.68	0.62	0.57	0.51	0.44	0.36	0.25	5
4	0.90	0.97	0.99	1.00		1.00	1.00	0.99	0.98	0.96	0.94	0.91	0.89	0.86	0.83	0.80	0.78	0.73	0.68	0.63	0.57	0.51	0.43	0.32	6
5	0.87	0.95	0.98	1.00	1.00		1.00	1.00	0.99	0.98	0.96	0.94	0.92	0.90	0.87	0.85	0.82	0.78	0.73	0.68	0.63	0.57	0.50	0.39	7
6	0.83	0.92	0.96	0.99	1.00	1.00		1.00	1.00	0.99	0.98	0.96	0.95	0.93	0.91	0.88	0.86	0.83	0.78	0.74	0.68	0.63	0.56	0.45	8
7	0.80	0.90	0.94	0.97	0.99	1.00	1.00		1.00	1.00	0.99	0.98	0.97	0.95	0.93	0.91	0.89	0.86	0.82	0.78	0.73	0.68	0.62	0.51	9
8	0.76	0.86	0.92	0.95	0.97	0.99	1.00	1.00		1.00	1.00	0.99	0.98	0.97	0.96	0.94	0.92	0.90	0.86	0.82	0.78	0.73	0.67	0.57	10
9	0.72	0.83	0.89	0.93	0.95	0.98	0.99	1.00	1.00		1.00	1.00	0.99	0.98	0.97	0.96	0.95	0.92	0.89	0.86	0.82	0.77	0.72	0.62	11
10	0.68	0.79	0.85	0.90	0.93	0.96	0.98	0.99	1.00	1.00		1.00	1.00	0.99	0.99	0.98	0.96	0.95	0.92	0.89	0.85	0.81	0.76	0.67	12
11	0.64	0.75	0.82	0.87	0.91	0.94	0.96	0.98	0.99	1.00	1.00		1.00	1.00	0.99	0.99	0.98	0.96	0.94	0.91	0.88	0.84	0.79	0.71	13
12	0.60	0.72	0.78	0.84	0.88	0.91	0.94	0.96	0.98	0.99	1.00	1.00		1.00	1.00	0.99	0.99	0.98	0.96	0.94	0.91	0.87	0.83	0.75	14
13	0.56	0.68	0.75	0.80	0.85	0.89	0.92	0.95	0.97	0.98	0.99	1.00	1.00		1.00	1.00	1.00	0.99	0.97	0.95	0.93	0.90	0.86	0.78	15
14	0.53	0.64	0.71	0.77	0.82	0.86	0.90	0.93	0.95	0.97	0.98	0.99	1.00	1.00		1.00	1.00	0.99	0.98	0.97	0.95	0.92	0.88	0.81	16
15	0.49	0.60	0.67	0.74	0.79	0.83	0.87	0.91	0.93	0.96	0.97	0.99	0.99	1.00	1.00		1.00	1.00	0.99	0.98	0.96	0.94	0.90	0.84	17
16	0.45	0.56	0.64	0.70	0.76	0.80	0.85	0.88	0.91	0.94	0.96	0.98	0.99	0.99	1.00	1.00		1.00	1.00	0.99	0.98	0.96	0.93	0.87	18
17	0.42	0.53	0.60	0.67	0.72	0.78	0.82	0.86	0.89	0.92	0.95	0.96	0.98	0.99	1.00	1.00	1.00		1.00	1.00	0.99	0.98	0.95	0.91	19
18	0.37	0.48	0.55	0.62	0.68	0.73	0.78	0.83	0.86	0.90	0.92	0.95	0.96	0.98	0.99	0.99	1.00	1.00		1.00	1.00	0.99	0.97	0.94	20
19	0.31	0.41	0.49	0.56	0.62	0.68	0.73	0.78	0.82	0.86	0.89	0.92	0.94	0.96	0.97	0.98	0.99	1.00	1.00		1.00	1.00	0.99	0.96	21
20	0.26	0.35	0.43	0.50	0.57	0.63	0.68	0.74	0.78	0.82	0.86	0.89	0.91	0.94	0.95	0.97	0.98	0.99	1.00	1.00		1.00	1.00	0.98	22
21	0.20	0.29	0.37	0.44	0.51	0.57	0.63	0.68	0.73	0.78	0.82	0.85	0.88	0.91	0.93	0.95	0.96	0.98	0.99	1.00	1.00		1.00	0.99	23
22	0.14	0.22	0.30	0.37	0.44	0.51	0.57	0.63	0.68	0.73	0.77	0.81	0.84	0.87	0.90	0.92	0.94	0.96	0.98	0.99	1.00	1.00		1.00	24
23	0.07	0.15	0.22	0.29	0.36	0.43	0.50	0.56	0.62	0.67	0.72	0.76	0.79	0.83	0.86	0.88	0.90	0.93	0.95	0.97	0.99	1.00	1.00		
24	-0.03	0.03	0.10	0.17	0.25	0.32	0.39	0.45	0.51	0.57	0.62	0.67	0.71	0.75	0.78	0.81	0.84	0.87	0.91	0.94	0.96	0.98	0.99	1.00	

TABLE XV. The percentage cross section uncertainties due to the energy scale response correction that correspond to a given percentage confidence level for $|\eta|<0.5$.

	Upper						Lower					
Bin	40%	68.3%	86%	90%	95%	99%	40%	68.3%	86%	90%	95%	99%
1	0.7	1.1	1.3	1.3	1.6	1.9	−0.7	−1.0	−1.3	−1.3	−1.6	−1.8
2	0.7	1.1	1.5	1.4	1.8	2.2	−0.7	−1.1	−1.5	−1.4	−1.7	−2.1
3	1.0	1.5	1.9	1.9	2.2	2.6	−0.9	−1.3	−1.8	−1.8	−2.2	−2.6
4	1.3	1.9	2.5	2.6	3.0	3.6	−1.3	−1.8	−2.4	−2.6	−3.0	−3.5
5	1.4	2.2	3.0	3.1	3.4	4.0	−1.4	−2.2	−2.9	−3.0	−3.3	−4.0
6	1.6	2.6	3.3	3.4	3.8	4.6	−1.5	−2.5	−3.1	−3.3	−3.6	−4.4
7	1.6	2.9	3.6	3.8	4.1	5.0	−1.6	−2.8	−3.5	−3.7	−4.0	−4.8
8	1.6	3.0	3.9	4.0	4.2	5.3	−1.7	−3.0	−3.8	−3.0	−4.2	−5.3
9	1.7	3.3	4.1	4.2	4.6	5.7	−1.7	−3.2	−4.1	−4.2	−4.5	−5.6
10	1.9	3.6	4.5	4.6	5.0	6.2	−1.8	−3.4	−4.3	−4.4	−4.7	−5.9
11	2.0	3.9	4.8	4.9	5.1	6.7	−1.8	−3.6	−4.6	−4.6	−4.9	−6.3
12	2.1	4.1	5.1	5.0	5.4	7.0	−2.0	−3.9	−5.0	−4.9	−5.2	−6.8
13	2.1	4.3	5.3	5.2	5.7	7.4	−2.1	−4.1	−5.2	−5.2	−5.6	−7.2
14	2.4	4.5	5.6	5.6	6.1	7.8	−2.3	−4.5	−5.5	−5.5	−6.0	−7.5
15	2.6	4.8	5.9	5.9	6.5	8.3	−2.5	−4.6	−5.7	−5.8	−6.4	−7.9
16	3.1	5.2	6.4	6.5	7.3	9.0	−2.9	−5.0	−6.2	−6.3	−7.0	−8.6
17	3.3	5.4	6.7	6.9	7.7	9.4	−3.1	−5.2	−6.4	−6.6	−7.5	−8.9
18	3.8	5.8	7.1	7.5	8.8	10.2	−3.7	−5.6	−7.0	−7.4	−8.4	−9.8
19	4.4	6.4	8.2	8.5	10.0	11.7	−4.3	−6.3	−7.8	−8.1	−9.4	−11.0
20	5.0	7.1	9.0	9.4	11.1	13.0	−4.9	−6.9	−8.8	−9.0	−10.6	−12.3
21	6.0	8.3	10.8	11.1	13.3	15.6	−5.7	−7.8	−10.0	−10.2	−12.0	−14.0
22	7.4	10.0	13.3	13.3	15.8	18.9	−7.0	−9.4	−12.3	−12.2	−14.5	−17.0
23	9.4	12.6	17.1	16.8	20.0	24.4	−9.0	−12.0	−15.7	−15.6	−18.2	−21.4
24	16.2	22.4	29.6	30.2	35.3	43.1	−14.6	−20.1	−25.5	−26.2	−29.6	−34.6

highest probability. The predictions using MRST($g\downarrow$) with $\mu=0.5E_T^{\max}$, and CTEQ3M with $\mu=2E_T^{\max}$, thus are inconsistent with our measurements with probabilities $\leqslant 0.4\%$.

B. The ratio of jet cross sections

The dimensionless inclusive jet cross section (Sec. IV A 2) is given by

$$\sigma_{\sqrt{s(\mathrm{GeV})}}=\frac{E_T^3}{2\pi}\frac{d^2\sigma}{dE_{\mathrm{T}}d\eta}, \tag{12.2}$$

where $d^2\sigma/dE_{\mathrm{T}}d\eta$ is given by Eq. (11.1). The ratio of inclusive jet cross sections for $|\eta|<0.5$ is calculated in bins of identical x_T:

$$R(x_T)=\frac{\sigma_{630}(x_T)}{\sigma_{1800}(x_T)}. \tag{12.3}$$

C. Uncertainties in the ratio of jet cross sections

Most of the systematic uncertainties in the inclusive jet cross section are highly correlated as a function of E_{T} and center-of-mass energy, and cancel when the ratio of the two cross sections is calculated. To determine the uncertainty in the ratio, all uncertainties are separated into three categories, depending on the correlation (ρ) as a function of E_{T} and c.m. energies. In most cases, complete correlation in E_{T} at one c.m. energy implies complete correlation between c.m. energies, but exceptions exist and are highlighted in the following sections.

1. Luminosity uncertainties

The luminosity calculation at $\sqrt{s}=630$ GeV shares many common uncertainties with the calculation at 1800 GeV (Sec. VI). The uncertainty from the fit to the world average (WA) $p\bar{p}$ total cross section determines the uncertainty in the luminosity at $\sqrt{s}=630$ GeV (Fig. 14). A 1σ shift in the mean value of the cross section at $\sqrt{s}=1800$ GeV directly impacts the central value of the cross section at $\sqrt{s}=630$ GeV, resulting in a shift of unequal magnitude but like direction. The magnitude of the shift at 630 GeV, subtracted in quadrature from the interpolation uncertainty, defines two uncertainty components: the shift, which is completely correlated with the 1800 GeV cross section uncertainty, and the remainder, which is added in quadrature with the other independent luminosity uncertainties. The uncertainty components in the WA elastic and single-diffractive $p\bar{p}$ cross sections are handled with the same procedure. Table XXV lists the systematic uncertainties due to the luminosity for the ratio.

TABLE XVI. The percentage cross section uncertainties due to the energy scale response correction that correspond to a given percentage confidence level for $0.1<|\eta|<0.7$.

	Upper						Lower					
Bin	40%	68.3%	86%	90%	95%	99%	40%	68.3%	86%	90%	95%	99%
1	0.7	1.1	1.4	1.4	1.6	2.0	−0.8	−1.1	−1.4	−1.4	−1.7	−1.9
2	0.8	1.2	1.6	1.6	1.9	2.3	−0.8	−1.2	−1.5	−1.5	−1.9	−2.2
3	1.1	1.6	2.1	2.1	2.5	2.9	−1.0	−1.5	−2.1	−2.2	−2.5	−2.9
4	1.3	2.1	2.7	2.9	3.2	3.9	−1.3	−2.0	−2.7	−2.8	−3.2	−3.8
5	1.5	2.4	3.1	3.2	3.6	4.2	−1.4	−2.3	−3.0	−3.1	−3.4	−4.2
6	1.6	2.7	3.4	3.6	3.9	4.9	−1.5	−2.6	−3.3	−3.5	−3.8	−4.6
7	1.6	3.0	3.7	3.9	4.1	5.1	−1.6	−2.9	−3.7	−3.9	−4.1	−5.0
8	1.7	3.2	4.0	4.1	4.4	5.5	−1.7	−3.1	−3.9	−4.0	−4.3	−5.4
9	1.8	3.6	4.4	4.5	4.8	6.1	−1.7	−3.4	−4.2	−4.3	−4.6	−5.8
10	1.9	3.8	4.7	4.7	5.0	6.4	−1.8	−3.5	−4.4	−4.5	−4.8	−6.2
11	2.1	4.0	5.0	5.0	5.3	6.9	−1.9	−3.8	−4.8	−4.8	−5.1	−6.6
12	2.1	4.2	5.3	5.1	5.6	7.2	−2.0	−4.0	−5.1	−5.0	−5.4	−6.9
13	2.3	4.4	5.5	5.5	6.0	7.7	−2.4	−4.3	−5.5	−5.5	−6.1	−7.6
14	2.6	4.7	5.8	5.9	6.4	8.1	−2.4	−4.5	−5.6	−5.6	−6.2	−7.7
15	2.9	5.0	6.2	6.3	7.2	8.8	−2.8	−4.8	−6.0	−6.1	−6.7	−8.2
16	3.2	5.3	6.6	6.8	7.7	9.2	−3.0	−5.1	−6.3	−6.5	−7.4	−8.8
17	3.6	5.7	7.0	7.3	8.3	9.8	−3.6	−5.5	−6.9	−7.2	−8.2	−9.6
18	4.0	6.0	7.5	7.9	9.3	10.9	−4.0	−5.9	−7.3	−7.6	−8.8	−10.3
19	4.7	6.7	8.6	8.9	10.4	12.2	−4.5	−6.5	−8.1	−8.4	−9.8	−11.4
20	5.4	7.6	9.9	10.1	12.1	14.2	−5.2	−7.3	−9.4	−9.6	−11.3	−13.2
21	6.5	8.8	11.8	11.9	14.2	16.9	−6.2	−8.2	−10.8	−10.9	−12.8	−15.0
22	7.8	10.5	14.1	13.9	16.5	19.8	−7.4	−9.7	−12.8	−12.6	−14.9	−17.8
23	9.9	13.4	18.2	18.0	21.4	26.5	−9.7	−13.0	−17.0	−17.1	−19.8	−23.5
24	17.2	24.4	32.2	33.0	38.3	47.3	−15.9	−22.1	−28.0	−28.8	−32.2	−37.1

2. Jet and event selection uncertainties

At 1800 GeV, the total uncertainty for jet cut efficiencies, the $\not{E}_T$ cut efficiency, and the vertex cut efficiency is 1%. An independent study at 630 GeV determined cut uncertainties that were smaller (Table XXVI). Despite some similarities in methodology, these uncertainties are all considered to be independent of one another in the ratio.

3. Resolution and unsmearing uncertainties

Uncertainty in the unsmearing correction is dominated by the uncertainty in the jet resolution measurement. In the case of $\sqrt{s}=1800$ GeV, the systematic uncertainty dominates; for $\sqrt{s}=630$ GeV, poor statistics result in a fit uncertainty that is larger in magnitude than the systematic uncertainty. The systematic uncertainties in the unsmearing correction are assumed to be uncorrelated between the c.m. energies, as are the fitting uncertainties. The magnitudes of the resolution and unsmearing uncertainties are illustrated in Fig. 63.

4. Energy scale uncertainties

The uncertainty in the inclusive jet cross section and in the ratio of cross sections is calculated using a Monte Carlo simulation. The event generator performs several steps for each $\sqrt{s}$ and each cross section bin in x_T. First, it generates a sample of jets with an x_T spectrum which matches that observed in data. Second, it closely imitates true running conditions by simulating luminosity, vertexing, and smearing effects; thus the energy scale corrections of each Monte Carlo jet will closely match the corrections in real data. Third, the uncertainties from the energy scale corrections are calculated. Finally, the weighted average uncertainties and correlations in each bin are combined to form a covariance matrix.

The jet $E_{\rm T}$ distribution must be identical to the observed (smeared) jet cross section in data. The Monte Carlo simulation:

(1) Randomly generates the initial parton momenta x_1 and x_2.

(2) Generates the corresponding p_T and other kinematic quantities for both of the final-state partons (which result in jets).

(3) Smears the jets according to the known resolution functions and then selects one jet at random.

(4) Checks that the selected jet falls within the desired x_T bin and has $|\eta^{\rm jet}|<0.5$ (or starts over).

(5) Generates a weight for the jet, to reproduce the steeply falling spectrum of the inclusive jet cross section, using either a theoretical weight based on CTEQ4M and the scale of the collision, or an experimental weight based on the ansatz from unsmearing.

TABLE XVII. The systematic error correlations for the inclusive jet cross section for $|\eta^{\rm jet}|<0.5$, and $0.1<|\eta^{\rm jet}|<0.7$. The correlation values above the diagonal are the correlations for $|\eta^{\rm jet}|<0.5$ and the correlations below the diagonal correspond to $0.1<|\eta^{\rm jet}|<0.7$. In both cases the correlation matrices are symmetric.

	1	2	3	4	5	6	7	8	9	10	11	12	13	14	15	16	17	18	19	20	21	22	23	24	
	1.00	1.00	0.99	0.98	0.97	0.96	0.95	0.93	0.92	0.91	0.90	0.89	0.88	0.86	0.86	0.84	0.83	0.82	0.80	0.78	0.75	0.71	0.66	0.53	1
		1.00	1.00	0.99	0.98	0.97	0.96	0.95	0.94	0.93	0.92	0.91	0.90	0.89	0.88	0.86	0.86	0.84	0.82	0.80	0.77	0.73	0.68	0.55	2
1	1.00		1.00	0.99	0.99	0.98	0.97	0.96	0.95	0.94	0.93	0.92	0.92	0.91	0.90	0.88	0.88	0.86	0.84	0.82	0.79	0.75	0.70	0.57	3
2	1.00	1.00		1.00	1.00	0.99	0.99	0.98	0.97	0.96	0.96	0.95	0.94	0.93	0.92	0.91	0.90	0.89	0.86	0.84	0.81	0.77	0.72	0.59	4
3	0.99	1.00	1.00		1.00	1.00	1.00	0.99	0.98	0.97	0.97	0.96	0.95	0.94	0.94	0.92	0.92	0.90	0.88	0.86	0.83	0.79	0.74	0.61	5
4	0.98	0.99	0.99	1.00		1.00	1.00	0.99	0.99	0.98	0.98	0.97	0.96	0.96	0.95	0.94	0.93	0.92	0.90	0.88	0.85	0.81	0.76	0.63	6
5	0.97	0.98	0.99	1.00	1.00		1.00	0.99	0.99	0.99	0.98	0.98	0.97	0.97	0.96	0.95	0.94	0.93	0.91	0.89	0.87	0.83	0.78	0.65	7
6	0.96	0.97	0.98	1.00	1.00	1.00		1.00	1.00	1.00	0.99	0.99	0.99	0.98	0.97	0.97	0.96	0.95	0.93	0.91	0.89	0.85	0.80	0.68	8
7	0.95	0.96	0.98	0.99	1.00	1.00	1.00		1.00	1.00	1.00	0.99	0.99	0.99	0.98	0.97	0.97	0.96	0.94	0.93	0.90	0.87	0.82	0.70	9
8	0.93	0.95	0.96	0.98	0.99	0.99	0.99	1.00		1.00	1.00	1.00	1.00	0.99	0.99	0.98	0.98	0.97	0.95	0.94	0.92	0.88	0.84	0.72	10
9	0.92	0.94	0.95	0.97	0.98	0.99	0.99	1.00	1.00		1.00	1.00	1.00	1.00	0.99	0.99	0.98	0.98	0.96	0.95	0.93	0.90	0.85	0.74	11
10	0.91	0.93	0.95	0.97	0.98	0.98	0.99	1.00	1.00	1.00		1.00	1.00	1.00	1.00	0.99	0.99	0.98	0.97	0.96	0.94	0.91	0.87	0.76	12
11	0.90	0.92	0.94	0.96	0.97	0.98	0.98	0.99	1.00	1.00	1.00		1.00	1.00	1.00	1.00	0.99	0.99	0.98	0.97	0.95	0.92	0.88	0.78	13
12	0.89	0.91	0.93	0.95	0.96	0.97	0.98	0.99	1.00	1.00	1.00	1.00		1.00	1.00	1.00	1.00	0.99	0.98	0.97	0.96	0.93	0.90	0.80	14
13	0.88	0.90	0.92	0.94	0.95	0.96	0.97	0.99	0.99	0.99	1.00	1.00	1.00		1.00	1.00	1.00	0.99	0.99	0.98	0.97	0.94	0.91	0.81	15
14	0.87	0.89	0.91	0.93	0.94	0.96	0.97	0.98	0.99	0.99	1.00	1.00	1.00	1.00		1.00	1.00	1.00	0.99	0.99	0.97	0.95	0.92	0.83	16
15	0.85	0.88	0.90	0.92	0.94	0.95	0.96	0.97	0.98	0.99	0.99	1.00	1.00	1.00	1.00		1.00	1.00	1.00	0.99	0.98	0.96	0.93	0.85	17
16	0.84	0.86	0.89	0.91	0.93	0.94	0.95	0.97	0.98	0.98	0.99	0.99	1.00	1.00	1.00	1.00		1.00	1.00	1.00	0.99	0.97	0.95	0.87	18
17	0.83	0.85	0.87	0.90	0.91	0.93	0.94	0.96	0.97	0.98	0.98	0.99	0.99	1.00	1.00	1.00	1.00		1.00	1.00	0.99	0.98	0.96	0.89	19
18	0.82	0.84	0.86	0.89	0.90	0.92	0.93	0.95	0.96	0.97	0.98	0.98	0.99	0.99	1.00	1.00	1.00	1.00		1.00	1.00	0.99	0.97	0.91	20
19	0.80	0.82	0.84	0.86	0.88	0.90	0.91	0.93	0.94	0.95	0.96	0.97	0.98	0.98	0.99	0.99	1.00	1.00	1.00		1.00	1.00	0.99	0.94	21
20	0.77	0.79	0.81	0.84	0.86	0.87	0.89	0.91	0.92	0.93	0.95	0.96	0.96	0.97	0.98	0.98	0.99	0.99	1.00	1.00		1.00	1.00	0.96	22
21	0.74	0.76	0.78	0.81	0.83	0.85	0.86	0.88	0.90	0.91	0.93	0.94	0.95	0.96	0.96	0.97	0.98	0.99	0.99	1.00	1.00		1.00	0.98	23
22	0.71	0.73	0.75	0.77	0.79	0.81	0.83	0.85	0.87	0.88	0.90	0.91	0.92	0.93	0.94	0.95	0.96	0.97	0.98	0.99	1.00	1.00		1.00	24
23	0.65	0.66	0.68	0.71	0.73	0.75	0.77	0.79	0.81	0.83	0.85	0.86	0.88	0.89	0.90	0.92	0.93	0.94	0.96	0.97	0.98	0.99	1.00		
24	0.52	0.53	0.55	0.57	0.59	0.61	0.63	0.66	0.68	0.70	0.73	0.75	0.77	0.79	0.80	0.82	0.84	0.86	0.88	0.91	0.93	0.95	0.98	1.00	

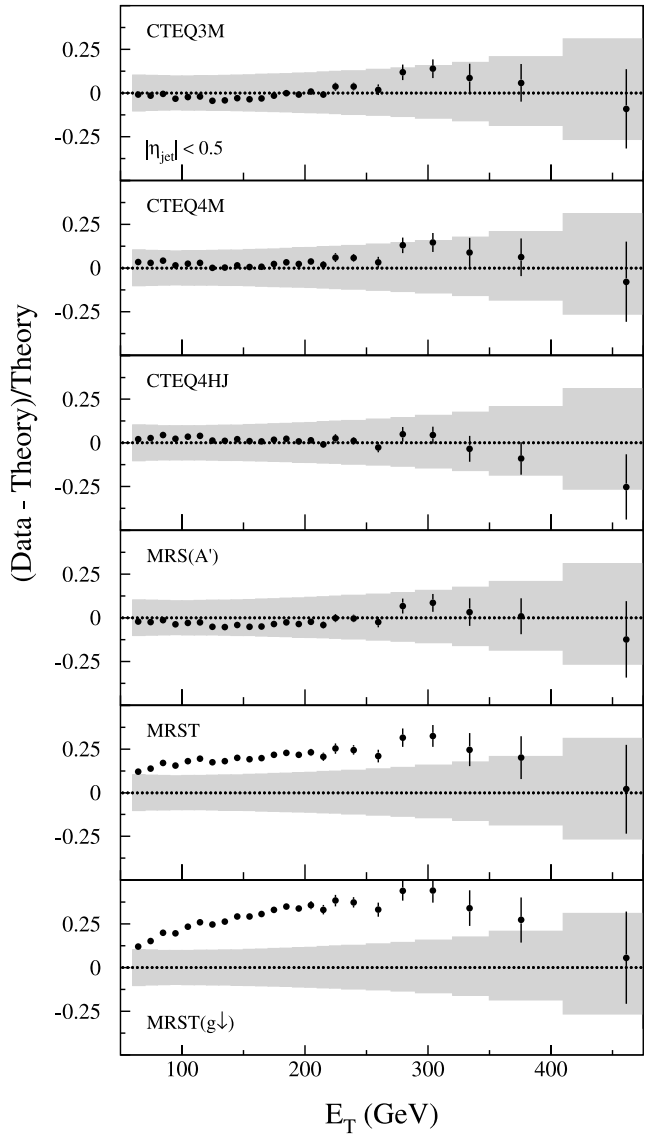

FIG. 53. The difference between data and JETRAD QCD predictions normalized to predictions for $|\eta|<0.5$. The shaded region represents the $\pm 1\sigma$ systematic uncertainties about the prediction.

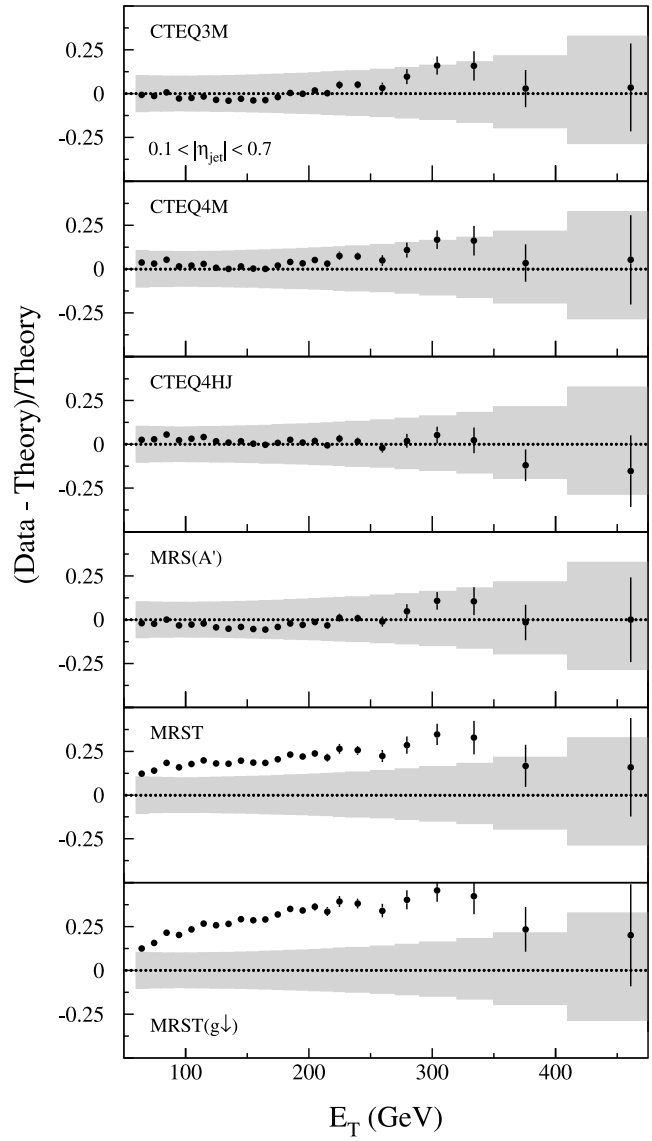

FIG. 54. The difference between data and JETRAD QCD predictions normalized to predictions for $0.1<|\eta|<0.7$. The error bars show the statistical uncertainties. The shaded region represents the $\pm 1\sigma$ systematic uncertainties about the prediction.

Because the generated jet distribution already represents the energy-scale-corrected jet E_T, and because the response correlation is given in terms of the energy before the response correction, the energy scale algorithm must be run "in reverse" to find the uncertainties and their correlations as a function of jet E_T and c.m. energy.

The ratio of inclusive jet cross sections is given in Eq. (12.2). The elements of the covariance matrix are

$$C_{ij}=\langle \hat{\rho}_{ij}\ \delta R_i\ \delta R_j\rangle, \tag{12.4}$$

where $\hat{\rho}$ expresses the correlation between the x_T bins i and j, and the uncertainties in the ratio δR may be expressed as

$$\delta R_i=\frac{\partial R_i}{\partial \sigma_i^{630}}\ \delta\sigma_i^{630}+\frac{\partial R_i}{\partial \sigma_i^{1800}}\ \delta\sigma_i^{1800}, \tag{12.5}$$

where the two partial derivatives possess opposite signs:

$$\frac{\partial R_i}{\partial \sigma_i^{630}}=\frac{1}{\sigma_i^{1800}}=\frac{R_i}{\sigma_i^{630}}$$

$$\frac{\partial R_i}{\partial \sigma_i^{1800}}=\frac{-\sigma_i^{630}}{(\sigma_i^{1800})^2}=-\frac{R_i}{\sigma_i^{1800}}. \tag{12.6}$$

Defining $x\equiv x_T$, the dependence of $\delta\sigma$ on jet energy is given by

$$\delta\sigma_i^a=\frac{\partial \sigma_i^a}{\partial x_i}\,\delta x_i^a=\frac{2}{a}\sin\theta_i\,\frac{\partial \sigma_i^a}{\partial x_i}\ \delta E_i^a\,. \tag{12.7}$$

TABLE XVIII. χ^2 comparisons between JETRAD and $|\eta|<0.5$ and $0.1<|\eta|<0.7$ data for $\mu=0.5E_T^{\max}$, $\mathcal{R}_{\rm sep}=1.3$, and various PDFs. There are 24 degrees of freedom.

PDF	μ	$\lvert\eta\rvert\leqslant 0.5$		$0.1\leqslant\lvert\eta\rvert\leqslant 0.7$	
		χ^2	Prob.	χ^2	Prob.
CTEQ3M	$0.50E_T^{\max}$	25.3	0.39	32.7	0.11
CTEQ4M	$0.50E_T^{\max}$	20.1	0.69	26.8	0.31
CTEQ4HJ	$0.50E_T^{\max}$	16.8	0.86	22.4	0.56
MRS(A′)	$0.50E_T^{\max}$	20.4	0.67	28.5	0.24
MRST	$0.50E_T^{\max}$	25.3	0.39	29.6	0.20
MRST($g\uparrow$)	$0.50E_T^{\max}$	21.6	0.60	30.1	0.18
MRST($g\downarrow$)	$0.50E_T^{\max}$	47.5	0.003	47.9	0.003
CTEQ3M	$0.25E_T^{\max}$	21.4	0.61	28.1	0.26
CTEQ3M	$0.50E_T^{\max}$	25.3	0.39	32.7	0.11
CTEQ3M	$0.75E_T^{\max}$	25.8	0.37	32.5	0.11
CTEQ3M	$1.00E_T^{\max}$	24.8	0.42	31.7	0.14

The cross section uncertainty is now expressed in terms of jet energy, the jet angle, the c.m. energy (a), and the slope of the dimensionless cross section. The final expression for the covariance matrix elements becomes

$$C_{ij}=\sum_{a,b}\sum_{k,l} q\frac{2}{a}\sin\theta_k\frac{2}{b}\sin\theta_l \times\frac{R_k}{\sigma_k^a}\frac{\partial\sigma_k^a}{\partial x_k}\frac{R_l}{\sigma_l^b}\frac{\partial\sigma_l^b}{\partial x_l}\langle\rho_{kl}^{ab}\ \delta E_k^a\ \delta E_l^b\rangle, \qquad (12.8)$$

where a and b indicate c.m. energies; ρ_{kl}^{ab} is the correlation between the uncertainties of the two jets whose energies fall

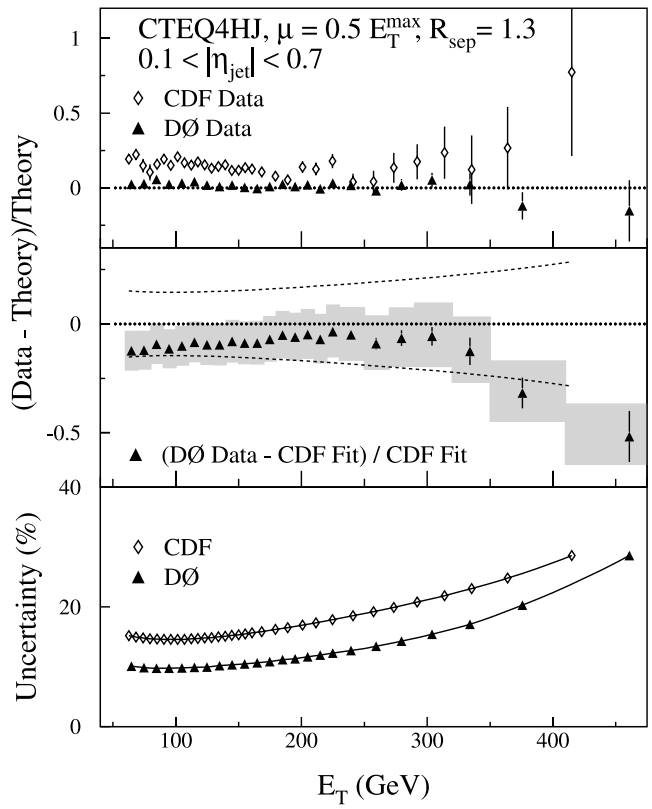

FIG. 55. Top: Normalized comparisons of our data and of the CDF data in Ref. [7] to the JETRAD prediction using CTEQ4HJ with $\mu=0.5E_T^{\max}$. Middle: Difference between our data and smoothed results of CDF normalized to the latter. The shaded region represents the $\pm1\sigma$ systematic uncertainties about the DØ data. The dashed curves show the $\pm1\sigma$ systematic uncertainties about the smoothed CDF data. Bottom: A comparison of the systematic uncertainties of the DØ measurement and the CDF measurement.

TABLE XIX. χ^2 comparisons between EKS and the data for $|\eta|<0.5$ and $0.1<|\eta|<0.7$ with $\mu=DE_T^{\max}$ or $DE_T^{\rm jet}$, $\mathcal{R}_{\rm sep}=1.3$, and various PDFs. There are 24 degrees of freedom.

PDF	D where $\mu=DE_T^{\rm xxx}$	$\lvert\eta\rvert<0.5$				$0.1<\lvert\eta\rvert<0.7$			
		$E_T^{\rm jet}$		$E_T^{\max}$		$E_T^{\rm jet}$		$E_T^{\max}$	
		χ^2	Prob.	χ^2	Prob.	χ^2	Prob.	χ^2	Prob.
CTEQ3M	0.25	21.1	0.63	17.9	0.81	32.3	0.12	—	—
CTEQ3M	0.50	20.7	0.66	19.3	0.74	33.7	0.09	33.3	0.10
CTEQ3M	0.75	20.4	0.67	19.4	0.73	33.3	0.10	33.0	0.10
CTEQ3M	1.00	20.2	0.68	19.5	0.73	32.9	0.11	32.7	0.11
CTEQ3M	1.25	20.4	0.68	19.8	0.71	32.8	0.11	32.8	0.11
CTEQ3M	1.50	20.8	0.65	20.3	0.68	33.1	0.10	33.1	0.10
CTEQ3M	1.75	21.5	0.61	21.2	0.63	33.5	0.09	33.6	0.09
CTEQ3M	2.00	22.4	0.55	22.1	0.57	34.2	0.08	34.3	0.08
CTEQ4M	0.50	19.4	0.73	18.2	0.80	33.8	0.09	34.3	0.08
CTEQ4HJ	0.50	—	—	23.3	0.50	—	—	—	—
CTEQ4A1	0.50	—	—	18.4	0.78	—	—	—	—
CTEQ4A2	0.50	—	—	18.3	0.79	—	—	—	—
CTEQ4A4	0.50	—	—	18.4	0.78	—	—	—	—
CTEQ4A5	0.50	—	—	19.2	0.74	—	—	—	—
MRS(A′)	0.50	—	—	19.3	0.74	—	—	36.8	0.05

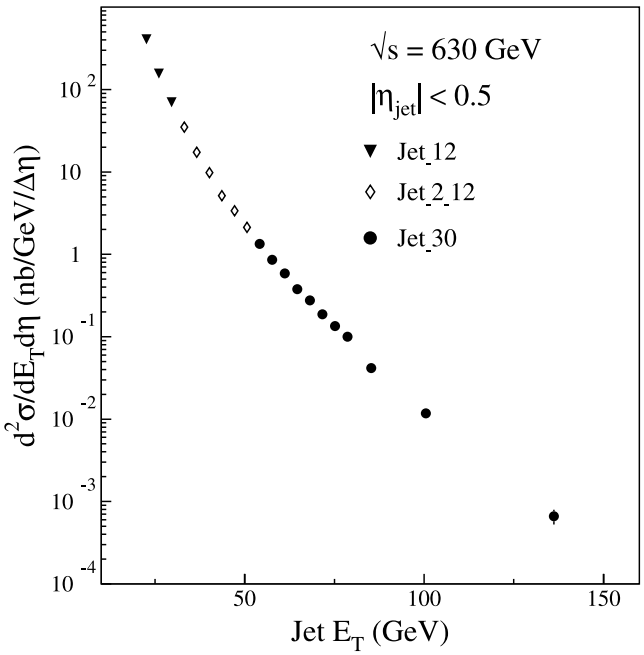

FIG. 56. The observed inclusive jet cross section for $\sqrt{s}=630$ GeV. Symbols indicate the three jet triggers (shaded triangles: Jet_12; hollow diamonds: Jet_2_12; shaded circles: Jet_30).

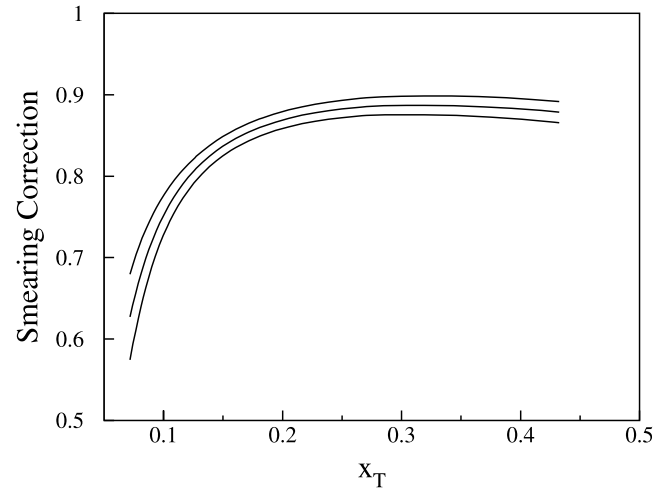

FIG. 57. The nominal unsmearing correction at $\sqrt{s}=630$ GeV is given by the central line. The outer curves depict the uncertainty in the unsmearing due to the uncertainties in the measurement of the resolution of the jet energy.

in bins k and l, originating from the data sets at $\sqrt{s}=a$ and b; and q is a factor that accounts for the negative sign in Eq. (12.6): $q=1$ when $a=b$, and $q=-1$ otherwise. The bracket notation indicates the average. The summations indicate the four relevant correlations, visually described in Fig. 64.

As mentioned previously, interpolation of the correlation matrix determines the values of ρ_{kl}^{ab} for the response uncertainty. For the completely correlated uncertainties, all ρ's take the value of unity; for the uncorrelated uncertainties, all ρ's are zero. The major contribution originates from the partially correlated response uncertainty.

5. Combined uncertainty in the ratio

The individual uncertainties of the earlier sections fall into several classifications, summarized in Table XXVII. Complete cancellation of uncertainties occurs when the uncertainties are completely correlated between c.m. energies. The components of the systematic uncertainties for the ratio of cross sections are plotted in Fig. 63 and given in Table XXVIII. The uncertainty in the energy scale correction dominates at each end of the spectrum; resolution and contributions from other sources (primarily the luminosity uncertainty) become important at intermediate values of x_T. Figure 65 plots the point-to-point uncertainty correlations between data points.

D. Results and comparison to theoretical predictions

The ratio between the inclusive jet cross sections at $\sqrt{s}$ = 630 and 1800 GeV is given in Table XXIX. Figures 66 and 67 show the ratios of cross sections compared with JETRAD predictions using different choices of PDF and renormalization scale. The measured ratios lie approximately 10% below the theoretical predictions, which have an uncertainty of approximately 10% (Sec. IV A 2). Table XXX lists the χ^2 distributions for the ratio of cross sections compared to selected theoretical predictions. The χ^2 values lie in the range 15.1–24 for 20 degrees of freedom (corresponding to probabilities in the range 28% to 77%). The best agreement occurs for extreme choices of renormalization scales: $\mu=(0.25,2.00)E_T^{\max}$. As expected, there is very little dependence on the choice of PDF.

TABLE XX. Unsmearing ansatz function parameters [see Eq. (11.3)] for the inclusive jet cross section for $|\eta|<0.5$ (in nb) at $\sqrt{s}=630$ and 1800 GeV and their uncertainties.

$\sqrt{s}$ (GeV)	Parameter	Value	Error matrix		
1800	A	23.43	4.48825×10^{-3}	-1.15352×10^{-3}	-6.70083×10^{-3}
	α	-5.04	-1.15352×10^{-3}	2.98882×10^{-4}	1.79044×10^{-3}
	β	8.23	-6.70083×10^{-3}	1.79044×10^{-3}	1.21005×10^{-2}
630	A	22.7	2.28649×10^{-2}	-8.62822×10^{-3}	-5.76500×10^{-2}
	α	-5.33	-8.62822×10^{-3}	3.28592×10^{-3}	2.24650×10^{-2}
	β	6.58	-5.76500×10^{-2}	2.24650×10^{-2}	0.16449×10^{-1}

TABLE XXI. Inclusive jet cross section for $|\eta|<0.5$ at $\sqrt{s}=630$ GeV.

Bin range E_T (GeV)	Plotted E_T (GeV)	Plotted x_T	Cross section $\pm$ statistical error (nb)	Systematic uncertainty (%)
21.0–24.5	22.6	0.07	$(2.56\pm0.03)\times10^{2}$	21.7
24.5–28.0	26.1	0.08	$(1.07\pm0.02)\times10^{2}$	17.2
28.0–31.5	29.6	0.09	$(5.14\pm0.16)\times10^{1}$	14.6
31.5–35.0	33.1	0.11	$(2.67\pm0.05)\times10^{1}$	13.0
35.0–38.5	36.7	0.12	$(1.37\pm0.04)\times10^{1}$	12.1
38.5–42.0	40.2	0.13	$(7.96\pm0.27)\times10^{0}$	11.5
42.0–45.5	43.7	0.14	$(4.24\pm0.20)\times10^{0}$	11.2
45.5–49.0	47.2	0.15	$(2.83\pm0.16)\times10^{0}$	11.0
49.0–52.5	50.7	0.16	$(1.81\pm0.13)\times10^{0}$	10.9
52.5–56.0	54.2	0.17	$(1.14\pm0.03)\times10^{0}$	10.9
56.0–59.5	57.7	0.18	$(7.35\pm0.21)\times10^{-1}$	11.0
59.5–63.0	61.2	0.19	$(5.07\pm0.17)\times10^{-1}$	11.1
63.0–66.5	64.7	0.21	$(3.29\pm0.14)\times10^{-1}$	11.3
66.5–70.0	68.2	0.22	$(2.42\pm0.12)\times10^{-1}$	11.5
70.0–73.5	71.7	0.23	$(1.64\pm0.10)\times10^{-1}$	11.8
73.5–77.0	75.2	0.24	$(1.18\pm0.08)\times10^{-1}$	12.1
77.0–80.5	78.7	0.25	$(8.79\pm0.72)\times10^{-2}$	12.4
80.5–94.5	85.2	0.27	$(3.69\pm0.23)\times10^{-2}$	13.6
94.5–112.0	100.5	0.32	$(1.05\pm0.11)\times10^{-2}$	16.2
112.0–196.0	136.2	0.43	$(5.81\pm1.19)\times10^{-4}$	20.4

Different renormalization scales can be selected for the different c.m. energies since there is no explicit theoretical need for identical scales at $\sqrt{s}=630$ and 1800 GeV. Figure 68 depicts a comparison between the ratio and theoretical predictions where the renormalization scales at the two c.m. energies are not equivalent. The resulting χ^2 indicate good agreement between the data and the predictions (Table XXXI).

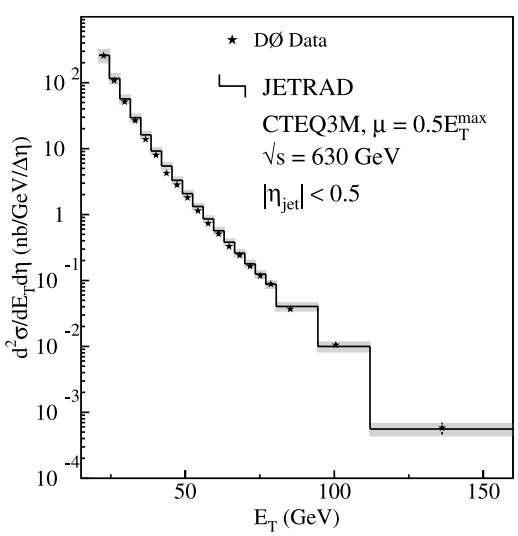

FIG. 58. The $|\eta|<0.5$ inclusive cross section at $\sqrt{s}=630$ GeV. Statistical uncertainties are not visible on this scale (except for the last point). The histogram represents the JETRAD prediction and the shaded band represents the $\pm1\sigma$ systematic uncertainty band about the prediction.

Since the systematic uncertainties are strongly correlated as a function of x_T, the normalization can deviate from the nominal value by a couple of standard deviations without greatly effecting the χ^2. It is therefore interesting to ask the question, "how well does the normalization of the data and the theoretical predictions agree?" To answer this question an additional analysis was carried out to measure the significance of the normalization difference between the data and the theoretical predictions. The data are reduced to a single value by fitting them to a constant (horizontal line), resulting in a value of 1.60 ± 0.08. The uncertainty is given by the statistical uncertainty of the fit. Each of the theoretical predictions is also treated in this manner, with each point in x_T point of the prediction is assigned a weight given by the statistical uncertainty of the corresponding point in the data (Table XXXII). The uncertainty in the value representing the theoretical prediction is assumed to be zero. The resulting χ^2 values are given in Table XXXII, and lie in the range 1.4–13.2 (corresponding to probabilities of 23% to 0.03%). In every case, discarding the shape information in favor of a comparison of normalization results in poorer agreement between data and the theory.

E. Conclusions

We have made the most precise measurement to date of the ratio of the inclusive jet cross sections at $\sqrt{s}=630$ and 1800 GeV. This measurement is nearly insensitive to the choice of parton distribution functions. The ratio of cross sections is therefore a more stringent test of QCD matrix elements. The NLO QCD predictions yield satisfactory agreement with the observed data for standard choices of renormalization scale or PDF. In terms of the normalization however, the absolute values of the standard predictions lie consistently higher than the data.

XIII. DIJET ANGULAR DISTRIBUTION

The dijet angular distribution is given by

$$\frac{1}{\sum\sigma}\frac{d^3\sigma}{dM\,d\chi\,d\eta_{\rm boost}}=\frac{1}{\sum N_i}\frac{N_i}{\Delta M\Delta\chi\Delta\eta_{\rm boost}} \tag{13.1}$$

where the invariant mass is calculated assuming massless jets:

$$M^2=2E_T^{\rm jet1}E_T^{\rm jet2}[\cosh(\Delta\eta)-\cos(\Delta\phi)], \tag{13.2}$$

the pseudorapidity of the center-of-mass of the dijet system is given by $\eta^\star=\frac{1}{2}(\Delta\eta)$; the pseudorapidity boost is given by $\eta_{\rm boost}=\frac{1}{2}(\eta_1+\eta_2)$; $\chi=\exp(|\Delta\eta|)=\exp(2|\eta^\star|)$; $E_T^{\rm jet1}$, η_1, and ϕ_1 refer to the values associated with the jet with the largest E_T in an event; $E_T^{\rm jet2}$, η_2, and ϕ_2 refer to the values associated with the jet with the second largest E_T in an event; $\Delta\eta=|\eta_1-\eta_2|$; $\Delta\phi=\phi_1-\phi_2$, and N_i is the number of events in a given χ and mass bin. If the individual jet masses

TABLE XXII. Percentage cross section uncertainties for $|\eta|<0.5$ at $\sqrt{s}=630$ GeV. The last row gives the nature of the bin-to-bin x_T correlations: 0 signifies uncorrelated uncertainties, 1 correlated, and p partially correlated.

x_T	Statistical	Jet selection	Luminosity	Trigger	Unsmearing	Energy scale	Total
0.07	1.3	0.2	4.4	2.4	8.4	19.4	21.7
0.08	2.1	0.2	4.4	0.9	5.5	15.6	17.2
0.09	3.2	0.2	4.4	0.3	3.8	13.3	14.6
0.11	1.8	0.2	4.4	0.6	2.8	11.9	13.0
0.12	2.5	0.2	4.4	0.2	2.2	11.0	12.1
0.13	3.4	0.2	4.4	0.1	1.8	10.5	11.5
0.14	4.7	0.1	4.4	0.0	1.6	10.2	11.2
0.15	5.8	0.1	4.4	0.0	1.4	9.9	11.0
0.16	7.3	0.1	4.4	0.0	1.3	9.8	10.9
0.17	2.2	0.1	4.4	1.1	1.3	9.9	10.9
0.18	2.8	0.1	4.4	0.4	1.2	10.0	11.0
0.19	3.4	0.1	4.4	0.2	1.2	10.1	11.1
0.21	4.2	0.2	4.4	0.1	1.2	10.3	11.3
0.22	4.9	0.2	4.4	0.0	1.2	10.6	11.5
0.23	6.0	0.2	4.4	0.0	1.2	10.8	11.8
0.24	7.0	0.2	4.4	0.0	1.2	11.2	12.1
0.25	8.2	0.2	4.4	0.0	1.2	11.6	12.4
0.27	6.3	0.2	4.4	0.0	1.2	12.8	13.6
0.32	10.6	0.3	4.4	0.0	1.3	15.5	16.2
0.43	20.4	0.3	4.4	0.0	1.5	19.8	20.4
Correlation	0	0	1	0	1	p	p

are taken into account, the change in the dijet invariant mass is less than 1% for jets used in this analysis. Since the bins of $\Delta\eta_{\rm boost}$ are constant and we plot the angular distribution for a given mass bin, ΔM, we choose to measure $d\sigma/d\chi$ which is uniform for Rutherford scattering)

$$\frac{1}{\sum\sigma}\frac{d\sigma}{d\chi}=\frac{1}{\sum N_i}\frac{N_i}{\Delta\chi}. \tag{13.3}$$

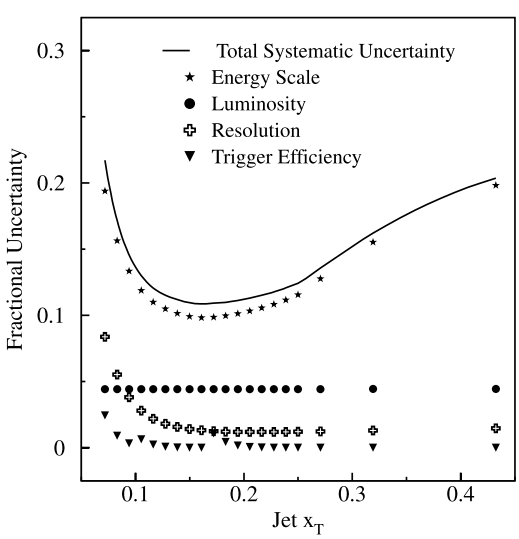

FIG. 59. Contributions to the $|\eta|<0.5$ at $\sqrt{s}=630$ GeV cross section uncertainty plotted by component.

A. Data selection

The selected data are events with two or more jets which satisfy the set of inclusive jet triggers and pass the standard jet and event quality requirements (Sec. VIII). Events are removed unless both of the leading two jets pass the jet quality requirements. The vertex of the event must be within 50

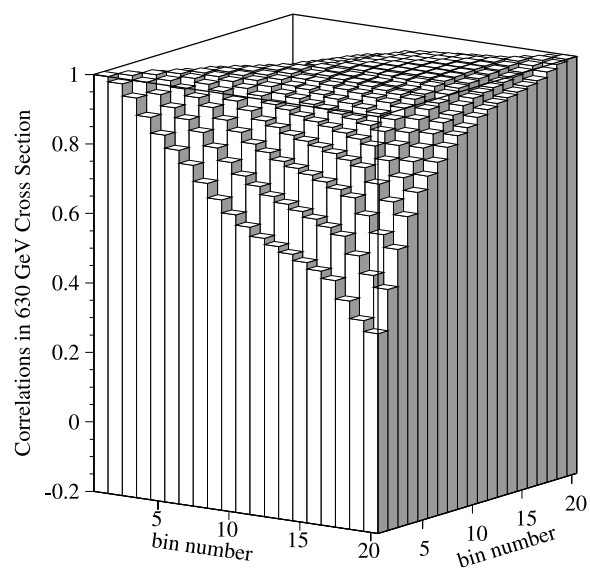

FIG. 60. The correlations for the total systematic uncertainty for the inclusive jet cross section for $|\eta|<0.5$ at $\sqrt{s}=630$ GeV (Table XXIII).

TABLE XXIII. The correlations for the total systematic uncertainty for the inclusive jet cross section for $|\eta|<0.5$ at $\sqrt{s}=630$ GeV and the ratio of cross sections. The correlation values above the diagonal are for the cross section at $\sqrt{s}=630$ GeV and the values below the diagonal correspond to the ratio of cross sections. In both cases the correlation matrices are symmetric.

		1.00	0.99	0.96	0.91	0.86	0.82	0.79	0.74	0.69	0.66	0.62	0.60	0.58	0.56	0.54	0.52	0.50	0.44	0.39	0.36	1
			1.00	0.99	0.96	0.93	0.90	0.87	0.83	0.79	0.76	0.73	0.70	0.69	0.67	0.65	0.63	0.61	0.56	0.51	0.48	2
1	1.00			1.00	0.99	0.97	0.95	0.93	0.90	0.87	0.84	0.82	0.79	0.78	0.77	0.75	0.73	0.72	0.67	0.62	0.59	3
2	0.98	1.00			1.00	0.99	0.98	0.97	0.94	0.92	0.90	0.88	0.86	0.85	0.84	0.83	0.81	0.80	0.76	0.71	0.68	4
3	0.95	0.99	1.00			1.00	1.00	0.99	0.97	0.96	0.94	0.93	0.91	0.90	0.89	0.88	0.87	0.85	0.82	0.77	0.74	5
4	0.90	0.95	0.98	1.00			1.00	1.00	0.99	0.97	0.96	0.95	0.94	0.93	0.92	0.91	0.90	0.89	0.85	0.81	0.78	6
5	0.84	0.91	0.95	0.99	1.00			1.00	0.99	0.99	0.98	0.97	0.96	0.95	0.94	0.94	0.93	0.92	0.88	0.85	0.82	7
6	0.79	0.87	0.93	0.97	0.99	1.00			1.00	1.00	0.99	0.98	0.98	0.97	0.97	0.96	0.95	0.94	0.91	0.88	0.85	8
7	0.74	0.83	0.89	0.95	0.98	0.99	1.00			1.00	1.00	0.99	0.99	0.98	0.98	0.97	0.97	0.96	0.94	0.91	0.88	9
8	0.68	0.77	0.84	0.91	0.94	0.96	0.97	1.00			1.00	1.00	0.99	0.99	0.99	0.98	0.98	0.97	0.95	0.93	0.90	10
9	0.62	0.72	0.80	0.87	0.91	0.94	0.96	0.99	1.00			1.00	1.00	1.00	0.99	0.99	0.99	0.98	0.97	0.94	0.92	11
10	0.57	0.67	0.76	0.84	0.89	0.92	0.95	0.98	0.99	1.00			1.00	1.00	1.00	0.99	0.99	0.99	0.97	0.95	0.93	12
11	0.52	0.63	0.72	0.80	0.86	0.90	0.93	0.97	0.98	0.99	1.00			1.00	1.00	1.00	0.99	0.99	0.98	0.96	0.94	13
12	0.47	0.58	0.68	0.76	0.83	0.87	0.90	0.95	0.97	0.98	0.99	1.00			1.00	1.00	1.00	0.99	0.98	0.97	0.95	14
13	0.43	0.54	0.64	0.73	0.80	0.84	0.88	0.93	0.95	0.97	0.99	0.99	1.00			1.00	1.00	1.00	0.99	0.97	0.95	15
14	0.39	0.50	0.60	0.70	0.76	0.82	0.85	0.91	0.94	0.96	0.98	0.99	0.99	1.00			1.00	1.00	0.99	0.98	0.96	16
15	0.34	0.46	0.56	0.66	0.73	0.78	0.83	0.88	0.91	0.94	0.96	0.98	0.99	0.99	1.00			1.00	0.99	0.98	0.97	17
16	0.30	0.41	0.52	0.62	0.69	0.75	0.79	0.85	0.89	0.92	0.95	0.97	0.98	0.99	0.99	1.00			1.00	0.99	0.98	18
17	0.25	0.37	0.47	0.57	0.65	0.71	0.76	0.82	0.86	0.89	0.93	0.95	0.96	0.98	0.99	0.99	1.00			1.00	0.99	19
18	0.14	0.25	0.36	0.46	0.55	0.61	0.66	0.73	0.78	0.82	0.86	0.90	0.92	0.94	0.96	0.97	0.98	1.00			1.00	20
19	-0.01	0.09	0.20	0.30	0.38	0.45	0.50	0.58	0.63	0.69	0.74	0.79	0.82	0.85	0.88	0.91	0.93	0.97	1.00			
20	-0.13	-0.04	0.06	0.15	0.24	0.30	0.36	0.44	0.50	0.56	0.62	0.68	0.72	0.75	0.79	0.83	0.86	0.93	0.98	1.00		

cm of $z=0$. The χ distributions were corrected for the efficiencies of the standard jet quality cuts and the $\not{E}_T$ cut.

To ensure that the jet triggers did not introduce a bias, the trigger requirement was verified by comparing the χ distribution of a lower trigger threshold to the χ distribution of the desired trigger threshold. It is known that the lower threshold trigger is 100% efficient in the desired region and thus a comparison would show an inefficiency in the desired trigger sample. No differences were seen. The E_T's of all second jets are well within the region of 100% jet reconstruction efficiency, so an additional E_T requirement on the second jet was not necessary. The final energy-scale-corrected E_T requirement placed on each trigger sample is summarized in Table XXXIII.

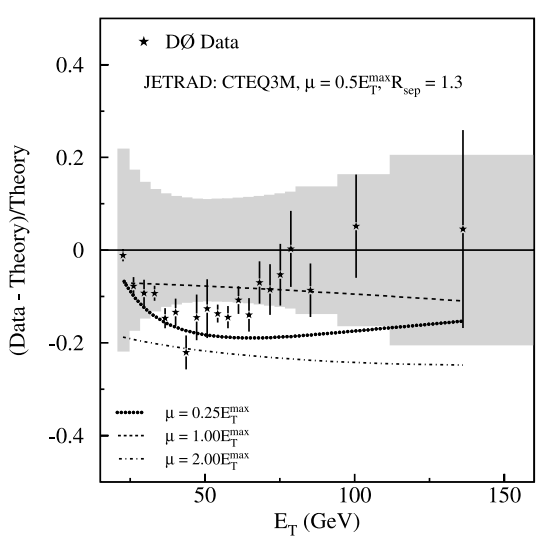

FIG. 61. The difference between the data and the prediction (JETRAD), divided by the prediction for $|\eta|<0.5$ at $\sqrt{s}=630$ GeV. The solid stars represent the comparison to the calculation using CTEQ3M with $\mu=0.5E_T^{\max}$. The shaded region represents the $\pm 1\sigma$ systematic uncertainties about the prediction. The effects of changing the renormalization scale are also shown (each curve shows the difference between the alternative prediction and the standard prediction).

B. Acceptance: Limits on mass and χ

Event acceptance is calculated using the kinematic relationships between mass, χ, and E_T shown in Fig. 69. Since an E_T requirement is placed only on the leading jet, the maximum χ with 100% acceptance is determined from the E_T requirement placed on the leading jet and the desired mass bin using the following formula:

$$M^2=2E_{T1}^2[\cosh(\ln(\chi))+1]. \tag{13.4}$$

In this formula the E_T's of the two leading jets are assumed to be identical. Four mass bins were chosen in order to maximize the number of events per χ bin, and to attain a maximum χ of 20 (corresponding to $\eta^\star=1.5$). These mass bins are listed in Table XXXIV.

Once the χ limit is known, a limit on $\eta_{\rm boost}$ can be calculated. The $\eta_{\rm boost}$ parameter is used to restrict the χ distribution to the physical limits of the detector (Fig. 70). The $\eta_{\rm boost}$ limit is calculated using

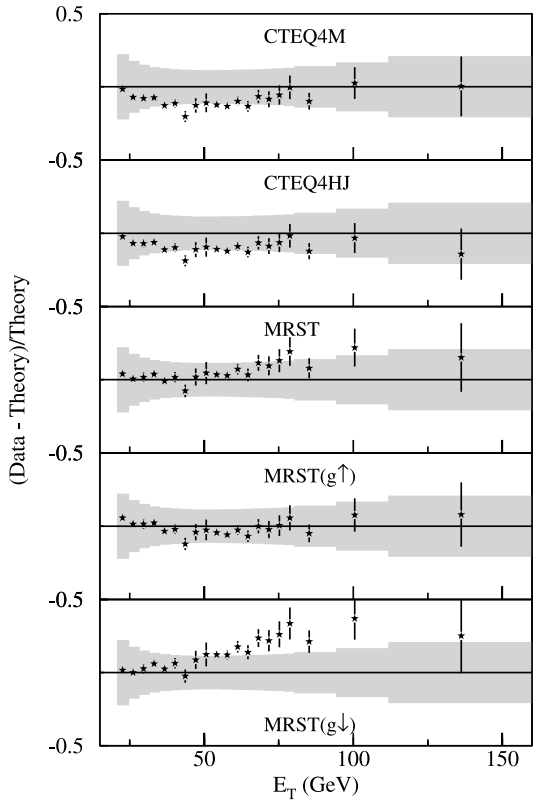

FIG. 62. The difference between the data and the prediction (JETRAD), divided by the prediction for $|\eta|<0.5$. The solid stars represent the comparison to the calculation using $\mu=0.5E_T^{\max}$ and the PDFs CTEQ4M, CTEQ4HJ, MRST, MRST($g\uparrow$), and MRST($g\downarrow$). The shaded region represents the $\pm 1\sigma$ systematic uncertainties about the prediction.

$$|\eta_{\text{boost}}|=||\eta^{\star}|-|\eta_{\max}||$$
$$=||1.5|-|3.0||=1.5, \qquad (13.5)$$

where $|\eta_{\max}|=3.0$ is the maximum η used for this analysis. The boost cut is chosen to be $\eta_{\text{boost}}\leqslant 1.5$. For $M>475$ GeV/c^2, $|\eta_{\text{boost}}|$ is kinematically restricted to a value less than 1.5. These mass bins are listed together with the average dijet

TABLE XXIV. χ^2 comparisons of the inclusive jet cross section for $|\eta|<0.5$ at $\sqrt{s}=630$ GeV with several theoretical predictions (20 degrees of freedom).

PDF	μ	χ^2	Prob.
CTEQ3M	$2E_T^{\max}$	40.5	0.4%
	$E_T^{\max}$	25.9	17%
	$0.5E_T^{\max}$	30.4	6.4%
	$0.25E_T^{\max}$	27.5	12%
CTEQ4M	$0.5E_T^{\max}$	24.2	24%
CTEQ4HJ	$0.5E_T^{\max}$	19.0	53%
MRST	$0.5E_T^{\max}$	22.6	31%
MRST($g\uparrow$)	$0.5E_T^{\max}$	14.9	78%
MRST($g\downarrow$)	$0.5E_T^{\max}$	51.8	0.01%

TABLE XXV. The uncertainties in the ratio of cross sections due to the luminosity calculation.

Source	Uncertainty (%)
World average $\overline{p}p$ cross section	± 3.2
Hardware efficiency	± 3.6
Geometric acceptance	± 0.8
Uncorrelated[a]	± 2.6
All sources[a]	± 4.2

[a]Includes trigger matching uncertainty.

TABLE XXVI. Uncertainty from jet and event selection.

	Uncertainty source	Uncertainty
1800 GeV	All selection	1% below 350 GeV
	Cut efficiencies	2% above 350 GeV
630 GeV	Jet cuts	0.12 to 0.53%
	$\not{E}_T$ cut	0.03%
	Vertex cut	0.006%

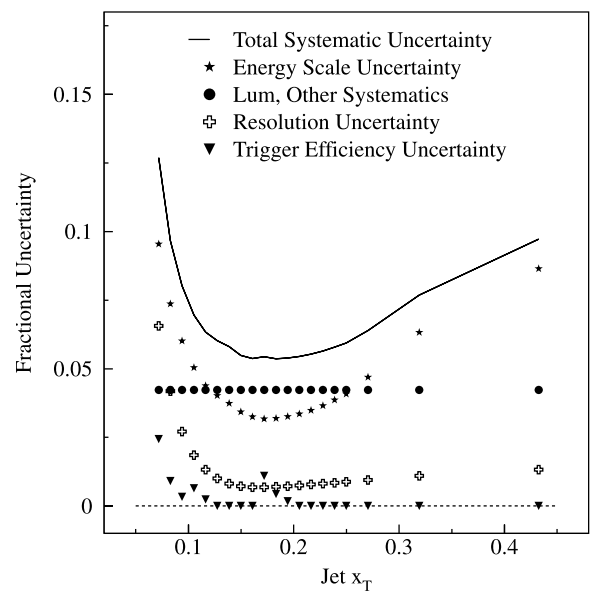

FIG. 63. The uncertainty components in the ratio of inclusive jet cross sections as a function of x_T plotted by component.

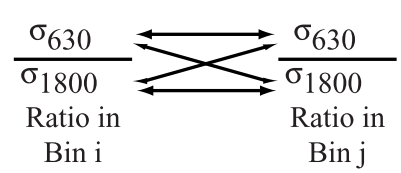

FIG. 64. Correlations between two ratio bins i and j. Arrows indicate the four possible correlation (ρ) terms. The uppermost arrow is $\rho_{ij}^{630-630}$, while the "↘" arrow is $\rho_{ij}^{630-1800}$.

TABLE XXVII. Uncertainty correlations in the ratio of cross sections. "0" indicates no correlation, "1" indicates complete correlation.

Uncertainty source	Correlation in $\sqrt{s}$	Jet E_T	Comments
Luminosity	Partial	1	
Filter match	0	1	1800 GeV only
Event cuts	0	0	
Jet cuts	0	0	
Resolution			
Fits	Partial	1	
Closure	1	1	
Unsmearing fits	0	1	
Energy scale			
Offset	Partial	1	
Response fit	1	Partial	
Response at 630 GeV	0	1	
Showering	1	1	

invariant mass, the maximum χ measured, and the number of events for each of four mass ranges in Table XXXIV.

C. Systematic studies

In order to study the systematic effects of the jet and event selection requirements, and the various corrections that are applied to the data, a series of systematic studies was performed. For each requirement or correction, we measured the effect on the angular distribution by varying the requirement or correction by an appropriate amount.

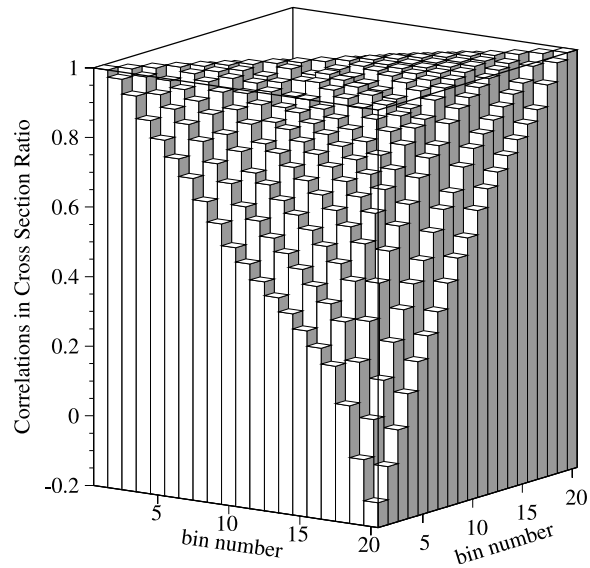

FIG. 65. The correlation matrix for the ratio of cross sections. Axes indicate the bin numbers.

To determine the systematic uncertainties on the shape of the angular distribution, each distribution is fit with a function: $F=A+B\chi+C/\chi+D/\chi^2+E/\chi^3$. The effect of varying each of the selection criteria or corrections is measured by taking the ratio of the distribution with the nominal selection criteria, and with the adjusted criteria (Fig. 71), giving the size of the systematic uncertainty.

The largest source of uncertainty involves the η dependence of the jet energy scale. Small uncertainties in the relative response as a function of η have large effects on the

TABLE XXVIII. Percentage uncertainties in the ratio of inclusive jet cross sections at $\sqrt{s}=630$ and 1800 GeV for $|\eta|<0.5$.

x_T	Statistical	Jet selection	Trigger match	Luminosity	Trigger efficiency	Unsmearing	Energy scale	Total
0.07	1.5	1.1	1.7	4.1	2.4	6.6	9.5	12.7
0.08	2.4	1.1	1.7	4.1	0.9	4.2	7.4	9.7
0.09	3.5	1.1	1.7	4.1	0.3	2.7	6.0	8.0
0.11	1.9	1.1	1.1	4.1	0.6	1.9	5.0	7.0
0.12	2.7	1.1	1.1	4.1	0.2	1.3	4.4	6.3
0.13	3.5	1.1	1.1	4.1	0.1	1.0	4.0	6.0
0.14	4.9	1.1	1.1	4.1	0.0	0.8	3.7	5.8
0.15	5.8	1.1	0.0	4.1	0.0	0.7	3.4	5.5
0.16	7.3	1.1	0.0	4.1	0.0	0.7	3.2	5.4
0.17	2.4	1.1	0.0	4.1	1.1	0.7	3.2	5.4
0.18	3.0	1.1	0.0	4.1	0.4	0.7	3.2	5.4
0.19	3.5	1.1	0.0	4.1	0.2	0.7	3.3	5.4
0.21	4.4	1.1	0.0	4.1	0.1	0.8	3.4	5.5
0.22	5.1	1.1	0.0	4.1	0.0	0.8	3.5	5.5
0.23	6.2	1.1	0.0	4.1	0.0	0.8	3.7	5.6
0.24	7.3	1.1	0.0	4.1	0.0	0.8	3.9	5.8
0.25	8.5	1.1	0.0	4.1	0.0	0.9	4.1	5.9
0.27	6.6	1.1	0.0	4.1	0.0	1.0	4.7	6.4
0.32	11.0	1.1	0.0	4.1	0.0	1.1	6.3	7.7
0.43	20.5	1.1	0.0	4.1	0.0	1.3	8.7	9.7

TABLE XXIX. The ratio of the inclusive jet cross sections for $|\eta|<0.5$ at $\sqrt{s}=630$ and 1800 GeV.

(x_T) Bin range	(x_T) Plotted	Ratio of cross sections ± statistical error	Systematic uncertainty (%)
0.067–0.078	0.072	1.72±0.03	12.7
0.078–0.089	0.083	1.64±0.04	9.7
0.089–0.100	0.094	1.62±0.06	8.0
0.100–0.111	0.105	1.67±0.03	7.0
0.111–0.122	0.116	1.57±0.04	6.3
0.122–0.133	0.127	1.59±0.06	6.0
0.133–0.144	0.139	1.48±0.07	5.8
0.144–0.156	0.150	1.63±0.09	5.5
0.156–0.167	0.161	1.64±0.12	5.4
0.167–0.178	0.172	1.64±0.04	5.4
0.178–0.189	0.183	1.62±0.05	5.4
0.189–0.200	0.194	1.67±0.06	5.4
0.200–0.211	0.205	1.60±0.07	5.5
0.211–0.222	0.216	1.74±0.09	5.5
0.222–0.233	0.228	1.69±0.10	5.6
0.233–0.244	0.239	1.78±0.13	5.8
0.244–0.256	0.250	1.81±0.15	5.9
0.256–0.300	0.271	1.74±0.11	6.4
0.300–0.356	0.319	1.85±0.20	7.7
0.356–0.622	0.432	1.83±0.38	9.7

angular distribution. The uncertainties in the jet energy scale are less than 2% up to an $|\eta|$ of 2.0 and become large near $|\eta|\approx 3.0$. The uncertainty in the showering correction is less than 2% for $|\eta|<2.0$ and becomes large at high $|\eta|$. The effect of the η-dependent energy scale uncertainties are given in Fig. 72(a).

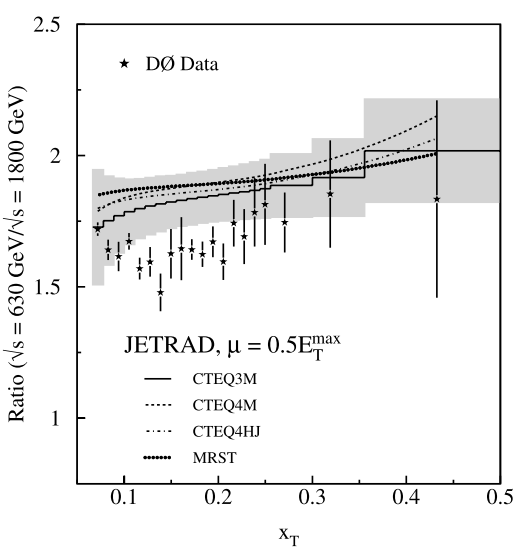

FIG. 66. The ratio of dimensionless cross sections for $|\eta|<0.5$ compared with JETRAD predictions with $\mu=0.5E_T^{\max}$ and the CTEQ3M, CTEQ4M, CTEQ4HJ, and MRST PDFs. The shaded band represents the $\pm 1\sigma$ systematic uncertainty band about the prediction.

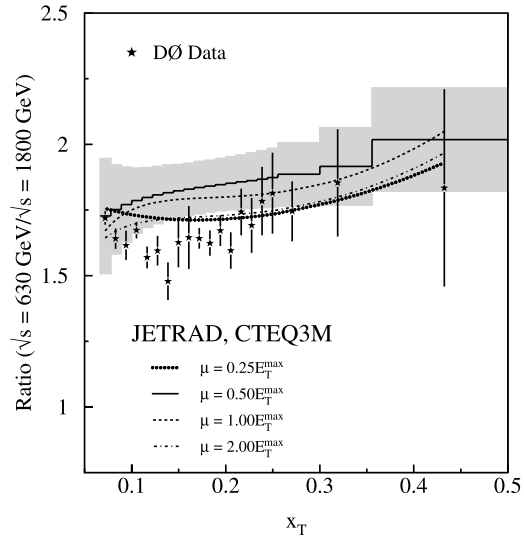

FIG. 67. The ratio of dimensionless cross sections for $|\eta|<0.5$ compared with JETRAD predictions with various values of μ and the CTEQ3M PDF. The shaded band represents the $\pm 1\sigma$ systematic uncertainty band about the prediction.

The resolution of our measurement of the jet energy can also affect the angular distribution. This was determined by measuring the difference between the smeared and unsmeared theory calculations. Since we are not unsmearing the data for the effects of η and E_T smearing, we apply this as an uncertainty in the measurement [Fig. 72(b)].

The effect on the angular distribution due to the η bias in the jet reconstruction algorithm (Sec. III G) was studied by applying a correction for the bias. The difference between the corrected and uncorrected distributions was 1% on average [Fig. 72(c)].

The overall energy scale does not affect the shape of the distribution, because a shift in the overall energy scale shifts the entire distribution in mass. The angular distribution changes very slowly with mass, so a small shift would not cause a significant change in the shape.

For the Jet_30 and Jet_50 triggers, an online MITOOL (see Sec. VII) requirement was used in the trigger for part of the run. To determine if the MITOOL requirement biased the an-

TABLE XXX. The calculated χ^2 for the ratio of cross sections (20 degrees of freedom).

PDF	Renormalization scale	χ^2	Prob.
CTEQ3M	$2E_T^{\max}$	17.9	60%
	$E_T^{\max}$	21.6	36%
	$0.75E_T^{\max}$	23.1	28%
	$0.5E_T^{\max}$	20.5	43%
	$0.25E_T^{\max}$	15.1	77%
CTEQ4M	$0.5E_T^{\max}$	22.4	32%
CTEQ4HJ	$0.5E_T^{\max}$	21.0	40%
MRST	$0.5E_T^{\max}$	22.2	33%
MRST($g\uparrow$)	$0.5E_T^{\max}$	19.5	49%
MRST($g\downarrow$)	$0.5E_T^{\max}$	24.1	24%

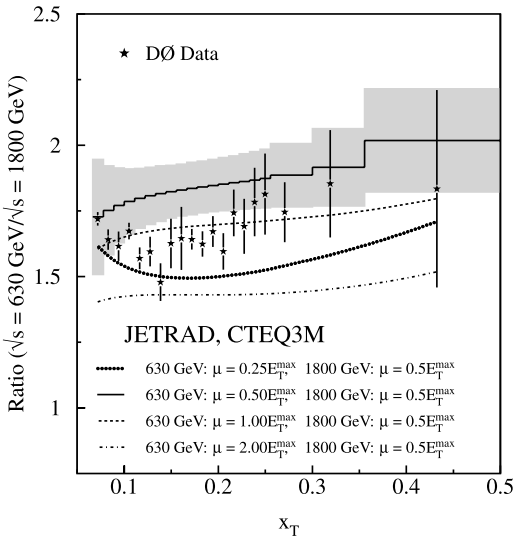

FIG. 68. The ratio of dimensionless cross sections for $|\eta|<0.5$ compared with JETRAD predictions with $\mu=0.5E_T^{\max}$ at $\sqrt{s}=1800$ GeV, $\mu=(0.25,1.0,2.0)E_T^{\max}$ at $\sqrt{s}=630$ GeV, and the CTEQ3M PDF. The shaded band represents the $\pm 1\sigma$ systematic uncertainty band about the prediction.

TABLE XXXII. Normalization-only predictions for the ratio of cross sections and the χ^2 comparison with the data (1.60 ± 0.08 for one degree of freedom).

PDF	Renormalization scale		Theory normalization	χ^2	Prob.
	$2E_T^{\max}$		1.75	3.3	6.8%
	$E_T^{\max}$		1.82	7.1	0.8%
CTEQ3M	$0.75E_T^{\max}$		1.87	10.7	0.1%
	$0.5E_T^{\max}$		1.85	9.5	0.2%
	$0.25E_T^{\max}$		1.70	1.5	22.9%
CTEQ4M	$0.5E_T^{\max}$		1.90	13.2	0.03%
CTEQ4HJ	$0.5E_T^{\max}$		1.87	10.7	0.1%
MRST	$0.5E_T^{\max}$		1.89	12.6	0.04%
MRST($g\uparrow$)	$0.5E_T^{\max}$		1.87	11.1	0.09%
MRST($g\downarrow$)	$0.5E_T^{\max}$		1.90	12.9	0.03%
	630 GeV	1800 GeV			
	$2E_T^{\max}$	$0.5E_T^{\max}$	1.46	2.7	10.2%
CTEQ3M	$E_T^{\max}$	$0.5E_T^{\max}$	1.71	1.8	18.1%
	$0.25E_T^{\max}$	$0.5E_T^{\max}$	1.44	3.7	5.4%

gular distribution, runs with no MITOOL requirement were compared to runs with the requirement. A small shape difference was seen and an uncertainty equal to the difference between the two measurements was assigned.

The effects of multiple interactions on the distributions were studied. A secondary interaction adds approximately 0.6 GeV of E_T per unit $\Delta\eta\times\Delta\phi$ (Fig. 20). Since the angular distribution is measured in regions in which the E_T's of the two leading jets are in excess of 50 GeV and are often above 100 GeV, the effect of this additional energy on the two leading jets is minimal. It is possible that a second interaction may produce a vertex which is incorrectly used as in the primary vertex for the leading two jets. This would cause an error in the measured η positions of the jets as well as the measured E_T of the jets. We studied the effect of not selecting the primary vertex by minimizing the S_T in the event (Sec. VII). This has a negligible effect on the angular distribution.

It is possible that the vertex produced by a second interaction is the only vertex found in the event. This would also cause an error in the measured η and E_T values of the jets. We studied the possibility of multiple interactions affecting the angular distribution in this manner by the following method. For a determined percentage of events, we switched the vertex to a randomly chosen vertex. The new vertex was based on the measured vertex distribution, which has an approximate mean of $z=0$ and a $\sigma\approx30$ cm. We then recalculated the η and E_T of the two leading jets in the event and measured the angular distribution. The percentage of events with a new vertex was determined based on the efficiency of vertex reconstruction for events with large E_T jets ($\approx70\%$), and the percentage of multiple interactions in the data used for this analysis ($\approx60\%$). The number of vertices switched was 20%, which is an estimate of the number of times that the vertex reconstruction is incorrect. The size of the effect is less than 2% and is dependent on the value of χ [see Fig. 72(d)].

The jet quality requirements and their corresponding efficiency corrections are necessary to remove noise from the event sample. Their effect on the shape of the angular distribution is minimal.

The DØ jet algorithm allows for the splitting and merging of jets. This can cause a shift in the η of the jet, and therefore affect the angular distribution. The effect on the shape of the distribution of removing those events in which either of the leading two jets were split or merged is minimal. Since the theoretical predictions are expected to properly address

TABLE XXXI. χ^2 comparisons for the ratio of cross sections for $|\eta|<0.5$ where the renormalization scale is mismatched between c.m. energies.

PDF	Renormalization scale 630 GeV	1800 GeV	χ^2	Prob.
	$2E_T^{\max}$	$0.5E_T^{\max}$	14.9	78%
CTEQ3M	$E_T^{\max}$	$0.5E_T^{\max}$	17.2	64%
	$0.25E_T^{\max}$	$0.5E_T^{\max}$	23.1	28%

TABLE XXXIII. The cut on the E_T of the leading jet to ensure that the trigger is 100% efficient.

Trigger	Corrected E_T limit on leading jet (GeV)
Jet_30	55.0
Jet_50	90.0
Jet_85	120.0
Jet_115	175.0

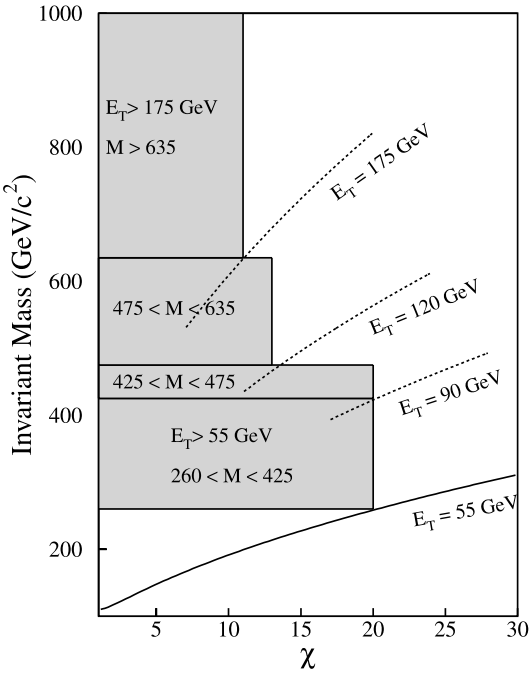

FIG. 69. In the mass versus χ plane, the curves shown are contours of constant E_{T}. The simplest form of uniform acceptance in this plane is a rectangle. For a chosen mass region, the limit on χ corresponds to the intersection of the lower mass limit and the E_{T} contour. The shaded regions shown are the mass bins chosen for this analysis.

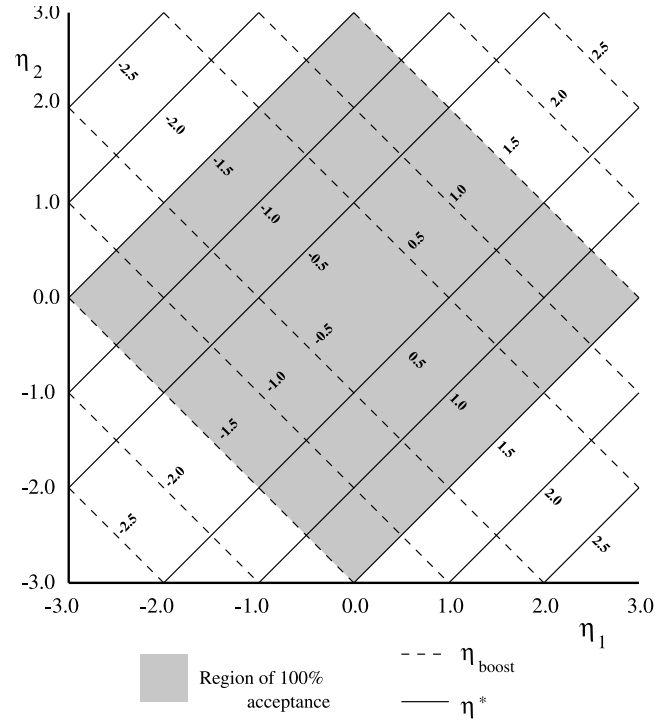

FIG. 70. The $|\eta|$'s of the two leading jets were required to be less than 3.0. For a maximum $\eta^\star$ of 1.5, the $|\eta_{\mathrm{boost}}|$ was chosen to less than 1.5 to restrict the measurement to a region of 100% acceptance.

merging and splitting, no uncertainty was assigned due to this effect.

D. Results and comparison to theory

The measurement of the dijet angular cross section is given in Table XXXV. The leading-order and next-to-leading-order theory predictions were obtained using the JETRAD parton-level event generator [13] with CTEQ3M and $\mu=0.5E_T^{\max}$. Four mass ranges are compared to the LO and NLO predictions of QCD in Fig. 73. The band at the bottom of each plot represents the $\pm 1\sigma$ systematic uncertainties. They are obtained by adding in quadrature all of the parameterized curves describing the shape uncertainties discussed earlier.

Also shown in Fig. 73, are comparisons to NLO theory predictions calculated using $\mu=E_T^{\max}$. With the large angular

TABLE XXXIV. The average mass, maximum χ measured, and the number of events after applying all kinematic cuts.

Trigger E_T threshold (GeV)	Mass range (GeV/c^2)	Average mass (GeV/c^2)	$\chi_{\max}$	Number of events
55	260–425	302	20	4621
90	425–475	447	20	1573
120	475–635	524	13	8789
175	>635	700	11	1074

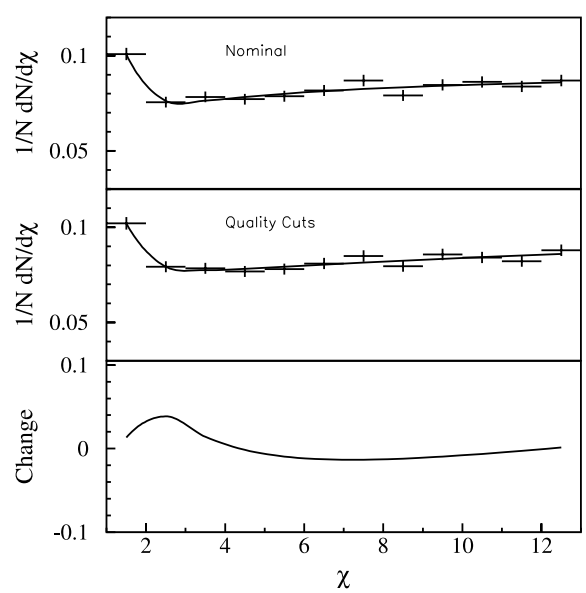

FIG. 71. Technique to determine changes in angular distribution due to systematic uncertainties. Top: Normalized angular distribution for the mass range 475–635 GeV/c^2 compared to a fit to the data. Middle: Normalized angular distribution for the mass range 475–635 GeV/c^2 after removing the jet quality cuts and a fit to the data. Bottom: The (ratio−1) of the two fits shows the effects of the jet quality cuts on the shape of the angular distribution.

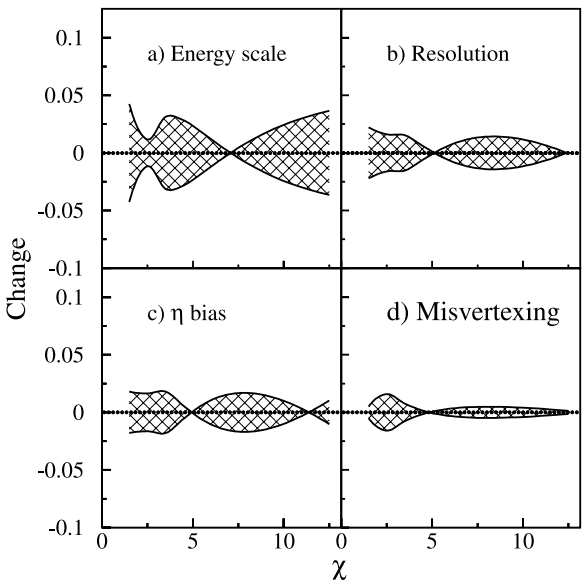

FIG. 72. Ratios of parametrized curves showing the effects of uncertainties on the shape of the angular distribution. Shown are the four largest uncertainties in the mass range 475–635 GeV/c^2.

reach measured, the angular distribution is sensitive to the choice of renormalization scale. The QCD theoretical predictions are in good agreement with the measured angular distributions.

E. Compositeness limits

A comparison to theory is made to test for quark compositeness (Sec. IV B). Predictions of the theory of compositeness are available at LO. In order to simulate NLO prediction with compositeness, we generated LO curves at various values of Λ. We measured the fractional differences between the LO angular distribution with $\Lambda=\infty$ and those with finite Λ values. We then multiplied the NLO prediction of the angular distribution by these fractional differences. The results are shown in Fig. 74 for the mass bin with $M>635$ GeV/c^2.

To remove the point-to-point correlated uncertainties, the distribution can be characterized by a single number: $R_\chi = N(\chi<X)/N(X<\chi<\chi_{\max})$, the ratio of the number of events with $\chi<X$ to the number of events between $X<\chi<\chi_{\max}$ (where $\chi_{\max}$ is given in Table XXXIV). The choice of the value of X in the definition of R_χ is arbitrary. To optimize the choice of X, the following study was performed. The percentage change in the largest mass bin between NLO QCD and NLO QCD with a contact term of $\Lambda_{LL}^{+}=2.0$ TeV was measured as a function of the definition of R_χ. The change due to compositeness increases as one chooses smaller values of X. However, the measurement error also increases for smaller values of X. Only the statistical error was used to optimize the choice of X so as not to bias the optimization with the data. The ratio of percentage change to percentage statistical error peaks at $X=4$; hence we chose $R_\chi=N(\chi<4)/N(4<\chi<\chi_{\max})$.

To determine the errors on R_χ, the nominal value was compared to the value after each systematic uncertainty was varied within error. Table XXXVI shows the size of the systematic uncertainties for the smallest and largest mass ranges.

Table XXXVII shows the experimental ratio R_χ for the different mass ranges with their statistical and their system-

TABLE XXXV. Dijet angular cross section $(100/N)(\mathrm{d}N/\mathrm{d}\chi)\pm$ statistical $\pm$ systematic uncertainties for the four mass bins (GeV/c^2).

χ	$260<M<425$			$425<M<475$			$475<M<635$			$M>635$		
	value±	stat.±	syst.	value±	stat.±	syst.	value±	stat.±	syst.	value±	stat.±	syst.
1.5	5.95 ±	0.35 ±	0.58	7.58 ±	0.66 ±	2.08	10.08 ±	0.33 ±	0.63	11.98 ±	0.99 ±	0.49
2.5	5.50 ±	0.33 ±	0.54	4.26 ±	0.50 ±	0.75	7.56 ±	0.28 ±	0.36	12.49 ±	1.01 ±	0.78
3.5	4.59 ±	0.30 ±	0.31	4.96 ±	0.53 ±	0.67	7.83 ±	0.29 ±	0.33	9.11 ±	0.86 ±	0.61
4.5	4.57 ±	0.30 ±	0.28	5.54 ±	0.56 ±	1.04	7.71 ±	0.28 ±	0.25	9.79 ±	0.89 ±	0.23
5.5	4.56 ±	0.30 ±	0.25	5.29 ±	0.55 ±	0.86	7.87 ±	0.29 ±	0.17	10.06 ±	0.91 ±	0.26
6.5	5.10 ±	0.32 ±	0.23	6.26 ±	0.60 ±	0.73	8.17 ±	0.29 ±	0.16	9.58 ±	0.88 ±	0.51
7.5	5.10 ±	0.32 ±	0.19	4.83 ±	0.53 ±	0.33	8.70 ±	0.30 ±	0.20	9.30 ±	0.87 ±	0.57
8.5	5.61 ±	0.34 ±	0.15	4.40 ±	0.50 ±	0.16	7.91 ±	0.29 ±	0.21	8.08 ±	0.81 ±	0.42
9.5	4.93 ±	0.32 ±	0.09	5.60 ±	0.57 ±	0.25	8.46 ±	0.30 ±	0.24	8.96 ±	0.85 ±	0.30
10.5	6.04 ±	0.35 ±	0.06	5.22 ±	0.55 ±	0.37	8.62 ±	0.30 ±	0.27	10.65 ±	0.93 ±	0.41
11.5	5.40 ±	0.33 ±	0.04	4.30 ±	0.50 ±	0.40	8.38 ±	0.30 ±	0.29			
12.5	5.33 ±	0.33 ±	0.08	4.75 ±	0.52 ±	0.52	8.69 ±	0.30 ±	0.36			
13.5	5.41 ±	0.33 ±	0.14	5.43 ±	0.56 ±	0.65						
14.5	5.40 ±	0.33 ±	0.20	5.69 ±	0.57 ±	0.70						
15.5	5.60 ±	0.34 ±	0.28	6.18 ±	0.60 ±	0.76						
16.5	4.81 ±	0.31 ±	0.30	4.70 ±	0.52 ±	0.57						
17.5	4.95 ±	0.32 ±	0.38	4.83 ±	0.53 ±	0.56						
18.5	5.78 ±	0.34 ±	0.53	5.01 ±	0.54 ±	0.55						
19.5	5.37 ±	0.33 ±	0.57	5.17 ±	0.55 ±	0.55						

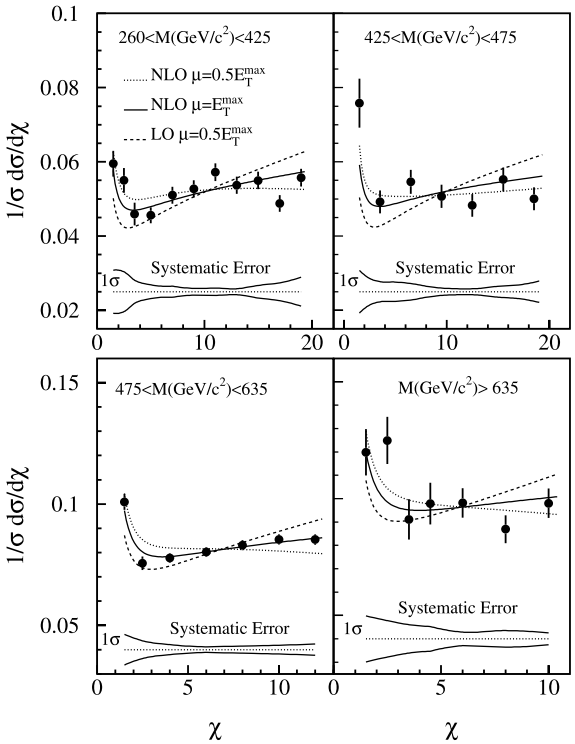

FIG. 73. Dijet angular distributions for DØ data (points) compared to JETRAD for LO (dashed line) and NLO predictions with renormalization-factorization scale $\mu=0.5E_T^{\max}$ (dotted line). The data are also compared to JETRAD NLO predictions with $\mu=E_T^{\max}$ (solid line). The errors on the data points are statistical only. The band at the bottom represents the $\pm 1\sigma$ systematic uncertainty.

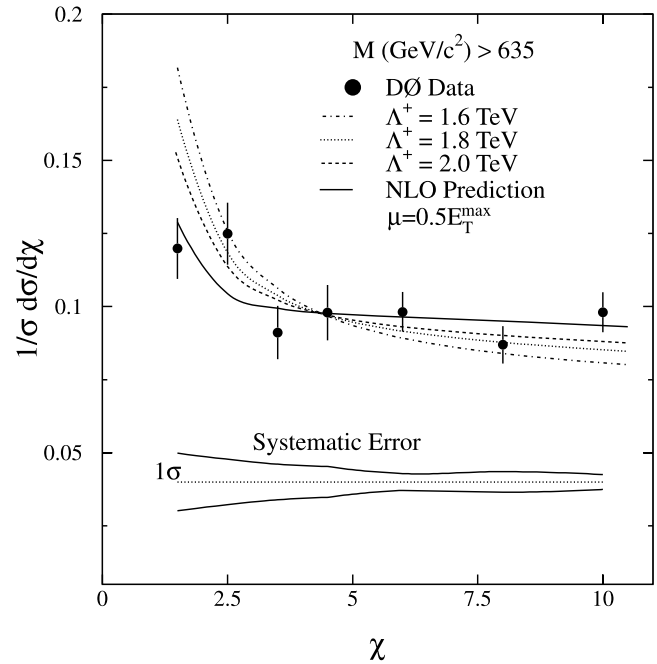

FIG. 74. Data compared to theory for different compositeness scales. See text for an explanation of the compositeness calculation. The errors on the points are statistical and the band represents the $\pm 1\sigma$ systematic uncertainty.

atic uncertainties, which are fully correlated in mass. Figure 75 shows R_χ as a function of M for two different renormalization scales, along with the theoretical predictions for different compositeness scales. The effects of compositeness should be greatest at the highest masses. Note that the two largest dijet invariant mass bins have a lower $\chi_{\max}$ value (Table XXXIV), and thus a higher value of R_χ is expected independent of compositeness assumptions. Also shown in Fig. 75 are the χ^2 values for the four degrees of freedom for different values of the compositeness scale.

The method chosen to obtain a compositeness limit uses Bayesian statistics [56]. The compositeness limit is determined using a Gaussian likelihood function for R_χ as a function of dijet mass. The likelihood function is defined as

$$L(\xi)=\frac{1}{|S|2\pi}\exp\left\{-\frac{1}{2}[d-f(\xi)]^T V^{-1}[d-f(\xi)]\right\}P(\xi) \tag{13.6}$$

where d is a 4 component vector of data points for the different mass bins, $f(\xi)$ is a 4 component vector of theory points for the different mass bins for different values of ξ where ξ is related to Λ (see below), V^{-1} is the inverse of the covariance matrix, and $P(\xi)$ is the prior probability distribution, $P(\xi)$. The covariance matrix is defined so that the element i,j of the covariance matrix, V_{ij}, is

$$V_{ij}=\Delta\sigma_i\Delta\sigma_j, \tag{13.7}$$

where $\Delta\sigma$ is the sum of the systematic and statistical uncertainties added in quadrature if $i=j$, and the systematic uncertainty only if $i\neq j$. The systematic uncertainties are assumed to be 100% correlated as a function of mass.

The compositeness limit depends on the choice of the prior probability distribution, $P(\xi)$. Motivated by the form of the Lagrangian, $P(\xi)$ is assumed to be flat in $\xi=1/\Lambda^2$. Since the dijet angular distribution at NLO is sensitive to the renormalization scale, each renormalization scale is treated as a different theory. To determine the 95% confidence level (C.L.) limit in Λ, a limit in ξ is first calculated by requiring that $Q(\xi)=\int_0^\xi L(R_\chi|\xi')d\xi'=0.95Q(\infty)$. The limit in ξ is then transformed into a limit in Λ. Table XXXVIII shows the 95% C.L. limit for the compositeness scale obtained for different choices of models. These results supersede those reported in [23] following the correction of an error in the

TABLE XXXVI. The systematic uncertainties on the measurement of R_χ for the smallest and largest mass ranges.

	Mass range	
	260–425 GeV/c^2	>635 GeV/c^2
Misvertexing	0.24	0.001
MITOOL	0.0076	0.000
Jet quality cuts	0.002	0.010
η bias	0.007	0.009
Energy scale	0.01	0.023
Resolution	0.004	0.010

TABLE XXXVII. The dijet angular ratio R_χ and its statistical and systematic uncertainty. Also listed are the JETRAD predictions with $\mathcal{R}_{\rm sep}=1.3$, the CTEQ3M PDF, and $\mu=0.5E_T^{\rm max}$ and $E_T^{\rm max}$.

Mass range GeV/c^2	$R_\chi \pm$ Stat. $\pm$ Syst.	Theory $\mu=0.5E_T^{\rm max}$	Theory $\mu=E_T^{\rm max}$
260–425	$0.191\pm0.0077\pm0.015$	0.198	0.180
425–475	$0.202\pm0.0136\pm0.010$	0.206	0.185
475–635	$0.342\pm0.0085\pm0.018$	0.342	0.344
>635	$0.506\pm0.0324\pm0.028$	0.506	0.458

program used to calculate the effects of compositeness in that paper. The resulting limits are reduced by approximately 150 GeV. If the prior distribution is assumed to be flat in $1/\Lambda^4$, the limits are slightly reduced, as shown in Table XXXIX.

Recently published results from CDF [19] on dijet angular distributions compare to the model in which all quarks are composite, yielding 95% confidence limits $\Lambda_{LL}^+>1.8$ TeV and $\Lambda_{LL}^->1.6$ TeV.

F. Coloron limits

Predictions of the dijet angular distribution with colorons are available at LO (Sec. IV C). To simulate NLO predictions, coloron LO predictions are generated for several values of $M_c/\cot\theta$. The fractional differences between the angular distribution with $M_c/\cot\theta=\infty$ and the distributions with finite values of $M_c/\cot\theta$ are measured. The coloron NLO predictions are then obtained by multiplying the NLO QCD prediction obtained using JETRAD by the LO fractional differences obtained above. The results are shown in Fig. 76.

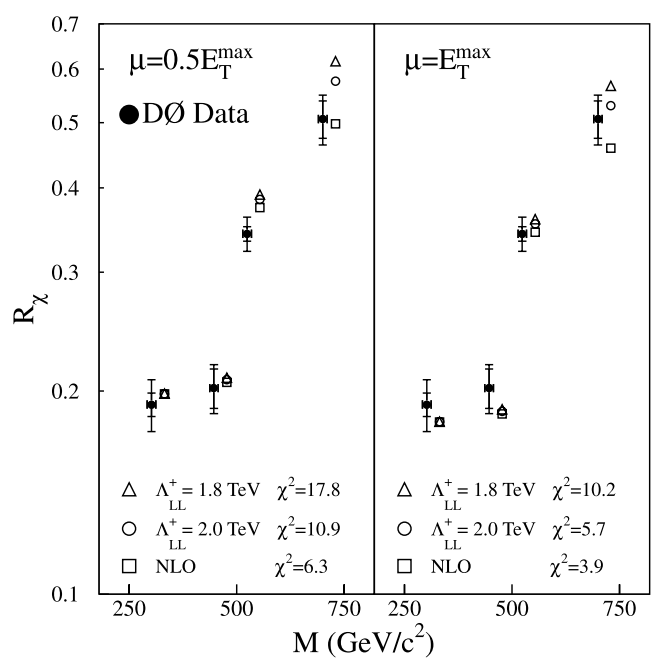

FIG. 75. R_χ as a function of dijet invariant mass for two different renormalization scales. The inner error bars are the statistical uncertainties and the outer error bars include the statistical and systematic uncertainties added in quadrature. The χ^2 values for the four degrees of freedom are shown for the different values of the compositeness scale. The data are plotted at the average mass for each mass range. The NLO points are offset in mass to allow the data points to be seen.

TABLE XXXVIII. The 95% confidence level limits for the left-handed contact compositeness scale for different models. The prior probability distribution is assumed to be flat in $1/\Lambda^2$.

Compositeness scale	$\mu=E_T^{\rm max}$	$\mu=0.5E_T^{\rm max}$
Λ_{LL}^+	2.0 TeV	2.1 TeV
Λ_{LL}^-	2.0 TeV	2.2 TeV
$\Lambda_{LL(ud)}^+$	1.8 TeV	1.8 TeV
$\Lambda_{LL(ud)}^-$	1.8 TeV	2.0 TeV

Limits on the coloron mass are calculated using the same method as in the previous section. For a renormalization scale of $\mu=E_T^{\rm max}$, the 95% C.L. limit on the coloron mass is $M_c/\cot\theta>759$ GeV/c^2. If $\mu=0.5E_T^{\rm max}$, the 95% C.L. limit is $M_c/\cot\theta>786$ GeV/c^2. The resulting limits are shown in Fig. 77. The shaded region shows the 95% C.L. exclusion region for the DØ dijet angular distribution measurement ($M_c/\cot\theta>759$ GeV/c^2). The horizontally-hatched region at large $\cot\theta$ is excluded by the model [38,40]. The diagonally-hatched region is excluded by the value of the weak-interaction ρ parameter ($M_c/\cot\theta>450$ GeV/c^2) [40]. The cross-hatched region is excluded by the CDF search for new particles decaying to dijets [41]. These limits are then converted into more general limits on color-octet vector current-current interactions: $\Lambda_{V_8}^->2.1$ TeV assuming $\alpha_S(M_Z)=0.12$ (Sec. IV B).

G. Conclusions

We have measured the dijet angular distribution over a large angular range. The data distributions are in good agreement with NLO QCD predictions. The compositeness limits depend on the choice of the renormalization-factorization scale, the model of compositeness, and the choice of the prior probability function. Models of quark compositeness with a contact interaction scale of less than 2 TeV are ruled out at the 95% C.L.

XIV. THE INCLUSIVE DIJET MASS SPECTRUM

The dijet mass spectrum is calculated using the relation

$$\kappa\equiv\frac{d^3\sigma}{dM\,d\eta_1\,d\eta_2}=\frac{N_iC_i}{\mathcal{L}_i\epsilon_i\Delta M\Delta\eta_1\Delta\eta_2}, \qquad (14.1)$$

TABLE XXXIX. The 95% confidence level limits for the left-handed contact compositeness scale for different models. The prior probability distribution is assumed to be flat in $1/\Lambda^4$.

Compositeness scale	$\mu=E_T^{\rm max}$	$\mu=0.5E_T^{\rm max}$
Λ_{LL}^+	2.0 TeV	2.0 TeV
Λ_{LL}^-	1.9 TeV	2.1 TeV
$\Lambda_{LL(ud)}^+$	1.7 TeV	1.7 TeV
$\Lambda_{LL(ud)}^-$	1.7 TeV	1.9 TeV

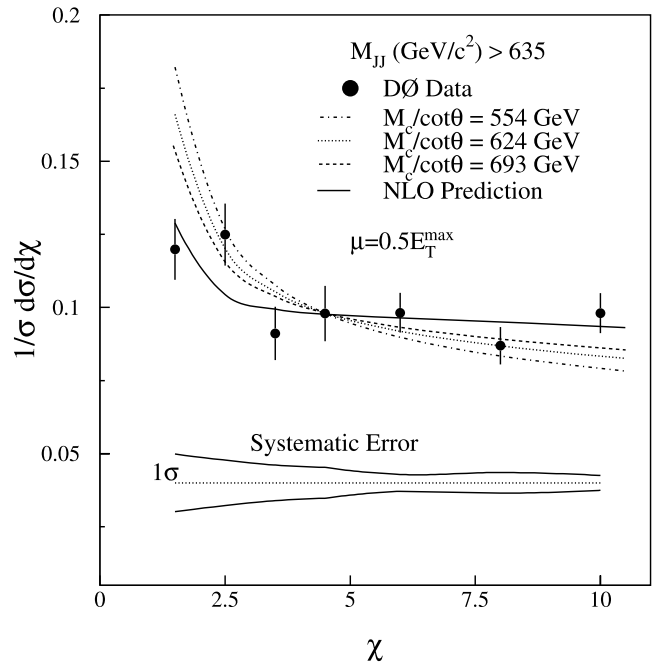

FIG. 76. DØ data compared to theory for different values of $M_c/\cot\theta$ (see text for details of the coloron distribution calculation). The errors on the points are statistical and the band represents the correlated $\pm 1\sigma$ systematic uncertainty.

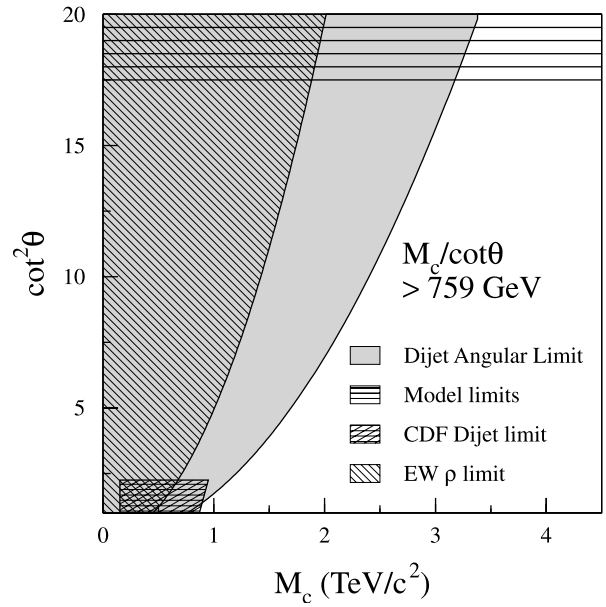

FIG. 77. Limits on the coloron parameter space: coloron mass M_c vs mixing parameter cot θ.

where N_i is the number of events in mass bin i, C_i is the unsmearing correction, $\mathcal{L}_i$ is the integrated luminosity, ϵ_i is the efficiency of the trigger, vertex selection, and the jet quality cuts, ΔM is the width of the mass bin, and $\Delta\eta_{1,2}$ are the widths of the pseudorapidity bins for jets 1 and 2. The dijet mass is calculated assuming massless jets using Eq. (13.2). If we define the mass using four vectors, $m^2=(E_1+E_2)^2-(\vec{p}_1+\vec{p}_2)^2$, the cross section changes by less than 2%.

A. Data selection

The selected data are events with two or more jets which satisfy the set of inclusive jet triggers and pass the standard jet and event quality requirements (see Sec. VIII). Events are removed unless both of the two leading jets pass the jet quality requirements. The vertex of the event must be within 50 cm of $z=0$. The efficiency for each event is then given by the product of the efficiencies ($\epsilon_{\text{jet}i}$) of the jet quality cuts, the efficiency (ϵ_{met}) of the cut on $\not{E}_T$, the efficiency ($\epsilon_{\text{trigger}}$) for an event to pass the trigger, and the efficiency (ϵ_{vertex}) for passing the vertex cut. The reciprocal of the resulting efficiencies (the event weights) is plotted as a function of M in Fig. 78. The efficiency of the vertex requirement is 90 $\pm 1\%$. The data are used to select a sample where both jets have pseudorapidity $|\eta^{\text{jet}}|<1.0$. To examine the inclusive dijet cross section more closely, two sub-samples are created where both jets satisfy either $|\eta^{\text{jet}}|<0.5$ or $0.5<|\eta^{\text{jet}}|<1.0$.

To determine the mass at which a given trigger (Jet_XX) becomes fully efficient, the event efficiencies are plotted for each of the triggers in the chosen mass ranges (Table XL) in Figs. 79 and 80. This plot shows that the triggers are >95% efficient for most of the data.

The mass spectra obtained from the triggers Jet_30, Jet_50 and Jet_85 are then scaled to match the Jet_115 mass spectrum by the scale factor S_{Filt} which is given by

$$S_{\text{Filt}_i}=\left(\frac{\mathcal{L}_{\text{Filt}_i}}{\mathcal{L}_{\text{Jet_115}}}\right)\times\frac{1}{\epsilon_{\text{vertex}_i}}. \tag{14.2}$$

The values of S_{Filt} used to scale the data in this analysis are given in Table XL. These scales (and the event weights) are then applied to the data to produce the mass spectra (two such spectra are depicted in Fig. 81). The error plotted for each point is given by the statistical errors for that bin.

B. Vertex selection biases

The vertex selection procedure chooses the vertex with the smallest value of S_T (Sec. VII). This selection criterion may be biased for events where both of the two leading jets have the same absolute rapidity. In this case the vertex chosen would be the one that minimizes the E_{T} for both of the leading jets and not necessarily the correct one. This bias was studied using the PYTHIA [57] MC event generator to generate events with multiple vertices at the same rate as the Jet_85 and Jet_115 triggers. For dijet events with $|\eta^{\text{jet}}|<1.0$ the number of incorrectly chosen vertices is 5%.

The effect on the dijet mass cross section is measured by calculating the ratio of the mass spectrum produced using the selected vertex to that of the correct vertex. The result of this calculation is given in Fig. 82 for $|\eta^{\text{jet}}|<1.0$ and shows that the effect is of the order of 1% and that it is reasonably uniform as a function of mass. A 2% uncertainty in the cross section, uncorrelated as a function of mass, was assumed.

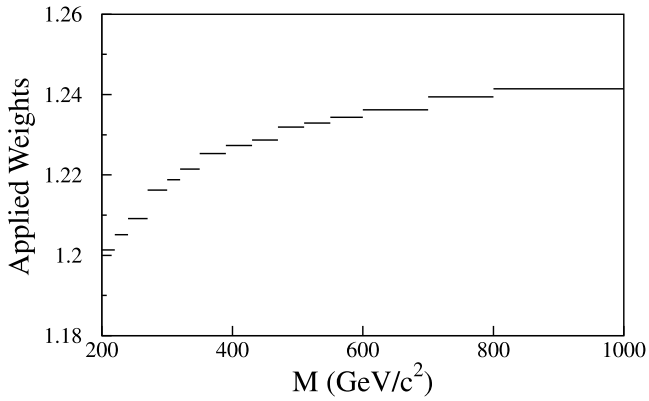

FIG. 78. The reciprocal of the event efficiencies ϵ_i for each mass bin.

C. Dijet mass resolution

The dijet mass resolutions were calculated using the measured single jet resolutions (Sec. X). The dijet mass resolutions depend on the E_T and η values of the two leading E_T jets in each event. Hence the mass resolutions are determined by using a Monte Carlo (MC) event generator to convolute the measured single jet resolutions (Table V). For each MC event generated, the individual particle jets are smeared by the measured single jet resolutions. The unsmeared and smeared dijet masses are calculated and used to determine the mass smearing. The values of the mass smearing are plotted in discrete mass bins and fitted to a Gaussian ansatz (see Fig. 83 for an example). The distribution is well-represented by a Gaussian with only a small fraction ($\ll$1%) of events forming a tail (due to events where the jets are reordered after smearing). The resolution at each of these masses is given by the width of the Gaussian. The results obtained for $|\eta^{\rm jet}|<1.0$ using the PYTHIA MC [57] are plotted in Fig. 84.

The mass resolutions are then fitted using the functional form:

TABLE XL. The mass ranges and scale factors for the triggers used in this analysis.

Data sets satisfying $\lvert\eta^{\rm jet}\rvert<1.0$, and $0.5<\lvert\eta^{\rm jet}\rvert<1.0$		
Trigger name	Mass range (GeV/c^2)	Scaling factor $S_{\rm Filt}$
Jet_30	200–270	289.3±14.4
Jet_50	270–350	21.7±1.1
Jet_85	350–550	1.845±0.005
Jet_115	550–1400	1.095±0.009
Data Set satisfying $\lvert\eta^{\rm jet}\rvert<0.5$		
Trigger name	Mass range (GeV/c^2)	Scaling factor $S_{\rm Filt}$
Jet_30	150–200	289.3±14.4
Jet_50	200–300	21.7±1.1
Jet_85	300–390	1.845±0.005
Jet_115	390–1400	1.095±0.009

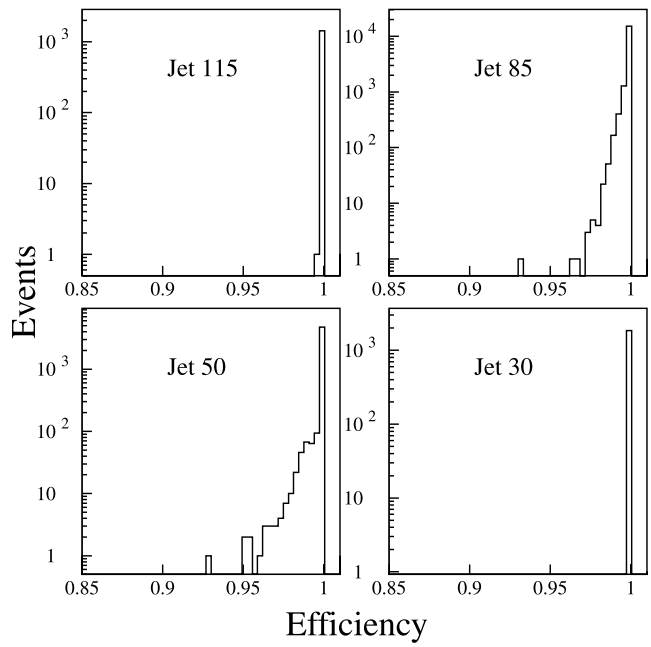

FIG. 79. The trigger efficiencies of the events included in the dijet mass spectrum. Note that most events have an efficiency greater than 99%.

$$\sigma(M)/M(\%)=\sqrt{A+BM+CM^2+DM^3}. \qquad (14.3)$$

The results are depicted in Fig. 84. The resulting fit parameters for all η regions considered in this analysis are given in Table XLI.

The mass resolution dependence on the MC generator used to convolute the single jet resolutions has been esti-

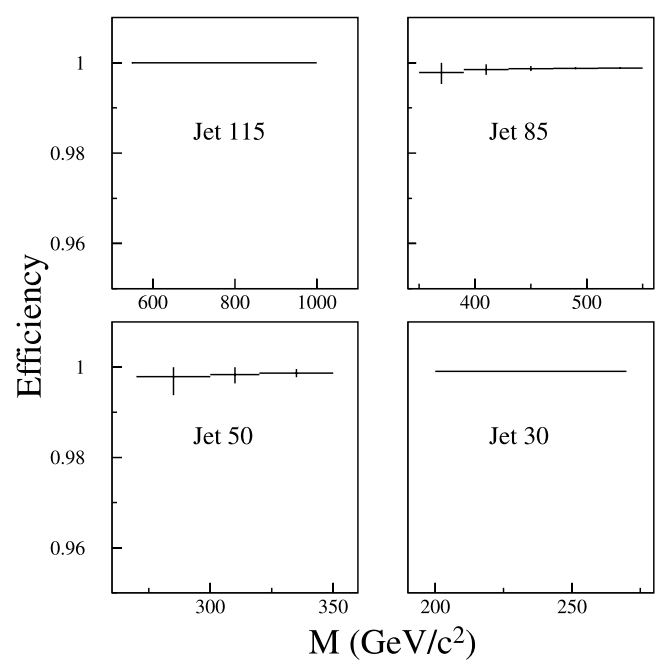

FIG. 80. The average trigger efficiencies for each trigger as a function of mass.

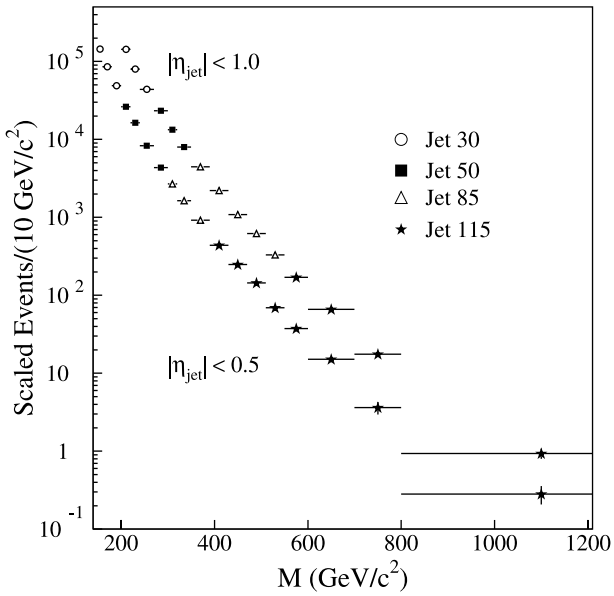

FIG. 81. The scaled dijet mass spectrum for $|\eta^{\rm jet}|<1.0$ and $|\eta^{\rm jet}|<0.5$.

mated by using the HERWIG [33] and JETRAD event generators. The JETRAD program is used at LO with renormalization scales of $\mu=(0.25,0.5,1.0)E_T^{\max}$ and $\mu=(0.25,0.5,1.0)\sqrt{\hat{s}}$ with CTEQ3M [35]. To ensure that the choice of PDF does not affect the resolutions, JETRAD was run with the CTEQ3L and MRS(A′) [36] PDFs. (See Fig. 85.)

D. Data unsmearing

The jet energy scale corrects only the average response to a jet. The steeply falling dijet mass spectrum is distorted by the jet energy resolution and, to a negligible extent, by the η resolution. The observed mass spectrum is corrected for resolution smearing by assuming a trial unsmeared spectrum

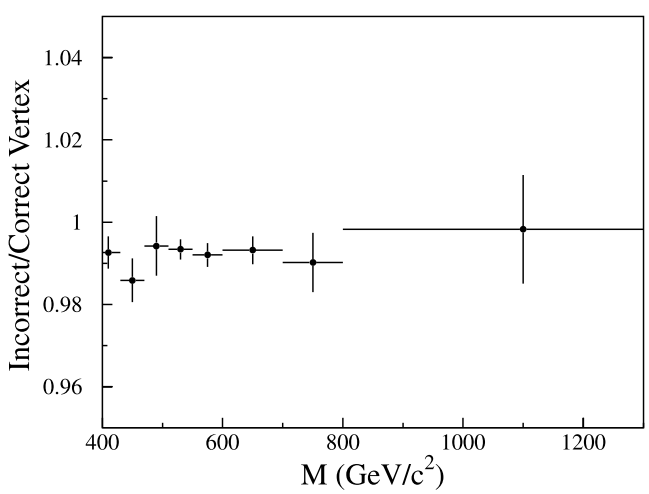

FIG. 82. The effect on the mass spectrum of incorrectly identified vertices for $|\eta^{\rm jet}|<1.0$.

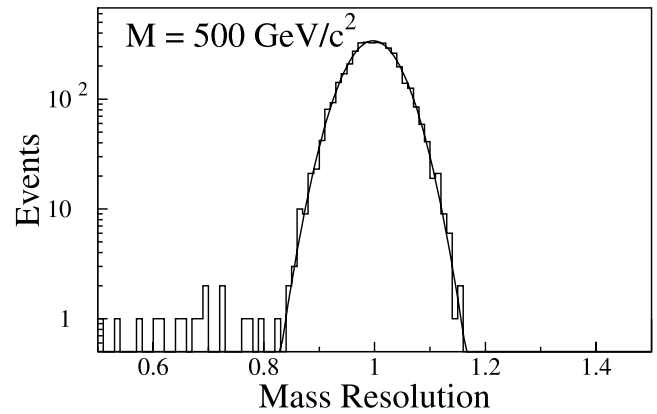

FIG. 83. The distribution of $M^{\rm smeared}/M^{\rm unsmeared}$ for PYTHIA-generated events with $|\eta^{\rm jet}|<1.0$ and $490<M^{\rm unsmeared}<510$ GeV/c^2.

$$F(M')=NM'^{-\alpha}\left(1-\frac{M'}{\sqrt{s}}\right)^{-\beta}, \tag{14.4}$$

which is convoluted with the measured mass resolutions

$$f(M)=\int F(M')\sigma(M'-M,M')dM', \tag{14.5}$$

such that the number of events in any mass bin i is given by integrating f over that bin. The data were fitted using a binned maximum likelihood method and the MINUIT package [58] to determine the values of N, α, and β. The smearing correction is given by

$$C_i=\frac{\int F(M)dM}{\int f\,dM}. \tag{14.6}$$

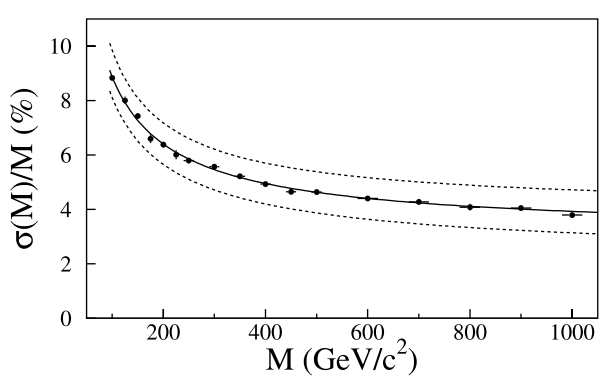

FIG. 84. The mass resolutions for $|\eta^{\rm jet}|<1.0$ generated using the PYTHIA MC. The solid curve and the MC data points show the resolutions determined using the nominal jet energy resolutions; the dashed lines show the resolutions determined with the $\pm 1\sigma$ jet energy resolution uncertainties.

TABLE XLI. Parametrizations of the mass resolutions (in percent) generated using the PYTHIA MC.

Data set	*A*	*B*	*C*	*D*
$\lvert\eta^{\rm jet}\rvert<1.0$	3.40 ± 1.01	0.761 ± 0.045	0.0302 ± 0.0032	0.0002 ± 0.0005
$\lvert\eta^{\rm jet}\rvert<0.5$	3.78 ± 0.94	0.701 ± 0.041	0.0231 ± 0.0025	0.0 ± 0.0003
$0.5<\lvert\eta^{\rm jet}\rvert<1.0$	5.24 ± 0.83	0.709 ± 0.058	0.0389 ± 0.0022	0.0 ± 0.0004

To account for any uncertainties in the choice of trial function the data are fitted with two additional functions:

$$F(M)=NM^{-\alpha}\left[1-\frac{M}{\sqrt{s}}+\gamma\left(\frac{M}{\sqrt{s}}\right)^2\right]^{-\beta}, \tag{14.7}$$

$$F(M)=NM^{-\alpha}\exp\left[-\beta\left(\frac{M}{100}\right)-\gamma\left(\frac{M}{100}\right)^2\right]. \tag{14.8}$$

The nominal smearing correction is given by the fit to the data using the trial function given in Eq. (14.4) and the obtained mass resolutions (Table XLI). The resulting fit for $\lvert\eta^{\rm jet}\rvert<1.0$ has a $\chi^2=10.3$ for 13 degrees of freedom and is given in Fig. 86. The magnitude of the correction is approximately 5% at 209 GeV/c^2 and drops to approximately 2% at 500 GeV/c^2, and then rises to 8% at 1 TeV/c^2. The uncertainty in the smearing correction is obtained by fitting the data with each of the trial functions and all of the mass resolutions generated with the different MC generators. The error is given by the maximum and minimum corrections obtained for each mass bin and is approximately 2%. The resulting smearing corrections are shown in Fig. 87.

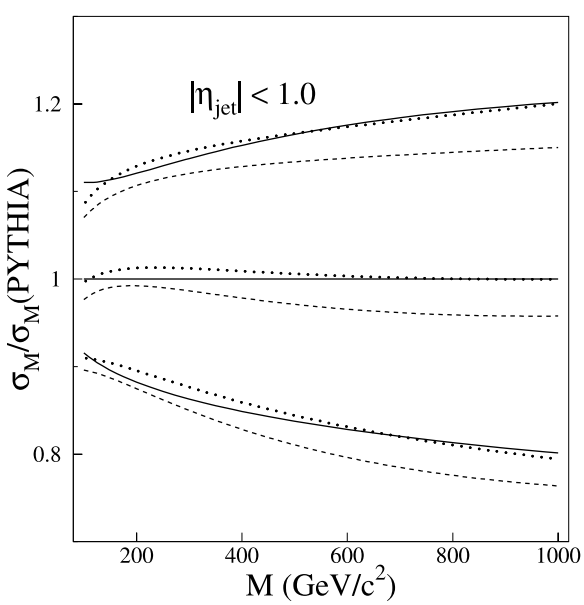

FIG. 85. A comparison of the mass resolutions for $\lvert\eta^{\rm jet}\rvert<1.0$ obtained by running PYTHIA (solid line), HERWIG (dashed line), and JETRAD (dotted line) with $\mu=0.5E_T^{\rm max}$ and the CTEQ3M PDF. The resolutions are divided by the nominal PYTHIA resolutions. The upper and lower curves show the effect of the $\pm1\sigma$ uncertainties on the measured jet resolutions.

E. Energy scale corrections

The uncertainties in the dijet mass cross section due to the energy scale have also been determined using a Monte Carlo program. The MC program generates two initial state partons each with a uniform distribution in x (the fraction of the proton momentum carried by the parton). The kinematic quantities of the two jets that result from this interaction are determined by generating a random value of χ from a uniform distribution. The jet $E_{\rm T}$ and η are uniquely determined for the event; it is assumed that the two jets are back-to-back in ϕ. The event is accepted if it satisfies the requirement $\lvert\eta^{\rm jet}\rvert<1.0$. Each event is weighted by $M^{-4.75}\times{\rm Pr}(x_1)\times{\rm Pr}(x_2)$ where ${\rm Pr}(x_{1,2})$ is the probability of finding a parton with momentum fraction x in the CTEQ4M PDF [14]. The exponent, -4.75, was chosen to obtain a dijet mass spectrum with similar normalization and shape as the data. Finally, each of the resulting jets has its $E_{\rm T}$ smeared by the measured single jet resolutions. Figure 88 shows a comparison of the mass spectrum produced by the Monte Carlo simulation and the data; the two are in reasonable agreement. The effect of changing the weight applied in the Monte Carlo simulation has been studied. If the weight is changed to $M^{-4.5}$ or $M^{-5.0}$ the resulting energy scale error changes by less than 1%.

The energy scale uncertainties are calculated by generating a sample of MC jet events (in which the jets are fully corrected) and applying the inverse of jet energy scale correction. This sample of uncorrected jets then have the nominal, high (nominal$+1\sigma$), and low (nominal-1σ) energy scale corrections applied. The error due to the energy scale is split into components: the uncorrelated error, the fully correlated error, a partially correlated error, and the error due to the showering correction. The resulting errors are plotted in Fig. 89 along with errors obtained from fitting the data with the high and low energy scale corrections applied. The errors obtained by the two methods are in agreement.

We calculated the correlation matrix for the partially correlated component of the energy scale uncertainty. The correlations have been calculated as a function of the jet energy (Sec. IX D); hence the relationship between the jet energy and the dijet mass spectrum needs to be determined. The correlation matrix for the dijet mass spectrum can be written as

$$\langle\delta\sigma_i\delta\sigma_j\rangle=\frac{\partial\sigma}{\partial M_i}\frac{\partial\sigma}{\partial M_j}\langle\delta M_i\delta M_j\rangle, \tag{14.9}$$

where δX represents the shift in variable X due to a systematic error parameter α; i and j denote mass bins and σ is the cross section. In the limit of massless jets, the dijet effective mass can be approximated by

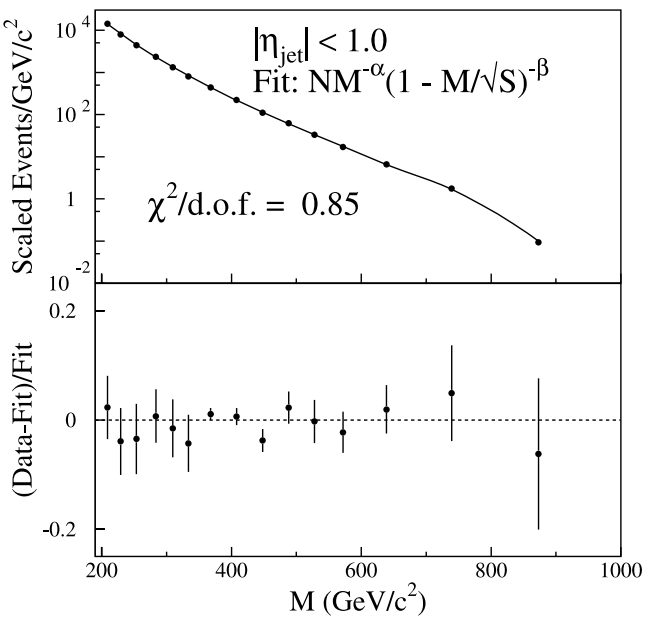

FIG. 86. Top: The fit to the data for $|\eta^{\rm jet}|<1.0$ using Eq. (14.4). Bottom: The residuals of the fit are plotted, (data – fit)/fit.

$$M_i=\sqrt{2E_{i1}E_{i2}(1-\cos\theta_{i12})} \tag{14.10}$$

where E_{i1} and E_{i2} are the energies, and θ_{i12} is the angle between the jets for event i. Hence

$$\delta M_i=\frac{\partial M_i}{\partial E_{i1}}\delta E_{i1}+\frac{\partial M_i}{\partial E_{i2}}\delta E_{i2}+\frac{\partial M_i}{\partial\cos\theta_{i12}}\delta\cos\theta_{i12}; \tag{14.11}$$

as we are only concerned with the energy scale, the angle error is ignored. Therefore

$$\frac{\partial M_i}{\partial E_{i1}}=\frac{E_{i2}}{M_i}(1-\cos\theta_{i12}), \tag{14.12}$$

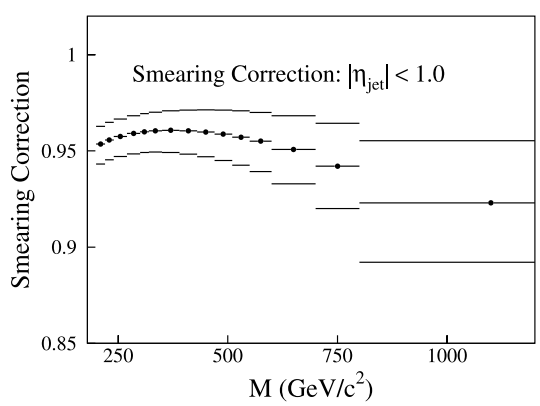

FIG. 87. The smearing correction factor to be applied to the data for $|\eta^{\rm jet}|<1.0$. The upper and lower curves represent the $\pm1\sigma$ uncertainties of the smearing correction.

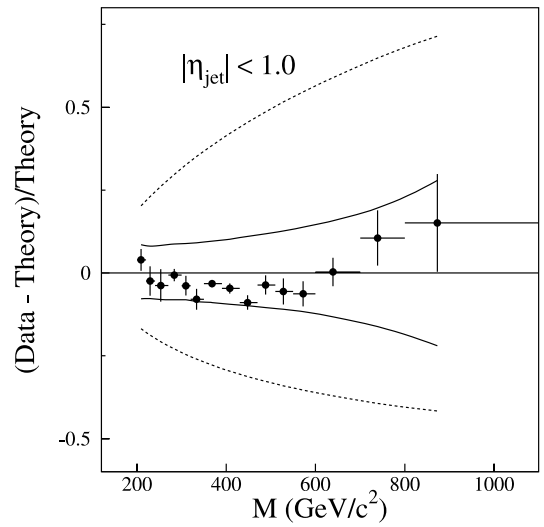

FIG. 88. A comparison of the data and the mass spectrum produced by the Monte Carlo simulations to study the energy scale uncertainties. The solid curves show the $\pm1\sigma$ energy scale uncertainties. The dashed curves show the MC predictions where the weights are set to $M^{-4.5}$ (upper) and $M^{-5.0}$ (lower).

$$\delta M_i=\frac{1}{M_i}(E_{i1}\delta E_{i2}+E_{i2}\delta E_{i1})(1-\cos\theta_{i12}) \tag{14.13}$$

and

$$\begin{aligned}\langle\delta M_i\delta M_j\rangle=&\frac{1}{M_iM_j}(1-\cos\theta_{i12})(1-\cos\theta_{j12})\\&\times(E_{i1}E_{j1}\langle\delta E_{i2}E_{j2}\rangle+E_{i2}E_{j1}\langle\delta E_{i1}E_{j2}\rangle\\&+E_{i1}E_{j2}\langle\delta E_{i2}E_{j1}\rangle+E_{i2}E_{j2}\langle\delta E_{i1}E_{j1}\rangle).\end{aligned} \tag{14.14}$$

Using this relationship, the correlations between jets due to the uncertainties in the jet energy scale can be translated into correlations between mass bins for the dijet mass cross section using the Monte Carlo program. The resulting correlations are plotted for a selection of mass bins in Fig. 90.

F. Summary of systematic uncertainties

In addition to the uncertainties in the luminosity, smearing correction, and the energy scale, there are uncertainties associated with the selection of the events that contribute to the data sample. These uncertainties are due to the jet quality cuts [see Eqs. (8.1), (8.2), (8.3), and (8.4)] as well as the procedure used to add hot cells back into jets (Sec. VIII A). These uncertainties contribute a 1% uncorrelated uncertainty to the cross section. In addition, the uncertainty due to the unsmearing is assumed to be fully correlated as a function of the dijet mass in each event.

A complete description of the systematic uncertainties in the dijet mass cross section is given in Table XLII. The total systematic error in each mass bin is given by the sum in quadrature of these errors. The uncertainties are combined

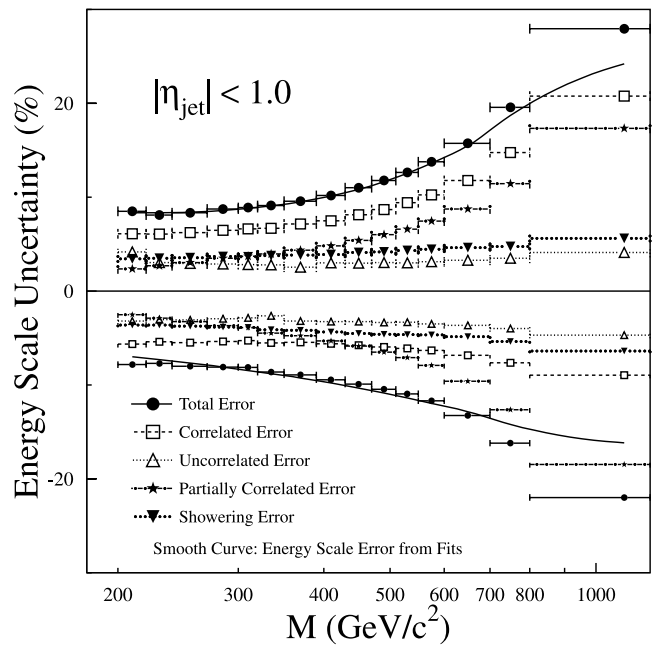

FIG. 89. The energy scale errors obtained from the Monte Carlo simulations. The full circles show the total energy scale uncertainties, the open squares show the correlated error, the open triangles show the uncorrelated error, and the stars show the partially correlated error. The curve shows the energy scale uncertainties obtained from fitting the data with the high and low energy scale corrections applied.

appropriately to obtain an overall correlation matrix for the bin-to-bin systematic uncertainties in the dijet mass spectrum.

G. Cross section

The dijet mass cross section is calculated using Eq. (14.1) for the pseudorapidity range $|\eta^{\rm jet}|<1.0$, in mass ranges starting at 200, 270, 350, and 550 GeV/c^2, corresponding to the jet $E_{\rm T}$ thresholds of 30, 50, 85, and 115 GeV.

The cross section for the mass spectrum is plotted in Fig. 91, and given in Table XLIII. The data are plotted at the mass-weighted average of the fit function for each bin ($\int MFdM/\int FdM$). The systematic uncertainties are dominated by the uncertainties in the jet energy scale, which are 7% (30%) for the 209 (873) GeV/c^2 mass bins. The bin-to-bin correlations of the uncertainties are shown in Fig. 92 and are given in Table XLIV [55].

The dijet mass cross section measurement was then repeated for $|\eta^{\rm jet}|<0.5$, and $0.5<|\eta^{\rm jet}|<1.0$. The resulting cross sections are given in Tables XLV and XLVI.

Most of the systematic uncertainties in the measurement of the inclusive dijet mass spectrum are highly correlated as a function of dijet mass and η and to a good approximation, cancel when a ratio of two cross sections is made. For this reason the cross section ratio for the rapidity ranges $|\eta^{\rm jet}|<0.5$ and $0.5<|\eta^{\rm jet}|<1.0$ will be calculated:

$$\frac{\kappa(|\eta^{\rm jet}|<0.5)}{\kappa(0.5<|\eta^{\rm jet}|<1.0)}. \qquad (14.15)$$

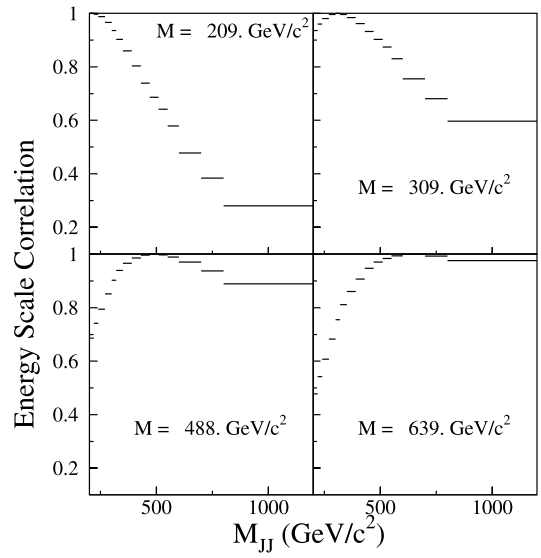

FIG. 90. The correlations between mass bins for $|\eta^{\rm jet}|<1.0$. The four plots show the mass correlations relative to four different mass bins: 200–220 GeV/c^2 (209 GeV/c^2 weighted average), 300–320 GeV/c^2 (309 GeV/c^2), 470–510 GeV/c^2 (488 GeV/c^2), and 600–700 GeV/c^2 (639 GeV/c^2).

The uncertainty in the theoretical prediction of this ratio due to the choice of PDF is less than 3%, and 6% from the choice of renormalization and factorization scale (excluding $\mu=0.25E_T^{\rm max}$). The luminosity matching error only contributes to those bins where the data from triggers Jet_30 and Jet_50 overlaps with the data from triggers Jet_85 and Jet_115 (i.e. for masses between 300 and 350 GeV/c^2). The errors from the vertex selection cancel when the data in a bin come from the same trigger for each of the cross sections. The errors due to the unsmearing and the (partially) correlated part of the energy scale are assumed to be correlated for

TABLE XLII. Common systematic errors on the cross section.

Source	Percentage error	Comment
Jet selection	1	Statistical Uncorrelated
Vertex selection	2	Systematic Uncorrelated
Luminosity scale	5.8	Systematic Fully correlated
Luminosity match Jet_30 Jet_50	4.9	Systematic Statistical Correlated for Jet_30 and 50
Unsmearing correction	0.5–3.0	Systematic Fully correlated
Energy scale	7.0–30.0	Systematic Mixture

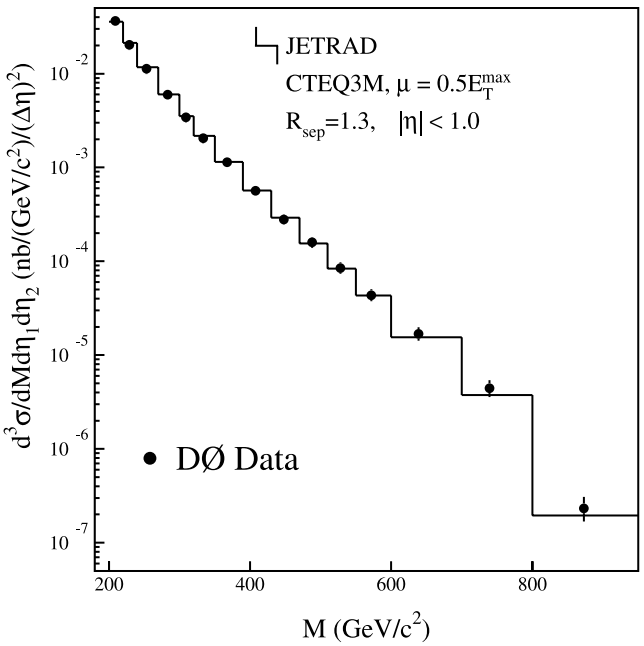

FIG. 91. Dijet mass cross section $d^3\sigma/dMd\eta_1d\eta_2$ for $|\eta^{\rm jet}|<1.0$. The DØ data are shown by the solid circles, with error bars representing the $\pm 1\sigma$ statistical and systematic uncertainties added in quadrature (in most cases smaller than the symbol). The histogram represents the JETRAD prediction.

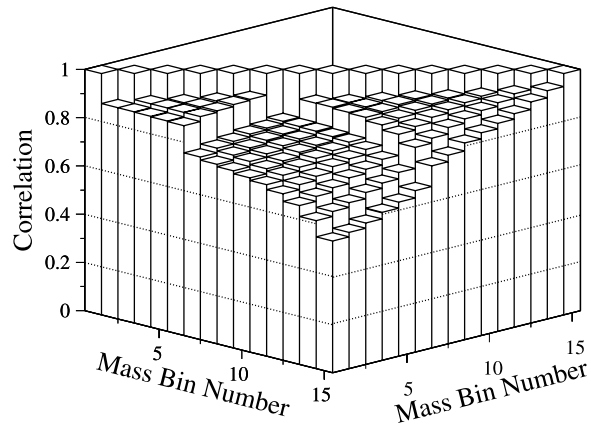

FIG. 92. The correlations between systematic uncertainties in bins of dijet mass (see Tables XLIII and XLIV) for $|\eta^{\rm jet}|<1.0$. The correlations are calculated using the average systematic uncertainty. The discontinuities arise from the uncorrelated errors (adjacent to correlations of 1.0) and to luminosity matching.

the two cross sections and mostly cancel out leaving small errors ($\ll 1\%$). In addition the uncertainty due to the hot cell restoration is assumed to be correlated between the two cross sections. All other errors are assumed to be uncorrelated between the two measurements. For the purposes of calculating a covariance matrix, the correlated energy scale and unsmearing errors are assumed to be fully correlated as a function of mass.

The resulting cross section ratios are given in Table XLVII and plotted in Fig. 93. Taking the ratio of the cross sections reduces the systematic uncertainties to less than 10%. The correlations of the systematic uncertainties are given in Table XLIV [55].

H. Comparison of data with theory

Figure 94 shows the ratio (data-theory)/theory for $|\eta^{\rm jet}|<1.0$ and the JETRAD prediction using CTEQ3M with $\mu=0.5E_T^{\max}$. The effect of varying the renormalization scale in the prediction is also shown; all are in good agreement ex-

TABLE XLIII. Dijet mass cross section for $|\eta^{\rm jet}|<1.0$. High (low) systematic uncertainties are the sum in quadrature of the uncertainties from the $\pm 1\sigma$ variations in the energy calibration, the unsmearing, the vertex corrections, luminosity matching, jet selection, and the uncertainty in the luminosity. Also included is the JETRAD prediction with $\mu=0.5E_T^{\max}$, $\mathcal{R}_{\rm sep}=1.3$, and the CTEQ3M PDF.

Mass bin (GeV/c^2)			N_i	Cross section	Systematic error		Theoretical
Min.	Max.	Weighted center		$\pm$ statistical error [nb/(GeV/c^2)/$(\Delta\eta)^2$]	Low (%)	High (%)	prediction [nb/(GeV/c^2)/$(\Delta\eta)^2$]
200	220	209.1	918	$(3.66\pm0.12)\times10^{-2}$	11.2	11.7	3.57×10^{-2}
220	240	229.2	507	$(2.03\pm0.09)\times10^{-2}$	11.1	11.4	2.12×10^{-2}
240	270	253.3	419	$(1.13\pm0.06)\times10^{-2}$	11.3	11.6	1.17×10^{-2}
270	300	283.4	2944	$(5.98\pm0.11)\times10^{-3}$	11.4	11.8	6.00×10^{-3}
300	320	309.3	1123	$(3.43\pm0.10)\times10^{-3}$	11.4	12.0	3.53×10^{-3}
320	350	333.6	1006	$(2.06\pm0.06)\times10^{-3}$	11.8	12.1	2.17×10^{-3}
350	390	367.6	8749	$(1.14\pm0.01)\times10^{-3}$	10.9	11.5	1.15×10^{-3}
390	430	407.8	4323	$(5.66\pm0.09)\times10^{-4}$	11.4	12.0	5.67×10^{-4}
430	470	447.9	2137	$(2.80\pm0.06)\times10^{-4}$	11.8	12.7	2.92×10^{-4}
470	510	488.0	1210	$(1.59\pm0.05)\times10^{-4}$	12.3	13.4	1.54×10^{-4}
510	550	528.0	646	$(8.47\pm0.33)\times10^{-5}$	12.7	14.2	8.36×10^{-5}
550	600	572.0	699	$(4.35\pm0.16)\times10^{-5}$	13.3	15.2	4.31×10^{-5}
600	700	638.9	542	$(1.68\pm0.07)\times10^{-5}$	14.8	17.1	1.55×10^{-5}
700	800	739.2	144	$(4.43\pm0.37)\times10^{-6}$	17.5	20.7	3.75×10^{-6}
800	1400	873.2	46	$(2.32\pm0.34)\times10^{-7}$	23.1	28.9	1.95×10^{-7}

TABLE XLIV. The systematic error correlations for the dijet cross section for $|\eta^{\rm jet}|<1.0$, and the ratio $\kappa(|\eta^{\rm jet}|<0.5)/\kappa(0.5<|\eta^{\rm jet}|<1.0)$. The correlation values above the diagonal are the correlations corresponding to the cross section and the correlations below the diagonal correspond to the ratio. In both cases the correlation matrices are symmetric.

	1	2	3	4	5	6	7	8	9	10	11	12	13	14	15	
	1.00	0.88	0.88	0.87	0.87	0.87	0.76	0.74	0.73	0.72	0.71	0.69	0.66	0.61	0.55	1
		1.00	0.89	0.89	0.89	0.89	0.78	0.77	0.76	0.74	0.73	0.71	0.68	0.63	0.56	2
1	1.00		1.00	0.90	0.90	0.90	0.79	0.78	0.77	0.76	0.75	0.73	0.70	0.65	0.59	3
2	0.58	1.00		1.00	0.90	0.91	0.80	0.79	0.79	0.78	0.77	0.75	0.72	0.68	0.61	4
3	0.61	0.60	1.00		1.00	0.91	0.81	0.80	0.80	0.79	0.78	0.77	0.74	0.70	0.64	5
4	0.61	0.59	0.63	1.00		1.00	0.82	0.82	0.81	0.81	0.80	0.79	0.76	0.73	0.67	6
5	0.52	0.51	0.54	0.54	1.00		1.00	0.89	0.90	0.89	0.89	0.87	0.85	0.81	0.76	7
6	0.56	0.54	0.57	0.58	0.87	1.00		1.00	0.90	0.90	0.89	0.88	0.87	0.84	0.78	8
7	0.60	0.58	0.62	0.63	0.54	0.58	1.00		1.00	0.91	0.91	0.90	0.89	0.86	0.82	9
8	0.60	0.58	0.61	0.62	0.53	0.57	0.63	1.00		1.00	0.91	0.91	0.90	0.88	0.84	10
9	0.59	0.58	0.61	0.62	0.53	0.57	0.62	0.63	1.00		1.00	0.92	0.91	0.90	0.86	11
10	0.58	0.57	0.60	0.61	0.53	0.56	0.61	0.62	0.62	1.00		1.00	0.92	0.91	0.89	12
11	0.59	0.58	0.61	0.63	0.53	0.58	0.62	0.63	0.63	0.62	1.00		1.00	0.93	0.92	13
12	0.60	0.58	0.62	0.63	0.54	0.58	0.63	0.62	0.62	0.61	0.63	1.00		1.00	0.95	14
13	0.58	0.56	0.59	0.61	0.53	0.56	0.61	0.60	0.60	0.59	0.61	0.62	1.00		1.00	15
14	0.53	0.52	0.55	0.57	0.50	0.53	0.56	0.56	0.56	0.55	0.57	0.58	0.58	1.00		
15	0.51	0.50	0.53	0.55	0.48	0.52	0.54	0.54	0.54	0.53	0.55	0.57	0.57	0.55	1.00	

cept for $\mu=0.25E_T^{\rm max}$ which lies approximately 30% below the data. Figure 95 shows (data-theory)/theory for JETRAD predictions with different choices of PDFs. Given the experimental and theoretical uncertainties, the predictions can be regarded as being in good agreement with the data. Figure 96 shows that the data and JETRAD predictions are in agreement for $|\eta^{\rm jet}|<0.5$ and $0.5<|\eta^{\rm jet}|<1.0$. The data are also in agreement, within the uncertainties, with the cross section measured by CDF [18].

A χ^2 can be calculated for each of the comparisons between the data (cross sections and ratio of cross sections) and the predictions. The χ^2 is given by

TABLE XLV. Dijet mass cross section for $|\eta^{\rm jet}|<0.5$. High (low) systematic uncertainties are the sum in quadrature of the uncertainties from the $\pm 1\sigma$ variations in the energy calibration, the unsmearing, the vertex corrections, luminosity matching, jet selection, and the uncertainty in the luminosity. Also included is the JETRAD prediction with $\mu=0.5E_T^{\rm max}$, $\mathcal{R}_{\rm sep}=1.3$, and the CTEQ3M PDF.

Mass bin (GeV/c^2)			N_i	Cross section	Systematic error		Theoretical
Min.	Max.	Weighted center		$\pm$ statistical error [nb/(GeV/c^2)/$(\Delta\eta)^2$]	Low (%)	High (%)	prediction [nb/(GeV/c^2)/$(\Delta\eta)^2$]
150	160	154.7	467	$(1.46\pm0.07)\times10^{-1}$	10.8	11.0	1.46×10^{-1}
160	180	168.9	552	$(8.69\pm0.37)\times10^{-2}$	10.5	10.5	9.03×10^{-2}
180	200	189.0	315	$(4.99\pm0.28)\times10^{-2}$	10.5	10.9	4.91×10^{-2}
200	220	209.1	2243	$(2.69\pm0.06)\times10^{-2}$	10.3	10.5	2.81×10^{-2}
220	240	229.2	1390	$(1.67\pm0.04)\times10^{-2}$	10.2	10.7	1.68×10^{-2}
240	270	253.3	1055	$(8.52\pm0.26)\times10^{-3}$	10.5	10.5	9.35×10^{-3}
270	300	283.4	550	$(4.47\pm0.19)\times10^{-3}$	10.7	10.8	4.82×10^{-3}
300	320	309.3	2671	$(2.78\pm0.05)\times10^{-3}$	9.1	10.0	2.86×10^{-3}
320	350	333.6	2434	$(1.69\pm0.03)\times10^{-3}$	9.9	9.9	1.78×10^{-3}
350	390	367.7	1823	$(9.50\pm0.22)\times10^{-4}$	9.9	10.3	9.49×10^{-4}
390	430	407.8	1459	$(4.52\pm0.12)\times10^{-4}$	10.3	10.8	4.78×10^{-4}
430	470	448.0	831	$(2.58\pm0.09)\times10^{-4}$	10.7	11.4	2.50×10^{-4}
470	510	488.0	480	$(1.49\pm0.07)\times10^{-4}$	11.1	12.1	1.35×10^{-4}
510	550	528.1	231	$(7.17\pm0.47)\times10^{-5}$	11.7	12.8	7.43×10^{-5}
550	600	572.2	156	$(3.87\pm0.31)\times10^{-5}$	12.4	13.7	3.91×10^{-5}
600	700	639.4	125	$(1.55\pm0.14)\times10^{-5}$	13.8	15.5	1.46×10^{-5}
700	800	739.8	30	$(3.71\pm0.68)\times10^{-6}$	16.5	19.3	3.72×10^{-6}
800	1400	878.1	14	$(2.86\pm0.77)\times10^{-7}$	22.0	27.8	2.08×10^{-7}

TABLE XLVI. Dijet mass cross section for $0.5<|\eta^{\rm jet}|<1.0$. High (low) systematic uncertainties are the sum in quadrature of the uncertainties from the $\pm 1\sigma$ variations in the energy calibration, the unsmearing, the vertex corrections, luminosity matching, jet selection, and the uncertainty in the luminosity. Also included is the JETRAD prediction with $\mu=0.5E_T^{\rm max}$, $\mathcal{R}_{\rm sep}=1.3$, and the CTEQ3M PDF.

Mass bin (GeV/c^2)			N_i	Cross section	Systematic error		Theoretical
Min.	Max.	Weighted center		$\pm$ statistical error [nb/(GeV/c^2)/$(\Delta\eta)^2$]	Low (%)	High (%)	prediction [nb/(GeV/c^2)/$(\Delta\eta)^2$]
200	220	209.1	275	$(4.39\pm0.26)\times10^{-2}$	12.3	12.7	4.56×10^{-2}
220	240	229.1	170	$(2.73\pm0.21)\times10^{-2}$	11.7	12.1	2.70×10^{-2}
240	270	253.2	139	$(1.49\pm0.13)\times10^{-2}$	12.0	12.4	1.49×10^{-2}
270	300	283.4	964	$(7.87\pm0.25)\times10^{-3}$	11.9	12.7	7.60×10^{-3}
300	320	309.3	371	$(4.55\pm0.24)\times10^{-3}$	12.1	12.3	4.46×10^{-3}
320	350	333.6	292	$(2.40\pm0.14)\times10^{-3}$	12.5	13.0	2.75×10^{-3}
350	390	367.6	2682	$(1.41\pm0.03)\times10^{-3}$	11.6	12.4	1.44×10^{-3}
390	430	407.8	1445	$(7.62\pm0.20)\times10^{-4}$	12.0	13.0	7.16×10^{-4}
430	470	447.9	689	$(3.64\pm0.14)\times10^{-4}$	12.6	13.6	3.70×10^{-4}
470	510	488.0	408	$(2.16\pm0.11)\times10^{-4}$	13.1	14.1	1.97×10^{-4}
510	550	528.1	219	$(1.16\pm0.08)\times10^{-4}$	13.4	15.0	1.07×10^{-4}
550	600	572.2	244	$(6.11\pm0.39)\times10^{-5}$	13.6	16.0	5.59×10^{-5}
600	700	639.4	192	$(2.40\pm0.17)\times10^{-5}$	14.7	17.5	2.05×10^{-5}
700	800	739.8	49	$(6.10\pm0.87)\times10^{-6}$	17.1	20.4	5.19×10^{-6}
800	1400	878.8	20	$(4.06\pm0.91)\times10^{-7}$	22.4	28.0	2.92×10^{-7}

$$\chi^2=\sum_{i,j}\ \delta_i V_{ij}^{-1}\delta_j\,, \tag{14.16}$$

where δ_i is the difference between the data and theory for mass bin i, and V_{ij} is element i,j of the covariance matrix:

$$V_{ij}=\rho_{ij}\Delta\sigma_i\Delta\sigma_j\,, \tag{14.17}$$

where $\Delta\sigma$ is the sum of the systematic error and the statistical error added in quadrature if $i=j$ and the systematic error if $i\neq j$, and ρ_{ij} is the correlation between the systematic uncertainties of mass bins i and j as given in Table XLIV. The systematic uncertainty is given by the fractional uncertainty times the theoretical prediction. The resulting χ^2 values are given in Table XLVIII for all of the theoretical choices described above. The choice of PDF and renormalization scale is varied; all choices are in good agreement with the data, except for $\mu=0.25E_T^{\rm max}$ which is excluded by the data.

I. Compositeness limits

The ratio of the mass spectra can be used to place limits on quark compositeness (Sec. IV B). Currently there are no NLO compositeness calculations available; therefore a LO event generator (PYTHIA) is used to simulate the effect of compositeness. The ratio of these LO predictions with compositeness, to the LO with no compositeness, is used to scale the JETRAD NLO prediction, shown in Fig. 97.

The data show no evidence of compositeness and are used to set 95% confidence level limits on $\Lambda_{LL}^{\pm}$. This was done using the same method that was used to extract compositeness limits from the dijet angular distribution (Sec. XIII E). Figure 98 shows the probability distribution for a theoretical prediction obtained using JETRAD with the CTEQ3M PDF and a renormalization scale of $\mu=E_T^{\rm max}$. The 95% C.L. limit on the compositeness scale is $\Lambda_{LL}^{+}>2.7$ TeV. Limits were

TABLE XLVII. The ratio $\kappa(|\eta^{\rm jet}|<0.5)/\kappa(0.5<|\eta^{\rm jet}|<1.0)$. The systematic uncertainties are the sum in quadrature of the uncertainties from the $\pm 1\sigma$ variations in the energy calibration, the unsmearing, the vertex corrections, luminosity matching, jet selection, and the uncertainty in the luminosity. Also shown is the JETRAD prediction with $\mu=0.5E_T^{\rm max}$, $\mathcal{R}_{\rm sep}=1.3$, and the CTEQ3M PDF.

Mass bin (GeV/c^2)		Ratio of mass spectra $\kappa(\|\eta^{\rm jet}\|<0.5)/\kappa(0.5<\|\eta^{\rm jet}\|<1.0)$	Theoretical
Min.	Max.	($\pm$ stat. error $\pm$ syst. error)	prediction
200	220	$0.613\pm0.039\pm0.037$	0.616
220	240	$0.614\pm0.050\pm0.030$	0.621
240	270	$0.570\pm0.051\pm0.029$	0.627
270	300	$0.568\pm0.030\pm0.027$	0.635
300	320	$0.610\pm0.034\pm0.050$	0.642
320	350	$0.705\pm0.044\pm0.058$	0.648
350	390	$0.672\pm0.020\pm0.032$	0.657
390	430	$0.593\pm0.022\pm0.030$	0.667
430	470	$0.708\pm0.036\pm0.037$	0.676
470	510	$0.690\pm0.046\pm0.036$	0.685
510	550	$0.620\pm0.058\pm0.033$	0.693
550	600	$0.634\pm0.065\pm0.033$	0.701
600	700	$0.647\pm0.074\pm0.034$	0.710
700	800	$0.608\pm0.141\pm0.035$	0.718
800	1400	$0.705\pm0.246\pm0.046$	0.711

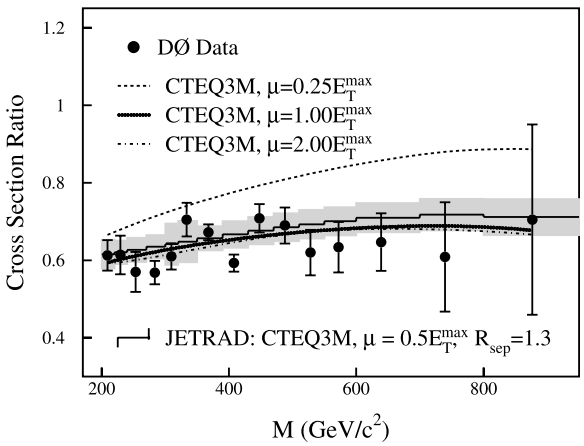

FIG. 93. The ratio of cross sections for $|\eta^{\rm jet}|<0.5$ and $0.5<|\eta^{\rm jet}|<1.0$ for data (solid circles) and theory (various lines). The error bars show the statistical uncertainties. The shaded region represents the $\pm 1\sigma$ systematic uncertainties about the prediction. The effects on the prediction of changing the renormalization scale are also shown.

also set for several different theoretical choices of PDF and renormalization scales for both the NLO JETRAD and LO compositeness predictions. The limits on the compositeness scale are summarized in Table XLIX. The dijet mass spectrum rules out quark compositeness models at the 95% confidence level where Λ_{LL}^{+} is below 2.7 TeV and Λ_{LL}^{-} is below 2.4 TeV.

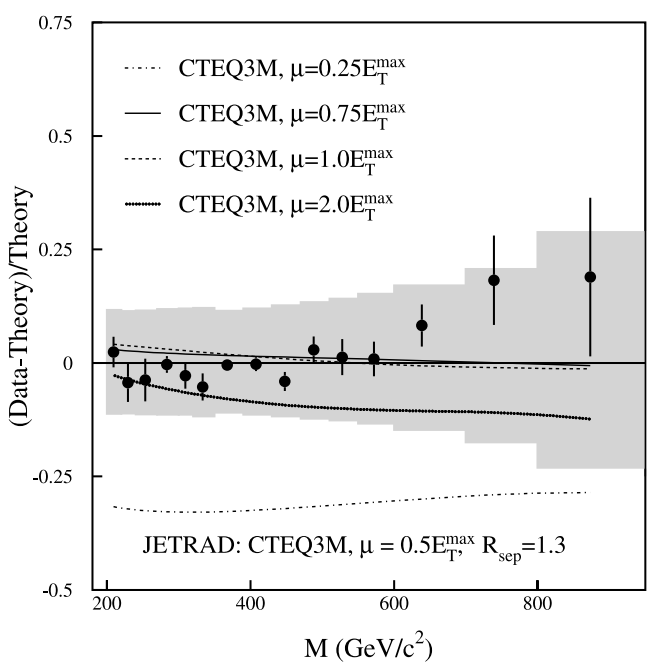

FIG. 94. The difference between the data and the prediction (JETRAD) divided by the prediction for $|\eta^{\rm jet}|<1.0$. The solid circles represent the comparison to the calculation using CTEQ3M with $\mu=0.5E_T^{\rm max}$. The shaded region represents the $\pm 1\sigma$ systematic uncertainties about the prediction. The effects of changing the renormalization scale are also shown (each curve shows the difference between the alternative prediction and the prediction using CTEQ3M with $\mu=0.5E_T^{\rm max}$).

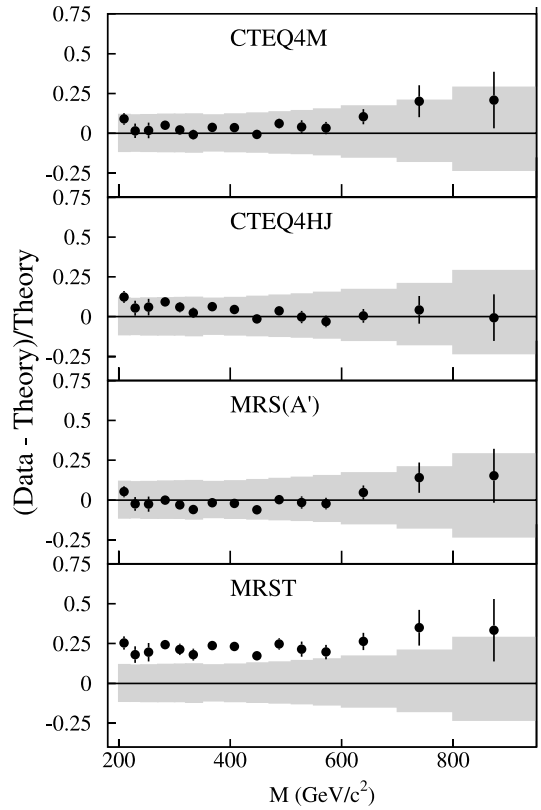

FIG. 95. The difference between the data and the prediction (JETRAD) divided by the prediction for $|\eta^{\rm jet}|<1.0$. The solid circles represent the comparison to the calculation using $\mu=0.5E_T^{\rm max}$ and the PDFs CTEQ4M, CTEQ4HJ, MRS(A′), and MRST. The shaded region represents the $\pm 1\sigma$ systematic uncertainties about the prediction.

Limits on models with color-singlet (octet) vector or axial contact interactions were also set using an analytic LO calculation [38] instead of the PYTHIA event generator. The resulting limits are given in Table L. The limits on the scale of $\Lambda_{V_8}^{-}$ can be converted into limits on a flavor-universal coloron [59], resulting in a 95% C.L. limit of $M_c/\cot\theta > 837$ GeV/c^2 (see Sec. IV C for a description of the theory).

The robustness of the confidence limits are tested in two ways. The first assumes that the systematic uncertainties are completely uncorrelated as a function of mass, which results in a degradation of the limit by 10 GeV (negligible compared to the scale of the limit). The second doubles the size of the systematic uncertainty, which results in a degradation of the limit by 20 GeV.

J. Conclusions

We have measured the inclusive dijet mass spectrum for a pseudorapidity range of $|\eta^{\rm jet}|<1.0$ and $200<M<1400$ GeV at $\sqrt{s}=1.8$ TeV to an accuracy of 10% to 30% as a function of mass. QCD NLO predictions, using several PDFs, show good agreement with the observed inclusive dijet mass spectrum.

The ratio of the inclusive dijet mass cross sections for $|\eta^{\rm jet}|<0.5$ and $0.5<|\eta^{\rm jet}|<1.0$ has also been measured with

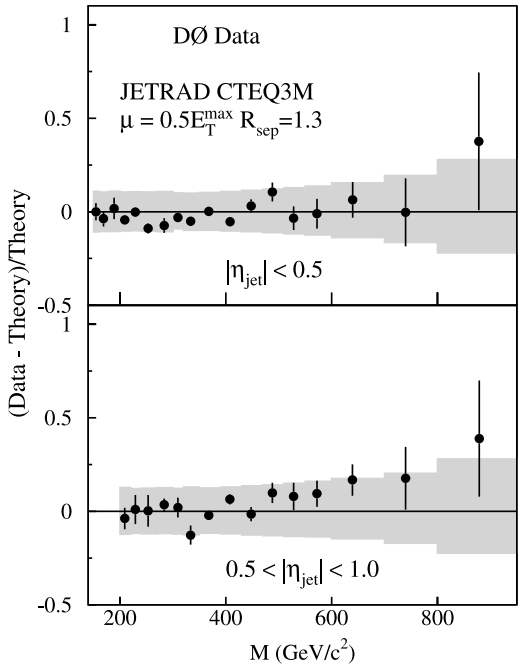

FIG. 96. The difference between the data and the prediction (JETRAD) divided by the prediction for $|\eta^{\rm jet}|<0.5$ and $0.5<|\eta^{\rm jet}|<1.0$. The solid circles represent the comparison to the calculation using CTEQ3M with $\mu=0.5E_T^{\rm max}$. The shaded region represents the $\pm 1\sigma$ systematic uncertainties about the prediction.

a systematic uncertainty that is less than 10%. The data distributions are in good agreement with NLO QCD predictions. Models of quark compositeness with a contact interaction scale of less than 2.2 TeV are excluded at the 95% confidence level.

XV. CONCLUSIONS

We have presented a series of measurements of high energy jets at the Fermilab Tevatron which are sensitive to the various components of QCD predictions: the parton distributions, the matrix elements, and the scales. Measurements of the cross section as a function of jet $E_{\rm T}$, and dijet invariant mass have been presented. By taking the ratio of the inclusive cross sections at two energies, both the experimental errors and the sensitivity to the parton distributions were reduced, providing a stringent test of the $E_{\rm T}$ dependence of the QCD matrix element at next-to-leading order. By looking at both the dijet angular distribution at fixed mass and the ratio of dijet invariant mass distributions in two different rapidity ranges, we have again minimized the experimental uncertainties and tested the angular dependence of the matrix element calculation.

We have made the most precise measurement to date of the inclusive jet cross section for $E_{\rm T}\geqslant 60$ GeV at $\sqrt{s}=1800$ GeV. No excess production of high-$E_{\rm T}$ jets is observed. QCD predictions are in good agreement with the observed cross section for standard parton distribution functions and different renormalization scales ($\mu=0.25-2.00E_{\rm T}$ where $E_{\rm T}=E_T^{\rm max}$ and $E_T^{\rm jet}$). We have also made the most precise measurement to date of the ratio of the inclusive jet cross sec-

TABLE XLVIII. The calculated χ^2 for $\kappa(|\eta^{\rm jet}|<1.0)$ (15 degrees of freedom), $\kappa(|\eta^{\rm jet}|<0.5)$ (18 DOF), and $\kappa(0.5<|\eta^{\rm jet}|<1.0)$ (15 DOF) and for the ratio $\kappa(|\eta^{\rm jet}|<0.5)/\kappa(0.5<|\eta^{\rm jet}|<1.0)$. The probability of obtaining a larger χ^2 is also given.

PDF	μ	$\kappa(\lvert\eta^{\rm jet}\rvert<1.0)$		$\kappa(\lvert\eta^{\rm jet}\rvert<0.5)$		$\kappa(0.5<\lvert\eta^{\rm jet}\rvert<1.0)$		Ratio	
		χ^2	Prob.	χ^2	Prob.	χ^2	Prob.	χ^2	Prob.
CTEQ3M	$0.25E_T^{\rm max}$	24.7	0.05	26.4	0.09	38.3	0.001	29.1	0.02
CTEQ3M	$0.50E_T^{\rm max}$	5.7	0.98	11.2	0.89	8.9	0.88	14.1	0.52
CTEQ3M	$0.75E_T^{\rm max}$	6.1	0.98	11.2	0.89	9.1	0.87	13.6	0.56
CTEQ3M	$1.00E_T^{\rm max}$	6.3	0.97	12.1	0.84	9.2	0.87	13.3	0.58
CTEQ3M	$2.00E_T^{\rm max}$	6.0	0.98	12.5	0.82	11.5	0.71	13.0	0.60
CTEQ3M	$0.25\sqrt{x_1x_2s}$	12.7	0.63	28.7	0.05	10.2	0.81	14.9	0.46
CTEQ3M	$0.50\sqrt{x_1x_2s}$	6.1	0.98	14.5	0.70	8.8	0.89	13.8	0.54
CTEQ3M	$1.00\sqrt{x_1x_2s}$	7.7	0.93	13.4	0.77	13.3	0.58	14.3	0.51
CTEQ4M	$0.50E_T^{\rm max}$	5.8	0.98	11.5	0.87	8.3	0.91	14.0	0.52
CTEQ4A1	$0.50E_T^{\rm max}$	5.8	0.98	13.1	0.79	8.1	0.92	14.1	0.52
CTEQ4A2	$0.50E_T^{\rm max}$	6.5	0.97	12.4	0.83	8.0	0.93	14.4	0.50
CTEQ4A4	$0.50E_T^{\rm max}$	5.8	0.98	11.7	0.86	8.5	0.90	14.5	0.49
CTEQ4A5	$0.50E_T^{\rm max}$	5.7	0.98	11.4	0.88	8.7	0.89	14.9	0.46
CTEQ4HJ	$0.50E_T^{\rm max}$	5.6	0.99	11.4	0.88	6.8	0.96	14.2	0.51
MRS(A′)	$0.50E_T^{\rm max}$	6.8	0.96	11.0	0.89	8.3	0.91	14.4	0.49
MRST	$0.50E_T^{\rm max}$	8.8	0.89	16.0	0.59	12.9	0.61	14.5	0.49
MRST($g\uparrow$)	$0.50E_T^{\rm max}$	8.4	0.91	16.7	0.54	10.2	0.81	14.2	0.51
MRST($g\downarrow$)	$0.50E_T^{\rm max}$	13.9	0.54	23.1	0.19	19.6	0.19	14.4	0.50

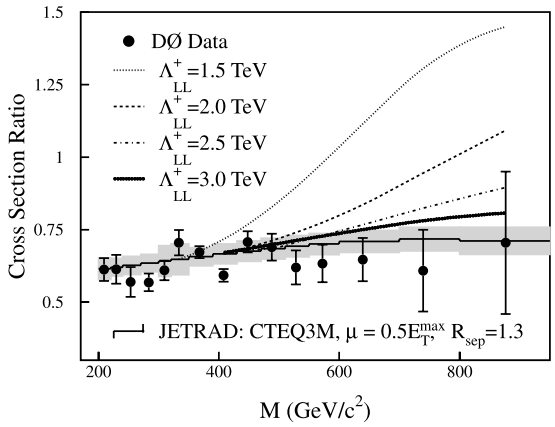

FIG. 97. The ratio of cross sections for $|\eta^{\rm jet}|<0.5$ and $0.5<|\eta^{\rm jet}|<1.0$ for data (solid circles) and theoretical predictions for compositeness models with various values of Λ^+_{LL} (various lines; see Sec. IV B for model details). The error bars show the statistical uncertainties. The shaded region represents the $\pm 1\sigma$ systematic uncertainties about the JETRAD prediction.

tions at $\sqrt{s}=630$ and 1800 GeV. The NLO QCD predictions yield satisfactory agreement with the observed data for standard choices of renormalization scale or PDF. In terms of the normalization however, the absolute values of the standard predictions lie consistently and significantly higher than the data.

We have measured the dijet angular distribution over a large angular range and the inclusive dijet mass spectrum for a pseudorapidity range of $|\eta^{\rm jet}|<1.0$. QCD NLO predictions, using several PDF's, show good agreement with the observed inclusive dijet mass spectrum. Since we found good agreement, the data have permitted us to provide sensitive limits on the existence of possible non-standard model phenomena.

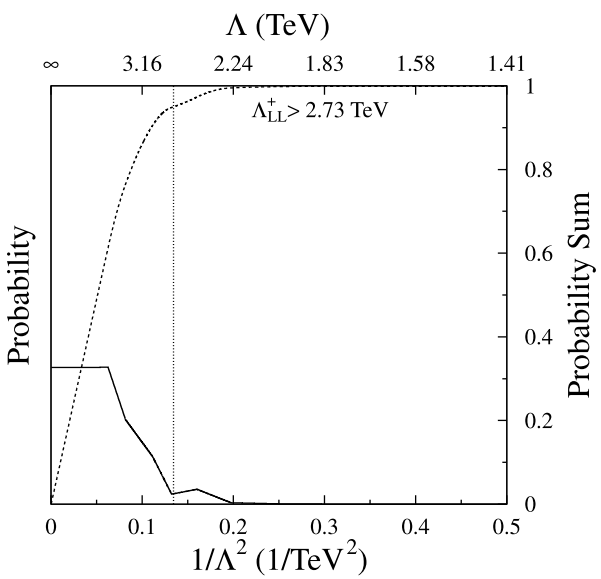

FIG. 98. The probability distribution (solid curve) $P(\sigma|\xi')P(\xi')/Q(\infty)$ for the theoretical prediction JETRAD with $\mu=E_T^{\rm max}$. The dashed curve shows the integral of the probability distribution and the dotted line shows the 95% C.L. limit on the compositeness scale, 2.73 TeV. The most probable value for the compositeness scale is $\Lambda^+_{LL}=\infty$.

TABLE XLIX. The 95% confidence level limits in TeV for the left-handed contact compositeness scales for different models.

PDF	Renorm. scale μ	Compositeness scale			
		Λ^+_{LL}		Λ^-_{LL}	
		$1/\Lambda^2$	$1/\Lambda^4$	$1/\Lambda^2$	$1/\Lambda^4$
CTEQ3M	$0.25E_T^{\rm max}$	3.51	3.21	2.87	2.80
CTEQ3M	$0.50E_T^{\rm max}$	2.93	2.45	2.56	2.38
CTEQ3M	$0.75E_T^{\rm max}$	2.88	2.43	2.52	2.36
CTEQ3M	$1.00E_T^{\rm max}$	2.73	2.38	2.49	2.35
CTEQ3M	$2.00E_T^{\rm max}$	2.84	2.39	2.48	2.35
CTEQ4M	$0.50E_T^{\rm max}$	2.92	2.45	2.55	2.38
CTEQ4A1	$0.50E_T^{\rm max}$	2.96	2.47	2.55	2.38
CTEQ4A2	$0.50E_T^{\rm max}$	2.74	2.39	2.53	2.36
CTEQ4A4	$0.50E_T^{\rm max}$	2.76	2.40	2.54	2.37
CTEQ4A5	$0.50E_T^{\rm max}$	2.96	2.47	2.58	2.39
CTEQ4HJ	$0.50E_T^{\rm max}$	2.87	2.42	2.58	2.38
MRS(A′)	$0.50E_T^{\rm max}$	2.97	2.47	2.59	2.39
MRST	$0.50E_T^{\rm max}$	3.00	2.50	2.58	2.39
MRST($g\uparrow$)	$0.50E_T^{\rm max}$	3.00	2.50	2.57	2.39
MRST($g\downarrow$)	$0.50E_T^{\rm max}$	2.93	2.45	2.57	2.38

ACKNOWLEDGMENTS

We thank the staffs at Fermilab and collaborating institutions, and acknowledge support from the Department of Energy and National Science Foundation (USA), Commissariata L'Energie Atomique and CNRS/Institut National de Physique Nucléaire et de Physique des Particules (France), Ministry for Science and Technology and Ministry for Atomic Energy (Russia), CAPES and CNPq (Brazil), Departments of Atomic Energy and Science and Education (India), Colciencias (Colombia), CONACyT (Mexico), Ministry of Education and KOSEF (Korea), CONICET and UBACyT

TABLE L. 95% confidence level limits in TeV for different contact compositeness scale for different models calculated using an analytic LO prediction [38] (see Sec. IV B for a description of the models).

Model	Interference term X	
	+1	−1
Λ^X_{LL}	2.2	2.2
Λ^X_V	3.2	3.1
Λ^X_A	3.2	3.1
$\Lambda^X_{(V-A)}$	2.7	2.7
$\Lambda^X_{V_8}$	2.0	2.3
$\Lambda^X_{A_8}$	2.1	2.1
$\Lambda^X_{(V-A)_8}$	1.7	1.9

(Argentina), The Foundation for Fundamental Research on Matter (The Netherlands), PPARC (United Kingdom), A.P. Sloan Foundation, and the A. von Humboldt Foundation.

APPENDIX: χ^2 STUDIES

In this paper we have made quantitative χ^2 comparisons between theoretical predictions and data to determine which predictions provide better agreement. The systematic uncertainties in the inclusive jet cross section (Secs. XI and XII) and the dijet mass spectrum (Sec. XIV) are highly correlated. An inappropriate definition of the uncertainties in χ^2 analyses may result in theoretical predictions that have an average normalization below the data yielding a better fit (Peelle's Pertinent Puzzle [60]). The first section of this appendix describes alternative methods for calculating the χ^2 and our choice of an appropriate method. The second section describes studies of the probability distributions for the analyses presented in this paper.

1. Definition of χ^2

The χ^2 is given by

$$\chi^2=\sum_{i,j}\ \delta_i V_{ij}^{-1}\delta_j\,, \tag{A1}$$

where δ_i is the difference between the data and the expected cross section for bin i, and V_{ij} is element i,j of the covariance matrix, with each element given by

$$V_{ij}=\rho_{ij}(\Delta\sigma_i^{\rm stat}\Delta\sigma_j^{\rm stat}\delta_{ij}+\Delta\sigma_i^{\rm sys}\Delta\sigma_j^{\rm sys}) \tag{A2}$$

where δ_{ij} is the Kronecker delta function, $\rho_{ij}=1$ for $i=j$, and ρ_{ij} is the correlation of the systematic uncertainties between cross section bins i and j.

The analyses presented in this paper are based on using the fractional systematic uncertainties in each bin, but there are several ways of calculating the impact of the absolute systematic uncertainty on the χ^2 values. We can use:

(1) Fractional uncertainty multiplied by the observed cross section.

(2) The fractional uncertainty multiplied by a smooth fit to the observed cross section [61] (which is normalized to the observed integrated cross section).

(3) The fractional uncertainty multiplied by a theoretical prediction.

This appendix discusses these choices. In previous publications of the inclusive jet cross section [8] and the dijet mass spectrum [25] the χ^2 values were calculated using the first option.

The choice of calculation for the absolute systematic uncertainty used in the χ^2 is investigated using the measurement of the dijet mass spectrum (Sec. XIV). A theoretical prediction, called the ansatz (A), based on a fit to the observed cross section (Fig. 86) is obtained by normalizing the fit to the observed integrated cross section [cf. option (2)]. We also define a floating ansatz (FA) through a multiplicative factor X that is used to change the normalization of the ansatz (FA$=X$A). A comparison between the ansatz and the data is given in Fig. 99.

If the systematic uncertainty is given by the product of the fractional uncertainty and the observed cross section in each bin [option (1)], the minimum value of the χ^2 of the floating ansatz is obtained for a normalization of $X=0.965$ (the dashed line in Fig. 99). This is clearly not the best visual fit to the observed cross section. When this test is repeated using option (2), the preferred normalization is $X=1.0$ (Fig. 100). Using several different predictions from JETRAD [option (3)] also yields $X=1.0$ as a best fit (not shown).

Calculating systematic uncertainties using the observed cross section per bin introduces a statistical component to the systematic uncertainty; i.e., when the cross section fluctuates to a small value in a given bin the absolute systematic uncertainty also fluctuates to a smaller value. The smaller values of cross section therefore appear to be more precise relative to any given theory. This bias has been called Peelle's Pertinent Puzzle [60].

We choose to rely on options (2) and (3) for determining systematic uncertainties. The choice depends on the question that is posed. In our work we wish to "Determine the probability that the theoretical prediction could have produced the observed number of events." This requires that we determine the systematic uncertainties using the theoretical predictions [option (3)]. For example, if we underestimated the integrated luminosity the number of predicted events would also be underestimated.

This choice of χ^2 definition means that the current results differ from those published previously for the inclusive jet cross section [8] and the dijet mass spectrum [25]. Table LI summarizes the differences in χ^2 values for the dijet mass analysis. The χ^2 values in Table LI are calculated using the same luminosity definition as given in Ref. [25], and differ from those given in Table XLVIII. The χ^2 changes most for theoretical predictions with the largest normalization differences with the data. If the theoretical prediction has a smaller normalization than the data then the size of the systematic uncertainties are reduced, hence increasing the value of the χ^2.

2. Probabilities

The probability that a given theoretical prediction agrees with the data for a given χ^2 is calculated assuming that the χ^2 is given by the standard distribution [62]

$$f(x;n)=\frac{x^{(n/2-1)}\exp(-x/2)}{2^{n/2}\Gamma(n/2)}, \tag{A3}$$

where n is the number of degrees of freedom (DOF) in the data. The probability of getting a value of χ^2 larger than the one obtained is then given by

$$P(\chi^2;n)=\int_{\chi^2}^{\infty} f(x;n)dx. \tag{A4}$$

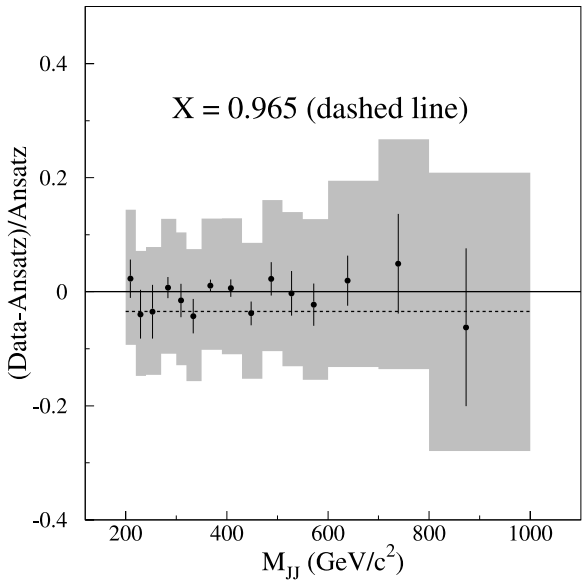

FIG. 99. The difference between the dijet mass cross section for $|\eta_{1,2}|<1.0$ and the ansatz (see text). The dashed line shows the best fit obtained by using the standard χ^2 and absolute systematic uncertainties obtained using the product of the fractional systematic uncertainties and the measured cross section in each bin [option (1)].

Hence, for the probabilities quoted in Secs. XI and XIV to be reliable, the χ^2 distribution for comparisons between theoretical predictions and the data must follow Eq. (A3).

The distribution of χ^2 for comparisons with the dijet mass spectrum was tested by developing a Monte Carlo program that generates many trial predictions based on the ansatz

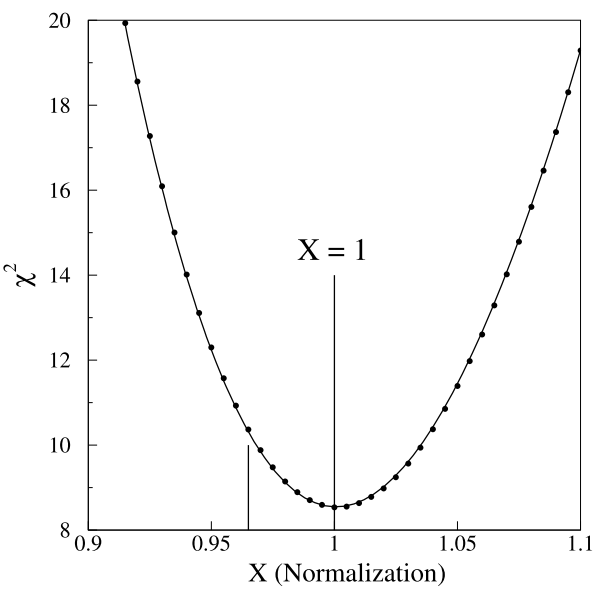

FIG. 100. The χ^2 for the ansatz as a function of the floating normalization X for option (2) (see text). The minimum χ^2 is obtained for a normalization of $X=1.0$. The short vertical line indicates a normalization of $X=0.965$, illustrating the bias of option (1).

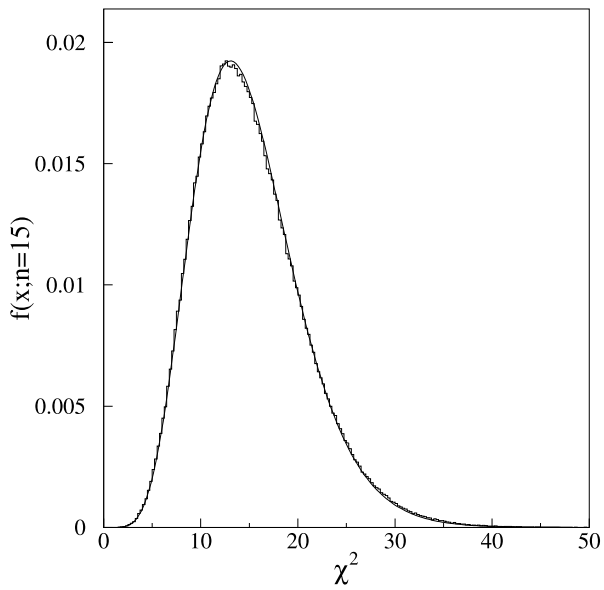

FIG. 101. The χ^2 distribution generated by sampling the ansatz cross section using only statistical fluctuations. The histogram shows the generated distribution, and the curve is a fit to the histogram using Eq. (A3). The fitted number of degrees of freedom is 15.08.

(with a total of 15 bins, or 15 degrees of freedom). The first step is to generate trials based on statistical fluctuations. The *true* number of events per bin is given by the ansatz. The trial spectra are then generated for each bin by sampling a Poisson distribution with a mean defined by the *true* number of events. The χ^2 for each of these trials is calculated using the difference between the *true* and the generated values.

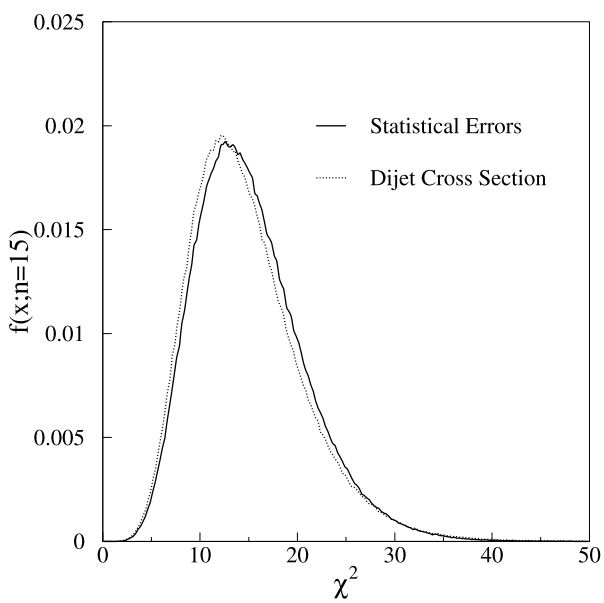

FIG. 102. The χ^2 distribution generated by sampling the ansatz cross section using only statistical fluctuations (solid curve), and fluctuations based on the uncertainties in the dijet cross section as a function of dijet mass (dotted curve).

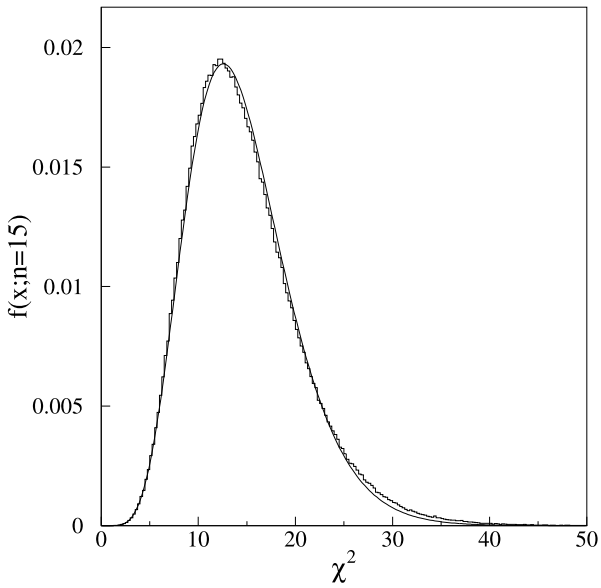

FIG. 103. The χ^2 distribution generated by sampling the ansatz cross section using all of the systematic uncertainties of the dijet cross section. The histogram shows the generated distribution and the curve is a fit to the histogram using Eq. (A3). The fitted number of degrees of freedom is 14.6 ± 0.2.

Figure 101 shows the χ^2 distribution for all of the generated trials. The distribution is fitted to Eq. (A3), with the best fit obtained for $n=15.08\pm0.20$, which is consistent with the expected value of $n=15$ for a normalized distribution of bins.

The final step is to assume that the uncertainties are the same as the uncertainties in the measurement of the dijet cross section. Trial spectra are generated using these uncertainties in order to obtain a χ^2 distribution (see the dotted curve in Fig. 102). It is clear that the χ^2 distribution is very similar to that predicted by Eq. (A3); hence any probability

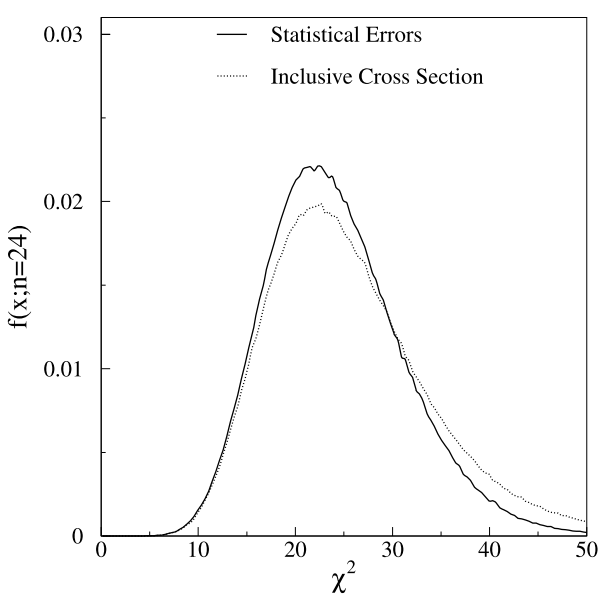

FIG. 104. The χ^2 distribution generated by sampling the inclusive jet cross section ansatz using only statistical fluctuations (solid curve), and fluctuations based on the uncertainties in the inclusive jet cross section (dotted curve).

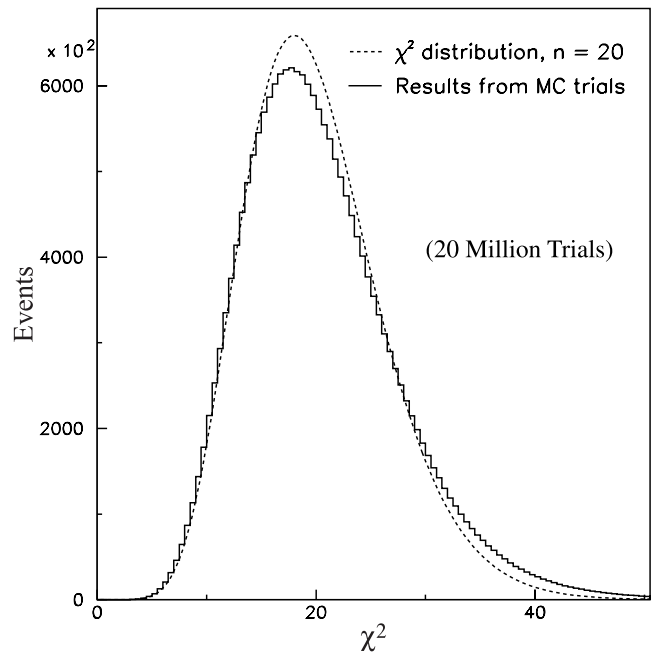

FIG. 105. The χ^2 distribution generated by sampling the ratio of inclusive jet cross sections ansatz using only statistical fluctuations (solid curve), and fluctuations based on the uncertainties in the inclusive jet cross section (dotted curve).

TABLE LI. The χ^2 for the cross section in dijet mass for $|\eta^{\rm jet}|<1.0$ (15 degrees of freedom).

PDF	μ	Published χ^2 [25]		Updated χ^2	
		χ^2	Probability	χ^2	Probability
CTEQ3M	$0.25E_T^{\max}$	12.2	0.66	28.9	0.02
CTEQ3M	$0.50E_T^{\max}$	5.0	0.99	5.8	0.98
CTEQ3M	$0.75E_T^{\max}$	5.3	0.99	5.9	0.98
CTEQ3M	$1.00E_T^{\max}$	5.4	0.99	6.1	0.98
CTEQ3M	$2.00E_T^{\max}$	4.2	1.00	6.4	0.97
CTEQ3M	$0.25\sqrt{x_1x_2s}$	8.6	0.90	14.6	0.48
CTEQ3M	$0.50\sqrt{x_1x_2s}$	4.8	0.99	6.8	0.96
CTEQ3M	$1.00\sqrt{x_1x_2s}$	5.1	0.99	8.9	0.88
CTEQ4M	$0.50E_T^{\max}$	4.9	0.99	6.3	0.97
CTEQ4A1	$0.50E_T^{\max}$	5.0	0.99	6.5	0.97
CTEQ4A2	$0.50E_T^{\max}$	5.7	0.99	7.2	0.95
CTEQ4A4	$0.50E_T^{\max}$	4.9	0.99	6.4	0.97
CTEQ4A5	$0.50E_T^{\max}$	4.8	0.99	6.2	0.98
CTEQ4HJ	$0.50E_T^{\max}$	5.4	0.99	6.8	0.96
MRS(A′)	$0.50E_T^{\max}$	6.3	0.97	6.9	0.96
MRST	$0.50E_T^{\max}$	6.2	0.98	10.9	0.76
MRST($g\uparrow$)	$0.50E_T^{\max}$	6.3	0.97	9.6	0.84
MRST($g\downarrow$)	$0.50E_T^{\max}$	6.5	0.97	16.7	0.33

generated using Eq. (A4) should be approximately right. The resulting χ^2 distribution was fitted using Eq. (A3) (Fig. 103) and yielded $n = 14.6 \pm 0.2$.

The study of the χ^2 distribution was repeated for the measurement of the inclusive jet cross section, which has 24 bins (DOF). Figure 104 shows the resulting distributions for statistical fluctuations (solid curve) and the systematic uncertainties in the inclusive jet cross section (dotted curve). The two distributions agree for χ^2 values below approximately 15, and then begin to diverge. The distribution based on the cross section uncertainties has a longer tail than the statistical χ^2 distribution. This implies that all the probabilities quoted in Sec. XI are slightly underestimated.

Finally, the ratio of inclusive jet cross sections (Sec. XII) was also examined with the results of the study given in Fig. 105. The resulting distribution is similar to the one obtained for the inclusive jet cross section, with the distribution based on the uncertainties having a larger tail than the standard χ^2 distribution. The maximum deviation between the probability obtained assuming the standard distribution and the measured distribution is 2.9%, and probabilities quoted in Sec. XII will therefore be slight underestimates of the correct probabilities.

The studies presented describe the χ^2 comparisons made between the observed data and the theoretical predictions. We have demonstrated that they give an accurate representation of the probability of agreement between a given theoretical prediction and the data.

[1] M. Gell-Mann, Phys. Lett. **8**, 214 (1964); G. Zweig, CERN report 8182/Th 401, 1964; G. Zweig, CERN report 8419/Th 412, 1964, reprinted in *Developments in Quark Theories of Hadrons*, edited by D.B. Lichtenberg and S.P. Rosen (Hadronic Press, Nonamtum, MA, 1980), Vol. 1, p. 22.

[2] J.I. Friedman, H.W. Kendall, and R.E. Taylor, Rev. Mod. Phys. **63**, 629 (1991).

[3] R.K. Ellis, W.J. Stirling, and B.R. Webber, *QCD and Collider Physics*, Cambridge Monographs on Particle Physics, Nuclear Physics and Cosmology: 8 (Cambridge University Press, Cambridge, England, 1996), p. 435, and references therein.

[4] UA1 Collaboration, G. Arnison *et al.*, Phys. Lett. B **172**, 461 (1986).

[5] UA2 Collaboration, J. Alitti *et al.*, Phys. Lett. B **257**, 232 (1990); UA2 Collaboration, J. Alitti *et al.*, Z. Phys. C **49**, 17 (1991).

[6] CDF Collaboration, F. Abe *et al.*, Phys. Rev. Lett. **70**, 1376 (1993).

[7] CDF Collaboration, F. Abe *et al.*, Phys. Rev. Lett. **77**, 438 (1996). Preliminary results from an extended data set have been shown by CDF; we compare to the CDF data which have been published.

[8] DØ Collaboration, B. Abbott *et al.*, Phys. Rev. Lett. **82**, 2451 (1999).

[9] AFS Collaboration, T. Akesson *et al.*, Phys. Lett. **118B**, 185 (1982).

[10] UA2 Collaboration, M. Banner *et al.*, Phys. Lett. **118B**, 203 (1982).

[11] F. Aversa, M. Greco, P. Chiappetta, and J.P. Guillet, Phys. Rev. Lett. **65**, 401 (1990).

[12] S.D. Ellis, Z. Kunszt, and D.E. Soper, Phys. Rev. Lett. **64**, 2121 (1990); Z. Kunszt and D.E. Soper, Phys. Rev. D **46**, 192 (1992).

[13] W.T. Giele, E.W.N. Glover, and D.A. Kosower, Nucl. Phys. **B403**, 633 (1993). We used JETRAD version 2.0.

[14] H.L. Lai *et al.*, Phys. Rev. D **55**, 1280 (1997), and references therein.

[15] A.D. Martin, R.G. Roberts, W.J. Stirling, and R.S. Thorne, Eur. Phys. J. C **4**, 463 (1998), and references therein.

[16] B. Abbott *et al.*, Eur. Phys. J. C **5**, 687 (1998).

[17] E. Eichten, K. Lane, and M.E. Peskin, Phys. Rev. Lett. **50**, 811 (1983); E. Eichten, I. Hinchcliffe, K. Lane, and C. Quigg, Rev. Mod. Phys. **56**, 579 (1984); **58**, 1065 (1986) (Addendum); K. Lane, hep-ph/9605257.

[18] CDF Collaboration, F. Abe *et al.*, Phys. Rev. D **48**, 998 (1993).

[19] CDF Collaboration, F. Abe *et al.*, Phys. Rev. Lett. **77**, 5336 (1996); **78**, 4307(E) (1997); **69**, 2896 (1992); **62**, 3020 (1989).

[20] V.D. Elvira, Ph.D. thesis, Universidad de Buenos Aires, 1995.

[21] DØ Collaboration, B. Abbott *et al.*, Phys. Rev. Lett. **86**, 2523 (2001).

[22] J. Krane, Ph.D. thesis, University of Nebraska, 1998.

[23] DØ Collaboration, B. Abbott *et al.*, Phys. Rev. Lett. **80**, 666 (1998).

[24] K. Fatyga, Ph.D. thesis, University of Rochester, 1996.

[25] DØ Collaboration, B. Abbott *et al.*, Phys. Rev. Lett. **82**, 2457 (1999).

[26] DØ Collaboration, B. Abbott *et al.*, Phys. Rev. Lett. **86**, 1707 (2001); L. Babukhadia, Ph.D. dissertation, University of Arizona, Tucson, 1999 (http://fnalpubs.fnal.gov/techpubs/theses.html). See EPAPS Document No. EPAPS:E-PRLTAO-86-054109 for data from this analysis. This document may be retrieved via the EPAPS homepage (http://www.aip.org/pubservs/epaps.html) or from ftp.aip.org in the directory /epaps/. See the EPAPS homepage for more information.

[27] Particle Data Group, D.E. Groom *et al.*, Eur. Phys. J. C **15**, 1 (2000), and references therein.

[28] DØ Collaboration, S. Abachi *et al.*, Nucl. Instrum. Methods Phys. Res. A **338**, 185 (1994).

[29] M. Abolins *et al.*, Nucl. Instrum. Methods Phys. Res. A **280**, 36 (1989); DØ Collaboration, S. Abachi *et al.*, *ibid.* **324**, 53 (1993); DØ Collaboration, H. Aihara *et al.*, *ibid.* **325**, 393 (1993).

[30] J. Huth *et al.*, in *Proceedings of Research Directions for the Decade*, Snowmass, 1990, edited by E.L. Berger (World Scientific, Singapore, 1992).

[31] S.D. Ellis, Z. Kunszt, and D.E. Soper, Phys. Rev. Lett. **69**, 3615 (1992).

[32] B. Abbott *et al.*, Fermilab-Pub-97/242-E.

[33] G. Marchesini *et al.*, Comput. Phys. Commun. **67**, 465 (1992). We used HERWIG version 5.8.

[34] DØ detector simulation package based on GEANT. GEANT by R. Brun and F. Carminati, CERN Program Library Long Writeup W5013, 1993.
[35] H.L. Lai *et al.*, Phys. Rev. D **51**, 4763 (1995).
[36] A.D. Martin, R.G. Roberts, and W.J. Stirling, Phys. Lett. B **354**, 154 (1995).
[37] A.D. Martin, R.G. Roberts, W.J. Stirling, and R.S. Thorne, Eur. Phys. J. C **14**, 133 (2000); H.L. Lai *et al.*, *ibid.* **12**, 375 (2000).
[38] R.S. Chivukula, A.G. Cohen, and E.H. Simmons, Phys. Lett. B **380**, 92 (1996).
[39] E.H. Simmons, Phys. Lett. B **226**, 132 (1989); **246**, 471 (1990); P. Cho and E.H. Simmons, *ibid.* **323**, 401 (1994); Phys. Rev. D **51**, 2360 (1995).
[40] E.H. Simmons, Phys. Rev. D **55**, 1678 (1997).
[41] CDF Collaboration, F. Abe *et al.*, Phys. Rev. D **55**, 5263 (1997).
[42] DØ Collaboration, B. Abbott *et al.*, Phys. Rev. D **61**, 072001 (2000).
[43] J. Bantly *et al.*, Fermilab-TM-2000, 1997.
[44] N. Amos *et al.*, Phys. Lett. B **242**, 158 (1990).
[45] CDF Collaboration, F. Abe *et al.*, Phys. Rev. D **50**, 5550 (1994).
[46] E811 Collaboration, C. Avila *et al.*, Phys. Lett. B **445**, 419 (1999).
[47] UA4 Collaboration, M. Bozzo *et al.*, Phys. Lett. **147B**, 4 (1984); UA4 Collaboration, D. Bernard *et al.*, Phys. Lett. B **186**, 2 (1987).
[48] CDF Collaboration, F. Abe *et al.*, Phys. Rev. D **50**, 5550 (1994).
[49] P. Aurenche *et al.*, Phys. Rev. D **45**, 92 (1992); F.W. Bopp, A. Capella, J. Ranft, and J. Tran Thanh Van, Z. Phys. C **51**, 99 (1991).
[50] T.L. Taylor Thomas, Ph.D. thesis, Northwestern University, 1997.
[51] DØ Collaboration, B. Abbott *et al.*, Nucl. Instrum. Methods Phys. Res. A **424**, 352 (1999).
[52] R. Wigmans, in *Experimental Techniques in High-Energy Nuclear and Particle Physics*, edited by T. Ferbel (World Scientific, Singapore, 1991).
[53] R. Snihur, Ph.D. thesis, Northwestern University, 2000; DØ Collaboration, B. Abbott *et al.*, Nucl. Phys. B (Proc. Suppl.) **79**, 494 (1999).
[54] G.D. Lafferty and T.R. Wyatt, CERN-PPE/94-72, 1994.
[55] See EPAPS Document No. E-PRVDAQ-64-006115 for cross sections and covariance matrices. This document may be retrieved via the EPAPS homepage (http://www.aip.org./pubservs/epaps.html) or from ftp.aip.org in the directory /epaps/. See the EPAPS homepage for more information.
[56] H. Jeffreys, *Theory of Probability* (Clarendon, Oxford, 1939, revised 1988), p. 94; F.T. Solmitz, Annu. Rev. Nucl. Sci. **14**, 375 (1964).
[57] T. Sjöstrand, Comput. Phys. Commun. **82**, 74 (1994). We used PYTHIA version 5.7.
[58] F. James, CERN Program Library Entry D506. We used MINUIT version 96.a.
[59] I.A. Bertram and E.H. Simmons, Phys. Lett. B **443**, 347 (1998).
[60] G. D'Agostini, hep-ph/9512295 v3, pp. 88–91.
[61] E. Kovacs (private communication).
[62] Particle Data Group, C. Caso *et al.*, Eur. Phys. J. C **3**, 1 (1998).